USING DETRITAL-ZIRCON GEOCHRONOLOGY AND (U-Th)/He THERMOCHRONOLOGY TO RE-EVALUATE THE TRIASSIC-JURASSIC TECTONIC SETTING OF NORTHERN LAURENTIA, CANADIAN ARCTIC

Derrick Midwinter

Thesis submitted to the

Faculty of Graduate and Postdoctoral Studies

in partial fulfillment of the requirements

for the M.Sc. degree in Earth Sciences

Ottawa-Carleton Geoscience Centre

Faculty of Science

University of Ottawa

Abstract

New geochronological and field data were examined from Triassic-Jurassic strata in the Sverdrup Basin, Arctic Canada. Detailed analysis of detrital-zircon data identified a pronounced near-syndepositional age-fraction in Triassic strata, which significantly is absent in Jurassic strata of the Sverdrup Basin suggesting a protracted history of magmatism and sediment dispersal from areas north of the basin during the Triassic. However, as a result of rifting, during the Early Jurassic, the northern source region became disconnected from the Sverdrup Basin, and opened the precursor basin (Amerasia Basin) to the Arctic Ocean.

Jurassic rifting of the Amerasia Basin would have had associated rift-flank uplift. Time-temperature models produced from zircon (U-Th)/He thermochronological data elucidate the unknown thermal history between the regional Devonian-Cretaceous unconformity in the southwestern Canadian Arctic suggesting ~4 km of addition deposition on Banks Island and ≤1 km of deposition towards the craton interior.

Résumé

Des nouvelles données géochronologiques et de terrain ont été examinées sur des roches sédimentaires d'âge Triasique-Jurassique dans le bassin Sverdrup de l'Arctique Canadien. Les analyses de données sur des zircons détritiques ont déterminées un âge synsédimentaire de la période Triasique qui est absente dans les roches jurassiques. Une histoire de magmatisme prolongée et de transport de sédiments des zones au nord du bassin a été conçue grâce aux données recueillies. Lors du développement du bassin d'Amerasia au début du Jurassique, la région d'origine des sédiments du nord c'est déconnecté du bassin Sverdrup.

L'extension du bassin de l'Amerasia pendant le Jurassique a été accompagnée du soulèvement de failles normales. Des modèles temps-température produits à partir des données de zircons (U-Th)/He thermochronologique ont résolu l'histoire thermique inconnue entre la discordance du Dévonien-Crétacé dans le sud-ouest de l'Arctique Canadien. Les données suggèrent la déposition ~4 km de sédiments sur l'Île de Banks et ≤1 km vers le craton intérieur.

Extended Abstract

New detrital-zircon U-Pb age data from Lower Triassic to Lower Jurassic strata from the Sverdrup Basin, in the Canadian Arctic, combined with previously published detrital-zircon data from the Sverdrup Basin have identified two distinct provenance signatures. The first assemblage is identical to the Devonian clastic wedge, and here is termed the recycled source. In contrast, a second assemblage is dominated by a broad spectrum of near-syndepositional Permian-Triassic ages derived from north of the basin, and here is termed the active margin source. Coeval strata in Yukon and Arctic Alaska exhibit a similar dual provenance signature. Previous studies have suggested that the source of these Permian-Triassic ages could be the Siberian Traps and Urals mountains, however, the former region would produce too narrow a range of ages, and zircons from the northernmost Urals do not form after the Permian.

Hafnium isotopic data from Permian-Triassic zircons exhibit εHf values consistent with the common evolved crustal signature of the Devonian clastic wedge detrital-zircon grains and Neoproterozoic-Paleozoic basement rocks in the Arctic Alaska-Chukotka microcontinent. Furthermore, newly identified volcanic ash beds throughout the Triassic section from the northern part of the Sverdrup Basin suggests a protracted history of magmatism to the north of the basin. We interpret that these zircon were sourced from a magmatically-active region to the north of the Sverdrup Basin, and which probably was part of a convergent margin fringing northern Laurentia from the northern Cordillera along the outboard edge of the Arctic Alaska-Chukotka microcontinent. Jurassic rifting isolated the Permian-Triassic source from the Sverdrup Basin and separated the northern landmass from the Sverdrup Basin, creating the Amerasia Basin.

The rifting to the north of the Sverdrup Basin would have had associated flank uplift on the rift shoulders. In the area fringing the basin in the southwestern Canadian Arctic, zircon (U-Th)/He thermochronology tests the extent of burial and/or uplift from two opposing thermal histories, 1) maximum burial occurred after deposition in the Devonian with protracted uplift in the late Paleozoic-Mesozoic, or 2) maximum burial occurred after protracted burial through the late Paleozoic-early Mesozoic with rapid uplift associated with Jurassic rifting. Forward modelling suggests that between the regional Devonian-Cretaceous unconformity, ~4 km to ≤1 km of strata is missing from the rifted Arctic margin towards the cratonic interior, respectively.

Acknowledgements

This project could not have been completed without the support of many individuals from different organizations. First and foremost, I'd like to thank my supervisors Dr. Thomas Hadlari and Dr. Bill Arnott for their continued guidance. Thomas Hadlari provided a strong vision throughout the process, offered unparalleled support and dealt with my puzzlement of where the project was going at times. Bill Arnott allowed a great environment for scientific discussion and always left me reinvigorated about my work when at times I was disenchanted with the research. I could not have asked for better advisors which made this project a truly positive experience.

I need to thank the folks at the Geological Survey of Canada SHRIMP lab, specifically Drs. Tom Pestaj, Nicole Rayner and most of all, Bill Davis, who were instrumental in the collection of detrital-zircon data. Many thanks to Dr. Keith Dewing, not only for planning and funding the field program required for this MSc, but for his continued mentorship over the years, for always being there to bounce ideas off of and for providing encouragement. Thanks to Dr. Rob Rainbird for being keen to have helpful discussions on southwestern Arctic geology. GSC's GEM program and the Polar Continental Shelf Project were vital for their logistical and financial support of this thesis. Furthermore, I thank my field assistants Kyle Sulphur and Pilipoosie Iqaluk for enduring my reign as camp-leader.

I am indebted to Jeremy Powell and his fervent guidance of the thermochronological method. This component of the thesis was able to be completed thanks in large part to his wonderful patience when teaching me the models and methods, and from Dr. David Schneider who generously gave his time, even though he was not my supervisor, to edit and provide direction on the manuscript and fund laboratory work.

Regardless of the fact that we were working on wildly removed topics, the Windermere research group was an excellent environment to be stationed in during my time at uOttawa. Huge thanks to the group, Curran, Dave, Dylan, Gerry, Lilian, Mike, Natasa, Viktor, and especially to my two amazing office-mates Katrina Angus and Anika Bergen for always being there to hear me drone on about my trials and tribulations in life or academia.

Lastly, I would like to thank my brothers and parents, Calvin, Nigel, James and Pam, who instilled my sense of curiosity with the world; they have had a truly profound impact on my life.

Thank you.

Table of Contents

Abstract ... ii

Résumé ... iii

Extended Abstract ... iv

Acknowledgements ... vi

Table of Contents ... viii

List of Figures ... xi

List of Tables ... xvi

CHAPTER 1 : Thesis Introduction ... 1

1.1 Thesis Rationale ... 1

1.2 Geologic Setting of Northern Laurentia ... 4

1.3 Study Area and Previous Work ... 6

1.4 Thesis Objectives and Structure ... 8

1.5 Methods ... 8

1.6 Statement of Contributions ... 9

CHAPTER 2 : Dual Provenance Signatures of the Triassic Northern Laurentian Margin from Detrital-Zircon U-Pb and Hf-Isotope Analysis of Triassic-Jurassic Strata in the Sverdrup Basin ... 11

2.0 Abstract ... 11

2.1 Introduction ... 12

2.2 Geologic Setting ... 14

2.2.1 Sverdrup Basin ... 14

2.2.2 Paleogeographic Restoration ... 18

2.2.3 Summary of Published U-Pb and Sm-Nd Provenance Data ... 21

2.2.4 Igneous Record of the Sverdrup Basin ... 23

2.3 Analytical Procedures ... 24

2.3.1 U-Pb Geochronology ... 24

2.3.2 Hafnium-Isotope Methods ... 26

2.4 Results ... 28

2.4.1 U-Pb Analyses ... 28

2.4.1.1 Bjorne Formation 28
2.4.1.2 Romulus Member of the Heiberg Formation 28
2.4.1.3 King Christian Formation of the Heiberg Group 29
2.4.2 Hf-Isotope Analyses 30
2.4.3 Volcanic Ash Beds 30
2.5 Discussion 31
2.5.1 Early Triassic Detrital-Zircon Provenance 31
2.5.2 Late Triassic Detrital-Zircon Provenance 35
2.5.3 Yukon Tanana Terrane 38
2.5.4 Provenance of Permian-Triassic Zircon 39
2.5.5 Early Jurassic Detrital-Zircon Provenance 41
2.5.6 Tectonic Setting of the Basin 43
2.6 Conclusion 44

CHAPTER 3 : Investigating the Paleozoic-Mesozoic Low-Temperature Thermal History of the Southwestern Canadian Arctic: Insights from (U-Th)/He Thermochronology 46
3.0 Abstract 46
3.1. Introduction 47
3.2 Geological Setting 49
3.2.1 Previous Thermal Modelling Studies 53
3.2.2 Regional Detrital-Zircon Geochronology Studies 55
3.3 (U-Th)/He Thermochronology 57
3.4 Analytical Methods 59
3.5 Analytical Results and Numerical Modelling 61
3.5.1 Zircon (U-Th)/He Dating 61
3.5.2 Banks Island 63
3.5.3 Victoria Island 68
3.5.4 Brock Inlier 72
3.6 Discussion 75
3.7 Conclusion 79

CHAPTER 4 : Thesis Conclusions and Areas for Future Research 81
4.1 Conclusions 81
4.2 Areas for Future Research 83

REFERENCES 86

APPENDICES

Appendix A: Detrital-Zircon Sample Information 112

Appendix B: U-Pb Geochronology 114

Appendix C: Zircon Hf Isotopic Data 118

Appendix D: Detrital-Zircon Spot Images 121

List of Figures

Figure 1.1: Map of the Arctic depicting names and locations of basins and regions mentioned in text. AA – Arctic Alaska; AACM – Arctic Alaska-Chukotka microcontinent; CH – Chukotka; PE – Pearya. Outline of AACM (black line) from Drachev (2011). Rotation of AACM away from the Canadian margin illustrated by black arrows (from Embry, 2000). Sverdrup Basin outline from Embry and Beauchamp (2008); Franklinian Basin from Anfinson et al. (2013); Arctic Platform from Dewing and Obermajer (2009); Amundsen Basin from Rainbird et al. (1996); Sverdrup Rim from Meneley et al. (1975). Blue circles represent detrital zircon (U-Th)/He samples for this study (Chapter 3); red circles represent detrital zircon U-Pb samples for this study (Chapter 2). 2

Figure 2.1: Circum-Arctic orogens, terranes, and locations modified from Colpron and Nelson (2011) and Pease et al. (2014). AA, Arctic Alaska; AACM, Arctic Alaska-Chukotka Microplate; CH, Chukotka; NSI, New Siberian Islands; NZ, Novaya Zemlya; PE, Pearya; SAS, South Anyui Suture Zone; SV, Svalbard; WI, Wrangel Island; YTT, Yukon Tanana Terrane. Black circles represent approximate detrital zircon sample locations from AA (Miller et al., 2006; Gottlieb et al., 2014); CH (Miller et al., 2006; Tuchkova et al., 2011; Amato et al., 2015); WI (Miller et al., 2010); and YTT (Beranek et al., 2010b; Beranek and Mortensen, 2011). The outlines of the SAS and AACM are from Drachev (2011). Red circles represent approximate location of εNd or εHf values from AA (Amato et al., 2009); Arctic Canada (Anfinson et al., 2012b; Morris, 2013); New Siberian Islands (Akinin et al., 2015), and Siberia (Malitch et al., 2010). 13

Figure 2.2: Sverdrup Basin map with detrital zircon sample and volcanic ash bed locations. Detrital zircon data references from Isachsen Formation (Røhr et al., 2010); Sandy Point and Deer Bay formations (Omma et al., 2011); Pat Bay Formation (Miller et al., 2006; Omma et al., 2011 – both from approximately the same location); Bjorne Formation (Miller et al., 2006 – location approximately the same as this study); Blind Fiord Formation (Omma et al., 2011). U-Pb data from Devonian clastic wedge (Anfinson et al., 2012a); εHf data from Devonian Clastic Wedge (Anfinson et al., 2012b). Lower Triassic strata: Blind Fiord Formation (brown); Bjorne Formation (orange). General southern outline of the Sverdrup Basin from Embry and Beauchamp (2008). Surface and sea bottom bedrock geology is from Okulitch (1991). The Sverdrup Rim was first described by Meneley et al. (1975)............... 15

Figure 2.3: Stratigraphic chart of the Sverdrup Basin modified from Embry and Beauchamp (2008); Paleozoic volcanics: Audhild (Trettin, 1988); Nansen (Mayr et al., 2002); ULV and Esayoo (Morris, 2013). Initial εNd values from sedimentary rocks show positive shift to more juvenile provenance in the Late Triassic and Late Cretaceous, and increased negative scatter in εNd values in the Early Cretaceous is from a greater contribution from basement rocks (Patchett et al., 2004). 17

Figure 2.4: General facies distribution during the Early Triassic (modified from figure 36.13 in Embry, 2011); Late Triassic (modified from figure 36.20 in Embry, 2011); and latest Triassic (modified from figure 14 in Embry and Beauchamp, 2008). Arrows represent general sediment transport direction, based on Embry (1991, 2009). 19

Figure 2.5: Triassic to Middle Jurassic published detrital zircon age spectra. Sverdrup Basin sources are: Sandy Point Formation (Omma et al., 2011); Pat Bay Formation (Miller et al., 2006; Omma et al., 2011); Bjorne Formation (Miller et al., 2006); Blind Fiord Formation (Omma et al., 2011); Triassic of Chukotka (Miller et al., 2006; Tuchkova et al., 2011; Amato et al., 2015); Triassic of Wrangel Island (Miller et al., 2010); Triassic of North Slope, Alaska (Gottlieb et al., 2014); Triassic of Lisburne Hills, Alaska (Miller et al., 2006); Triassic of the YTT Platform (Beranek et al., 2010b); Triassic of the YTT Overlap (Beranek and Mortensen, 2011); Devonian clastic wedge (Anfinson et al., 2012a). See Appendix A for U-Pb detrital zircon sample location, number, age, and reference. 22

Figure 2.6: Relative probability distribution and cumulative probability plots for three new detrital zircon samples from this study. Kernel density estimation represented by solid grey line. See Appendix B for complete isotopic analyses and Appendix D for zircon images. .. 29

Figure 2.7: Plot shows εHf values for sample data from the Heiberg Formation. Only grains younger than 340 Ma were analyzed. Solid lines isolate depleted mantle (DM) and chondritic uniform mantle (CHUR). See Appendix C for error measurements. Dashed lines separate fields described as juvenile (0-5 epsilon units below DM), intermediate (5-12 epsilon units below DM), and evolved (>12 epsilon units below DM) following Bahlburg et al. (2011) and Gehrels and Pecha (2014). 30

Figure 2.8: (A) X-ray diffraction traces from volcanic ash beds; (B) Stratigraphic log from Bunde Fiord, Axel Heiberg Island highlighting stratigraphic location of volcanic ash beds. Ash beds not to scale. Location of Bunde Fiord highlighted by grey square in Figure 2.2; (C and D) Photographs of volcanic ash beds observed in Bunde Fiord, length of hammer is 50 cm. 32

Figure 2.9: Illustration of the detrital age spectra grouped by signatures of the *Recycled Source* and the *Active Margin Source*. Data from the Isachsen Fm (Røhr et al., 2010), from studies in the Canadian Arctic (Miller et al., 2006; Omma et al., 2011; Anfinson et al., 2012a), from Russia (Miller et al., 2006, 2010; Tuchkova et al., 2011; Amato et al., 2015), from Alaska (Miller et al., 2006; Gottlieb et al., 2014), from Yukon (Beranek et al., 2010b; Beranek and Mortensen, 2011), and compiled results from this study as (A) relative probability distributions and (B) cumulative probability plots. 34

Figure 2.10: (A) T_{DM} values from εHf, other than T_{DM} from Arctic Alaska and Esayoo volcanics which used T_{DM} from εNd values; (B) εHf values for sample data and relevant Hf isotope data comparisons. Grey box and black arrow represent interpreted average crustal evolution trajectories assuming present-day $^{176}Lu/^{177}Hf$ = 0.0093 (Vervoort and Patchett, 1996;

Bahlburg et al., 2011; Gehrels and Pecha, 2014). εNd values from Arctic Alaska and Esayoo volcanics converted to εHf (see Eq. 1; Vervoort et al., 1999) Data sets are as follows; detrital zircon from Neoproterozoic to Upper Devonian strata of the Franklinian Basin (Anfinson et al., 2012b); Carboniferous to Triassic zircon from igneous rocks of the northwestern Siberian Craton (Malitch et al., 2010); New Siberian Islands basement rocks (Akinin et al., 2015); Neoproterozoic to Devonian igneous rocks of Seward Peninsula, Arctic Alaska (Amato et al., 2009); Lower Permian Esayoo Volcanics from eastern Sverdrup Basin ca. 276 Ma, (Morris, 2013). See Appendix C for complete values and error for each sample and study area. 36

Figure 2.11: Evolution of the northern margin of Laurentia adapted from paleographical maps of Plafker and Berg (1994) and Nokleberg et al. (2000). Outline of YTT (orange polygon) is from Nelson et al. (2006). Axis of Hanna Trough and Arctic Alaska Basin is from Gottlieb et al. (2014). Proposed tectonic model: In the Triassic, the Sverdrup basin occupied a retro-arc position to Chukotka along strike with the Triassic basin adjacent to the Yukon Tanana terrane arc; Early Jurassic extension to form the proto-Amerasia basin cut off the Sverdrup Basin from the AACM; and in the Early Cretaceous during the post-rift stage of Sverdrup Basin, the Amerasia and Canada basins opened as the South Anyui Ocean closed. 42

Figure 3.1: Map of the Arctic depicting the names and location of basins and regions mentioned in the text. AA - Arctic Alaska; AACM - Arctic Alaska-Chukotka microcontinent; CH - Chukotka; PE – Pearya. Outline of AACM (black line) from Drachev (2011). Rotation of AACM away from the Canadian margin illustrated by the black arrows (from Embry, 2000). Sverdrup Basin from Embry and Beauchamp (2008); Franklinian Basin from Anfinson et al. (2013); Arctic Platform from Dewing and Obermajer (2009); Amundsen Basin from Rainbird et al. (1996). Red-dashed polygon identifies the location of map in Figure 3.2..... 50

Figure 3.2: Simplified lithotectonic map of south Arctic Islands and northwestern Laurentia (adapted from Ault et al., 2013) showing locations of (U-Th)/He samples dated in this study, (U-Th)/He apatite sample locations of Ault et al. (2009, 2013) within the Slave craton, and of Anfinson et al. (2013) within the Franklinian Basin. Outline of Arctic Alaska represents the restored position prior to the opening of proto-Amerasia Basin, based on Nokleberg et al. (2000). Large black arrow represents progressive late Paleozoic-early Mesozoic cooling/unroofing of the Slave craton, interpreted by Ault et al. (2013). Select wells (x) referenced from Issler et al. (2005, 2012), Dewing et al. (2007), and Dewing and Obermajer (2009). Banks graben is a Jurassic rift structure (Dewing and Obermajer, 2009). Sverdrup Basin outline from Embry and Beauchamp (2008). AACM – Arctic Alaska-Chukotka microcontinent; AP – Anderson Plain; EI – Eglinton Island; PP – Prince Patrick Island; WCSB – Western Canada Sedimentary Basin. 52

Figure 3.3: U-Pb detrital zircon spectra as reference for zircon inheritance for (U-Th)/He samples dated in this study: Banks Island – Devonian Parry Islands Formation (PI-8: Anfinson et al., 2012b); Victoria Island - Lower Cambrian sandstone (Sample C-E; Hadlari et al., 2012);

Brock Inlier - Neoproterozoic Nelson Head Formation on Victoria Island (Rayner and Rainbird, 2013); Neoproterozoic strata of the Shaler/Mackenzie Mountain Supergroup (Rainbird et al., 1992, 1996, 1997; Villeneuve et al., 1998).. 55

Figure 3.4: (U-Th)/He zircon date versus eU diagram, and (U-Th)/He zircon date versus equivalent spherical radius (ESR) diagram, separated by study area. Major tectonic events of northern Laurentia are highlighted by black boxes on the right. The three different deposition ages for the sample locations are indicated by a horizontal dotted black line. The large coloured polygons correspond to the duration of sediment accumulation within the basin (same colour scheme as Figure 3.1). 62

Figure 3.5: Forward thermal history models from Devonian strata of Banks Island using zircon (U-Th)/He data. Single zircon date and eU shown on each graph as squares with associated errors. The timing of the inheritance curves is derived from the U-Pb detrital studies (Fig. 3). Thermal model A has peak burial ca. 200 Ma; thermal model B has peak burial ca. 355 Ma. Time-temperature plot shows thermal pathways 1-3; Cretaceous burial of 2 km based on Dewing and Obermajer (2009). Forward models illustrate the expected ZHe inheritance date-eU curves for: (1) maximum temperature at 100ºC; (2) maximum temperature at 140ºC; (3) maximum temperature at 180ºC. Inheritance curves correspond to date-eU trends for zircon between 26-46 μm ESR, and describe the effect of the pre-depositional history and accumulated damage on ZHe dates. The solid line in each inheritance curve represents the projected date-eU trend for a zircon with a 36 μm ESR (mean value)................................. 67

Figure 3.6: (A) Vitrinite reflectance and RockEval Tmax data for Muskox D-87 well on Banks Island (Dewing et al., 2007). Blue diamonds are RockEval Tmax values (converted) and green squares are vitrinite reflectance (%Ro), EasyRo calibration used from Sweeney and Burnham (1990); (B) peak burial ca. 200 Ma; (C) peak burial ca. 355 Ma; corresponding best-fit curves (green line) using Basin Mod 5.4 software compared against t-T path 1 from Figure 5A and B (black line). 69

Figure 3.7: Forward thermal history models from Cambrian strata of Victoria Island using zircon (U-Th)/He data. Single zircon date and eU shown on each graph as square with associated error. The timing of the inheritance curves is derived from the U-Pb detrital-zircon studies (Fig. 3). Thermal model A has peak burial ca. 200 Ma; thermal model B has peak burial ca. 355 Ma. Time-temperature plot shows thermal pathways 1-3; passive margin sedimentation of 2 km based on Dewing et al. (2013); Devonian clastic thickness of 2 km based on Patchett et al. (2004); Cretaceous burial is interpreted. Forward models illustrate the expected ZHe inheritance date-eU curves for: (1) maximum temperature at 110ºC; (2) maximum temperature at 140ºC; (3) maximum temperature at 170ºC. Inheritance curves correspond to date-eU trends for zircon between 31-67 μm ESR, and describe the effect of the pre-depositional history and accumulated damage on ZHe dates. The solid line in each inheritance curve represents the projected date-eU trend for a zircon with a 45 μm ESR (mean value). 71

Figure 3.8: Forward thermal history models from Neoproterozoic strata of the Brock Inlier using zircon (U-Th)/He data. Single zircon date and eU shown on each graph as square with associated error. The timing of the inheritance curves is derived from the U-Pb detrital studies (Fig. 3). Thermal model A has peak burial ca. 200 Ma; thermal model B has peak burial ca. 355 Ma. Time-temperature plot shows thermal pathways 1-3; Amundsen Basin accumulation (3 km) and preservation (1 km), and passive margin sedimentation of 0.3 km based on Rainbird et al. (2016); Devonian clastic thickness of 2 km based on Patchett et al. (2004); Cretaceous burial is based on Jones et al. (1992). Forward models illustrate the expected ZHe inheritance date-eU curves for: (1) maximum temperature at 100ºC; (2) maximum temperature at 120ºC; (3) maximum temperature at 160ºC. Inheritance curves correspond to date-eU trends for zircon between 31-59 μm ESR, and describe the effect of the pre-depositional history and accumulated damage on ZHe dates. The solid line in each inheritance curve represents the projected date-eU trend for a zircon with a 43 μm ESR (mean value). 74

Figure 3.9: Synoptic north-south cross section of southwestern Canadian Arctic for the scenario of maximum burial at 200 Ma showing (B) Triassic pre-rift and (C) Jurassic syn-rift phase of the Amerasia Basin, with subsequent uplift until deposition commenced in the Cretaceous (ca. 135 Ma). Location of cross section on Figure 2, and note vertical scale change between (B) and (C). Thickness constraints for cross section sourced from Bird and Houseknecht (2011) for Kugparuk 3-11-11 well; from Hubbard et al. (1987) for Dinkum Graben; from Dewing and Embry (2007) for E-76, C-68, D-16, F-36 wells; from Ault et al. (2013) for the Slave craton. For discussion on other Victoria Island and Brock Inlier constraints, see Results section.. 78

Figure 4.1: (A) Relative probability distribution grouped by signatures of the “Active margin source” and the “Recycled Source”. Evolution of the northern margin of Laurentia during the Triassic and Jurassic: (B) in the Triassic, the Sverdrup Basin (green) occupied a retro-arc position to Chukotka along strike with the Triassic basin (grey) adjacent to Yukon Tanana terrane (orange); (C) Early Jurassic extension created the proto-Amerasia Basin and cut-off the Sverdrup Basin from the Arctic Alaska-Chukotka microcontinent; red arrows indicate active margin source, blue arrows indicate the recycled source; black circles represent U-Pb sample locations for (A); for complete legend see Fig. 2.11. 82

Figure 4.2: (A) Plausible time-temperature pathways for each region from ZHe (black) and VRo models (green) for two thermal histories: thermal maximum in the Triassic (solid line) and thermal maximum in the Devonian (dashed line). Synoptic north-south cross section of southwestern Canadian Arctic for the scenario of maximum burial at 200 Ma showing (B) Triassic pre-rift and (C) Jurassic syn-rift phase of the Amerasia Basin, with subsequent uplift until deposition commenced in the Cretaceous (ca. 135 Ma). Note the vertical scale change between (B) and (C). See Figure 3.9 for constraints.. 84

List of Tables

Table 3.1: Sample coordinates and stratigraphic position of samples from the southwestern Arctic 60

Table 3.2: Single zircon (U-Th)/He data from samples of the southwestern Arctic 64

Chapter 1 : Thesis Introduction

1.1 Thesis Rationale

The Sverdrup Basin, located in the Canadian Arctic Islands, provides a continuous Carboniferous to Cenozoic geologic history of northern Laurentia. Much of the tectonic history of the basin is understood, with one notable exception, the pre-rift phase of the Arctic Ocean. The development of the Arctic Ocean is tied to the tectonic history of the Sverdrup Basin and northern Laurentia. The Sverdrup Basin records the tectonic evolution of this developing oceanic basin during its pre-, syn-, and post-rift phases that span the Triassic to Cretaceous. With the pre-rift phase of the Arctic Ocean being poorly understood, Triassic-Jurassic strata from the northern Sverdrup Basin are ideal for studying the tectonic setting of northern Laurentia prior to rifting of what eventually became the modern Arctic Ocean, as well as to elucidate the exact timing of initial rifting. The Arctic Ocean opened in two phases: (1) during the Jurassic-Cretaceous the Arctic Alaska-Chukotka microcontinent to the north of the Sverdrup Basin rotated counter-clockwise away from northern Laurentia and formed the Amerasia Basin – the two basins separated by a narrow paleohigh termed the Sverdrup Rim (**Fig. 1.1**) (2) the Cretaceous-Cenozoic opening of the Eurasia Basin related to the northward migration of the mid-Atlantic spreading ridge. The Amerasia and Eurasia basins make up the modern Arctic Ocean and are separated by the Lomonosov Ridge and Alpha-Mendeleev Ridge (**Fig. 1.1**). The focus of this thesis is to investigate the tectonic setting of northern Laurentia prior to the opening of the Amerasia Basin, and the effect Jurassic rifting had on the thermal history of the southwestern Canadian Arctic.

In the circum-Arctic the rapidly growing number of studies using detrital-zircon geochronology have developed a highly resolved understanding of Early Mesozoic provenance (e.g., Miller et al., 2006, 2010; Omma et al., 2011; Miller et al., 2013; Bue and Andresen, 2014;

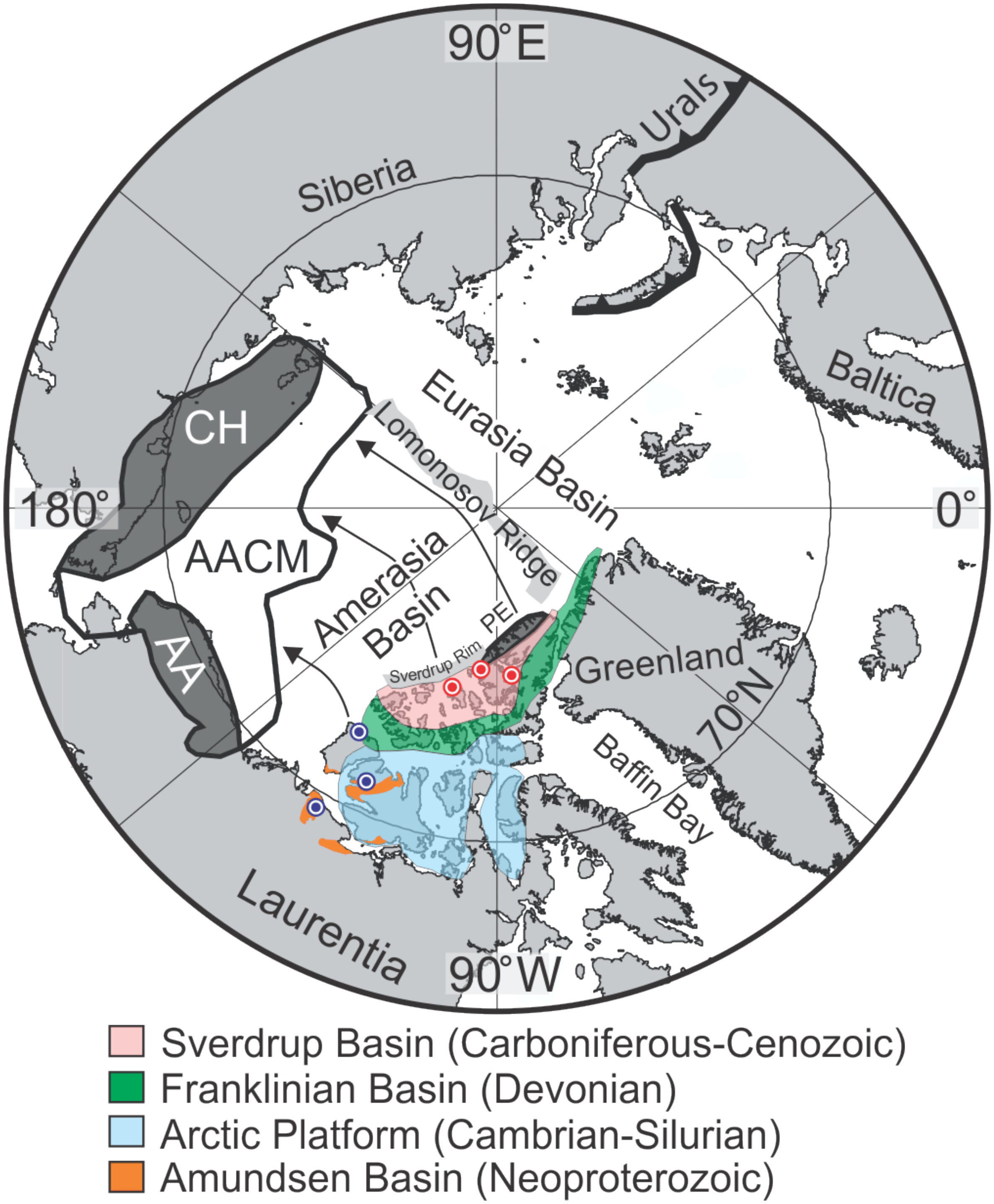

Figure 1.1: Map of the Arctic depicting names and locations of basins and regions mentioned in text. AA – Arctic Alaska; AACM – Arctic Alaska-Chukotka microcontinent; CH – Chukotka; PE – Pearya. Outline of AACM (black line) from Drachev (2011). Rotation of AACM away from the Canadian margin illustrated by black arrows (from Embry, 2000). Sverdrup Basin outline from Embry and Beauchamp (2008); Franklinian Basin from Anfinson et al. (2013); Arctic Platform from Dewing and Obermajer (2009); Amundsen Basin from Rainbird et al. (1996); Sverdrup Rim from Meneley et al. (1975). Red circles represent detrital-zircon U-Pb samples for this study (Chapter 2), blue circles represent detrital-zircon (U-Th)/He samples for this study (Chapter 3).

Gottlieb et al., 2014; Amato et al., 2015; Zhang et al., 2015; Anfinson et al., 2016), however the Triassic provenance systems of the Sverdrup Basin remain largely unresolved One of the primary issues is the presence of a 240-210 Ma zircon age-fraction in Late Triassic strata in the Sverdrup Basin. Previous studies have suggested this sub-population was sourced from the Ural Mountains in northeastern Russia (**Fig. 1.1**; Omma et al., 2011; Anfinson et al., 2016); but no coeval plutonic or igneous units exist in that region. The purpose of this study, therefore, is to fill important gaps in the detrital-zircon data set from Latest Triassic-Early Jurassic sediment, and augment that data set with complementary isotope and field data from northeastern Sverdrup Basin (**Fig 1.1**) to better understand the provenance of the Triassic zircon age-fraction. The use of hafnium isotopic data, which previously has not been used to analyse Triassic-aged zircons from the Sverdrup Basin, enables comparison with other εHf and εNd data from basement rocks and other detrital-zircon samples to identify similarities or differences in crustal origin. These data aid in interpreting the pre-rift tectonic setting of northern Laurentia, with further refinement provide by U-Pb data that helps to better constrain the timing of initial Jurassic rifting north of the Sverdrup Basin; specifically, once Triassic-aged detrital zircons disappear from Jurassic strata it can be assumed that initial rifting in the Amerasia Basin had separated this sediment source from the Sverdrup Basin.

During rifting the margins of the rift are typically uplifted (e.g. van der Beek et al., 1994). However because the Sverdrup Basin experienced continuous subsidence and sedimentation during the opening of the Amerasia Basin, it is not a useful basin to constrain the extent of uplift associated with Jurassic rifting. Older sedimentary basins to the south of the Sverdrup Basin contain a geological record that spans the Neoproterozoic to Devonian (**Fig. 1.1**). This region in the southwestern Canadian Arctic has a widespread Devonian-Cretaceous unconformity, and the goal is to assess the missing geologic record across the unconformity. Zircon (U-Th/He) thermochronology (ZHe), a method seldom used in strata bordering the Sverdrup Basin, can test the thermal history of Neoproterozoic-Devonian strata and therein elucidate the amount of uplift and/or burial associated with rifting in the Amerasia Basin. To date a small number of studies have investigated the thermal history in the southwestern Canadian Arctic Islands (Dewing and Obermajer, 2009), Mackenzie Delta (Issler et al., 2012), Mackenzie Corridor (Issler et al., 2005; Powell et al., 2016), and Slave craton (Ault et al., 2009; Ault et al., 2013). This thesis, therefore, provides a new ZHe dataset from Neoproterozoic to Devonian sandstones forming a transect from Banks Island, located near the rifted Canadian margin and formed from the counter-clockwise opening of the Amerasia Basin, towards the southeast of Victoria Island and Brock Inlier, which is closer to the cratonic interior of Laurentia.

1.2 Geologic Setting of Northern Laurentia

The Canadian Arctic records a nearly continuous depositional history from the Neoproterozoic to the Cenozoic. The geologic events and tectono-sedimentary packages of northern Laurentia are briefly summarized here: (1) Meso- to Neoproterozoic sedimentation in the Amundsen Basin (**Fig. 1.1**), considered to be an embayment of an epeiric sea that covered northwestern Laurentia and preserved in the Brock Inlier, Victoria Island and Banks Island (Young et al., 1979), and post-dated the Grenvillian orogeny but pre-dated the breakup of Rodinia (Rainbird et al., 1996) (2) rifting of a landmass, proposed to be southern Siberia (Ernst et al., 2016), away from the northern margin of Laurentia in the middle Cryogenian, and represented by Franklin dykes dated at ~720 Ma (Heaman et al., 1992); (3) following continental breakup of Rodinia, the passive northern margin accumulated Cambrian siliciclastics that unconformably overlie Neoproterozoic strata, and in turn are overlain by an extensive carbonate platform, termed the Arctic Platform, which persisted until the Silurian, (**Fig. 1.1**); (4) tectonically quiescent conditions were terminated in the Silurian-Early Devonian as western

Baltica collided with eastern Greenland during the Caledonian orogeny followed by collision of a northern landmass comprising continental fragments including the Arctic Alaska-Chukotka microcontinent (AACM) and Pearya (**Fig. 1.1**), with the northern Laurentian margin during the Middle-Late Devonian Ellesmerian orogen (Embry, 1988a). This two-step orogen resulted in widespread clastic sedimentation over northern Laurentia, in addition to the development of a foreland basin (Franklinian Basin; **Fig. 1.1**) adjacent to the southward advancing Ellesmerian collisional zone. The Franklinian Basin, up to 10 km thick, consists of two parts: a deep-water basin in the north fringed by a continental shelf to the south with sediment derived from the Caledonian orogen (Trettin, 1987), and the uppermost clastic interval termed the Devonian clastic wedge that covers an area of over 200,000 km^2 and is derived from the Ellesmerian orogen; (5) rift initiation of the Sverdrup Basin in the Early Carboniferous with the rift-phase ending in the Early Permian (Embry & Beauchamp, 2008); (6) rifting of the proto-Amerasia Basin in the Jurassic with seafloor spreading commencing in the Early Cretaceous in association with the initial pulse of the high Arctic large igneous province (HALIP) with the bounding limit of rotation represented by either the Lomonosov Ridge or Alpha-Mendeleev Ridge (e.g. Oakey and Saltus, 2016; Petrov et al., 2016); (7) Paleocene-Eocene seafloor spreading in Baffin Bay (**Fig. 1.1**) resulted in the counter-clockwise rotation of Greenland into Ellesmere Island, known as the Eurekan orogeny, and uplifted (i.e. inverted) the Sverdrup Basin (e.g., Heron et al., 2015).

Much of the focus of this thesis is in the Sverdrup Basin which is filled with ~13 km of strata that overlie the Silurian-Devonian Franklinian Basin and records a continuous sedimentary history from the Early Carboniferous to Cenozoic (Balkwill, 1978). The basin was initiated by Early Carboniferous extension following the Ellesmerian orogeny, and was oriented in a general north-south direction through the reactivation of older faults in the underlying Franklinian Basin (Harrison, 1995). Volcanism accompanied Lower Carboniferous to Lower Permian extension, but was mostly confined to the northeastern part of the Sverdrup Basin (Trettin, 1988; Mayr et al., 2002). The Late Paleozoic part of the basin fill is characterized by distinct shelf to deep basin sedimentary systems whereas Triassic strata are dominated by shallow and marginal marine siliciclastics up to 4 km thick that filled residual accommodation in the deep, central part of the Paleozoic basin. During the Mesozoic, the main sediment source for the Sverdrup Basin was the exposed Devonian clastic wedge to the south and east of the basin (Patchett et al., 2004). However as noted earlier, a distinctive Permian-Triassic-aged zircon age-fraction appears in Triassic strata, and based on facies distribution, indicates a source to the north of the basin (Embry, 2009). The Sverdrup Basin, considered tectonically quiescent from the Early Permian to the Jurassic, became separated from the northern Arctic Alaska-Chukotka landmass in the Jurassic with the opening (rifting) of the Amerasia Basin. Note that coeval magmatism is not observed in the Sverdrup Basin. While the timing and mechanism of the separation of the AACM from northern Laurentia has been the subject of several competing models, the counter-clockwise rotational opening model is most widely accepted (e.g., Grantz et al., 1979, 2011; Embry, 1990). Later, during the Early to Late Cretaceous, the post-rift phase of the Amerasia Basin is marked by the initiation of seafloor spreading and also magmatism and sedimentation in the Sverdrup Basin belonging to HALIP (e.g., Evenchick et al., 2015). Deposition in the Sverdrup Basin was terminated when the basin was inverted (uplifted) during the Paleocene-Eocene Eurekan orogeny.

1.3 Study Area and Previous Work

The study area for the geochronological component of this research was spread over the northern Canadian Arctic Islands. Fieldwork was conducted on northern Axel Heiberg Island on Bunde Fiord, and archival Geological Survey of Canada samples collected on Ellef Ringnes and Ellesmere islands were examined for detrital-zircon geochronology. Previous workers, principally Miller et al. (2006); Omma et al. (2011); Anfinson et al. (2016), conducted detrital-zircon provenance studies in Triassic-Jurassic strata of the Sverdrup Basin. Significantly, one of the principal unsampled intervals in the Upper Triassic-Lower Jurassic Heiberg Formation was successfully sampled in this study, and also recently by Anfinson et al. (2016). Furthermore, no study to-date has incorporated hafnium data to compliment the detrital-zircon dataset.

Samples for the thermochronological study were from archival Geological Survey of Canada samples from the southwestern Canadian Arctic on Banks Island, Brock Inlier and Victoria Island. While previous thermal history studies cover a broad geographic area of northern Canada, almost no zircon (U-Th)/He thermochronological data has been collected in the study area. New ZHe data from this study fills a regional gap in data between the Sverdrup Basin and the sub-Arctic Mackenzie Delta/Corridor region. There have been attempts to elucidate the Paleozoic-Cenozoic thermal history of strata in the Canadian Arctic Islands and sub-Arctic region from a variety of thermochronological methods, including, apatite fission track (AFT) and vitrinite reflectance (Ro) within the eastern Sverdrup Basin (Arne et al., 2002), apatite and zircon thermochronology (AHe, ZHe) from the Devonian clastic wedge (Anfinson et al., 2013), Ro from bore hole data from various Arctic islands (Dewing and Obermajer, 2009), AFT and Ro data from the Mackenzie Delta (Issler et al., 2012), thermochronology data from the Mackenzie Corridor (AFT, Issler et al., 2005; ZHe, Powell et al., 2016), and AHe data from the Slave craton (Ault et al., 2009, 2013). Furthermore, the previous AHe and ZHe results from the Franklinian Basin (Anfinson et al., 2013) were not modeled, which is an important process for the interpretation of a thermal history (see Ch. 3.3). Previous studies have suggested that sedimentation continued after deposition of Upper Devonian strata, but was completely eroded prior to renewed sedimentation in the Jurassic-Cretaceous (e.g., Miall, 1976, 1979; Issler et al., 2005; 2012; Powell et al., 2016). This theory is tested with new ZHe data using improved thermochronological methods and modeling of detrital-zircon populations (Guenthner et al., 2015).

1.4 Thesis Objectives and Structure

This thesis comprises two parts, representing two research papers written in journal format, and differentiated based on their respective analytical technique: Chapter 2 is primarily a detrital-zircon geochronological investigation whereas Chapter 3 is primarily a study of detrital-zircon thermochronology.

The goal of Chapter 2 is to identify provenance regions during deposition of the Triassic-Jurassic succession in the Sverdrup Basin. These data, complemented with Hf isotope and field data, provide insight into the tectonic setting of northern Laurentia. Chapter 3 draws on one of the conclusions from the geochronological work, specifically, if rifting began at ca. 200-190 Ma, would the related uplift be recorded as a cooling event in the Neoproterozoic-Devonian sedimentary strata of the southwestern Canadian Arctic? Results from the thermochronology study are then used to evaluate whether maximum burial occurred at the end of the Ellesmerian orogeny followed by protracted uplift until the Cretaceous, or, as initially proposed by Miall (1976), did deposition continue uninterrupted into the Mesozoic?

1.5 Methods

In this study the principal analytical technique used to determine the provenance of Triassic-Jurassic strata in the Sverdrup Basin is U-Pb detrital-zircon geochronology. In general, zircons from each sandstone sample exhibit a unique spectrum of formative ages, which then can be used to interpret the tectonic setting of the depositional basin (e.g., Cawood et al., 2012). Details of U-Pb geochronology methodology are discussed further in Chapter 2.3.1. Geochronology data are supplemented with Hf isotope detrital-zircon geochemistry, which provides further insight into the crustal source region and therefore its tectonic setting. εHf data can help determine the magmatic origin of the detrital zircon, for instance whether it crystallized in a compressive arc-setting versus a continental extensional setting. Hafnium isotope methodology is discussed further in Chapter 2.3.2. Furthermore, the discussion of the tectonic setting of northern Laurentia is augmented by the observation of volcanic ash beds in the field, which were verified using x-ray diffraction (XRD).

The third analytical technique used in this thesis is detrital-zircon (U-Th)/He thermochronology, which is a low temperature thermochronometer used to help constrain the timing and magnitude of burial and exhumation. (U-Th)/He dating relies on the concentration of ^{4}He that accumulates in the zircon as a product of radioactive decay from ^{238}U, ^{235}U, and ^{232}Th. At high temperatures, the ^{4}He will diffuse out of the system, but once the system has sufficiently cooled the system becomes closed and ^{4}He retained – it is the timing of closure that is used to interpret the timing and extent of uplift and associated erosion. However zircons in this study are detrital, which introduces further complexity related to each zircon’s unique pre-depositional history and hence its unique closure temperature and amount of retained ^{4}He. To account for this issue, the ZHe ages need to be modelled to more accurately estimate the extent and timing of burial and exhumation. In this thesis the software HeFTY is used to determine plausible time-temperature histories for the dataset. See Chapter 3.3 for a more detailed discussion of the methodology of ZHe thermochronology. In situations where too few ZHe ages are available for a given sample, the dataset can be augmented with vitrinite reflectance (Ro) data, a commonly used thermal maturity indicator for assessing the amount of kerogen in a sedimentary rock.

1.6 Statement of Contributions

Chapter 2 is a reproduction of a manuscript accepted for publication in the journal *Lithosphere*.

Midwinter, D., Hadlari, T., Davis, W.J., Dewing, K., and Arnott, R.W.C. 2016. Insights into the tectonic evolution of the Triassic northern Laurentian margin from detrital-zircon U-Pb and Hf isotope analysis of Triassic-Jurassic strata in the Sverdrup Basin. Lithosphere. doi:10.1130/L517.1.

- T. Hadlari worked with the first author on the interpretation of the data and was instrumental in the development and construction of the countless drafts.

- W.J Davis and staff at the SHRIMP lab at the Geological Survey of Canada worked on the sample preparation, data collection and synthesis, and assisted with the final data tables.

- K. Dewing and R.W.C Arnott helped refine the manuscript.

Chapter 3 is a reproduction of a manuscript submitted for publication in the journal *Canadian Journal of Earth Sciences*.

Midwinter, D., Powell, J., Schneider, D.A., and Dewing, K. 2016. Investigating the Paleozoic-Mesozoic low-temperature thermal history of the southwestern Canadian Arctic: insights from (U-Th)/He thermochronology. Canadian Journal of Earth Sciences, accepted with revisions.

- J. Powell assisted and greatly helped the first author with the modelling software HeFTY, as well as principally providing edits for the methodology section of the manuscript.

- D.A Schneider helped refine the manuscript, specifically the format, discussion and interpretation components.

- K. Dewing supported the manuscript with a vitrinite reflectance model to augment the ZHe data on Banks Island as well as provided useful edits and comments to the regional geology and discussion sub-chapters.

Chapter 2 : Dual Provenance Signatures of the Triassic northern Laurentian Margin from Detrital-Zircon U-Pb and Hf-Isotope Analysis of Triassic-Jurassic Strata in the Sverdrup Basin

2.0 Abstract

The tectonic setting of northern Laurentia prior to the opening of the Arctic Ocean is the subject of numerous tectonic models. By better understanding the provenance of detrital zircon in the Canadian Arctic prior to rifting, both the pre-rift tectonic setting and timing of rifting can be better elucidated. In the Sverdrup Basin, two distinct provenance assemblages are identified from new detrital-zircon U-Pb data from Lower Triassic to Lower Jurassic strata in combination with previously published detrital-zircon data. The first assemblage comprises an age spectrum identical to that of the Devonian clastic wedge in the Canadian Arctic and is termed the recycled source. In contrast, the second assemblage is dominated by a broad spectrum of near-syndepositional Permian–Triassic ages derived from north of the basin and is termed the active margin source. Triassic strata of Yukon and Arctic Alaska exhibit a similar dual provenance signature, whereas in northeastern Russia, Chukotka contains only the active margin source. Complementary hafnium isotopic data on Permian–Triassic zircon have εHf values that are consistent with the common evolved crustal signature of the Devonian clastic wedge detrital-zircon grains and Neoproterozoic–Paleozoic basement rocks in the Arctic Alaska–Chukotka microcontinent. Furthermore, newly identified volcanic ash beds throughout the Triassic section from the northern part of the Sverdrup Basin, along with abundant Permian–Triassic detrital zircon, suggest a protracted history of magmatism to the north of the basin. We interpret that these zircons were sourced from a magmatically active region to the north of the Sverdrup Basin, and in the context of a rotational model for opening of Amerasia Basin, this was probably part of a convergent margin fringing northern Laurentia from the northern Cordillera along the outboard

edge of Arctic Alaska and Chukotka terranes. In Early Jurassic strata, Permian–Triassic zircons decrease substantially, implying the diminution of the active margin as a sediment source as initial rifting isolated the Permian–Triassic source from the Sverdrup Basin.

2.1 Introduction

Siliciclastic sedimentary successions can provide an important record of the tectonic setting and tectonic evolution of a basin through stratigraphic and detrital-zircon patterns. Previous efforts to interpret the tectonic evolution of the Sverdrup Basin have been made (e.g., Balkwill, 1978; Embry and Beauchamp, 2008), but important gaps in knowledge remain. Incipient rifting of the proto–Amerasia Basin in the Jurassic–Cretaceous (Embry, 1990, 1991; Houseknecht and Bird, 2011) was followed by opening of the Amerasian ocean basin, which separates Arctic Canada, Alaska, and northeastern Russia (e.g., Grantz et al., 1979) (**Fig. 2.1**).

Previous detrital-zircon studies in the Sverdrup Basin (Miller et al., 2006; Omma et al., 2011) have identified a detrital-zircon signature in Triassic–Jurassic strata that resembles that of the underlying Devonian clastic wedge (e.g., Anfinson et al., 2012a). Those studies also identified several different zircon assemblages in Triassic–Jurassic strata in the Sverdrup Basin and compared their age spectra to those from other Triassic strata in the circum-Arctic. Those previous detrital-zircon studies (Miller et al., 2006; Omma et al., 2011) in the Sverdrup Basin lacked data from the Late Triassic–Early Jurassic Heiberg Formation. This paper provides new detrital-zircon data from this interval, which serves to constrain the provenance of the Sverdrup Basin during the Triassic–Jurassic. Also, U-Pb detrital-zircon ages are augmented with εHf isotopic data for Permian–Triassic zircon grains. These data provide important insight into the nature of the source terrane and magmatism (cf. Vervoort and Patchett, 1996).

Figure 2.1: Circum-Arctic orogens, terranes, and locations modified from Colpron and Nelson (2011) and Pease et al. (2014). AA, Arctic Alaska; AACM, Arctic Alaska-Chukotka Microplate; CH, Chukotka; NSI, New Siberian Islands; NZ, Novaya Zemlya; PE, Pearya; SAS, South Anyui Suture Zone; SV, Svalbard; WI, Wrangel Island; YTT, Yukon Tanana Terrane. Black circles represent approximate detrital zircon sample locations from AA (Miller et al., 2006; Gottlieb et al., 2014); CH (Miller et al., 2006; Tuchkova et al., 2011; Amato et al., 2015); WI (Miller et al., 2010); and YTT (Beranek et al., 2010b; Beranek and Mortensen, 2011). The outlines of the SAS and AACM are from Drachev (2011). Red circles represent approximate location of εNd or εHf values from AA (Amato et al., 2009); Arctic Canada (Anfinson et al., 2012b; Morris, 2013); New Siberian Islands (Akinin et al., 2015), and Siberia (Malitch et al., 2010).

2.2 Geologic Setting

2.2.1 Sverdrup Basin

The Sverdrup Basin is located in the Canadian Arctic Archipelago (**Fig. 2.2**) and records near continuous sedimentation from the Carboniferous to the Paleogene (Embry and Beauchamp, 2008). The basin is underlain by an up to 10-km-thick sedimentary pile of Devonian clastic wedge strata that were deformed during the Late Devonian–Early Carboniferous Ellesmerian orogeny (Embry, 1991). Strata equivalent to the Devonian clastic wedge are widely distributed, including the northern Cordillera of North America, Arctic Alaska, and northern Russia (Amato et al., 2009; Beranek et al., 2010a; Drachev, 2011; Lemieux et al., 2011). The Ellesmerian orogeny was succeeded by initial rifting of the Sverdrup Basin that began in the Early Carboniferous and ended in the Permian (Embry and Beauchamp, 2008). Current models suggest that following the Permian, the Sverdrup Basin was tectonically quiescent and underwent thermal subsidence until rifting recommenced in the Jurassic (e.g., Embry and Beauchamp, 2008).

The Triassic stratigraphy of the Sverdrup Basin (**Fig. 2.3**) is controlled by repetitive transgressive-regressive events (e.g., Embry, 1988b; Embry and Beauchamp, 2008). Early Triassic units of the Sverdrup Basin comprise the Blind Fiord Formation, which consists of shale and siltstone representing mid-outer shelf, slope, and deeper basin-floor deposits, and the Bjorne Formation, which consists mostly of sandstone confined to the basin margins interpreted to represent deltaic deposits (Embry, 1986). These two siliciclastic units mark the first major clastic influx into the basin with the accumulation of 2000 m of strata in the basin center (Embry, 1991). The Middle Triassic is marked by a major transgression that deposited bituminous source rocks of the Murray Harbour Formation (Embry and Beauchamp, 2008). These strata are overlain by

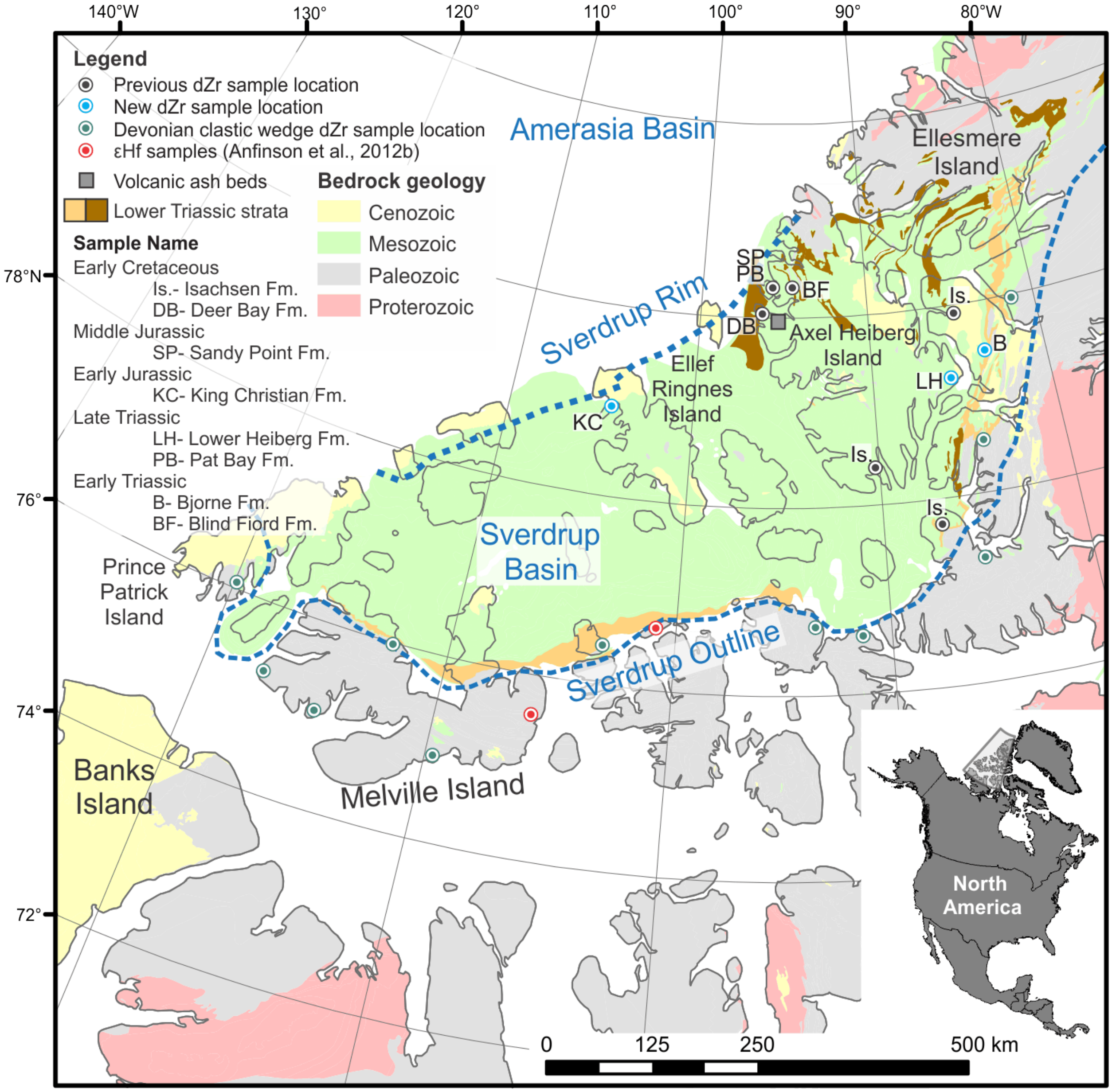

Figure 2.2: Sverdrup Basin map with detrital-zircon sample and volcanic ash bed locations. Detrital-zircon data references from Isachsen Formation (Røhr et al., 2010); Sandy Point and Deer Bay formations (Omma et al., 2011); Pat Bay Formation (Miller et al., 2006; Omma et al., 2011 – both from approximately the same location); Bjorne Formation (Miller et al., 2006 – location approximately the same as this study); Blind Fiord Formation (Omma et al., 2011). U-Pb data from Devonian clastic wedge (Anfinson et al., 2012a); εHf data from Devonian Clastic Wedge (Anfinson et al., 2012b). Lower Triassic strata: Blind Fiord Formation (brown); Bjorne Formation (orange). General southern outline of the Sverdrup Basin from Embry and Beauchamp (2008). Surface and sea bottom bedrock geology is from Okulitch (1991). The Sverdrup Rim was first described by Meneley et al. (1975).

clastic and/or carbonate rocks of the Roche Point Formation, which represents a short-lived regression (Embry, 1991). Earliest Carnian transgression deposited the Hoyle Bay Formation above the Roche Point Formation. Progradation of sandstone-rich, shallow marine deposits (Pat Bay Formation) extended across the basin during the late Carnian (Embry, 1993) and was terminated by a major transgression in the latest Carnian–early Norian that deposited prodelta mud and silt of the Barrow Formation (Embry, 1991). These strata progressively coarsen upward into marginal marine to non-marine sandstones of the Heiberg Formation (Embry, 1988b).

The Heiberg Formation in the central and eastern parts of the basin is subdivided into three predominantly sandstone-rich members (Embry, 1983a)—the Romulus, Fosheim, and Remus (**Fig. 2.3**). These members are stratigraphically equivalent to the Heiberg Group that comprises five formations in the western part of the basin (**Fig. 2.3**; Embry, 1983b). The formations of the Heiberg Group consist of the sandstone-rich deltaic Skybattle Formation overlain unconformably by marine mudstone of the Grosvenor Island Formation with the Triassic–Jurassic boundary occurring in its upper part (Embry and Suneby, 1994). These strata then coarsen upward into sandstone-rich strata of the deltaic Maclean Strait Formation with the upper part containing the base-Sinemurian boundary. Farther upward, these strata are overlain by marine shale of the Lougheed Island Formation capped by the sandstone-dominant King Christian Formation.

During the Triassic there were two principal sources of sediment into the basin determined by the general facies distributions shown in **Figure 2.4** (Embry, 2009). Sediment transport was directed into the basin from the southern and eastern margins, indicating a southern and eastern sediment source area. U-Pb zircon data (Miller et al., 2006; Anfinson et al., 2012a) and Sm-Nd isotopic data (Patchett et al., 2004) are consistent with recycling from the Devonian

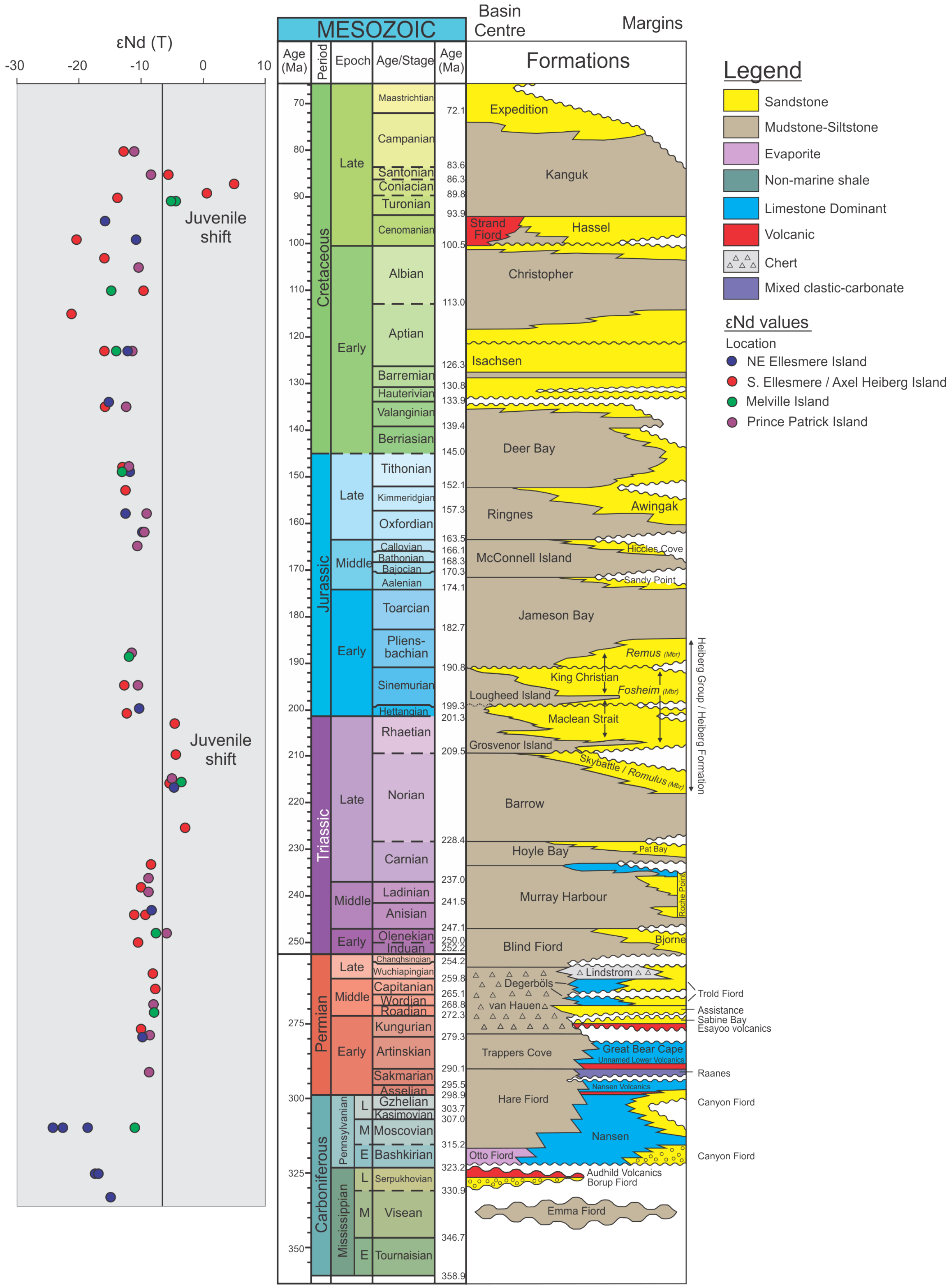

Figure 2.3: Stratigraphic chart of the Sverdrup Basin modified from Embry and Beauchamp (2008); Paleozoic volcanics: Audhild (Trettin, 1988); Nansen (Mayr et al., 2002); ULV and Esayoo (Morris, 2013). Initial εNd values from sedimentary rocks show positive shift to more juvenile provenance, highlighted by crossing the (arbitrary) vertical line, in the Late Triassic and Late Cretaceous, and increased negative scatter in εNd values in the Early Cretaceous is from a greater contribution from Shield (Patchett et al., 2004).

clastic wedge and older north Laurentian strata (e.g., Hadlari et al., 2012, 2014). The facies indicate that another Triassic sediment source was derived from north of the basin (Embry, 2009), which is consistent with sandstone samples with detrital-zircon age spectra that are different from those on the south side of the basin (Miller et al., 2006; Omma et al., 2011).

In the Jurassic–Cretaceous, a narrow paleohigh, the Sverdrup Rim (**Fig. 2.2**), separated the Sverdrup Basin from the rift grabens of the proto–Amerasia Basin (Meneley et al., 1975; Embry, 1993). The northern source region was fully separated from northern Laurentia by the opening of the Amerasia Basin in the Cretaceous (Embry, 2009).

2.2.2 Paleogeographic Restoration

The tectonic interpretation of the Arctic region prior to the opening of the Amerasia Basin is complex and is the subject of much debate (e.g., Grantz et al., 1979; Embry, 1990; Lawver and Scotese, 1990; Lane, 1997; Lawver et al., 2002; Grantz et al., 2011; Pease, 2011; Pease et al., 2014). The region that is central to reconstruction is typically referred to as the Arctic Alaska–Chukotka microcontinent (AACM; **Fig. 2.1**), a lithospheric block occupying northeastern Russia, Arctic Alaska, and their respective offshore shelves (Pease et al., 2014). The AACM was separated from the Siberian craton by the Anyui Ocean, which closed when the Amerasia Basin and Arctic Ocean opened. The timing and mechanism of this opening is the subject of several different models (Grantz et al., 1979; Embry, 1990; Lane, 1997; Nokleberg et al., 2000; Miller et al., 2006; Kuzmichev, 2009; Grantz et al., 2011; Lawver et al., 2011).

This paper tests the rotational opening model of Grantz et al. (1979, 2011) and Embry (1990) that places the AACM against the Canadian Arctic Islands margin prior to the Cretaceous. Restoration of the AACM to its location prior to separation and rotation from the northern Laurentian margin places the North Slope of Alaska adjacent to Banks and Prince Patrick islands. As a result, the provenance of the Sverdrup Basin during the Triassic should

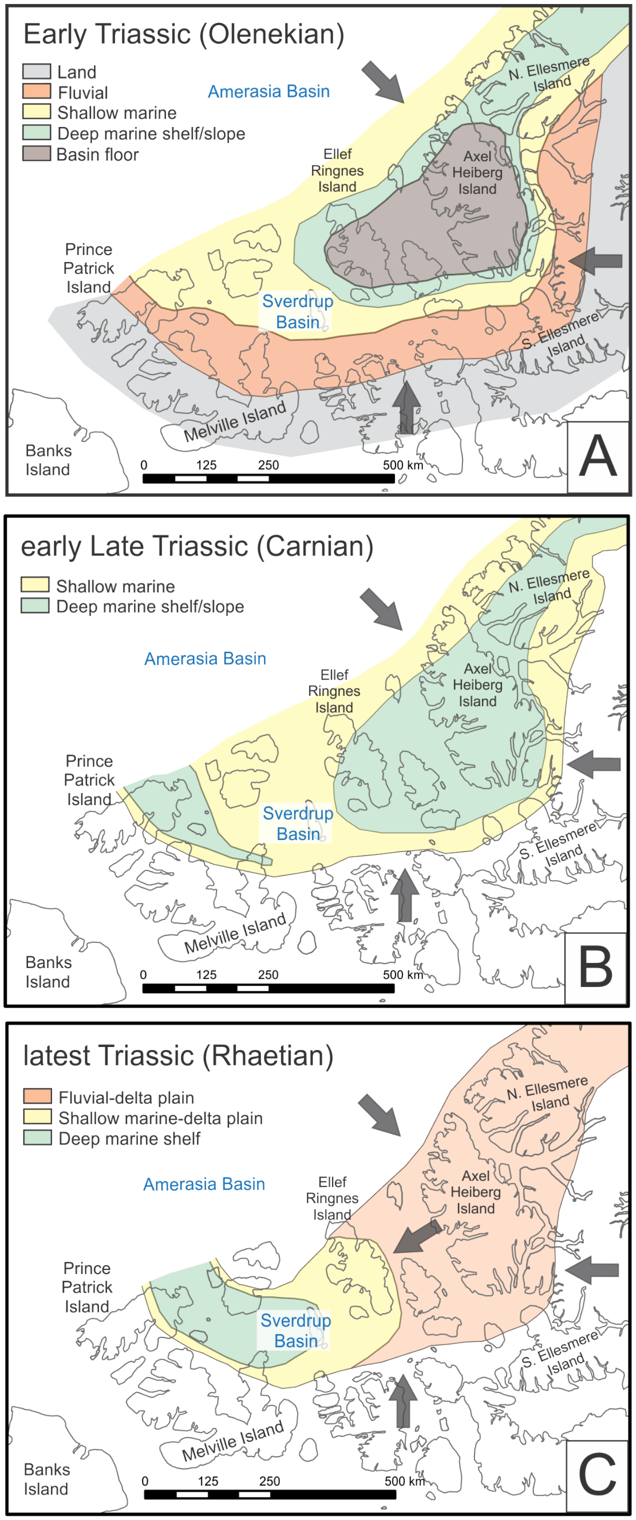

Figure 2.4: General facies distribution during the Early Triassic (modified from figure 36.13 in Embry, 2011); Late Triassic (modified from figure 36.20 in Embry, 2011); and latest Triassic (modified from figure 14 in Embry and Beauchamp, 2008). Arrows represent general sediment transport direction, based on Embry (1991, 2009).

resemble that of the North Slope of Arctic Alaska and Chukotka, since the Sverdrup Basin, Hanna Trough, and Arctic Alaska Basin would have formed a continuous sedimentary basin from the Carboniferous to Jurassic (e.g., Gottlieb et al., 2014). Seismic interpretation of an extinct spreading ridge has a trend that is parallel to the shelves offshore of the western Canadian Arctic Islands and Chukotka (Pease et al., 2014, and references therein).

In a restored position, the outboard margin of the AACM is typically interpreted to have been a passive margin to the Anyui and Angayucham oceans in the Triassic (Nokleberg et al., 2000; Miller et al., 2006; Sokolov et al., 2009; Tuchkova et al., 2009; Miller et al., 2010; Tuchkova et al., 2011; Miller et al., 2013; Amato et al., 2015). This was followed in the Cretaceous by collision with the Siberian craton–Verkhoyansk margin, known as the South Anyui suture (SAS; **Fig. 2.1**), after closure of Anyui Ocean and concomitant opening of the Amerasia Basin (e.g., Drachev, 2011; Houseknecht and Bird, 2011; Laverov et al., 2013; Amato et al., 2015). The SAS contains remnants of a Jurassic–Early Cretaceous convergent system, made up of island arc, continental terrane and oceanic basin rocks (Kuzmichev, 2009; Drachev, 2011; Amato et al., 2015).

It is not clear whether the SAS extends south of the New Siberian Islands (NSI), and therefore is part of the AACM, or if it extends north of the NSI, and therefore is unrelated to the AACM (see discussion in Kuzmichev, 2009; Pease, 2011; Pease et al., 2015). Detrital zircons from the Triassic Burustas Formation, exposed on the NSI, have a strong fraction of ca. 252 Ma zircon that, in addition to geochemical and petrographical characteristics of the zircon, are consistent with zircon ages from Siberian Trap magmatism (Miller et al., 2006), possibly indicating that the NSI were connected to Southern Taimyr and Siberia in the Early Mesozoic (e.g., Kuzmichev and Pease, 2007). Recent studies (Ershova et al., 2015; Pease et al., 2015) show a Baltican detrital-zircon character in the Carboniferous that changes to Uralian in the Permian.

2.2.3 Summary of Published U-Pb and Sm-Nd Provenance Data

The overall detrital-zircon spectrum for the Devonian clastic wedge in the Canadian Arctic has a characteristic signature of 700–360 Ma ages and a broad spectrum of Proterozoic ages (**Fig. 2.5**; Anfinson et al., 2012a, 2012b). Studies of strata tectonostratigraphically equivalent to the Devonian clastic wedge confirm a consistent and diagnostic detrital-zircon signature of this clastic package across northwestern Laurentia and the AACM (Beranek et al., 2010a, 2010b; Drachev, 2011; Lemieux et al., 2011; Anfinson et al., 2012a, 2012b), which could have been ultimately derived from Paleozoic arc rocks of the AACM (e.g., Amato et al., 2009, 2015; Lemieux et al., 2011; Hadlari et al., 2014). Analyses of detrital zircon from Triassic strata on the North Slope of Alaska (Gottlieb et al., 2014) and Triassic and Jurassic strata (Bjorne and Pat Bay formations: Miller et al., 2006; Sandy Point Formation: Omma et al., 2011) from the Sverdrup Basin have a similar signature as the Devonian clastic wedge (**Fig. 2.5**). Sedimentary recycling of detrital zircon is a common way that younger strata can mirror the detrital-zircon spectra of older strata (Hadlari et al., 2015), and so the signature of the Devonian clastic wedge provides a useful reference curve for circum-Arctic Mesozoic spectra (**Fig. 2.5**).

Triassic strata within the Sverdrup Basin (Blind Fiord and Pat Bay formations: Omma et al., 2011) have a detrital-zircon signature that has been attributed to a source in western Siberia (e.g., Taimyr, Urals, and Siberian Traps, **Fig. 2.1**; Miller et al., 2006, 2013). The diagnostic age fraction for the northern Sverdrup Basin source is a nearly continuous spectrum of near-syndepositional Permian–Triassic ages (**Fig. 2.5**). Embry (1993, 2009) postulated a northwestern provenance for Lower and Upper Triassic strata of the Sverdrup Basin based on lithofacies distribution (**Fig. 2.4**) and that this sediment source remained active until the lower Middle Jurassic. The northern source of Triassic sediment in the Sverdrup Basin, with its characteristic Permian– Triassic zircon, is observed elsewhere in the Arctic (**Fig. 2.5**), specifically in Chukotka

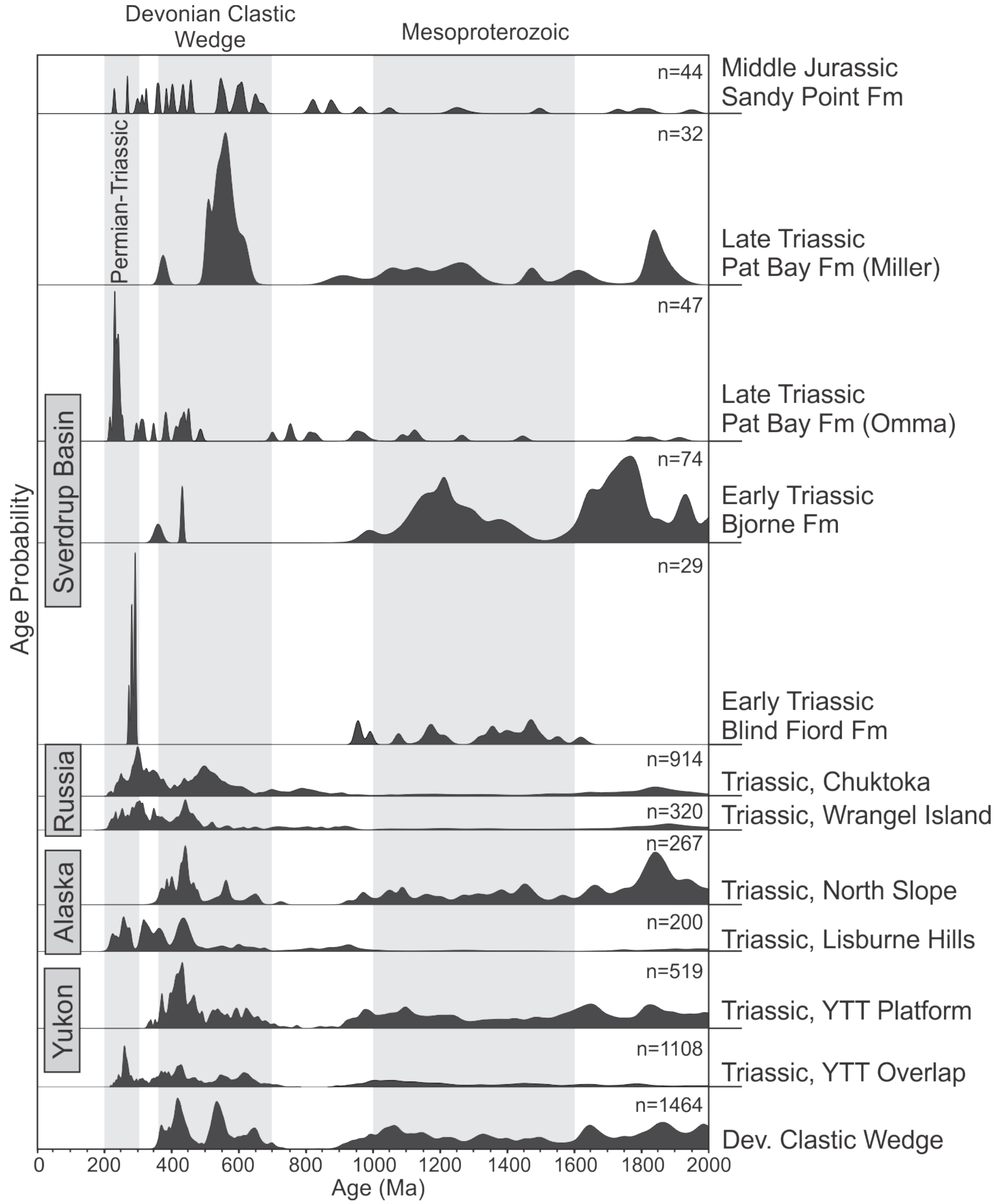

Figure 2.5: Triassic to Middle Jurassic published detrital-zircon age spectra. Sverdrup Basin sources are: Sandy Point Formation (Omma et al., 2011); Pat Bay Formation (Miller et al., 2006; Omma et al., 2011); Bjorne Formation (Miller et al., 2006); Blind Fiord Formation (Omma et al., 2011); Triassic of Chukotka (Miller et al., 2006; Tuchkova et al., 2011; Amato et al., 2015); Triassic of Wrangel Island (Miller et al., 2010); Triassic of North Slope, AK (Gottlieb et al., 2014); Triassic of Lisburne Hills, AK (Miller et al., 2006); Triassic of the YTT Platform (Beranek et al., 2010b); Triassic of the YTT Overlap (Beranek and Mortensen, 2011); Devonian clastic wedge (Anfinson et al., 2012a). See Appendix A for U-Pb detrital zircon sample location, number, age, and reference.

(Miller et al., 2006; Tuchkova et al., 2011; Amato et al., 2015), Wrangel Island (Miller et al., 2006, 2010), and Lisburne Hills, Alaska (Miller et al., 2006). The Western Interior Platform adjacent to the Yukon Tanana terrane has a similar dual detrital-zircon signature with one source displaying strong similarities to the Devonian clastic wedge, whereas the other source has abundant near-syndepositional Permian–Triassic ages derived from arc rocks of the Yukon Tanana terrane (Beranek et al., 2010b; Beranek and Mortensen, 2011).

Sm-Nd isotopic data from Carboniferous to Cretaceous sedimentary rock samples from the Sverdrup Basin have a nearly uniform εNd signature throughout the basin's history (**Fig. 2.3**), which is interpreted to represent the progressive recycling of Devonian clastic wedge strata during the Mesozoic (Patchett et al., 2004). Two excursions to more positive εNd isotopic values occurred during the Late Triassic–earliest Jurassic and Late Cretaceous (**Fig. 2.3**). Patchett et al. (2004) hypothesized that the Nd isotopic shift in the Late Triassic–earliest Jurassic resulted from a minor volcanic contribution to the basin, although no evidence of volcanism had been identified at that time. The shift in the Late Cretaceous is consistent with sedimentary input from juvenile volcanic rocks of the HALIP (e.g., Buchan and Ernst, 2006; Estrada and Henjes-Kunst, 2013; Oakey and Saltus, 2016).

2.2.4 Igneous Record of the Sverdrup Basin

The earliest record of volcanism within the Sverdrup Basin is the Lower Carboniferous Audhild volcanics (Trettin, 1988; Embry and Beauchamp, 2008), which coincided with early rifting. Mafic volcanic rocks within Early Permian carbonates of the Nansen Formation have been interpreted to mark the end of the Asselian stage (Mayr et al., 2002; Embry and Beauchamp, 2008). Early Permian volcanic rocks are termed the Unnamed Lower volcanics (ULV) at the base of the Great Bear Cape Formation, and the Esayoo volcanics in the Sabine Bay Formation (Morris, 2013). The Esayoo volcanics have been interpreted as intra-plate basalts with alkaline to transitional affinities (Cameron and Muecke, 1996). Although there are no previously reported records of Triassic to Jurassic volcanic rocks in the Sverdrup Basin, magmatism was active during the Cretaceous as part of HALIP (e.g., Evenchick et al., 2015).

2.3 Analytical Procedures

2.3.1 U-Pb Geochronology

Samples of the Bjorne Formation and Romulus Member were collected from Ellesmere Island by the authors in 2011, and the King Christian Formation sample was collected by Carol Evenchick in 2010. U-Pb ages of detrital zircon were analyzed by secondary ion microprobe, and performed using the sensitive high resolution ion microprobe (SHRIMP) at the Geological Survey of Canada (GSC), Ottawa. SHRIMP analytical procedures followed those described by Stern (1997), with standards and U-Pb calibration methods following Stern and Amelin (2003). Briefly, zircon were cast in 2.5-cm-diameter epoxy mounts along with fragments of the GSC laboratory standard zircon (z6266, with $^{206}Pb/^{238}U$ age = 559 Ma). The midsections of the zircon were exposed using 9, 6, and 1 μm diamond compound, and the internal features of the zircon (such as zoning, structures, alteration, etc.; Appendix D) were characterized in backscattered electron mode utilizing a Zeiss Evo 50 scanning electron microscope. Mount surfaces were evaporatively coated with 10 nm of high-purity Au. Analyses were conducted using a $^{16}O^-$ primary beam, projected onto the zircon at 10 kV. The sputtered area used for analysis was ~18 μm in diameter with a beam current of ~8–9 nA. The count rates at ten masses including background were measured over five scans with a single electron multiplier and a pulse-counting system with dead time of 23 ns. Offline data processing used SQUID 2.5 software written by Ludwig (2003). The 1s external errors of $^{206}Pb/^{238}U$ ratios reported in Appendix B incorporate a ±1.0% error in calibrating the standard zircon (see Stern and Amelin, 2003). No fractionation correction was applied to the Pb-isotope data; common Pb correction utilized the Pb composition of the surface blank (Stern, 1997). Isoplot v. 3.00 (Ludwig, 2003) was used to calculate weighted means.

Probability density function plots use ages based on the concordia age calculation method (Ludwig, 1998) as outlined in Nemchin and Cawood (2005) to avoid using different isotopic ratios for age interpretations based on an arbitrary age cut-off and to be able to evaluate probability of concordance for Phanerozoic zircons for which the traditional discordance measurement is subject to very large errors. Rather than picking a subjective cut-off between using $^{206}Pb/^{238}U$ and $^{207}Pb/^{206}Pb$ age, which is common practice in the literature (e.g., 1200 Ma for Omma et al., 2011; 1000 Ma for Anfinson et al., 2012a), the concordia function calculates a single age based on the relative errors of the measured $^{206}Pb/^{238}U$ and $^{207}Pb/^{206}Pb$ ratios (Ludwig, 1998). The approach outlined by Nemchin and Cawood (2005) involves a minimum degree of decision making and the use of probability of concordance as a screening parameter to reduce bias. In this study, a sample is not included if either the probability of concordance is <0.01 or if discordance measurements are <-5 or >5 (Appendix B).

When comparing multiple samples, the probability density function (PDF) is assumed to represent all the possible ages in the samples, and all the zircon ages must fall within the PDF curve. Accordingly, the area below the curve for each sample is comparable. Another comparative technique uses the cumulative distribution function (CDF). Although similar to the PDF, the CDF sums the probabilities with increasing age but requires equivalence in the population size. This step function does not account for uncertainties in the measured values. In spite of the differences, a PDF and CDF display the same information, but each has its own strength: PDFs are easier to use when evaluating the presence or absence of specific ages in age distributions, whereas CDFs are more useful when assessing similarities or differences within a set of age distributions (Guynn and Gehrels, 2010). Kernel density estimation (KDE) is displayed with PDF in **Figure 2.6**. An advantage of KDE is that the bandwidth is adaptive; therefore, with sparse data density, the density estimate becomes increasingly smooth. Kernel plots were produced using Density Plotter software (Vermeesch, 2012). Results are presented in **Figure 2.6** with full U-Pb analytical data are compiled in Appendix B and images of the zircon are compiled in Appendix D.

2.3.2 Hafnium-Isotope Methods

Two samples were analyzed for Hf isotopes with grains selected specifically for their Permian-Triassic U-Pb zircon ages with a total of 24 analyses conducted. Hf analyses were conducted with a Photon excimer laser and a Nu Plasma multicollector inductively coupled plasma mass spectrometer in time-resolved analyses mode at the GSC, Ottawa. Data were acquired using either a 40, 50, or 60 mm beam size selected based on grain size of the target.

CHUR values of $^{176}Lu/^{177}Hf = 0.0336$ and $^{176}Hf/^{177}Hf = 0.282785$ are from Bouvier et al. (2008). The depleted mantle model based on $^{176}Lu/^{177}Hf = 0.03902$ and $^{176}Hf/^{177}Hf = 0.28327$ and new crust model age calculations utilized values of Dhuime et al. (2011) ($^{176}Lu/^{177}Hf$ = 0.03781 and $^{176}Hf/^{177}Hf = 0.28316$). ^{176}Lu decay constant of 1.867×10^{-11} yr^{-1} was used (Söderlund et al., 2004).

Elemental fractionation of Lu and Hf was measured and corrected based on the 91500 standard and an accepted $^{176}Lu/^{176}Hf$ value of 0.000309 (Blichert-Toft, 2008). Measured values were approximately 15% higher than accepted values with a reproducibility of approximately 23% at 95% confidence. Reproducibility of the $^{176}Lu/^{176}Hf$ value was better than 5% for the 6266 standard.

Accuracy and reproducibility were monitored by replicate analyses of four zircon standards (91500, Temora 2, 6266, and Mud Tank), each showing excellent agreement with published data for these standards (Woodhead and Hergt, 2005; Wu et al., 2006; Blichert-Toft, 2008). Based on internal precision, each of the standards exhibits excess scatter as indicated by high mean square of weighted deviates (MSWD), and external errors in the range from 0.9 to 1.2 epsilon units at 2σ are required. A minimum external error of 1.2 ε (2σ) is assumed for the data.

Hafnium data are presented on Hf-evolution diagrams that show εHf values at the time of crystallization based on the measured $^{206}Pb/^{238}U$ and $^{207}Pb/^{206}Pb$ ratios. In order to make use of the greater number of Nd isotopic data reported for potential source rocks, published neodymium isotopic data are converted to "equivalent" Hf isotope values based on the high degree of correlation established between the two systems (Vervoort et al., 1999). The equation, derived by Vervoort et al. (1999), was utilized to calculate equivalent εHf values.

$$\varepsilon Hf = 1.36\ \varepsilon Nd + 2.95;\ r^2 = 0.86 \qquad (1)$$

This conversion allows comparison of more geographically widespread εNd data on the Hf evolution plot.

For the calculation of hafnium-depleted model ages (T_{DM}), crustal evolution trajectories assume present-day $^{176}Lu/^{177}Hf$ ratio of 0.0093 of typical felsic crust (Vervoort and Patchett, 1996; Amelin et al., 2000; Gehrels and Pecha, 2014). These model ages or crustal residence ages for zircon provide a qualitative estimate of the time of separation of the source rocks, or their precursors, from a hypothetical depleted mantle reservoir (Bahlburg et al., 2011). While these model ages do not necessarily provide real age information, they are useful for comparative analyses. When comparing the model ages (T_{DM}) of this study with other published isotopic studies, no conversion was applied to the T_{DM} if it was originally calculated from εNd values. Full Hf analytical results for this study and the cited comparative references can be found in Appendix C.

2.4 Results

2.4.1 U-Pb Analyses

2.4.1.1 Bjorne Formation

The Bjorne Formation is more than 1000 m thick along the southern and eastern margins of the Sverdrup Basin and, along with the Blind Fiord Formation, represents the first significant episode of siliciclastic deposition in the basin. It has been subdivided into the predominantly sandstone Cape Butler, Pell Point, and Cape O'Brien members (Embry, 1986). A single sample was analyzed for detrital-zircon geochronology from the Cape O'Brien Member (Olenekian) on central Ellesmere Island. Zircon ages fall into three modes—a tight late Silurian peak (ca. 460–420 Ma); a broad range of Paleo- to Mesoproterozoic (ca. 2100–950 Ma); and Archean (ca. 3000–2500 Ma) ages (**Fig. 2.6**). The robust, Caledonian-aged peak has 10 grains (~10% of the sample population), with the major peak at 430 Ma. The Mesoproterozoic range, the primary age fraction, has 74 grains (~76% of the sample) with several peaks at 1650, 1450, and 1100 Ma. The Archean range has 12 grains (~13% of the sample) with two minor peaks at 2760 and 2530 Ma.

2.4.1.2 Romulus Member of the Heiberg Formation

On central Axel Heiberg Island (Depot Point), a sample was collected from the Romulus Member in the lower part of the Heiberg Formation. The Romulus Member is interpreted to be part of a delta front and is given a Norian age (Embry, 1983a, and references therein). Detrital-zircon ages can be divided into three distinct fractions—ca. 2580–1690 Ma, 920–750 Ma, and 560–215 Ma—with a notable absence of Mesoproterozoic ages (**Fig. 2.6**). The Cambrian to Triassic zircon fraction has 30 grains (~63% of the sample population) with peaks at 425 and 270 Ma. The Neoproterozoic ages, of which there are five grains (~10% of the sample), has one peak

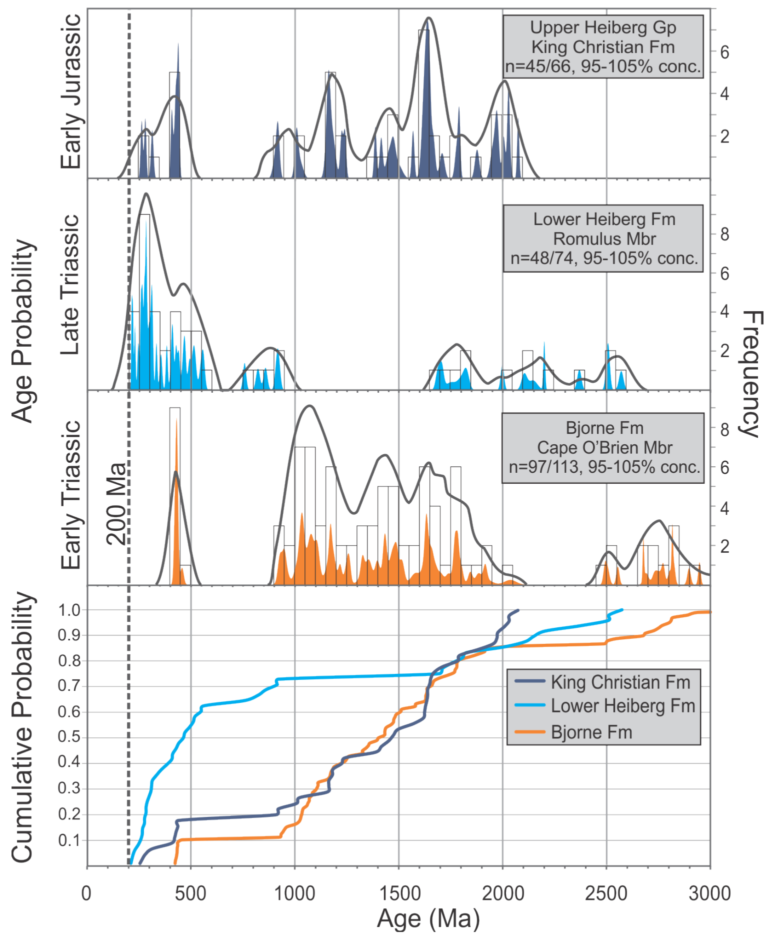

Figure 2.6: Relative probability distribution and cumulative probability plots for three new detrital-zircon samples from this study. Kernel density estimation represented by solid gray line. See Appendix B for complete isotopic analyses and Appendix D for zircon images.

at ca. 850 Ma. The Paleoproterozoic ages have a broad spectrum with three peaks, 2500, 2150, and 1750 Ma (~27% of the sample).

2.4.1.3 King Christian Formation of the Heiberg Group

The Sinemurian to Pliensbachian King Christian Formation sample is from western Ellef Ringnes Island, where the formation is the thickest (180 m) in the basin, and here the unit is interpreted to be a deltaic deposit (Embry, 1983b). Zircon ages have two distinct age ranges—specifically Paleozoic and Precambrian age fractions. The Paleozoic ages range from ca. 441 to 262 Ma with peaks at 425 and 275 Ma (~18% of the sample). The Precambrian can be subdivided into a Tonian-age range and a Paleo- to Mesoproterozoic range. The Tonian zircon, specifically ca. 1020–910 Ma, makes up 8% of the sample. The predominant age range is ca.

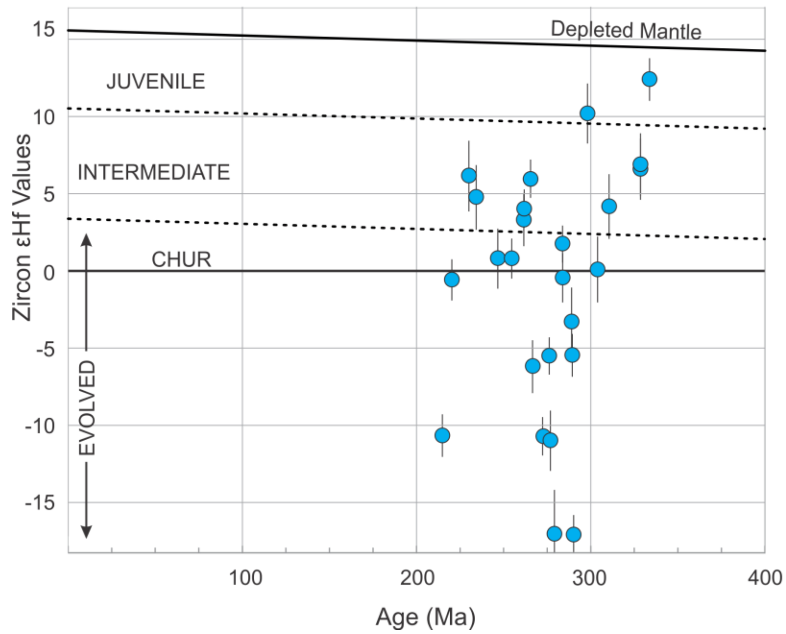

Figure 2.7: Plot shows εHf values for sample data from the Heiberg Formation/Group. Only grains younger than 340 Ma were analyzed. Solid lines isolate depleted mantle (DM) and chondritic uniform mantle (CHUR). See Appendix C for calculated error values. Dashed lines separate fields described as juvenile (0-5 epsilon units below DM), intermediate (5-12 epsilon units below DM), and evolved (>12 epsilon units below DM) following Bahlburg et al. (2011) and Gehrels and Pecha (2014).

2100–880 Ma with peaks at 2000, 1650, 1450, and 1200 Ma (73% of the sample), which is similar to the zircon age distribution in the Bjorne Formation (**Fig. 2.6**).

2.4.2 Hf-Isotope Analyses

Twenty-four zircon grains were analyzed to provide further information on the source of Permian–Triassic zircon from the Lower Heiberg and King Christian formations. The εHf values range from +16 to -17 with no discernible εHf groupings within the data (**Fig. 2.7**). There is no trend (R^2 = 0.06) of εHf values becoming more depleted as the U-Pb age of the zircon decreases. T_{DM} values show a broad spectrum, but the majority of ages are Meso- to Neoproterozoic.

2.4.3 Volcanic Ash Beds

The study location along northern Axel Heiberg Island (**Fig. 2.2**) represents a geographically proximal location within the Sverdrup Basin to the proposed northern sediment source. At Bunde Fiord, ochreous horizons were commonly observed in marine mudstones of the

Blind Fiord, Murray Harbour, Hoyle Bay, and Barrow formations (**Fig. 2.8**). The ochre layers are typically less than 10 cm thick and laterally continuous, and they are interpreted to be volcanic ash beds due to their field properties (color, moisture, and plasticity). X-ray powder diffraction (XRD) using CuKα radiation with a scanning speed of 1°2θ/min show that these ash beds consist of quartz, hydrotalcite, illite, jarosite, with lesser zircon and halloysite (**Fig. 2.8A**). Halloysite is derived from the dissolution of volcanic glass or weathered volcanic ash with a crystalline structure similar to kaolinite (Joussein et al., 2005). Similarly, hydrotalcite is formed from volcanic glass, and it has been produced experimentally by a reaction between basaltic glass and seawater (Crovisier et al., 1982). Hall and Stamatakis (2000) observed hydrotalcite infilling the molds left by the dissolution of volcanic glass shards. Collectively, the presence of volcanically derived minerals and macroscopic textural characteristics confirm that the ochreous layers are volcanic ash beds.

2.5 Discussion

2.5.1 Early Triassic Detrital-Zircon Provenance

The detrital-zircon signature from the Bjorne Formation is remarkably similar to samples from the Devonian clastic wedge (Anfinson et al., 2012a) and is consistent with sample AE1 reported by Miller et al. (2006). The detrital-zircon signature of the Bjorne Formation is similar to Triassic strata from the North Slope of Alaska (Gottlieb et al., 2014) and similar aged strata from the northwestern Cordillera (**Fig. 2.9A**), the latter being recycled from the strata of northwestern Laurentia (Beranek et al., 2010b). Collectively the geographically dispersed areas suggest a common, areally expansive source, which most probably was the Devonian clastic wedge and equivalents (**Fig. 2.9B**), and so provenance is from a recycled source.

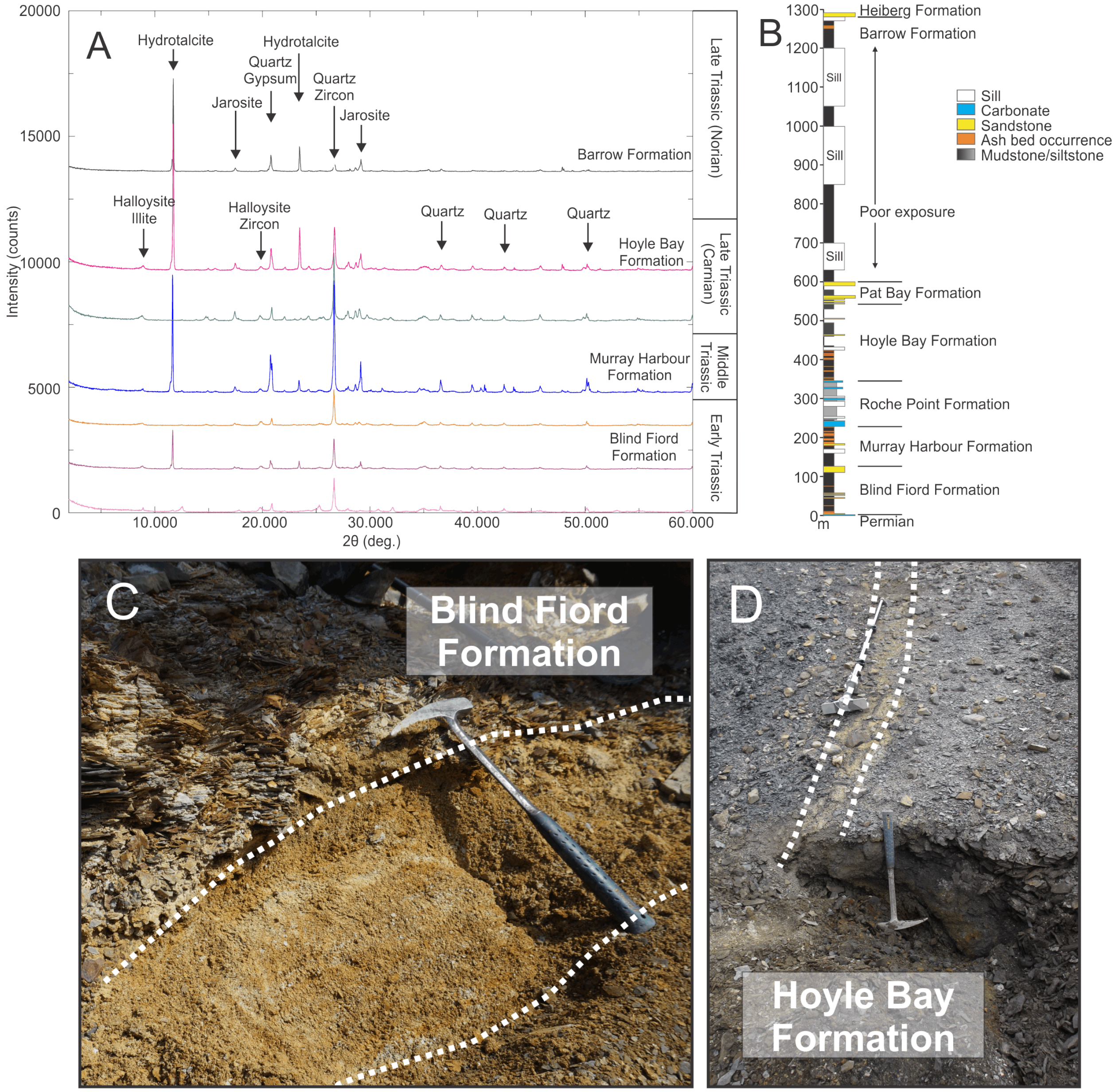

Figure 2.8: (A) X-ray diffraction traces from volcanic ash beds; (B) Stratigraphic log from Bunde Fiord, Axel Heiberg Island highlighting stratigraphic location of volcanic ash beds. Ash beds not to scale. Location of Bunde Fiord highlighted by grey square in Figure 2.2; (C and D) Photographs of volcanic ash beds observed in Bunde Fiord, length of hammer is 50 cm.

A sample from the Blind Fiord Formation has a wholly different signature interpreted to represent the northern source to the basin (Omma et al., 2011). Notable is the occurrence of a suite of Permian ages (ca. 290–265 Ma) and the absence of Caledonian and Ellesmerian orogen ages that typify the Devonian clastic wedge (ca. 700–360 Ma). Omma et al. (2011) suggested the source of the young ages was either Early Permian basaltic magmatic activity within the basin (e.g., Thorsteinsson, 1974), or mid-Permian syenites associated with the Uralian orogeny in the Taimyr region in central Russia (e.g., Vernikovsky et al., 1995; Zhang et al., 2013). The majority of Permian volcanic rocks are observed within the northern part of the Sverdrup Basin, which suggests there were probably volcanic equivalents to the north of the basin. The Lower Permian volcanic rocks in the Sverdrup Basin (the Esayoo, the Unnamed Lower volcanics [ULV], or equivalents) could provide the limited age range of Permian zircon within the Blind Fiord Formation; basalts may be able to supply zircon even though they typically have poor zircon potential (Rioux et al., 2012; Candan et al., 2015; Iles et al., 2015). The converted εNd values and the T_{DM} from the Esayoo volcanics (ca. 276 Ma) are comparable to Hf isotope data from similar aged zircon from this study (**Fig. 2.10**). Long distance transport from the Urals is unlikely to produce the tight range of Permian ages within the Blind Fiord Formation, particularly because Uralide granitoids formed at an almost constant rate from 370 Ma to 250 Ma, older in the south and younger in the north (Vernikovsky et al., 1995; Bea et al., 2002). Granitoids in the northern Urals have ages from ca. 300 to 280 Ma, and post-tectonic granitoids dated at ca. 260 Ma (Pease et al., 2015), probably related to the Siberian LIP. Transport from the Urals is possible but would likely provide a broad spectrum of U-Pb ages rather than narrow peaks as seen in the Blind Fiord Formation.

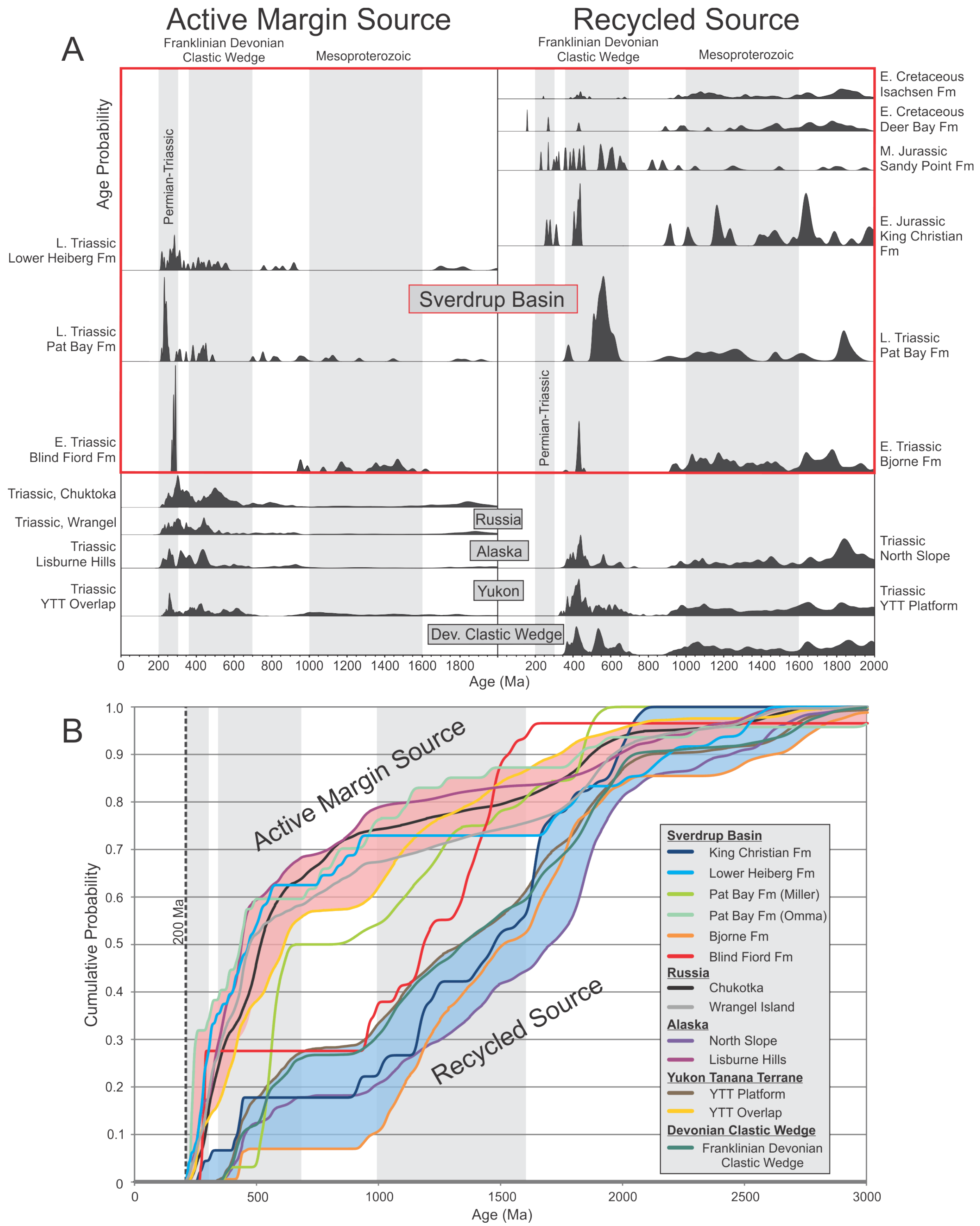

Figure 2.9: Illustration of the detrital age spectra grouped by signatures of the *Recycled Source* and the *Active Margin Source*. Data from the Isachsen Fm (Røhr et al., 2010), from studies in the Canadian Arctic (Miller et al., 2006; Omma et al., 2011; Anfinson et al., 2012a), from Russia (Miller et al., 2006, 2010; Tuchkova et al., 2011; Amato et al., 2015), from Alaska (Miller et al., 2006; Gottlieb et al., 2014), from Yukon (Beranek et al., 2010b; Beranek and Mortensen, 2011), and compiled results from this study as (A) relative probability distributions and (B) cumulative probability plots.

2.5.2 Late Triassic Detrital-Zircon Provenance

2.5.2.1 Pat Bay Formation

Detrital-zircon U-Pb age data of the Pat Bay Formation (Miller et al., 2006; Omma et al., 2011) vary considerably between samples indicative of two different sources during deposition (e.g., Embry, 2009). Sample AE2 from Miller et al. (2006) has an assemblage of ages that overlap within the Devonian clastic wedge spectrum, including a single 376 Ma age, an age fraction of ca. 620–505 Ma, and a broad range of Paleo- to Mesoproterozoic ages. Miller et al. (2006) hypothesized the sample represented sediment derived from north of the Sverdrup Basin because those ages were unknown in northern Canada at the time. Subsequent studies (e.g., Lemieux et al., 2011; Anfinson et al., 2012a) report abundant ca. 700–500 Ma zircon ages from rocks of the Late Devonian clastic wedge as well as the Silurian flysch (Beranek et al., 2015). A prominent ca. 700–500 Ma age-fraction coupled with an absence of Permian–Triassic zircon ages would suggest a source much like Silurian and Devonian strata in the Franklinian Basin; these strata were probably ultimately derived from rocks in Arctic Alaska–Chukotka of Timanide age (e.g., Cecile et al., 1991; Amato et al., 2009, 2014). In contrast, the later work of Omma et al. (2011) reported a prominent range of near-syndepositional ages (ca. 255–217 Ma), in addition to a broad Paleozoic spectrum (ca. 490–295 Ma), which is indicative of derivation from the active margin source region.

2.5.2.2 Lower Heiberg Formation

The Lower Heiberg Formation (Romulus Member) sample has a similar detrital-zircon signature to the Pat Bay sample analyzed by Omma et al. (2011). As with the two previous northerly-derived samples from the Pat Bay and Blind Fiord formations, there is a prominent near-syndepositional–age fraction in the Lower Heiberg Formation with a continuous spectrum of ca. 300–215 Ma ages. In contrast to the Pat Bay and Blind Fiord formations, there is a notable

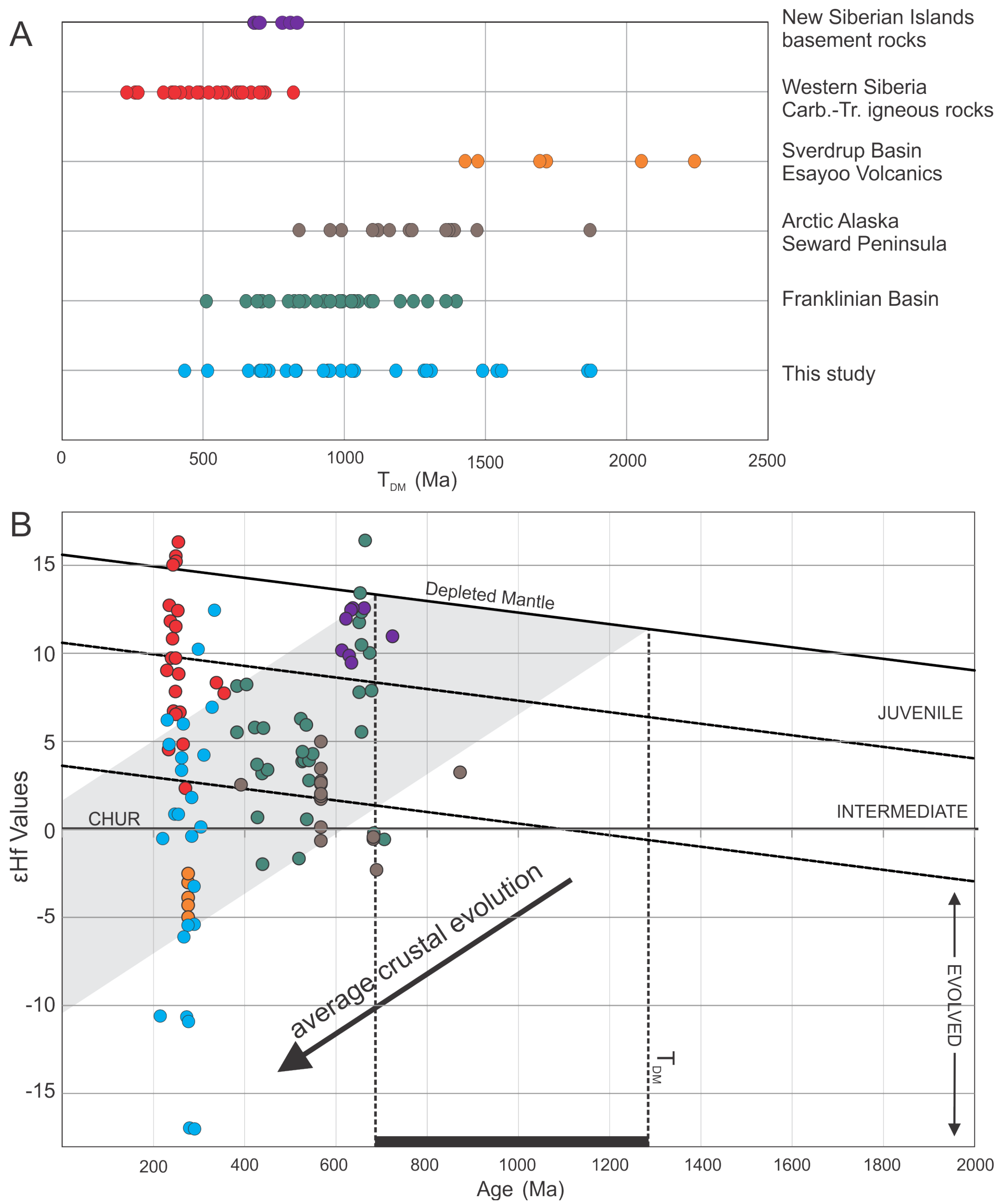

Figure 2.10: (A) T_{DM} values from εHf, other than T_{DM} from Arctic Alaska and Esayoo volcanics which used T_{DM} from εNd values; (B) εHf values for sample data and relevant Hf isotope data comparisons. Grey box and black arrow represent interpreted average crustal evolution trajectories assuming present-day $^{176}Lu/^{177}Hf = 0.0093$ (Vervoort and Patchett, 1996; Bahlburg et al., 2011; Gehrels and Pecha, 2014). εNd values from Arctic Alaska and Esayoo volcanics converted to εHf (see Eq. 1; Vervoort et al., 1999) Data sets are as follows; detrital zircon from Neoproterozoic to Upper Devonian strata of the Franklinian Basin (Anfinson et al., 2012b); Carboniferous to Triassic zircon from igneous rocks of the northwestern Siberian Craton (Malitch et al., 2010); New Siberian Islands basement rocks (Akinin et al., 2015); Neoproterozoic to Devonian igneous rocks of Seward Peninsula, Arctic Alaska (Amato et al., 2009); Lower Permian Esayoo Volcanics from eastern Sverdrup Basin ca. 276 Ma, (Morris, 2013). See Appendix C for complete values and error for each sample and study area.

absence of Mesoproterozoic ages (**Fig. 2.9A**) that are typically present in Laurentian strata (e.g., Hadlari et al., 2012). The consistent zircon signatures from the Blind Fiord, Pat Bay, and Lower Heiberg formations are similar to those reported from Triassic strata of the AACM from Lisburne Hills, North Slope of Alaska, Wrangel Island, and Chukotka (**Fig. 2.9**). Samples from the Upper Triassic Otuk Formation from the Lisburne Hills have an age fraction from ca. 275–220 Ma, in addition to Carboniferous, Lower Paleozoic ages, and minor Mesoproterozoic ages (Phanerozoic peaks at 420, 355, 315, 255, and 220 Ma) (Miller et al., 2006). The detrital-zircon signature from Triassic strata along the North Slope is remarkably similar to the Devonian clastic wedge with a strong age fraction of ca. 700–360 Ma and a broad spectrum of Proterozoic ages (Gottlieb et al., 2014). When comparing detrital-zircon data from the Lisburne Hills and the North Slope, the two regions have notably different age distributions, which strongly resemble the pattern of the two different provenance signatures within the Sverdrup Basin (**Fig. 2.9**).

Similar to Lisburne Hills, Triassic samples from Wrangel Island and Chukotka document a general assemblage of near-syndepositional zircon ages and a minor representation of Mesoproterozoic ages (Miller et al., 2006, 2010; Tuchkova et al., 2011; Amato et al., 2015). More specifically, Wrangel Island samples have nearly continuous ages from ca. 480 to 205 Ma (Phanerozoic peaks at 440, 350, 305, 250, and 230 Ma) (Miller et al., 2010), and samples from Chukotka (Miller et al., 2006; Tuchkova et al., 2011; Amato et al., 2015) have a range of ca. 405–216 Ma (robust Phanerozoic peaks at 500, 300, and 250 Ma). Both regions have minor contributions from the Paleoproterozoic to Silurian. In summary, both the Sverdrup Basin and the broader AACM share the active margin source, which is consistent with the rotational model for the opening of the Arctic Ocean. Alternatively, Zhang et al. (2015) presented a reconstruction in which littoral currents allow for the redistribution of detrital material from the Polar Urals and Taimyr during the Triassic due to the sublithospheric spreading associated with the Siberian mantle plume at 252 Ma, precisely defined by Burgess and Bowring (2015), which does not explain the post–Siberian Trap range of detrital-zircon ages of 240–210 Ma.

2.5.3 Yukon Tanana Terrane

A similar pattern of dual detrital-zircon spectra is observed along the northwestern margin of Laurentia in the Yukon. Sediment recycled from western interior basins of Laurentia has a detrital-zircon signature consistent with derivation from a Devonian clastic wedge-type source (Beranek et al., 2010b)—namely broad Phanerozoic peaks at 450, 420, and 365 Ma—and a wide spectrum of Proterozoic and Lower Paleozoic ages (YTT platform, **Fig. 2.9**). This signature remains relatively stable through Early to Late Triassic strata.

The other provenance signature is from sediment derived from the west, along the active margin of the Yukon-Tanana terrane (YTT). The YTT is a pericratonic terrane that comprises a series of deformed arc, back-arc, and continental margin assemblages (Colpron et al., 2006; Nelson et al., 2006). During the Middle Permian it was separated from ancestral North America by a back-arc basin, the Slide Mountain Ocean (Plafker and Berg, 1994); however, the closure of the back-arc basin in the Late Permian and shortening across the YTT and the western margin of Laurentia (Klondike orogeny) formed a Triassic foreland to back-arc basin to the east of the YTT (Beranek and Mortensen, 2011). Detrital-zircon signatures from Triassic strata sourced from the convergent, western margin of the YTT exhibit a suite of near-syndepositional Permian–Triassic zircon ages (Beranek and Mortensen, 2011).

The two provenance signatures from Triassic strata of the YTT, specifically an active margin source and a recycled source, share a close resemblance to the dual provenance signature of Triassic strata of the Sverdrup Basin and Arctic Alaska (**Fig. 2.9B**). This suggests that the tectonic setting for YTT basin could have been similar to the tectonic setting of the Sverdrup Basin during the Triassic.

2.5.4 Provenance of Permian-Triassic Zircon

Identifying source(s) for the consistently near-syndepositional–aged zircon in Triassic strata throughout the Sverdrup Basin and AACM is essential to understanding the tectonic setting of the Sverdrup Basin during the early Mesozoic. The broad range of εHf values from this study of U-Pb zircon ages between 330 and 200 Ma is interpreted to record a mixed source with a combination of juvenile, intermediate, and evolved crust (**Fig. 2.7**). Other εHf or εNd values from the circum-Arctic display a variety of isotopic compositions and T_{DM}. The ca. 710–380 Ma zircon population from Devonian strata of the Franklinian Basin provides εHf values (Anfinson et al., 2012b) that are congruent with a juvenile to intermediate source (**Fig. 2.10B**) in the AACM. Neoproterozoic to Devonian igneous rocks from Arctic Alaska have converted εNd values that are slightly less juvenile than the Devonian strata (Amato et al., 2009). The T_{DM} of both studies overlap with the T_{DM} of Permian–Triassic zircon of the Lower Heiberg Formation with predominantly Meso- to Neoproterozoic model ages (**Fig. 2.10A**). It is plausible that the lithospheric source involved during the formation of the older zircon record was reincorporated during the Permian–Triassic magmatism in the AACM.

The other proposed source for Permian–Triassic zircon in the Sverdrup Basin is from the Siberian region (e.g., Urals, Taimyr, and NSI: **Fig. 2.1**; Omma et al., 2011; Miller et al., 2013, and references therein). Miller et al. (2013) and Zhang et al. (2015) recently outlined possible sources of the younger zircon ages, which included the Carboniferous to Early Permian plutonic belts from the northernmost Urals; granites as young as ca. 250 Ma from the southern Urals; mafic magmatism (ca. 252 Ma) from the initiation of the Siberian Traps; earliest Triassic felsic and mafic magmatism in the Taimyr region; Permian–Triassic to Triassic rift-related magmatism in the Kara Sea; and granites and syenites (ca. 249–241 Ma) and basalts from southern and central Taimyr. The εHf values from Carboniferous to Triassic magmatic rocks along the northwestern part of the Siberian Craton are substantially more juvenile (Malitch et al., 2010) than similar-aged zircon within the Sverdrup Basin. The T_{DM} of the Siberian zircon are younger than the T_{DM} from this study, which suggests that the Siberian region was not a source region for the Sverdrup Basin during the Triassic. The εHf data from basement rocks of the NSI are within the spectrum of εHf and T_{DM} values of Arctic Alaska and Devonian strata from northern Canada, and these data interpreted to represent juvenile magmatic addition during the Neoproterozoic (Akinin et al., 2015).

The new observations of volcanic ash beds throughout the Triassic section on Axel Heiberg Island are noteworthy because they are a record of ash air fall on the northern side of the basin. To date there have been no observations of volcanic ash beds in Triassic strata from the southern Sverdrup Basin, implying that ash transport was confined to the northern part of the basin and not carried a great distance; otherwise they would be widely distributed throughout the basin. A stratigraphic section of Triassic strata from ~200 km south of Bunde Fiord had no observable volcanic ash beds (Embry, 1983b); therefore, Triassic zircon being sourced from the north of the basin supports the sediment provenance direction suggested by Embry (2009), rather than the near-syndepositional zircon originating from a great distance east of the basin (e.g., Urals, Taimyr; Omma et al., 2011; Miller et al., 2013; Anfinson et al., 2016). If the active margin outboard of the YTT along the western margin of Laurentia was generating the Permian–Triassic zircon observed within Triassic strata, then the same tectonic process could generate similar-aged zircon along the outboard margin of the AACM. This is consistent within the framework of the rotational model, with the Devonian clastic wedge (e.g., Lemieux et al., 2011; Anfinson et al., 2012b) derived from an Arctic Alaska–Chukotka arc such as at Seward Peninsula (Amato et al., 2009); it is logical that a similar arc in the Triassic (**Fig. 2.11**) would incorporate a similar evolved εHf signature and T_{DM}.

2.5.5 Early Jurassic Detrital-Zircon Provenance

The Lower Jurassic King Christian Formation sample has a similar cumulative trend to sediment that would be sourced from erosion of the Devonian clastic wedge. There is a peak at 420 Ma and a broad range of Proterozoic ages that are similar to the detrital-zircon signature of the Bjorne Formation (**Fig. 2.9A**). The difference between the King Christian Formation and the southerly-sourced Bjorne Formation is the presence of three young zircon grains (315, 279, and 262 Ma), which could have been cannibalized from Triassic strata. Zircon assemblages in the Middle Jurassic to Early Cretaceous (Sandy Point, Deer Bay, and Isachsen formations) are consistent with the provenance signature of the Devonian clastic wedge with minor recycled Permian–Triassic zircon (Røhr et al., 2010; Omma et al., 2011; **Fig. 2.9A**). Previous authors (Embry, 1993; Embry and Beauchamp, 2008; Embry, 2009) proposed that Jurassic extension dismembered the northern sediment source region and prevented communication with the Sverdrup Basin by trapping sediment in extensional basins such as the proto–Amerasia Basin. The new detrital-zircon data from the Heiberg Group suggest that the provenance change occurred below the King Christian Formation and above the Romulus Member, which is equivalent to the Skybattle Formation (**Fig. 2.3**; ca. 210–190 Ma). After deposition of the King Christian Formation in the Early Jurassic, there was no longer a supply of near-syndepositional zircon into the basin. The Early Jurassic onset of rifting is supported by the presence of upper Heiberg Group strata at the base of half-grabens on Prince Patrick Island (Harrison and Brent, 2005). Deposition of the Isachsen Formation occurred after the breakup unconformity at ca. 130 Ma (Embry and Beauchamp, 2008). Detrital-zircon ages from the Lower Cretaceous Isachsen sandstone exhibit only a single grain (ca. 244 Ma) younger than 400 Ma (Røhr et al., 2010).

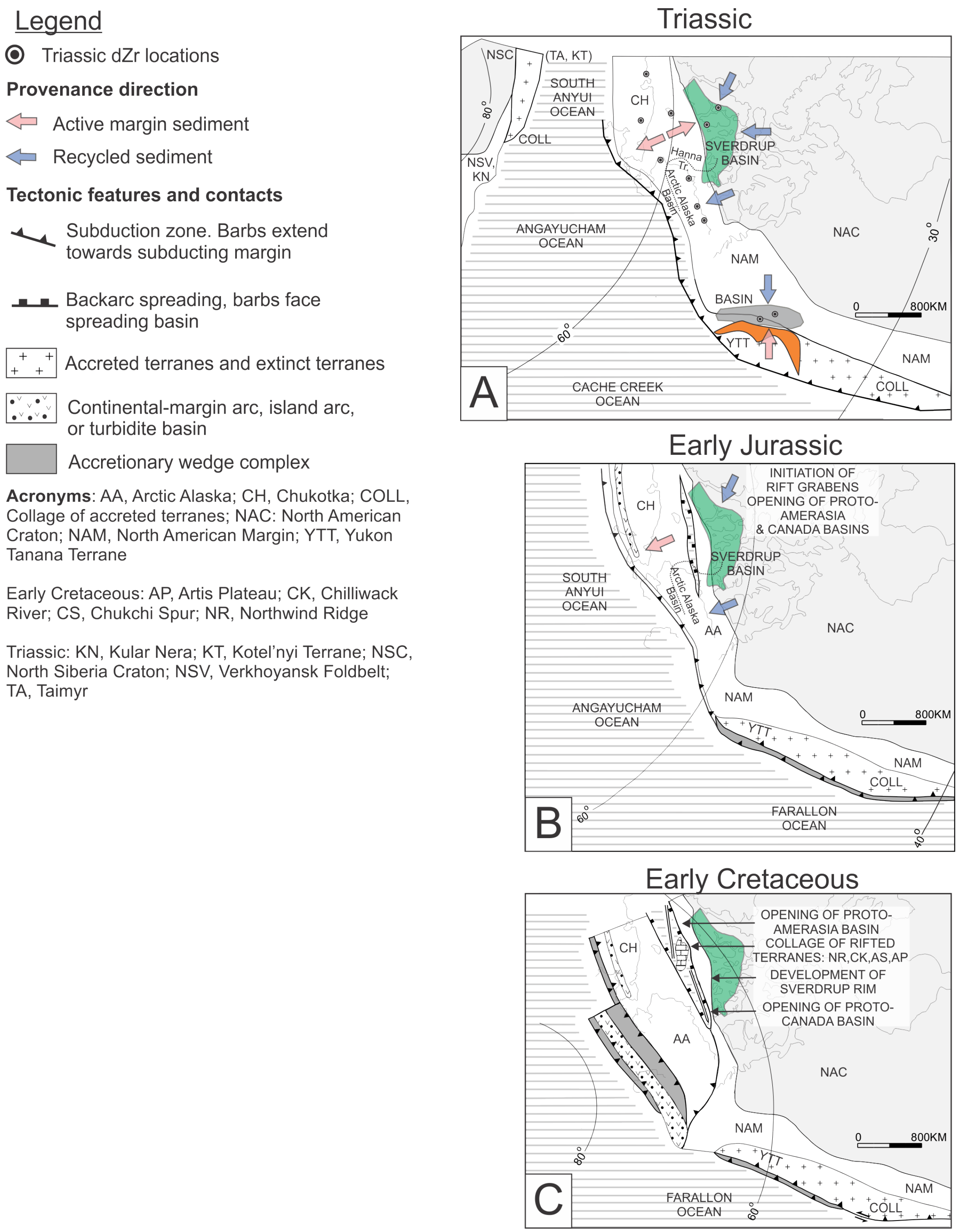

Figure 2.11: Evolution of the northern margin of Laurentia adapted from paleographical maps of Plafker and Berg (1994) and Nokleberg et al. (2000). Outline of YTT (orange polygon) is from Nelson et al. (2006). Axis of Hanna Trough and Arctic Alaska Basin from Gottlieb et al. (2014). Proposed tectonic model: In the Triassic, the Sverdrup basin occupied a retro-arc position to Chukotka along strike with the Triassic basin adjacent to the Yukon Tanana terrane arc; Early Jurassic extension to form the proto-Amerasia basin cutoff the Sverdrup Basin from the AACM; and in the Early Cretaceous during the post-rift stage of Sverdrup Basin, the Amerasia and Canada basins opened as the South Anyui Ocean closed.

2.5.6 Tectonic Setting of the Basin

The abundance of Permian–Triassic detrital zircon and confirmation of Triassic volcanic ash beds in the Sverdrup Basin suggests that the region to the north was tectonically active during the Triassic, and likely part of the Permian as well. We interpret that the combination of volcanic ash beds and identification of remarkably similar dual detrital-zircon provenance patterns from the Sverdrup Basin, YTT, and AACM allows for an interpretation of the outboard margin of the AACM as convergent, as shown in **Figure 2.11** (adapted from Plafker and Berg, 1994; Nokleberg et al., 2000), thereby providing a geodynamic model for rifting in the Jurassic concurrent with closure of the South Anyui ocean basin. The Nokleberg et al. (2000) reconstruction is modified by indicating that rifting of the proto–Amerasia Basin developed as a retro-arc system driven by a subducting slab, which in turn caused AACM to rift from northern Laurentia (as proposed by Kuzmichev, 2009). During slab rollback, retro-arc extension can occur far inboard from the convergent plate boundary (Lawton and McMillan, 1999; Hadlari and Rainbird, 2011), which is how we interpret the Jurassic to Early Cretaceous rifting of the Sverdrup Basin. Our detrital-zircon data support the hypothesis of Embry (2009) that crustal extension dismembered the northern sediment source from the Sverdrup Basin and show that this transition occurred in the Early Jurassic (**Fig. 2.11**), in contrast to Arctic Alaska, which continued to receive sediment from Chukotka in the Jurassic and into the Albian–Aptian (Moore et al., 2015).

The lack of near-syndepositional zircon in Jurassic–Cretaceous strata is important to understanding the nature of the basin because during the syn-rift phase (ca. 190–130 Ma); there is a limited record of magmatism other than the single 158 Ma zircon grain within the Deer Bay Formation. The breakup unconformity (130 Ma; see Embry and Beauchamp, 2008) coincides with the onset of extensive magmatism in the Sverdrup Basin as part of the HALIP event (e.g., Evenchick et al., 2015). Post-rift phase magmatism persisted for more than 30 m.y.

The South China Sea provides an analog for the Sverdrup and Amerasia basins. The South China Sea formed in a retro-arc setting and had limited syn-rift magmatism and persistent magmatism in the post-rift phase (Franke, 2013). Slab roll back is thought to have been the driving mechanism in South China Sea causing back-arc extension (Zhou and Li, 2000; Doust and Sumner, 2007). Rifting began at 110 Ma (Li et al., 2008), and generation of oceanic crust likely began ca. 40–30 Ma (Franke, 2013, and references therein), which indicates a protracted period of extension with no associated magmatic activity followed by extensive post-rift magmatism, similar to the Cretaceous record of the Sverdrup Basin and possibly also Amerasia Basin.

2.6 Conclusion

The Sverdrup Basin has two identifiable detrital-zircon provenance signatures during the Triassic—an active margin source to the north and a recycled source to the south and east of the basin. These two signatures are similar to the two distinct sources observed in Arctic Alaska and the YTT. A hypothetical northwestern convergent margin of Laurentia would explain the remarkable similarity in the source age profiles of the Sverdrup Basin and the overlap assemblage between YTT and the North American craton. The presence of volcanic ash beds throughout Triassic strata, apparently restricted to the northern margin of the basin, indicates that volcanic activity that lasted more than ~50 m.y was relatively proximal to this northern margin, which is consistent with a convergent outboard margin of the AACM during the Triassic. Previous interpretations attributed the source of the Permian–Triassic zircon to be in Russia, specifically the Siberian Traps, Uralian granites, and Taimyr magmatism, none of which make for an ideal candidate for the spectrum of ages, particularly for the Middle to Late Triassic zircon within sandstones of the Sverdrup Basin. The more negative εHf values of Permian–Triassic zircon compared to juvenile values of Permian– Triassic igneous rocks in Siberia support that the provenance was from the AACM instead of western Siberia. The contribution of U-Pb detrital-zircon geochronology, εHf isotope values, and newly described volcanic ash beds from Triassic strata of the Sverdrup Basin help to develop an argument that active magmatism north of the basin supplied Permian–Triassic zircon. Furthermore, the provenance signature from Jurassic strata suggests initial rifting isolated the Sverdrup Basin from the active margin source by the Early Jurassic.

Chapter 3 : Investigating the Paleozoic-Mesozoic Low-Temperature Thermal History of the Southwestern Canadian Arctic: Insights from (U-Th)/He Thermochronology

3.0 Abstract

The Amerasia Basin, located between the Canadian Arctic margin and Arctic Alaska, formed by the counterclockwise plate rotation of the Arctic Alaska-Chukotka microcontinent from northern Laurentia during the Jurassic-Cretaceous. This extensional period would have associated uplift on the rift shoulder which would be recorded as a cooling event in the samples collected from the Neoproterozoic strata of the Amundsen Basin, Cambrian strata of the Arctic Platform, and Devonian strata of the Franklinian Basin. Furthermore, to understand the extent of exhumation on the rift shoulder, the samples form a north-south transect from Banks Island, located proximal to the rifted Canadian margin, to Victoria Island and Brock Inlier towards the Laurentian craton. Additionally, the southwestern Canadian Arctic has a widespread Devonian-Cretaceous unconformity. New zircon (U-Th)/He thermochronology (ZHe) and modelling of organic maturity data (%Ro) can evaluate the thickness of the missing sedimentary package and the amount of erosion between this regional unconformity. ZHe and %Ro models identify the thermal maximum for each study area between the missing late Paleozoic-early Mesozoic interval, which is then interpreted as 3.7-4.5 km of burial proximal to the rifted Canadian margin and less than 1 km of burial near the interior craton whereas the amount of erosion, 2.3-3.5 km, is similar across the region. While the extent of burial and exhumation can be constrained from ZHe and %Ro models, it is more challenging to evaluate the timing of these events. This paper investigated two thermal histories, 1) maximum burial occurred in the Late Devonian followed by gradual unroofing until renewed Cretaceous deposition, or 2) the region undergoes late Paleozoic-early Mesozoic burial, with a thermal maximum prior to Jurassic rifting, followed by uplift. The ZHe models for both scenarios produce acceptable time-temperature pathways, so the

data cannot discount either thermal history. If there was continued deposition into the Mesozoic on Banks Island, it could represent a continuation of the Sverdrup or Arctic Alaska basins margins, both of which record a similarly thick sedimentary package during this interval compared to the estimated thickness from the ZHe and %Ro models.

3.1. Introduction

Understanding of the pre-Jurassic thermal history along the margins of the Canadian Arctic Islands is limited, despite its importance in the geodynamic evolution of the Sverdrup Basin and the northern Laurentian margin. A regional unconformity spanning Late Devonian to Jurassic-Cretaceous time has been documented south of the Sverdrup Basin, over the Arctic Platform and into the Mackenzie Corridor (**Fig. 3.1**; Miall, 1976; Jones et al., 1992; Wheeler et al., 1996). This unconformity shows a marked jump between higher thermal maturity Paleozoic strata below the unconformity and lower thermal maturity Mesozoic strata above.

Some studies indicate that the increase in maturity was a consequence of burial by (now eroded) Upper Devonian strata, such as on Banks Island where Embry (1988) estimated ~5 km of missing Upper Devonian-Lower Carboniferous strata, and more recently Dewing and Obermajer (2009) interpreted ~1.7-2.7 km of eroded Upper Devonian strata. Conversely, seismic and field data from Banks Island has provided evidence that the now eroded strata were deposited during a more protracted period of Devonian to Triassic deposition (Miall, 1976). On the southwest margin of the Sverdrup Basin on Prince Patrick Island an estimated 4.2 km of strata is missing between the Devonian-Jurassic unconformity, with the age of eroded strata undetermined (Harrison and Brent, 2005).

Elsewhere in the southwestern Canadian Arctic (**Fig. 3.2**), thermochronological studies on either side of the unconformity have indicated deposition continued after the Devonian. In the Mackenzie-Beaufort Basin, there was an estimated 4 km of missing Permian-Jurassic strata

(Issler et al., 2012). Further south in the Mackenzie Corridor, 2.6-3.7 km of Carboniferous-Triassic strata was eroded prior to burial in the Cretaceous (Issler et al., 2005); however the timing of burial and uplift is not conclusive from thermal maturity and thermochronology data with estimated maximum burial in either the Triassic or Permian, before subsequent cooling in either the Jurassic or Triassic (Tr./Jr.: Issler et al., 2005; Perm./Tr.: Powell et al., 2016). Nearby sedimentary packages in the Mackenzie-Beaufort Basin and Anderson Plain have been studied using apatite fission track thermochronology (AFT; Issler et al., 2012), and indicate exhumation prior to deposition of Jurassic-Cretaceous sediment. To the south, progressive late Paleozoic-early Mesozoic unroofing of the Slave craton has been documented from apatite (U-Th)/He thermochronology (AHe) and was interpreted to be the result of dynamic topography (**Fig. 3.2**; Ault et al., 2009, 2013). More recently, detrital-zircon geochronology data indicates that rifting in the Amerasia Basin commenced in the earliest Jurassic (ca. 200-190 Ma; Hadlari et al., 2016; Midwinter et al., 2016), and therefore uplift and erosion associated with rifting should be recorded as cooling events along the flanks of the Sverdrup and Amerasia basins.

We report new (U-Th)/He zircon thermochronology results from Banks Island, Victoria Island and the Brock Inlier in an attempt to constrain the magnitude of Devonian to Cretaceous burial and unroofing events by testing the two burial histories, with either the thermal maximum occurring just prior to rifting in the proto-Amerasia Basin or immediately after deposition of the Devonian clastic wedge. The benefit of using zircon as the thermochronometer is its ubiquity, resistance, and typically high U-Th concentration, in addition to its ability to constrain exhumation histories at shallow crustal conditions. Furthermore, the relationship between radiation damage and diffusion of helium from zircon (Guenthner et al., 2013) explains significant dispersion in ZHe dates given a variety of pre-depositional histories experienced by each individual zircon in the study areas.

3.2 Geological Setting

The geology from the Brock Inlier to Banks Island records multiple tectonic events and preserves parts of a sedimentary history that stretches from the Neoproterozoic to the Cenozoic. Meso- to Neoproterozoic strata ("Sequence B"; Young et al., 1979) of the Brock Inlier post-date the Grenvillian orogeny (ca. 1200-1000 Ma) and pre-date the break-up of Rodinia (ca. 780-720 Ma). These represent deposition of sediment in an intracratonic tectonic environment (Amundsen Basin) considered to be an embayment of an epeiric sea that covered northwestern Laurentia between the amalgamation and later break-up of Rodinia (Young, 1981; Rainbird et al., 1996). Sequence B strata exposed on the Brock, Minto (Victoria Island), and Cape Lambton (Banks Island) inliers (**Fig. 3.1**; Rainbird et al., 1996) are part of the Neoproterozoic (Tonian-Cryogenian) Shaler Supergroup, and have a maximum thickness of over 4 km. The units that were sampled for (U-Th)/He dating are the Nelson Head and Boot Inlet formations from the Brock Inlier, which are overlain by >1 km of younger Neoproterozoic strata, and the Nelson Head Formation in the Minto Inlier where it is overlain by 2-3 km of Neoproterozoic strata based on stratigraphic sections (Rainbird et al., 1994). Along the northwestern Laurentian margin, ca. 723 Ma Natkusiak Formation flood basalts and ca. 718 Ma sills on Victoria Island of the Franklin LIP, related to the breakup from Siberia (Ernst et al., 2016), marks the onset of rifting along the margin of the Amundsen Basin (Heaman et al., 1992; Rainbird et al., 1998).

By the Cambrian, northwestern Laurentia was an established passive margin (Harrison, 1995; Durbano et al., 2015). Lower Cambrian sandstone, sampled for (U-Th)/He dating on both Victoria Island and Brock Inlier (**Fig. 3.2**), unconformably overlie strata of Sequence B. Above Lower Cambrian strata, an extensive carbonate platform developed and persisted through the Silurian, although the shelf margin stepped back several times (de Freitas et al., 1999; Dewing et al. 2015). Lower Silurian to Lower Devonian sediment was deposited into the northeast part of

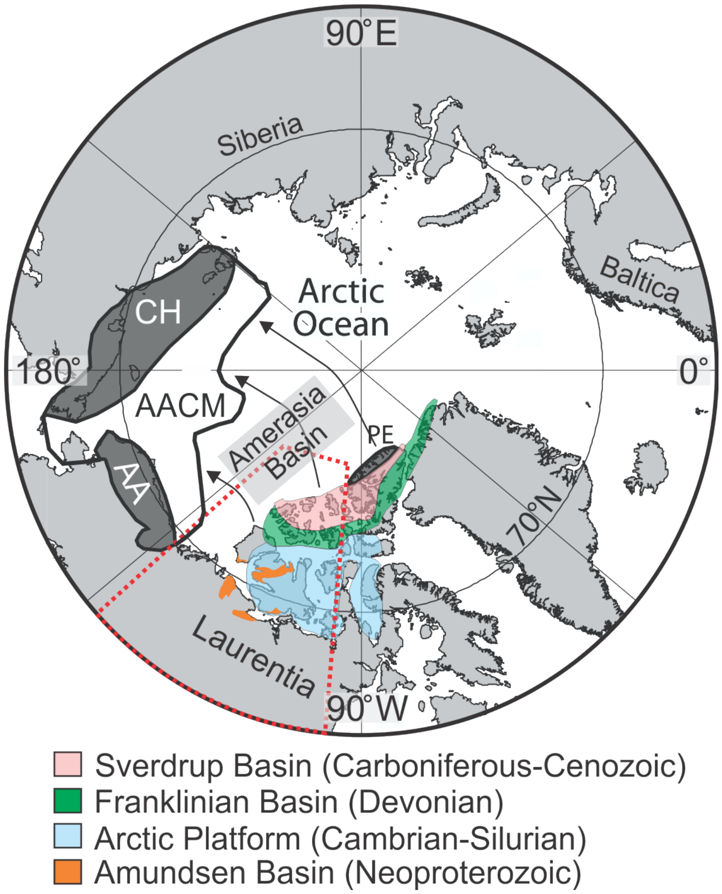

Figure 3.1: Map of the Arctic depicting the names and location of basins and regions mentioned in text. AA - Arctic Alaska; AACM - Arctic Alaska-Chukotka microcontinent; CH - Chukotka; PE – Pearya. Outline of AACM (black line) from Drachev (2011). Rotation of AACM away from the Canadian margin illustrated by the black arrows (from Embry, 2000). Sverdrup Basin from Embry and Beauchamp (2008); Franklinian Basin from Anfinson et al. (2013); Arctic Platform from Dewing and Obermajer (2009); Amundsen Basin from Rainbird et al. (1996). Red dashed polygon identifies the location of map in Figure 3.2.

the Arctic Islands from the Caledonian orogen, produced by the collision of Laurentia and Baltica. Late Silurian to Early Devonian north-south oriented folds, arches or reverse faults are likely related to this event (Miall, 1986). The Coppermine Arch was a regional high during Late Silurian times, and a NW trending thrust fault that parallels the arch axis, juxtaposes Proterozoic strata over Ordovician strata (Jones et al., 1992). This sequence of weakly deformed to undeformed lower Paleozoic strata is termed the Arctic Platform.

By the Middle Devonian, the onset of widespread clastic sedimentation began with the Ellesmerian orogeny, resulting from the collision of a northern landmass into northern Laurentia (Embry, 1988a). The orogen produced a foreland basin (Franklinian Basin, **Fig. 3.1**) in front of the southwestern-directed propagating collisional zone. The Upper Devonian (Frasnian–Famennian) Parry Islands Formation, sampled for (U-Th)/He dating on Banks Island (**Fig. 3.2**), is the uppermost formation in the Franklinian Basin and represents the youngest preserved succession of proximal Ellesmerian orogen foreland basin sedimentation (Embry, 1988a). Preserved Middle-Upper Devonian clastic strata in the Franklinian Basin are estimated to be between 4 km (Embry, 1988a) and 5 km (Embry and Klovan, 1976; Harrison, 1995) thick. Patchett et al. (2004) estimated that the Devonian clastic wedge blanketed the Arctic Platform and Canadian Shield with up to 2 km of sediment. Deformation related to the Ellesmerian orogeny is widespread across the Canadian Arctic Islands (Harrison, 1995)

Rifting in the early Carboniferous led to the development of the Sverdrup Basin (**Fig. 3.1**), accumulating sediment over the deformed lower Paleozoic strata of the Ellesmerian orogen, with rifting persisting until the early Permian followed by thermal subsidence through to Jurassic time (Embry and Beauchamp, 2008). The axial region of the Sverdrup Basin contains ~3 km of upper Paleozoic strata, up to 9 km of Mesozoic strata, and upwards of 3 km of Cenozoic strata (Trettin et al., 1991). Rifting of the proto-Amerasia Basin began in the Jurassic, with consequent seafloor spreading in the Cretaceous, separating the Arctic Alaska-Chukotka microcontinent (AACM) from Arctic Canada (Embry, 1990, 2000). Lastly, the basin was tectonically inverted by the Paleocene-Eocene Eurekan orogeny due to the rotation of Greenland into Ellesmere Island (e.g., Heron et al., 2015).

Using the rotational opening plate tectonic model of Grantz et al. (1979, 2011) and Embry (1990), the location of the AACM (**Fig. 3.1**) prior to its Jurassic-Cretaceous separation and rotation from the northern Laurentian margin places Arctic Alaska adjacent to Banks and Prince Patrick islands (**Fig. 3.2**). Initial rifting produced grabens on Banks and Prince Patrick islands, containing rocks as old as Middle and Early Jurassic, respectively (Miall, 1979; Harrison

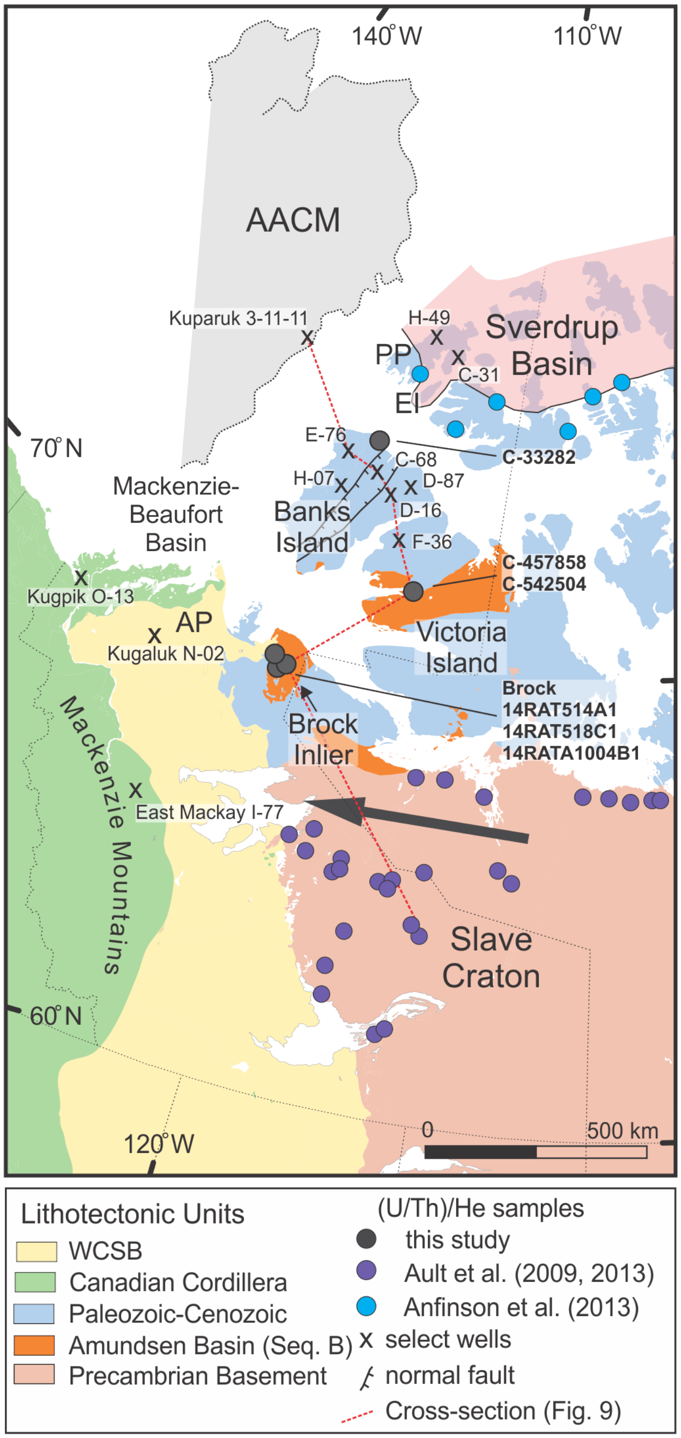

Figure 3.2: Simplified lithotectonic map of south Arctic Islands and northwestern Laurentia (adapted from Ault et al., 2013) showing locations of (U-Th)/He samples dated in this study, (U-Th)/He apatite sample locations of Ault et al. (2009, 2013) within the Slave craton, and of Anfinson et al. (2013) within the Franklinian Basin. Outline of Arctic Alaska represents the restored position prior to the opening of proto-Amerasia Basin, based on Nokleberg et al. (2000). Large black arrow represents progressive late Paleozoic-early Mesozoic cooling/unroofing of the Slave craton, interpreted by Ault et al. (2013). Select wells (x) referenced from Issler et al. (2005, 2012), Dewing et al. (2007), and Dewing and Obermajer (2009). Banks graben is a Jurassic rift structure (Dewing and Obermajer, 2009). Sverdrup Basin outline from Embry and Beauchamp (2008). AACM – Arctic Alaska-Chukotka microcontinent; AP – Anderson Plain; EI – Eglinton Island; PP – Prince Patrick Island; WCSB – Western Canada Sedimentary Basin.

and Brent, 2005). Midwinter et al. (2016) proposed that initial rifting commenced at ca. 200 Ma, which may have fostered uplift and erosion in the southwestern Arctic, south of the Sverdrup Basin. New zircon (U-Th)/He thermochronological data can provide new estimates on the amount of burial and erosion prior to and following Early Jurassic rifting.

3.2.1 Previous Thermal Modelling Studies

There have been several studies estimating the modern and paleo-thermal gradients in the Mackenzie Corridor and Arctic Islands (Feinstein et al., 1996; Majorowicz and Embry, 1998; Issler et al., 2005; Dewing and Obermajer, 2009; Chen et al., 2010; Hu et al., 2010; Issler et al., 2011, 2012). Bottom hole temperatures (BHT) from 156 wells within the Arctic Islands were used to determine the average modern temperature gradient of 31 ± 7°C/km, and a Cretaceous-Tertiary gradient of 28 ± 9°C/km (Majorowicz and Embry, 1998). More recent work noted the current geothermal gradient to be 23 ± 7°C/km from 86 wells within the basin, although the scatter of BHT at depths greater than 2 km is >40°C (Chen et al., 2010). South of the Sverdrup Basin margin, Majorowicz and Embry (1998) and Dewing and Obermajer (2009) interpreted higher heat flow in the Franklinian Basin on Banks Island with the zone of high modern and paleo-heat flow perhaps attributed to the rifted margin of the Amerasia Basin.

Vitrinite reflectance is an organic maturity parameter used for constraining maximum burial in sedimentary basins. Because vitrinite reflectance is non-retrograde, various techniques have been proposed to estimate erosion from Ro-depth relationships (Dow, 1977; Corcoran and Dore, 2005). Following the methodology of Dow (1977), Dewing and Obermajer (2009) interpreted a Ro curve with a 0.6% Ro value at surface in the Muskox D-87 well on Banks Islands as indicating the removal of 2.7 km of sediment at this location.

In the Beaufort-Mackenzie Basin, the modern geothermal gradient is 25-30°C/km, whereas the southeast margin of the basin towards the Anderson Plain is marked by higher geothermal gradients (30-50°C/km), which could reflect a higher contribution of heat production from less extended continental crust and possibly contributions from subsurface fluid flow (Issler et al., 2011). Thermal maturity data (Ro) from the Kugpik O-13 well (**Fig. 3.2**), indicates a %Ro step across the Jurassic-Permian unconformity of 0.2%, which is interpreted to represent up to 4 km of strata removed prior to Jurassic deposition (Issler et al., 2012). It is unknown if the %Ro step is partially attributed to higher paleo-temperatures in the pre-rift Permian strata from either deeper burial or elevated heat flow. AFT data from the Anderson Plain Kugaluk N-02 well suggests Triassic exhumation with 1-2 km of Cretaceous-Cenozoic reburial that was subsequently removed by erosion (Issler et al., 2012).

Further south, from the East MacKay I-77 well in the Mackenzie Plain (**Fig. 3.2**), the modern geothermal gradient is measured at 32.6°C/km with a paleo-thermal gradient interpreted to be 41°C/km from the Carboniferous to Triassic (Issler et al., 2005). While there are no preserved Carboniferous to Jurassic strata in the region, the maximum burial was modeled in the Late Triassic (213 ± 20 Ma) using AFT data integrated with shale compaction models, with an estimated missing thickness of 2.7-3.6 km of Carboniferous to Triassic strata (Issler et al., 2005).

On the Slave craton south of the Canadian Arctic Islands (**Fig. 3.2**), modelling of AHe data suggest that Paleozoic burial exceeded 3 km and reached maximum temperatures, ranging from 80-140°C, in Carboniferous to Middle Triassic time (Ault et al., 2009, 2013). Subsequent erosion occurred during the Paleozoic-Mesozoic, with a western migration of unroofing from ca. 340-225 Ma (Ault et al., 2013). The Ault et al. (2013) thermal histories require near-surface conditions by the end of the Jurassic, prior to 45-80 °C of Cretaceous reheating and subsequent erosion in the Cenozoic.

3.2.2 Regional Detrital-Zircon Geochronology Studies

The interpretation of zircon (U-Th)/He datasets can be complicated due to the effects of pre-depositional thermal histories that the zircon have witnessed. To assess this complexity, an understanding of the provenance ages for the sedimentary successions is vital when constructing time-temperature plots for the study areas. The Devonian strata of Banks Island are part of the areally expansive Devonian clastic wedge (Anfinson et al., 2012a, 2012b). U-Pb detrital zircon age data from the Late Devonian Parry Islands Formation from northeastern Banks Island (**Fig. 3.3**), the youngest of the Franklinian Basin deposits (Embry and Klovan, 1976), identified two primary detrital-zircon sub-populations of ca. 700-380 Ma (44%) and ca. 2100-900 Ma (50%),

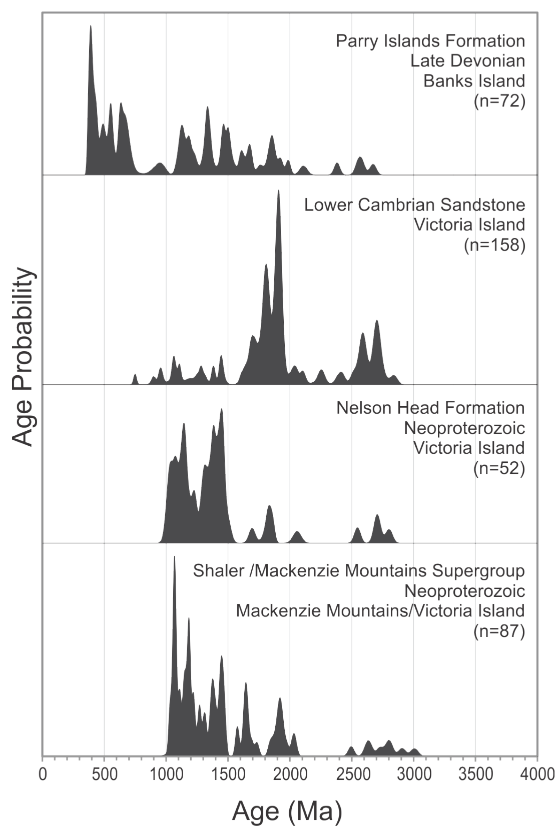

Figure 3.3: U-Pb detrital zircon spectra as reference for zircon inheritance for (U-Th)/He samples dated in this study: Banks Island – Devonian Parry Islands Formation (PI-8: Anfinson et al., 2012b); Victoria Island - Lower Cambrian sandstone (Sample C-E; Hadlari et al., 2012); Brock Inlier - Neoproterozoic Nelson Head Formation on Victoria Island (Rayner and Rainbird, 2013); Neoproterozoic strata of the Shaler/Mackenzie Mountain Supergroup (Rainbird et al., 1992, 1996, 1997; Villeneuve et al., 1998).

with a secondary detrital-zircon population of 2700-2350 Ma (5%; sample PI-8 of Anfinson et al., 2012b).

Detrital-zircon U-Pb data from the Cambrian passive margin of northern Laurentia show two unique age signatures (Hadlari et al., 2012). Hadlari et al. (2012) noted that samples from the Mackenzie Mountains are dominated by detrital zircon ages reflecting provenance from the Archean craton and Paleoproterozoic orogens, whereas detrital-zircon ages from Victoria Island have minor age ranges at ca. 1450-900 Ma (14%), a predominant age population in the Paleoproterozoic, ca. 2100-1600 Ma (59%), and an Archean sub-population at ca. 2850-2500 Ma (22%; **Fig. 3.3**). There is one grain with an U-Pb age of 749 ± 24 Ma, assumed to be either part of the Franklin LIP during to the breakup of Rodinia (ca. 720 Ma) or the Gunbarrel LIP (ca. 780 Ma; Ernst and Bleeker, 2010); however, this Neoproterozoic age from Victoria Island makes up less than 0.25% of the data set (Hadlari et al., 2012).

Detrital-zircon data from the Neoproterozoic Nelson Head Formation (Rayner and Rainbird, 2013) display an overwhelming component of Mesoproterozoic ages (ca. 1500-1000 Ma, 83%) with minor Paleoproterozoic (ca. 2100-1700 Ma, 9%) and Archean (ca. 2800-2500 Ma, 8%) components (**Fig. 3.3**). The (U-Th)/He samples collected as part of this study come from two Neoproterozoic units, the Nelson Head Formation and overlying Boot Inlet Formation, the latter of which recorded a 900 Ma age of deposition based on Re-Os data (van Acken et al., 2013). The youngest detrital grains in the units sampled from the Nelson Head Formation are ca. 1000 Ma (Rayner and Rainbird, 2013); therefore, the inferred age of deposition for these two units is between ca. 1000-900 Ma. The broader provenance studies of Neoproterozoic strata from the Shaler and Mackenzie Mountain supergroups (**Fig. 3.3**) display a similar distribution of U-Pb ages with populations from ca. 1500-1000 Ma (67%), ca. 2100-1600 Ma (24%), and ca. 3000-2500 Ma (9%; Rainbird et al., 1992, 1996; Villeneuve et al., 1998).

3.3 (U-Th)/He Thermochronology

We analyzed samples along a north-south transect between the Sverdrup Basin and Slave craton, divided into three study areas: Banks Island, Victoria Island and the Brock Inlier (**Fig. 3.2**). The one sandstone sample collected on northern Banks Island is representative of the youngest part of the Late Devonian Franklinian Basin. Two sandstone samples collected on Victoria Island are representative of the basal Arctic Platform, which began accumulating sediment in the Early Cambrian on the passive margin of northern Laurentia. Three Neoproterozoic sandstone samples and one Cambrian sample were collected from the Brock Inlier. The Cambrian sandstone is similarly belongs to the Arctic Platform whereas the Neoproterozoic samples are representative of the Amundsen Basin.

Zircon (U-Th)/He thermochronology is based upon the retention of alpha particles (^{4}He), produced during ^{238}U, ^{235}U and ^{232}Th decay. Whereas radiogenic helium readily diffuses from the crystal structure at high temperatures, zircon becomes increasingly retentive of helium as temperature decreases. This temperature range between open and closed system behaviour is termed the partial retention zone (PRZ) and typically corresponds to ~130-200°C for helium in zircon (Reiners et al., 2004; Hourigan et al., 2005; Wolfe and Stockli, 2010). During burial and reheating, zircon crystals that reside at high temperatures within or exceeding the PRZ for sufficient time may lose radiogenic helium through thermal diffusion, effectively resetting the (U-Th)/He system. Recent studies suggest that zircon crystals that have accumulated radiation damage in the crystal lattice over geologic timescales may be sensitive to a broader range of temperatures than previously reported (Guenthner et al., 2013). Progressive radiation damage increases tortuosity of helium diffusion pathways, impeding thermal diffusion and resulting in a more retentive helium system. However, as radiation damage continues to increase past a certain threshold, fast-diffusion pathways are formed throughout the crystal lattice resulting in increased diffusivity of helium in zircon (Guenthner et al., 2013). A useful proxy for radiation damage is the effective uranium (eU) concentration (eU = U + 0.235 • Th). When integrated over the time that the zircon has resided at lower temperatures than required for thermal annealing of radiation damage, eU concentrations can be used to estimate zircon-specific diffusion kinetics (Guenthner et al., 2013, 2014). ZHe date-eU trends may be negative or positive dependent on the sample's thermal history. Negative correlations, in which ZHe dates decrease with increasing eU, are commonly seen in rocks that have experienced long residence times at low temperatures in the uppermost crust (Guenthner et al., 2014; Powell et al., 2016). Reiners et al. (2002) also noted that diffusivity scales with grain volume, suggesting that grain dimensions strongly influence helium diffusion.

Zircon sampled for ZHe thermochronology in this study have presumed different U-Pb ages based on the regional detrital studies (**Fig. 3.3**; Anfinson et al., 2012b; Hadlari et al., 2012; Rayner and Rainbird, 2013). The broad provenance expected in a single sample means that the pre-depositional history of zircon, including inherited helium and radiation damage, must be considered when assessing relationships between post-depositional thermal history and ZHe date-eU trends. In an effort to account for variable and unknown pre-depositional histories, Guenthner et al. (2015) introduced the concept of the 'inheritance envelope' for ZHe data from sedimentary samples. The inheritance envelope accounts for detrital histories that range from the oldest U-Pb date to the depositional age of the rock to investigate how well post-depositional thermal histories explain ZHe data. This concept is important, as the kinetics of helium diffusion in zircon with extensive pre-depositional histories will be significantly different than those with zero-inheritance due to the effects of long-term radiation damage accumulation in the crystal structure. A zero-inheritance grain is one that has experienced no pre-depositional radiation damage accumulation and has no inherited radiogenic helium, either because it is syndepositional (i.e. a near-zero U-Pb age at time of deposition) or was fully reset and rapidly exhumed immediately prior to burial in the basin. For example, given a high eU concentration, helium diffusion will occur at lower temperatures in a zircon with an extensive pre-depositional history compared to a zircon with the equivalent eU concentration but zero-inheritance. Correspondingly, the more damaged zircon will have a younger ZHe date (Guenthner et al., 2014). At low eU values, a zircon with inherited radiation damage will have lower helium diffusivity, and an older date than a zero-inheritance grain (Guenthner et al., 2015). ZHe dates from a sample that is only partially thermally reset should be bound between the zero-inheritance (i.e. depositional age, youngest U-Pb detrital zircon age) and maximum-inheritance curves (Guenthner et al., 2015). In this study, inheritance curves are used to represent probable detrital-zircon provenance with respect to the sample location and age. Furthermore, grain size has an impact on eU values (Reiners et al., 2002), so a "grain size envelope" can also be used to bound the curves from the minimum, average, and maximum equivalent spherical radius values.

3.4 Analytical Methods

Forty-four zircon grains from seven samples (**Table 3.1**) were selected for (U-Th)/He thermochronology, conducted at the Thermochronology Research and Instrumentation Laboratory (U-Th)/He facility at the University of Colorado at Boulder, USA. Samples were crushed, sieved (63-250 µm), washed and processed via methylene iodide (MI) heavy liquid techniques at the University of Ottawa, Canada. Despite careful processing, no apatite was recovered. Individual zircon grains are handpicked using a Leica M165 binocular microscope equipped with a calibrated digital camera and capable of both reflected and transmitted, polarized light. The grains are screened for quality, including crystal size, shape, and the presence of inclusions. After characterization, grains are placed into small Nb tubes that are then crimped on both ends. This Nb packet is then loaded into an ASI Alphachron He extraction and measurement line. The packet is placed in the UHV extraction line (~3x10^{-8} torr) and heated with a diode laser to ~800-1100°C for 5 to 10 m to extract the radiogenic ^{4}He. The degassed ^{4}He is then spiked with approximately 13 ncc of pure ^{3}He, cleaned via interaction with two SAES getters, and analyzed on a Balzers PrismaPlus QME 220 quadrupole mass spectrometer. Degassed grains are then removed from the line, and taken to a Class 10 clean lab for dissolution. Apatite grains, still enclosed in the Nb tubes, are placed in 1.5 mL Cetac vials, spiked with a ^{235}U-^{230}Th tracer in HNO_3, capped, and baked in a lab oven at 80°C for 2 h. Zircon are dissolved using Parr large-capacity dissolution vessels in a multi-step acid-vapor dissolution process. Grains (including the Nb tube) are placed in Ludwig-style Savillex vials, spiked with a ^{235}U-^{230}Th tracer, and mixed with 200 mL of Optima grade HF. The vials are then capped, stacked in a 125 mL Teflon liner, placed in a Parr dissolution vessel, and baked at 220°C for 72 h. After cooling, the vials are uncapped and dried down on a 90°C hot plate until dry. The vials then undergo a second round of acid-vapor dissolution, this time with 200 mL of Optima grade HCl in each vial that is baked at 200°C for 24 h. Vials are then dried down a second time on a

Table 3.1: Sample coordinates and stratigraphic position of samples from the southwestern Arctic

Sample Name	Location	Unit	Age	Latitude (N)	Longitude (W)
C-033289	Banks Island	Hecla Bay Formation /Parry Islands Formation	Latest Devonian (Famennian-Frasnian)	74.134	-118.670
C-457858	Victoria Island	unnamed Cambrian Sandstone	Early Cambrian (Series 2)	71.433	-115.435
C-542504		unnamed Cambrian Sandstone	Early Cambrian (Series 2)	71.499	-114.993
Brock	Brock Inlier	Mount Clark Fm	Early Cambrian	69.150	-121.883
14RAT514A1		Boot Inlet Formation	Neoproterozoic (Tonian)	69.006	-122.664
14RAT518C1		Nelson Head Formation	Neoproterozoic (Tonian)	69.348	-122.918
14RATA1004B1		Nelson Head Formation	Neoproterozoic (Tonian)	69.342	-122.945

hot plate. Once dry, 200 mL of a 7:1 HNO_3:HF mixture is added to each vial, the vial is capped, and cooked on the hot plate at 90°C for 4 h. Once the minerals are dissolved, regardless of the dissolution process, they are diluted with 1 to 3 mL of doubly-deionized water, and taken to the ICP-MS lab for analysis. Mineral standards of Durango apatite (31.5 Ma) and Fish Canyon Tuff zircon (28.2 Ma) are routinely analyzed (degassed and dissolved) in conjunction with the samples with each run to ensure data integrity. Sample solutions, along with standards and blanks, are analyzed for U, Th, and Sm content using a Thermo Element 2 magnetic sector mass spectrometer. Once the U, Th, and Sm contents have been measured, He dates and all associated data are calculated on a custom spreadsheet made by CU TRaIL staff.

3.5 Analytical Results and Numerical Modelling

3.5.1 Zircon (U-Th)/He Dating

We report 44 (U-Th)/He zircon dates from seven samples of the southwestern Arctic's lower stratigraphic record (**Table 3.1**). Results are plotted in **Figure 3.4** as individual zircon (U-Th)/He dates versus eU concentration and equivalent spherical radius (ESR). ZHe dates have a significant degree of dispersion, with a range of >1000 m.y. between single crystal dates within the Neoproterozoic, Devonian, and Triassic-Cretaceous (**Table 3.2**). Similarly, the samples have a broad distribution of eU values varying by 1000s of ppm. A few zircon with anomalously young ZHe dates (<15 Ma) and correspondingly high eU concentrations (2415-4235 ppm) are viewed as outliers and are not considered in our modeling or discussion.

Based on our new ZHe dates and available independent geological constraints, we use thermal history modeling in an attempt to constrain the magnitude of burial and exhumation, and the maximum temperatures reached for each sample. Furthermore, we try to resolve if either of the following two lower Paleozoic-early Mesozoic thermal histories are viable with the ZHe data: A) sedimentation continued after deposition of the Devonian clastic wedge with maximum

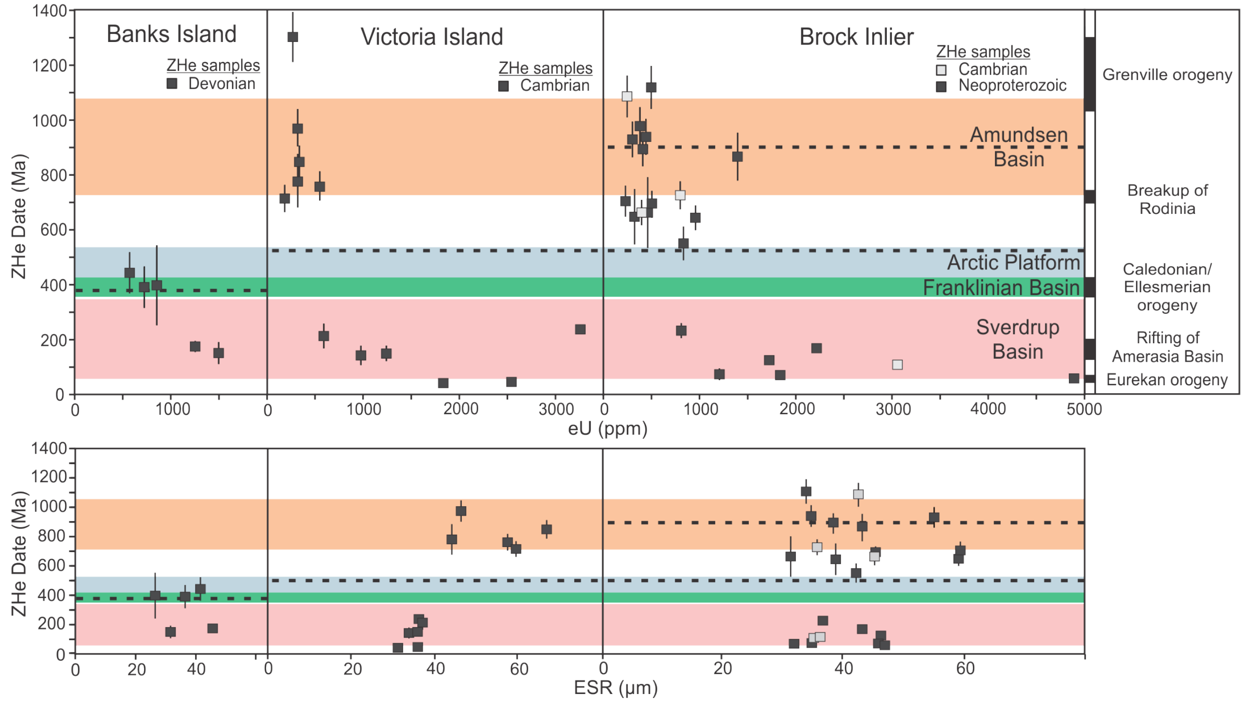

Figure 3.4: (U-Th)/He zircon date versus eU diagram, and (U-Th)/He zircon date versus equivalent spherical radius (ESR) diagram, separated by study area. Major tectonic events of northern Laurentia are highlighted by black boxes on the right. The three different deposition ages for the sample locations are indicated by a horizontal dotted black line. The large coloured polygons correspond to the duration of sediment accumulation within the basin (same colour scheme as Figure 3.1)

burial in the Triassic prior to rapid cooling in Jurassic-Cretaceous as a result of uplift along the rifted margin of the Amerasia Basin (Miall, 1976; Hadlari et al., 2016; Midwinter et al., 2016); or B) maximum burial occurred in the latest Devonian with protracted cooling until the Cretaceous. We assume the following for each model: 1) the mean surface temperature is 0°C, 2) a geothermal gradient between 25-40°C/km, and 3) the thermal maximum is defined by the onset of rifting in Model A (ca. 200 Ma), or the end of the Devonian in Model B (ca. 355 Ma).

To assess the hypothesis of continued burial during the Carboniferous to Triassic and subsequent cooling in the Jurassic against the previous model of maximum burial in the Devonian, plausible t-T histories were modeled using the HeFTy software program (version 1.8.3; Ketcham, 2005). Commonly, inverse modeling of age data evaluates many t-T histories to find the path that is statistically consistent with the analytical data; however, this is somewhat complicated by the diverse pre-depositional thermal history experienced by each zircon in a detrital population. This can be circumvented through a forward modeling approach (Guenthner et al., 2014; Powell et al., 2016), which can incorporate the possible pre- and post-depositional thermal histories observed in our ZHe date-eU trends. Below, thermal models from the three regions are discussed with respect to our analytical data and incorporate available independent geologic constraints.

3.5.2 Banks Island

One sample was collected from Upper Devonian strata, either the upper part of the Weatherall Formation or the lowest part of the Parry Islands Formation. The five dates from our sample range from 443 ± 75 Ma to 150 ± 40 Ma. The Banks Island sample generally has lower eU values than samples from Brock Inlier and Victoria Island with a bimodal population of ZHe dates in the Silurian-Devonian and the Jurassic. Although a negative date-eU correlation exists, it is not as pronounced as the date-eU trends of Victoria Island and Brock Inlier samples. No trends were observed between ZHe date and ESR (**Fig. 3.4**). The zircon grains from the sample have a smaller average grain size than the other samples, with an average ESR of 36 μm.

Palynological reports from northern Banks Island provide a Frasnian age (383-372 Ma) for the sampled unit (Sweet, 1973; Norris, 1974). The sample is located on the western side of the Banks graben (**Fig. 3.2**), which preserved Mesozoic strata as old as the Middle Jurassic Awingak Formation (ca. 165 Ma); however outside of the graben, the oldest Mesozoic sediment preserved is the Lower Cretaceous Isachsen Formation (ca. 135 Ma; Miall, 1979). There are variable pre-depositional U-Pb ages with the majority of the U-Pb zircon ages ranging from ca. 700-380 Ma to ca. 2100-900 Ma (Anfinson et al., 2012b). Zircon (U-Th)/He dates from the Middle to Upper Devonian samples of the Franklinian Basin north of Banks Island were reported by Anfinson et al. (2013). Although their results were not modeled, the majority of the reported

Table 3.2: Single zircon (U-Th)/He data from samples of the southwestern Arctic

Sample Name	ESR[1] (μm)	Mass (μg)	U (ppm)	Th (ppm)	Th/U	He (nmol/g)	eU (ppm)	Ft[1]	Corr. Age[1] (Ma)	Full Unc.[1] (Ma)
Banks Island (Devonian)										
C33289zr01	36.5	2.12	703.4	90.8	0.129	1088.5	725	0.70	390.3	75.6
C33289zr02	45.7	4.35	1084.7	716.8	0.661	891.1	1253	0.75	174.0	20.1
C33289zr03	26.5	0.93	803.9	215.2	0.268	1117.9	854	0.60	397.1	145.9
C33289zr05	31.7	1.44	1252.9	1040.5	0.831	796.1	1497	0.65	150.1	39.8
C33289zr06	41.6	3.92	508.0	274.6	0.541	1022.3	573	0.73	442.6	75.0
Victoria Island (Cambrian)										
C524504zr02	59.6	5.27	116.5	295.1	2.532	597.6	186	0.79	713.0	49.9
C524504zr03	56.3	6.59	168.6	430.2	2.552	1631.1	270	0.78	1302.0	91.1
C524504zr04	36.3	1.49	2596.8	2814.1	1.084	2841.1	3258	0.67	236.2	16.5
C524504zr05	57.6	6.06	447.9	432.3	0.965	1898.6	549	0.79	759.1	53.1
C524504zr06	66.9	6.85	231.1	452.3	1.957	1342.7	337	0.82	846.5	59.3
C524504zr07	46.4	2.60	233.0	370.6	1.590	1340.5	320	0.74	971.3	68.0
C457858zr01	37.2	2.69	450.6	599.3	1.330	475.8	591	0.70	211.8	45.0
C457858zr02	44.2	3.90	223.6	414.0	1.851	1037.3	321	0.74	778.1	97.4
C457858zr04	36.1	2.30	1660.7	3750.7	2.258	427.8	2542	0.68	45.5	9.9
C457858zr05	31.3	1.53	1224.6	2589.7	2.115	257.2	1833	0.64	40.4	11.5
C457858zr06	44.5	3.84	2952.7	5456.6	1.848	77.3	4235	0.74	4.6	0.5
C457858zr07	34.0	1.95	696.7	1194.8	1.715	501.4	978	0.67	141.2	35.1
C457858zr08	36.0	1.95	966.3	1171.1	1.212	690.5	1242	0.69	148.8	28.1
Brock Inlier (Cambrian)										
Brock.zr01	36.3	1.25	4251.9	3293.6	0.775	2105.5	5026	0.67	114.3	8.0
Brock.zr03	35.2	1.36	2659.7	1691.9	0.636	1187.2	3057	0.66	107.2	7.5
Brock.zr04	35.7	1.10	749.3	209.8	0.280	2247.6	799	0.67	724.7	50.7
Brock.zr06	45.3	2.33	360.5	159.8	0.443	1114.7	398	0.74	661.8	46.3
Brock.zr08	42.6	2.24	196.7	215.5	1.095	1142.1	247	0.72	1085.2	76.0
Brock Inlier (Neoproterozoic)										
14RAT514zr01	34.9	1.35	1896.3	1359.1	0.717	1342.0	2216	0.66	167.4	11.7
14RAT514zr02	32.0	0.76	2405.5	1396.5	0.581	72.5	2734	0.63	7.8	0.6
14RAT514zr03	34.8	1.05	416.8	340.0	0.816	2181.1	497	0.66	1118.1	78.3
14RAT514zr04	43.2	1.88	734.6	415.8	0.566	1879.1	832	0.73	549.5	61.1
14RAT514zr05	38.4	1.84	6967.7	4352.2	0.625	2038.1	7990	0.69	67.9	11.5
14RAT514zr06	36.5	1.14	691.3	1133.9	1.640	2337.3	958	0.67	642.8	45.0
14RAT514zr07	31.4	0.91	177.2	222.7	1.257	595.2	230	0.64	703.3	56.3
14RAT518C1zr01	46.9	6.11	1710.0	542.3	0.317	522.1	1837	0.76	69.3	9.0
14RAT518C1zr02	42.2	3.75	276.7	203.4	0.735	859.7	324	0.73	646.5	100.8
14RAT518C1zr04	43.2	1.88	235.5	281.5	1.195	1178.3	302	0.72	928.3	65.0
14RAT518C1zr05	38.4	1.84	386.8	237.0	0.613	1686.5	443	0.69	937.7	65.6
14RAT518C1zr06	32.0	1.89	1121.7	357.9	0.319	310.9	1206	0.66	72.5	21.2
14RAT518C1zr07	46.3	4.75	748.3	259.4	0.347	772.7	809	0.75	231.4	27.0
14RAT518C1zr08	43.8	4.48	1987.8	1819.9	0.916	139.9	2415	0.74	14.5	2.1
14RATA1004B1zr01	45.4	2.70	1143.3	1071.6	0.937	5167.6	1395	0.74	865.6	87.2
14RATA1004B1zr03	45.9	3.98	1374.9	1482.2	1.078	872.3	1723	0.75	123.8	16.1
14RATA1004B1zr04	38.8	2.23	359.6	430.1	1.196	1228.8	461	0.71	661.7	128.7
14RATA1004B1zr05	55.1	4.48	283.4	413.1	1.458	1692.9	380	0.78	976.9	69.0
14RATA1004B1zr06	59.1	4.69	417.1	370.8	0.889	1590.6	504	0.80	691.7	48.9
14RATA1004B1zr07	47.1	2.68	3828.1	4531.3	1.184	1131.9	4893	0.74	57.3	5.0
14RATA1004B1zr09	59.4	6.75	339.7	297.7	0.876	1701.4	410	0.80	892.8	62.5

[1] Abbreviations as followed: ESR - equivalent spherical radius; Ft - alpha ejection correction, calculated using the method of Farley (2002); Cor. Age - corrected age; Full Unc. - uncertainty including the estimate for the uncertainty in the alpha ejection correction

ZHe dates are older than the depositional ages of the sampled units indicating the zircon have not been thermally reset.

The two different thermal histories are tested with three forward models produced for each scenario: heating from the Devonian to Triassic with subsequent rapid cooling from Jurassic rifting (**Fig. 3.5A**), and rapid heating in the Devonian followed by protracted cooling until the Cretaceous (**Fig. 3.5B**). The time of deposition is chosen at 380 Ma. Subsequent to a post-200 Ma cooling episode inferred from the initiation of rifting in the proto-Amerasia Basin (Midwinter et al., 2016), reheating is assumed to have commenced in the Early Cretaceous rather than the Middle Jurassic due to the sample's location outside of the Jurassic graben. Additional assumptions are that maximum reheating occurs at 55 Ma, which coincides with the youngest part of the Eurekan Sound Formation in this area (Miall, 1979). Cretaceous to Cenozoic temperatures are constrained to 80°C on the basis of preserved Cretaceous stratigraphy (Miall et al., 1979). In **Figure 3.5**, we present t-T models defined by maximum heating at 100°C, 140°C, and 180°C (paths 1, 2, 3, respectively), with each forward model showing inheritance date-eU curves for 380 Ma (zero-inheritance), 700 Ma, 900 Ma and 2100 Ma to highlight the difference in date-eU trends for the end-members of the detrital zircon U-Pb age sub-populations. The ZHe models fail to explain the analytical data at 180ºC for both scenarios, but it cannot resolve between the two candidate t-T paths at 100ºC and 140ºC (paths 1, 2: **Fig. 3.5**).

To further constrain the t-T paths, vitrinite reflectance and RockEval Tmax data for Muskox D-87 exploration well (**Fig. 3.6A**) on NE Banks Island are used to corroborate the thermal histories from the ZHe forward modelling. Data from Muskox D-87 indicate a vitrinite reflectance value (%Ro) of about 0.7% at the top of the preserved Weatherall Formation (Frasnian, Upper Devonian in this area; Embry and Klovan, 1976). Vitrinite reflectance measures the amount of light returned from woody organic particles in the rock (e.g., Hartkopf-

Fröder et al., 2015). Rock-Eval pyrolysis experiments produce a thermal maturity parameter (Tmax) that can be converted to a vitrinite reflectance equivalent (Behar et al. 2001). These parameters record the maximum thermal stress of the rock, and are non-retrograde.

The ZHe forward models were then checked against 1D burial history models of the Muskox D-87 well using Basin Mod 5.4 software (published by Platte River Associates). Model input data were formation thickness, lithology and age of the formations. Crustal heat flow through time and the amount of section that was deposited and subsequently eroded were estimated and entered into the model. Using these input parameters, a depth versus thermal maturity curve was produced by the model (**Fig. 3.6A**). These modeled depth versus maturity curves were compared to the measured thermal maturity values. The crustal heat flow over time and the amount of sediment deposition and subsequent erosion were varied until a reasonable fit was generated by the software between the modeled maturity and the measured maturity values. Model output is a t-T curve that can be compared to those used in the ZHe forward models (**Fig. 3.6B and C)**. While the modeled solutions are not unique, the models presented are the best fits to the data that we could obtain for the two burial scenarios and are representative of the family of solutions. Model input data are included in the supplemental data to this paper.

The model using maximum burial at 200 Ma obtained a fit between the model and the measured thermal maturity values using: 1) heat flow of 45 mW/m^2 up to 210 Ma, rising to 60 mW/m^2 at time of rifting (200 Ma), then decreasing to 45 mW/m^2 at 140 Ma; 2) deposition of 2000 m of Late Devonian strata on top of the existing 1800 m of Devonian strata, erosion of 300 m during earliest Carboniferous time, followed by deposition of 1700 m of upper Paleozoic and Mesozoic strata (using the relative stratigraphic thicknesses preserved in the Jameson Bay C-31 well on Prince Patrick Island), erosion of 2300 m between 200-132 Ma, 1650 m of Cretaceous burial and 2750 m of Tertiary erosion. The resulting t-T curve (**Fig. 3.6B**) shows a maximum

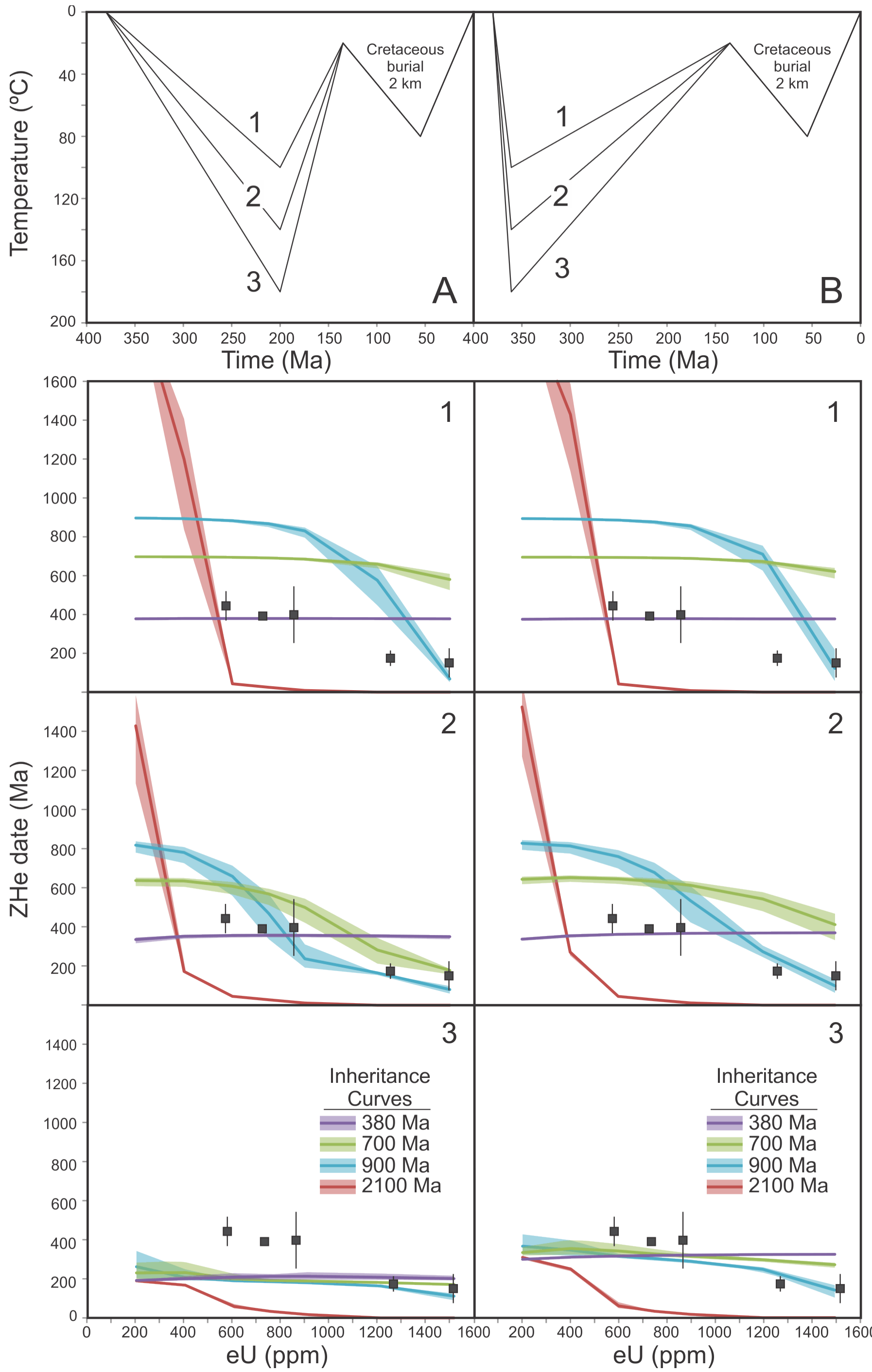

Figure 3.5: Forward thermal history models from Devonian strata of Banks Island using zircon (U-Th)/He data. Single zircon date and eU shown on each graph as square with associated error. The timing of the inheritance curves is derived from the U-Pb detrital studies (Fig. 3). Thermal model A has peak burial ca. 200 Ma; thermal model B has peak burial ca. 355 Ma. Time-temperature plot shows thermal pathways 1-3; Cretaceous burial of 2 km based on Dewing and Obermajer (2009). Forward models illustrate the expected ZHe inheritance date-eU curves for: (1) maximum temperature at 100ºC; (2) maximum temperature at 140ºC; (3) maximum temperature at 180ºC. Inheritance curves correspond to date-eU trends for zircon between 26-46 μm ESR, and describe the effect of the pre-depositional history and accumulated damage on ZHe dates. The solid line in each inheritance curve represents the projected date-eU trend for a zircon with a 36 μm ESR (mean value).

temperature of 106°C at around 210 Ma, similar to ZHe forward model shown in path 1 (**Fig. 3.5A**). Acceptable fits could not be obtained for higher temperature curves shown in paths 2 or 3 (**Fig. 3.5A**); therefore, path 1 is the favourable thermal history.

The model using maximum burial at the end of Devonian clastic wedge deposition (360 Ma) obtained a fit between the model and the measured thermal maturity values using: 1) heat flow of 55 mW/m^2 up to 210 Ma, rising to 60 mW/m^2 at time of rifting (200 Ma), then decreasing to 45 mW/m^2 at 140 Ma; 2) deposition of 4500 m of Late Devonian sandstone above the 1.4 km of existing Devonian clastic wedge (total Devonian clastic wedge thickness of 6.3 km), 3.5 km of erosion between 355-132 Ma, deposition of 1.7 km of Cretaceous strata and 2.7 km of Tertiary erosion. The resulting t-T curve (**Fig. 3.6C**) shows a maximum temperature of 107°C at about 355 Ma, similar to zircon forward model shown in path 1 (**Fig. 3.5B**). Acceptable fits could not be obtained for higher temperature curves shown in paths 2 or 3 (**Fig. 3.5B)**.

3.5.3 Victoria Island

The two Victoria Island samples were collected from Cambrian sandstone near Minto Inlet (Quyuk Formation; Durbano et al., 2015). The sandstone contains trilobites belonging to the late Early Cambrian (or Late Cambrian series 2; Hadlari et al., 2012). The majority of the detrital-zircon U-Pb ages are from a range of 2100-1500 Ma. The passive margin of the Arctic Platform developed an approximately 2 km thick succession from the Cambrian to Silurian (Dewing et al., 2013). Subsequent deposition of the Devonian clastic wedge placed another ~2 km (Patchett et al., 2004) of sediment over the region. The only comparable temperature data are %Ro values from the Victoria Island F-36 well, which has ~1.2% Ro (~150°C) in Silurian strata (Dewing et al., 2007) and Rock-Eval Tmax of 477°C (~170°C) from Lower Devonian shale from the northern part of the island (unpublished Geological Survey of Canada data). The %Ro at the base of the Lower Cretaceous-Eocene Eureka Sound Group is nearly consistent across the Arctic

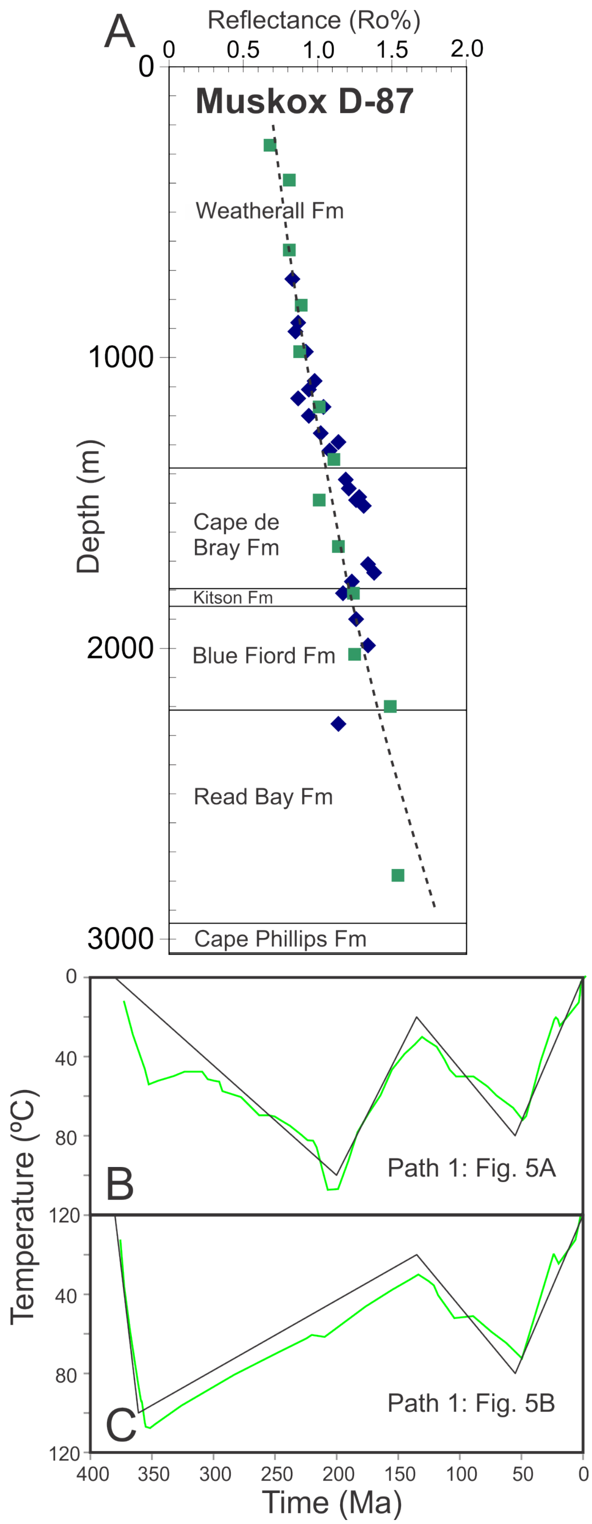

Figure 3.6: (A) Vitrinite reflectance and RockEval Tmax data for Muskox D-87 well on Banks Island (Dewing et al., 2007), blue diamonds are RockEval Tmax values (converted) and green squares are vitrinite reflectance (%Ro), EasyRo calibration used from Sweeney and Burnham (1990); (B) peak burial ca. 200 Ma; (C) peak burial ca. 355 Ma; corresponding best-fit curves (green line) using Basin Mod 5.4 software compared against t-T path 1 from Figure 5A and B (black line).

to produce a ~0.4% Ro indicative of a uniform sedimentary blanket across the central and western Canadian Arctic Islands (Bustin, 1986), so it is assumed there was reheating during the Cretaceous-Cenozoic boundary near our sample locations, but less than that on Banks Island.

The two samples yielded twelve single ZHe zircon dates with significant dispersion, ranging from 1302 ± 91 Ma to 40 ± 12 Ma. Six of the ZHe ages retain an age older than that of deposition. The date-eU comparison exhibits a strongly negative correlation. The Victoria Island sample has bimodal population of ZHe ages, with dates in the Neoproterozoic and in the Mesozoic; however, there is variance within these broad groupings. There are two sub-populations of grain dimensions identified, (**Fig. 3.4**) displaying a positive correlation in ZHe date-ESR diagram. The zircon from the two samples have an average ESR of 45 μm.

The burial history of Victoria Island is assumed to reflect that of Banks Island; however, with the absence of post-Devonian strata on Victoria Island, the Mesozoic burial history is more challenging to elucidate. Three t-T models assess the thermal history for both continued Carboniferous to Triassic heating (**Fig. 3.7A**), or maximum burial in the Devonian with protracted cooling until the Cretaceous (**Fig. 3.7B**). The depositional age is assumed to be 520 Ma. Using a cooler paleo-thermal gradient of 25°C/km with the Cambrian-Silurian passive margin succession, heating is to 50°C, compared to 60°C in the Devonian using a 30°C/km paleo-thermal gradient with the convergent margin succession. Because our ZHe data are unable to resolve the lower temperature history from Jurassic to present, forward models follow stratigraphic constraints that suggest Jurassic cooling to 40°C, and Cretaceous reheating to 60°C. Each forward model shows inheritance date-eU curves for 520 Ma (non-inheritance), 900 Ma, 1500 Ma, 2100 Ma and 3000 Ma to demonstrate the difference in date-eU trends for the predominant detrital zircon U-Pb sub-populations. In **Figure 3.7**, the models reach maximum heating at 110°C, 140°C, and 170°C (paths 1, 2, 3) with acceptable t-T paths when heating of

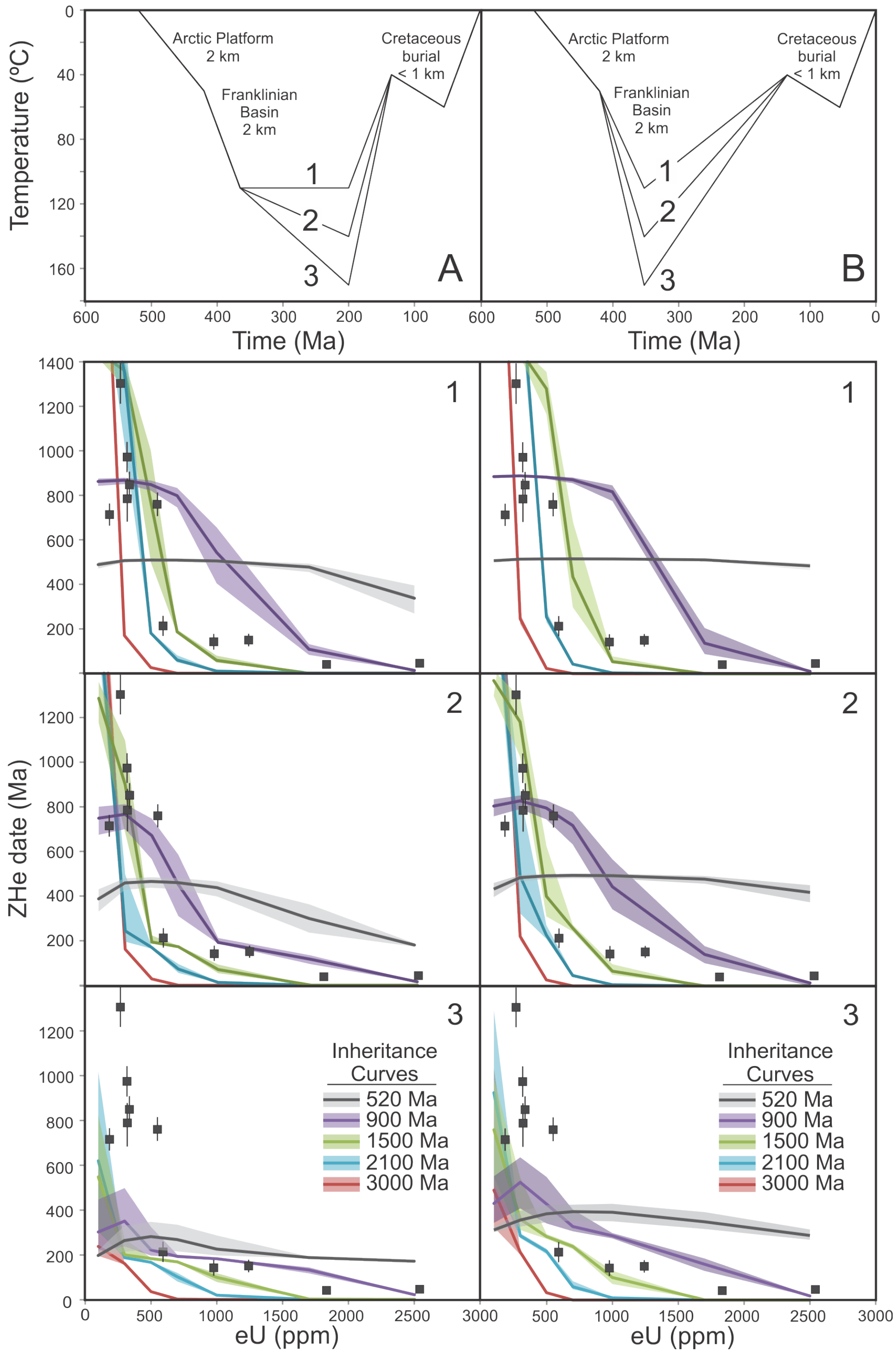

Figure 3.7: Forward thermal history models from Cambrian strata of Victoria Island using zircon (U-Th)/He data. Single zircon date and eU shown on each graph as square with associated error. The timing of the inheritance curves is derived from the U-Pb detrital studies (Fig. 3). Thermal model A has peak burial ca. 200 Ma; thermal model B has peak burial ca. 355 Ma. Time-temperature plot shows thermal pathways 1-3; passive margin sedimentation of 2 km based on Dewing et al. (2013); Devonian clastic thickness of 2 km based on Patchett et al. (2004); Cretaceous burial is interpreted. Forward models illustrate the expected ZHe inheritance date-eU curves for: (1) maximum temperature at 110ºC; (2) maximum temperature at 140ºC; (3) maximum temperature at 170ºC. Inheritance curves correspond to date-eU trends for zircon between 31-67 μm ESR, and describe the effect of the pre-depositional history and accumulated damage on ZHe dates. The solid line in each inheritance curve represents the projected date-eU trend for a zircon with a 45 μm ESR (mean value).

less than or equal to 30°C is invoked. Paths 1 and 2 (**Fig. 3.7**) are favoured due to the analytical data in agreement with the 2100-1500 Ma inheritance curves. The 170°C model (path 3) fails to explain half of the data.

3.5.4 Brock Inlier

Three samples were collected from Neoproterozoic strata of the Brock Inlier. Two samples are from the Nelson Head Formation, while the third sample is from the lower part of the overlying Boot Inlet Formation. The Brock Inlier preserves about ~1 km of Neoproterozoic strata above the Nelson Head Formation (Rainbird et al., 2016), whereas elsewhere in the Amundsen Basin another ~2-3 km of younger Neoproterozoic strata is preserved on Victoria Island (Rainbird et al., 1994). Above the Neoproterozoic strata is the unconformity with Cambrian strata of the Arctic Platform. The predominant zircon provenance ages for the Nelson Head Formation are between 1500-1000 Ma, which defines >90% of the data. The Brock Inlier preserves ~0.3 km of Cambrian-Ordovician strata (Rainbird et al., 2016), but possesses minimal Devonian strata even though 2 km of Devonian siliciclastics were interpreted to have blanketed the region (Patchett et al., 2004). Above the regional Devonian-Cretaceous unconformity, at the base of the Lower Cretaceous Langton Bay Formation, Yorath and Cook (1981) identified incised valleys, and interpreted the valley fill to be Jurassic in age; there are, however, no paleontological reports confirming this. The earliest deposition over the region is assumed to have commenced with the early Albian Langton Bay Formation (ca. 110 Ma) and terminated with the late Albian Horton Bay Formation (ca. 100 Ma), confirmed by paleontological data (Jeletzky, 1966). Cretaceous sediment has been measured as up to 0.6 km thick on the Brock Inlier (Jones et al., 1992), and 2 km on the Anderson Plain (Issler et al., 2012). Furthermore, the Slave Craton has an estimated Cretaceous burial of ≤1.4 km from vitrinite reflectance of sedimentary xenoliths (Stasiuk et al., 2006), or ≤1.6 km from thermochronometry modelling

(Ault et al., 2013). Thermal models from the Anderson Plain (Issler et al., 2012) and the Slave craton (Ault et al., 2009, 2013), suggest minimal Late Cretaceous reheating from ~20-80°C.

Three samples from the Brock Inlier yielded 24 ZHe dates from Neoproterozoic to Cambrian strata. The Cambrian sandstone is assumed to be of similar age and detrital zircon provenance as the Early Cambrian samples collected from Victoria Island, with five single ZHe dates ranging from 1085 ± 76 Ma to 107 ± 8 Ma. The Neoproterozoic samples, from the Nelson Head and Boot Inlet formations, yielded 19 ages with significant dispersion, ranging from 1118 ± 78 Ma to 57 ± 5 Ma with four of the ages greater than the assumed depositional age of 900 Ma (**Fig. 3.8**). Similar to the Victoria Island samples, there is a negative date-eU correlation. While no correlation exists between ZHe date and ESR, there are two sub-populations of grain dimensions identified (**Fig. 3.4**). The zircon from the three Neoproterozoic samples have an average ESR of 43 μm.

Three t-T models are used for each of the two thermal models in order to evaluate our data against proposed heating of the Neoproterozoic strata during the Devonian to Triassic (**Fig. 3.8A**), or maximum burial in the Devonian with protracted cooling until the Cretaceous (**Fig. 3.8B**). The depositional age is presumed to be 900 Ma (van Acken et al., 2013). The forward models assume maximum burial of 3 km by 720 Ma, when rifting of Rodinia resulted in cooling, preserving 1 km of Neoproterozoic strata prior to Cambrian deposition. We invoke limited (10°C) Cambrian-Ordovician heating, with 60°C of heating occurring from deposition of the Devonian clastic wedge. Forward models reach 40°C during Jurassic cooling and 60°C during Cretaceous reheating. **Figure 3.8** shows the three modeled t-T paths (1, 2, 3) reaching maximum heating at 100°C, 120°C, and 160°C for the two burial histories. If temperatures reach 160°C at maximum burial (path 3, **Fig. 3.8**), the model fails to explain our data. Similar to Victoria Island, when we invoke heating equal to or less than 20°C during the Carboniferous-Triassic, the models

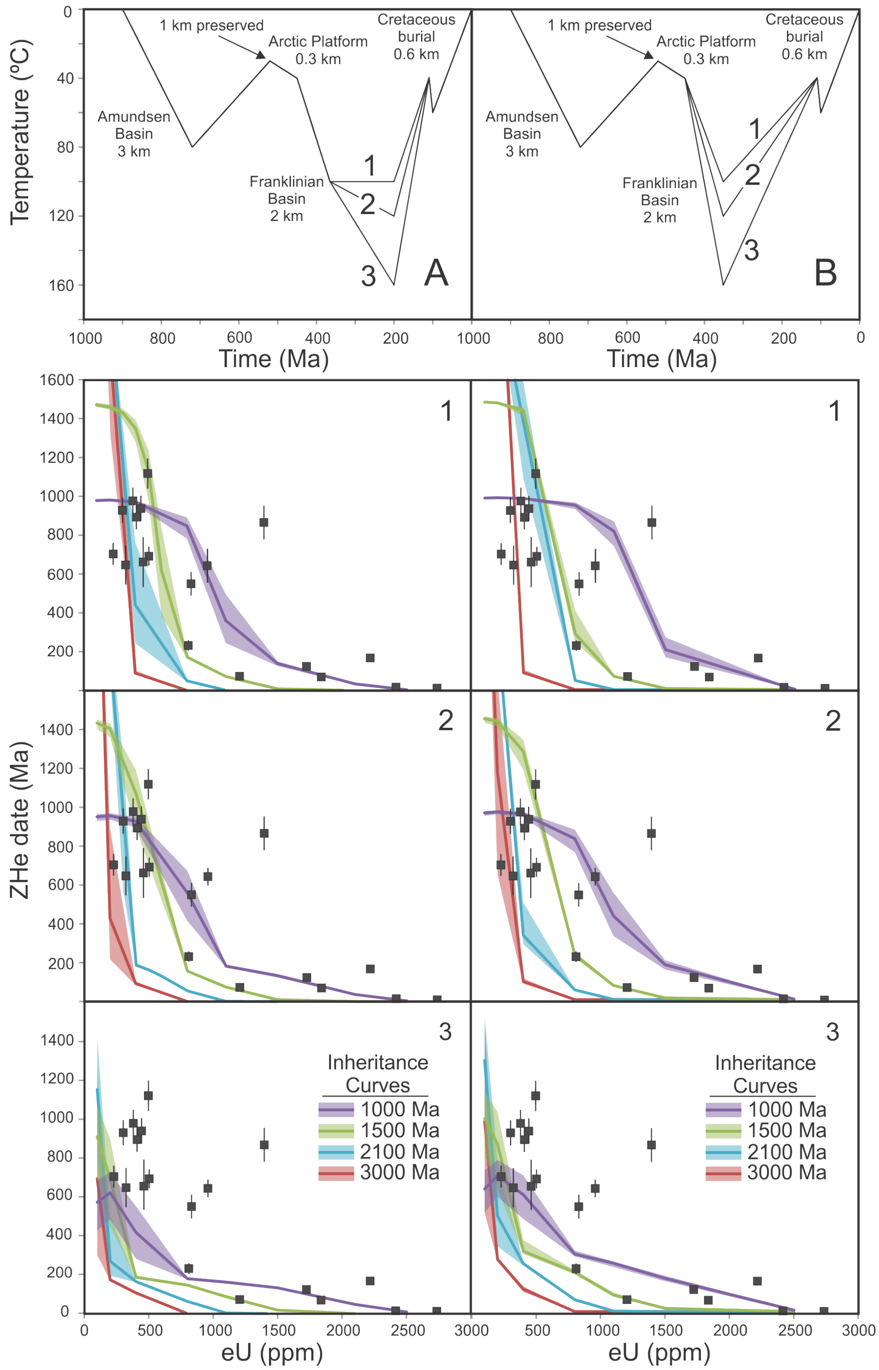

Figure 3.8: Forward thermal history models from Neoproterozoic strata of the Brock Inlier using zircon (U-Th)/He data. Single zircon date and eU shown on each graph as square with associated error. The timing of the inheritance curves is derived from the U-Pb detrital-zircon studies (Fig. 3). Thermal model A has peak burial ca. 200 Ma; thermal model B has peak burial ca. 355 Ma. Time-temperature plot shows thermal pathways 1-3; Amundsen Basin accumulation (3 km) and preservation (1 km), and passive margin sedimentation of 0.3 km based on Rainbird et al. (2016); Devonian clastic thickness of 2 km based on Patchett et al. (2004); Cretaceous burial is based on Jones et al. (1992). Forward models illustrate the expected ZHe inheritance date-eU curves for: (1) maximum temperature at 100ºC; (2) maximum temperature at 120ºC; (3) maximum temperature at 160ºC. Inheritance curves correspond to date-eU trends for zircon between 31-59 µm ESR, and describe the effect of the pre-depositional history and accumulated damage on ZHe dates. The solid line in each inheritance curve represents the projected date-eU trend for a zircon with a 43 µm ESR (mean value).

are acceptable. Each forward model shows inheritance date-eU curves for 1000 Ma (youngest U-Pb age), 1500 Ma, 2100 Ma and 3000 Ma to highlight the difference in date-eU trends for the predominant detrital zircon U-Pb age sub-populations. Paths 1 and 2 (**Fig. 3.8**) both represent acceptable thermal histories.

3.6 Discussion

The ZHe dates examined in this investigation exhibit a significant degree of dispersion with eU concentrations varying by 1000s ppm, which likely is a consequence of protracted thermal histories. The date-eU plots (**Fig. 3.4**) reveal a strongly negative correlation for all the samples that may be a result of a reheating episode or a sustained period through the zircon PRZ (Guenthner et al., 2014, 2015). The candidate t-T paths from the forward models (path 1: **Fig. 3.5;** paths 1-2: **Fig. 3.7, 3.8**) illustrate that the maximum burial temperatures from Banks Island to Brock Inlier do not exceed 140°C. Temperatures higher than this are not supported by our analytical data as the inheritance curves match nearly none of the data points. Burial history models of one well from Banks Island also support the lower end of the time-temperature models, with maximum temperature of about 105-110°C (**Fig. 3.6**). There are two notable grouping in the date-eU trends: 1) zircon with relatively low eU values (100s ppm) and a ZHe date often greater than the age of deposition, possibly due to low radiation damage and higher closure temperatures, and 2) younger ZHe ages with generally higher eU values (1000s ppm), probably due to increased radiation damage and increased diffusivity. These two groups reflect the broad range of pre-depositional histories and associated radiation damage within each sample, contributing to significant dispersion in ZHe dates and eU concentrations.

The t-T paths based on ZHe forward models and VRo inverse models assess the magnitude of burial and uplift between the Devonian-Cretaceous unconformity for either of the two end-member thermal histories: (A) protracted heating continuing from the Devonian to the Triassic, with rapid cooling as a result of Jurassic rifting, or (B) rapid heating in the latest Devonian with protracted cooling until the Cretaceous.

The models from Banks Island identify either 3.7 km (2.0 km in the latest Devonian and 1.7 km in the Carboniferous-Triassic) or 4.5 km (latest Devonian) of missing thickness with a thermal maximum of 105-110°C. The model for continued burial into the Triassic suggests a thinner stratigraphic package due to high heat flow as a result of rifting in the proto-Amerasia Basin. On both Victoria Island and Brock Inlier, the modeled maximum temperatures are 130°C and 120°C, respectively, which represents less than 1 km of additional burial between the Devonian-Cretaceous unconformity.

These thickness results are similar to previous studies that quantify the preserved thickness of late Paleozoic-early Mesozoic strata in the Canadian Arctic and Arctic Alaska. North of Banks Island is Prince Patrick Island (**Fig. 3.2**) where preserved Carboniferous to Triassic strata of the Sverdrup Basin is estimated to be ~4.5 km thick, determined from field mapping, well data and seismic profiles from the SW to NE of the island (Harrison and Brent, 2005). This is in marked contrast to the 9 km of Mississippian to Lower Jurassic strata in the axis of the Sverdrup Basin (5 km of upper Paleozoic strata and up to 4 km of Triassic siliciclastic sediments; (Embry and Beauchamp, 2008). The Mississippian to Early Jurassic sequence in Arctic Alaska has a typical thickness of 2 km (Moore et al., 1994) and reaches up to 6 km in parts of the Arctic Alaska Basin axis (Hubbard et al., 1987). Along the Alaska (Beaufort) Rift shoulder, this sequence is ~1 km in the Kuparuk 3-11-11 well (**Fig. 3.2**). Towards the axis of the Hanna Trough, this sequence thickens dramatically to 9.5 km (6 km of Upper Devonian-Permian and 3.5 km of Permian-Early Jurassic; Sherwood et al., 2002). Previous investigations of the thickness of missing strata between the Devonian and Cretaceous unconformity in the southwestern Canadian Arctic provide a range of values. Data from the Mackenzie Delta suggests up to 4 km of missing Permian to Jurassic strata (Issler et al., 2012). Embry (1988) suggested that Banks Island was missing up to 5 km of post-Devonian strata, whereas Anfinson et al. (2013) interpret that their Franklinian Basin Devonian samples were not buried to depths greater than 7 km.

One of the goals of this study was to assess how plausible both hypotheses are with regards to the new ZHe data. The t-T thermal models cannot discount either maximum burial in the Triassic or the Devonian. The scenario with the maximum burial in the Devonian is the generally accepted thermal history followed by gradual uplift, erosion and recycling of material into the Sverdrup Basin (e.g. Embry and Beauchamp, 2008), but there is support for the alternative thermal history of continued deposition into the early Mesozoic (Lerand, 1973; Miall, 1976). Since the ZHe data cannot resolve between the two, we will review the evidence of continued deposition into the Triassic to test the plausibility of this thermal history (**Fig. 3.9**). Burial from southerly-derived sediment in the late Paleozoic-early Mesozoic is consistent with further inboard unroofing to the south over the Mackenzie Platform (Powell et al., 2016) and Slave craton (Ault et al., 2013) which had migrating western unroofing from ca. 340-225 Ma. Miall (1976) provided indirect evidence to postulate that upper Paleozoic and Mesozoic rocks may have been deposited over Banks Island, specifically a wedge of possible upper Paleozoic strata imaged on seismic data from offshore Banks Island (Lerand, 1973) and the observation that sandstone of the Lower Cretaceous Isachsen Formation is coarser than the Devonian siliciclastics in the region indicating that the Isachsen Formation was derived from another source. Furthermore, sandstone from the Upper Cretaceous Kanguk Formation on northern Banks Island contains pebble-sized coral fragments of Early Permian age (Miall, 1979).

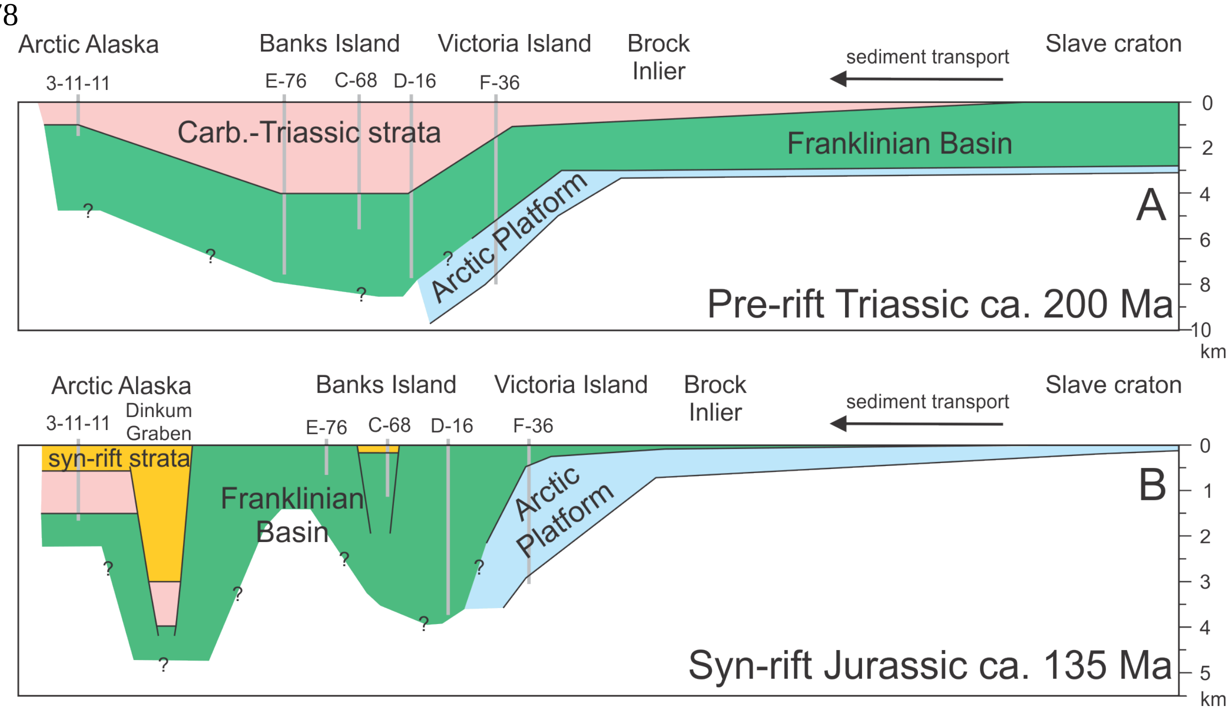

Figure 3.9: Synoptic north-south cross section of southwestern Canadian Arctic for the scenario of maximum burial at 200 Ma showing (B) Triassic pre-rift and (C) Jurassic syn-rift phase of the Amerasia Basin, with subsequent uplift until deposition commenced in the Cretaceous (ca. 135 Ma). Location of cross section on Figure 2, and note vertical scale change between (B) and (C). Thickness constraints for cross section sourced from Bird and Houseknecht (2011) for Kugparuk 3-11-11 well; from Hubbard et al. (1987) for Dinkum Graben; from Dewing and Embry (2007) for E-76, C-68, D-16, F-36 wells; from Ault et al. (2013) for the Slave craton. For discussion on other Victoria Island and Brock Inlier constraints, see Results section.

The Early Jurassic extensional period, marked by the rift onset unconformity of the Sverdrup Basin (ca. 200-190 Ma; Hadlari et al., 2016; Midwinter et al., 2016) provides a mechanism for uplift and exhumation on the rift shoulders from the Jurassic to Early Cretaceous, the syn-rift phase of the Amerasia Basin. It was not until after the breakup unconformity (ca. 130 Ma; cf. Embry and Beauchamp, 2008), which marks the end of uplift prior to Cretaceous deposition (**Fig. 3.9B**), that seafloor spreading and the creation of oceanic crust allowed for the counterclockwise rotation of the AACM from northern Laurentia (Embry, 1990, 200). Outside of the Sverdrup and Arctic Alaska basins, the syn-rift strata are only preserved in these extensional features.

On central Banks Island, ~0.4 km of Lower Jurassic (?) to Lower Cretaceous strata was intersected by a well (Castel Bay C-68) that are inferred to have been deposited in a narrow graben (Miall, 1979), and the small grabens and half-grabens on Prince Patrick Island preserve Lower Jurassic strata (Harrison and Brent, 2005). The Mackenzie-Beaufort Basin preserves ~1 km of Jurassic-Lower Cretaceous syn-rift sediment (Issler et al., 2012), whereas in Arctic Alaska, the Dinkum Graben and related half grabens contain more than 3 km of Jurassic-Lower Cretaceous strata (Hubbard et al., 1987). While Carboniferous-Triassic pre-rift strata are clearly not preserved in the southwestern Canadian Arctic, recent analysis of seismic data from the Alaska, the Dinkum Graben and related half grabens contain more than 3 km of Jurassic-Lower Cretaceous strata (Hubbard et al., 1987). While Carboniferous-Triassic pre-rift strata are clearly not preserved in the southwestern Canadian Arctic, recent analysis of seismic data from the Dinkum Graben (Houseknecht and Connors, 2016) identified a thin Mississippian-Triassic succession overlying Devonian strata. From these lines of evidence, it is challenging to conclusively determine whether Banks Island had continued deposition into the Mesozoic. It is less likely that the regions of Victoria Island and Brock Inlier had burial into the Triassic given the low amount of additional heating after the Devonian from the ZHe models and the late Paleozoic-early Mesozoic unroofing in the cratonic interior. Yet on Banks Island, proximal to the rifted margin, the ZHe and VRo models, the comparison of syn-rift strata preserved or missing in the southwestern Arctic, and the geologic evidence from Miall (1976, 1979), it remains plausible for deposition to have persisted after the Late Devonian with Jurassic-Cretaceous uplift linked to the opening of the Amerasia Basin. If there was continued sedimentation into the Triassic, Banks Island could represent a continuation of the margins of either the Sverdrup or Arctic Alaska basins.

3.7 Conclusion

The intra-sample zircon (U-Th)/He age dispersion from Banks Island, Victoria Island and the Brock Inlier and strongly negative date-eU correlations indicate a protracted residence in the shallow crust. Using ZHe date, eU values, and grain size, we are able to evaluate several temperature-time models of late Paleozoic-Mesozoic basin evolution in order to resolve the thermal maximum and magnitude of burial and exhumation. The models also assess two different thermal histories, a scenario of continued late Paleozoic-early Mesozoic deposition with the thermal maximum prior to Jurassic rifting, and a scenario of maximum burial in the Devonian. Whereas the ZHe and VRo models can constrain the maximum temperature, the models cannot resolve the timing of maximum burial; therefore, the data cannot exclude either scenario. When evaluating the magnitude of burial between the Devonian-Cretaceous unconformity, the north-south transect of our study reveals variable amounts of missing strata, decreasing south towards the craton (≤1 km), with substantial sedimentary accumulation on Banks Island (~3.7-4.5 km). The amount of exhumation along the transect is less variable with a similar amount on Banks Island (2.3-3.5 km), Victoria Island (2.0-2.7 km) and Brock Inlier (2.3-3.3 km) indicative of potentially more uniform uplift. ZHe thermochronology, in conjunction with VRo modeling, is able to discern the thermal maximum of each sampled region with its broad pre-depositional history of the detrital zircons, but in this case is unable to resolve the timing of the thermal maximum.

Chapter 4 : Thesis Conclusions and Areas for Future Research

4.1 Conclusions

The primary conclusions reached in this study are:

(1) Triassic strata in the Sverdrup Basin exhibit two distinct detrital zircon signatures (**Fig. 4.1A**). The northerly-derived detritus consists of abundant near-syndepositional Permian-Triassic zircon that contrasts with the mostly southerly-derived source consisting of detritus sourced from the Devonian clastic wedge. The near-syndepositional age of the northern zircon assemblage suggests that magmatism in the northern area was more or less coincident with sedimentation in the Sverdrup Basin. This sediment source, along with the ‘recycled’ southern source, is remarkably similar to the dual detrital zircon assemblage reported from Arctic Alaska, and also the Triassic foreland basin in the Yukon Tanana terrane on the western margin of Laurentia.

(2) With the combination of complementary Hf data and the discovery of volcanic ash beds, the previous interpretations of the Uralian/Siberian source for Permian-Triassic zircons can be discounted in favour of a new paleogeographic model that extends the northwestern convergent margin of Laurentia to the outboard margin of the Arctic Alaska–Chukotka microcontinent (**Fig. 4.1B**).

(3) The onset of rifting and initiation of the Amerasia Basin has previously been interpreted to be during the Middle Jurassic. New U-Pb ages from the Early Jurassic King Christian Formation suggest rifting commenced sometime in the earliest Jurassic (200-190 Ma). The sample, from the northern region of the Sverdrup Basin lacks the distinctive near-syndepositional Permian-Triassic zircon age-fraction. This, therefore, is interpreted to indicate that the northern provenance region had became disconnected from the Sverdrup Basin as AACM

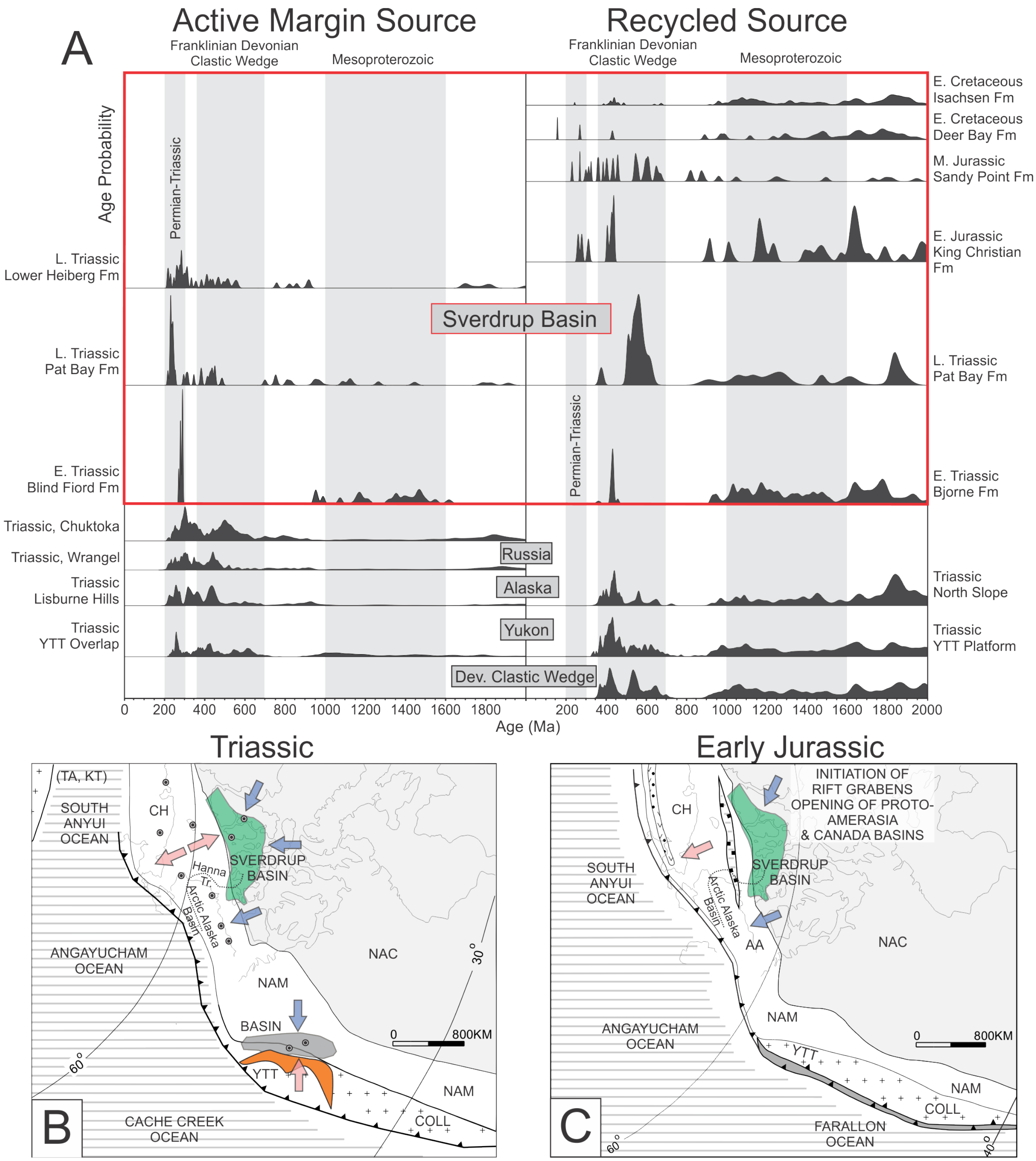

Figure 4.1: (A) Relative probability distribution grouped by signatures of the "Active margin source" and the "Recycled Source". Evolution of the northern margin of Laurentia during the Triassic and Jurassic: (B) in the Triassic, the Sverdrup Basin (green) occupied a retro-arc position to Chukotka along strike with the Triassic basin (grey) adjacent to Yukon Tanana terrane (orange); (C) Early Jurassic extension created the proto-Amerasia Basin and cut-off the Sverdrup Basin from the Arctic Alaska-Chukotka microcontinent; red arrows indicate active margin source, blue arrows indicate the recycled source; black circles represent U-Pb sample locations for (A); for complete legend see Fig. 2.11.

began to separate from northern Laurentia because of early rifting in the proto-Amerasia Basin (**Fig. 4.1C**).

(4) In the southwestern Canadian Arctic the late Paleozoic-early Mesozoic thermal history in the interval between the regional Devonian to Cretaceous unconformity has been a source of much debate. New ZHe models, with complementary Ro data, suggest that there could have been deposition that continued into the Triassic with rapid cooling as a result of uplift associated with Early Jurassic rifting of the Amerasia Basin (**Fig. 4.2**).

(5) The amount of missing strata between the Devonian-Cretaceous unconformity, regardless of the timing of maximum burial, is thicker close to the rifted margin (**Fig. 4.2B**) than towards the craton interior, with an estimated ~4 km of strata missing on Banks Island compared to ≤1 km on Victoria Island and the Brock Inlier (**Fig. 4.2A**).

4.2 Areas for Future Research

- Use U-Pb zircon geochronology to date the volcanic ash beds samples from Bunde Fiord. This work is essential to constrain the age(s) of magmatic activity

- Sandstone samples were collected from a stratigraphic section through the Heiberg Formation on Ellesmere Island and have yet to be processed for detrital zircons. It would be beneficial to have detrital-zircon signatures from each member to further pinpoint when the northern source became eliminated.

- There are no Hf data from the Blind Fiord or Pat Bay formations, both of which have Permian-Triassic zircon. It would be interesting if these samples displayed the same broad array of εHf values observed in this study, or if the range is reduced.

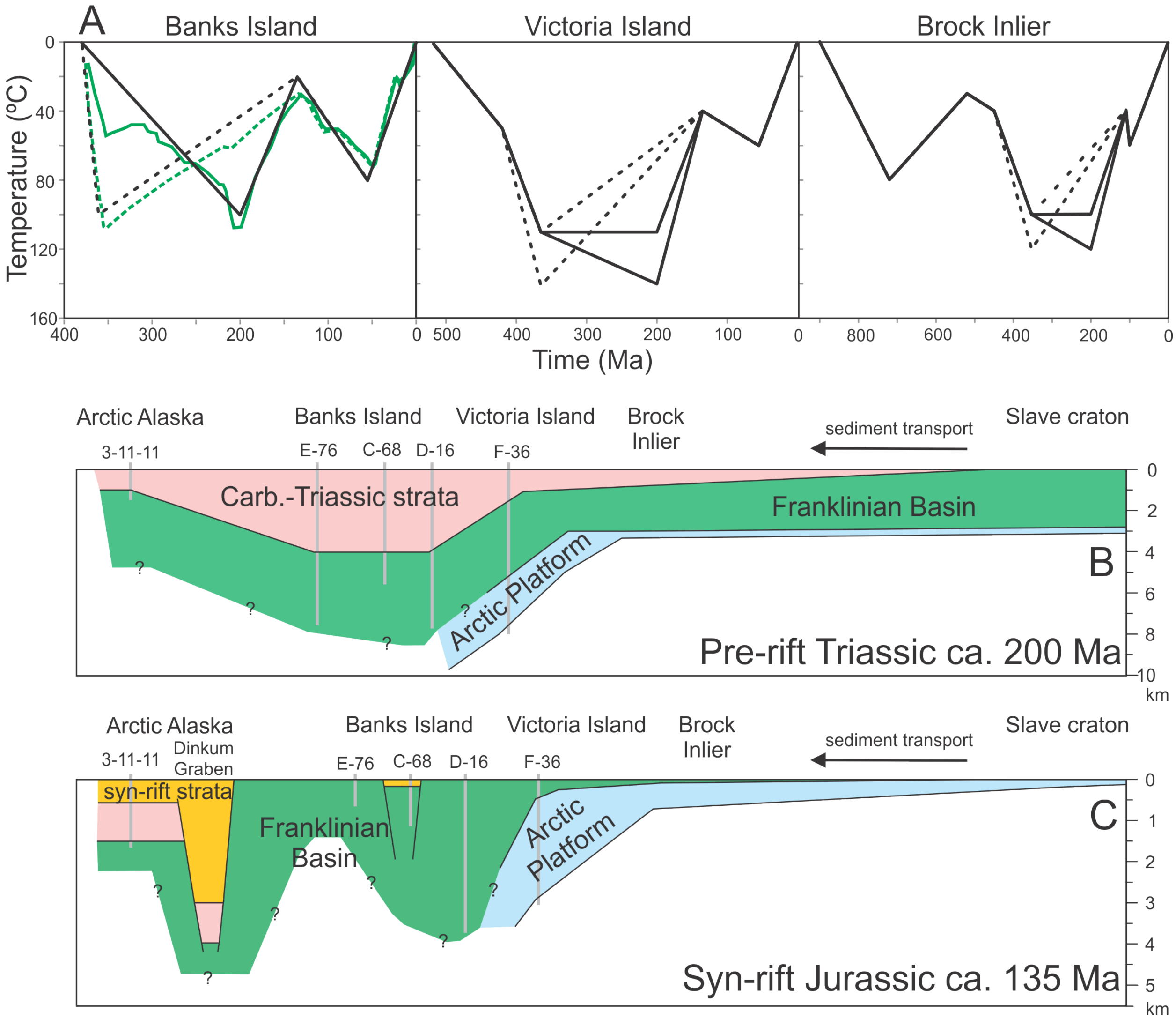

Figure 4.2: (A) Plausible time-temperature pathways for each region from ZHe (black) and VRo models (green) for two thermal histories: thermal maximum in the Triassic (solid line) and thermal maximum in the Devonian (dashed line). Synoptic north-south cross section of southwestern Canadian Arctic for the scenario of maximum burial at 200 Ma showing (B) Triassic pre-rift and (C) Jurassic syn-rift phase of the Amerasia Basin, with subsequent uplift until deposition commenced in the Cretaceous (ca. 135 Ma). Note the vertical scale change between (B) and (C). See Figure 3.9 for constraints.

- The thermochronology data would benefit from additional ages on Banks Island. Due to the small zircon sample size in this study, the thermal models along the Canadian rifted margin could be expanded by including data from Prince Patrick Island. Further benefit would be obtained from the construction of lower-temperature models with the recovery of apatite, as apatite can provide better resolution for lower-temperature thermal histories.

References

Akinin, V.V., Gottlieb, E.S., Miller, E.L., Polzunenkov, G.O., Stolbov, N.M., and Sobolev, N.N. 2015. Age and composition of basement beneath the De Long archipelago, Arctic Russia, based on zircon U-Pb geochronology and O-Hf isotopic systematic from crustal xenoliths in basalts of Zhokov Island. Arktos, **1**, doi: 10.1007/s41063-015-0016-6.

Amato, J.M., Toro, J., Miller, E.L., Gehrels, G.E., Farmer, G.L., Gottlieb, E.S., and Till, A.B. 2009. Late Proterozoic–Paleozoic evolution of the Arctic Alaska–Chukotka terrane based on U-Pb igneous and detrital zircon ages: Implications for Neoproterozoic paleogeographic reconstructions. Geological Society of America Bulletin, **121**(9-10): 1219-1235.

Amato, J.M., Aleinikoff, J.N., Akinin, V.V., McClelland, W.C., and Toro, J. 2014. Age, chemistry, and correlations of Neoproterozoic–Devonian igneous rocks of the Arctic Alaska–Chukotka terrane: An overview with new U-Pb ages: *in* Till, A.B., and Dumoulin, J.A., eds., Reconstruction of a Late Proterozoic to Devonian Continental Margin Succession, Northern Alaska, its Paleogeographic Significance, and Contained Base-Metal Sulfide Deposits. Geological Society of America Special Paper, **506**: 29–58.

Amato, J.M., Toro, J., Akinin, V.V., Hampton, B.A., Salnikov, A.S., and Tuchkova, M.I. 2015. Tectonic evolution of the Mesozoic South Anyui suture zone, eastern Russia: A critical component of paleogeographic reconstructions of the Arctic region. Geosphere, **11**(5): 1530-1564.

Amelin, Y., Lee, D.-C., Halliday, A.N. 2000. Early-middle Archaean crustal evolution deduced from Lu-Hf and U-Pb isotopic studies of single zircon grains. Geochimica et Cosmochimica Acta, **64**: 4205-4225.

Anfinson, O.A., Embry, A.F., and Stockli, D.F. 2016. Geochronologic Constraints on the Permian–Triassic Northern Source Region of the Sverdrup Basin, Canadian Arctic Islands. Tectonophysics, doi:10.1016/j.tecto.2016.02.041

Anfinson, O.A., Leier, A.L., Embry, A.F., and Dewing, K. 2012a. Detrital zircon geochronology and provenance of the Neoproterozoic to Late Devonian Franklinian basin, Canadian Arctic Islands. Geological Society of America Bulletin, **124(**3-4): 415-430.

Anfinson, O.A., Leier, A.L., Gaschnig, R., Embry, A.F., and Dewing, K. 2012b. U–Pb and Hf isotopic data from Franklinian Basin strata: insights into the nature of Crockerland and the timing of accretion, Canadian Arctic Islands. Canadian Journal of Earth Sciences, **49(**11): 1316-1328.

Anfinson, O.A., Leier, A.L., Dewing, K., Guest, B., Stockli, D.F., and Embry, A.F. 2013. Insights into the Phanerozoic tectonic evolution of the northern Laurentian margin: detrital apatite and zircon (U–Th)/He ages from Devonian strata of the Franklinian Basin, Canadian Arctic Islands. Canadian Journal of Earth Sciences, **50**(7): 761-768.

Arne, D.C., Grist, A.M., Zentilli, M., Collins, M., Embry, A.F., and Gentzis, T. 2002. Cooling of the Sverdrup Basin during Tertiary basin inversion: implications for hydrocarbon exploration. Basin Research, **14**(2): 183-205.

Ault, A.K., Flowers, R.M., and Bowring, S.A. 2009. Phanerozoic burial and unroofing history of the western Slave craton and Wopmay orogen from apatite (U–Th)/He thermochronometry. Earth and Planetary Science Letters, **284**(1): 1-11.

Ault, A.K., Flowers, R.M., and Bowring, S.A. 2013. Phanerozoic surface history of the Slave craton. Tectonics, **32**(5): 1066-1083.

Bahlburg, H., Vervoort, J.D., and DuFrane, S.A. 2011. Plate tectonic significance of Middle Cambrian and Ordovician siliciclastic rocks of the Bavarian Facies, Armorican Terrane Assemblage, Germany—U–Pb and Hf isotope evidence from detrital zircons. Gondwana Research, **17**(2): 223-235.

Balkwill, H. R. 1978. Evolution of Sverdrup Basin. American Association of Petroleum Geologists Bulletin, **62**: 1004–1028.

Bea, F., Fershtater, G., and Montero, P. 2002. Granitoids of the Uralides: Implications for the evolution of the orogeny, *in* Brown, D., Juhlin, C., and Puchkov, V., eds., Mountain Building in the Uralides: Pangea to the Present. American Geophysical Union Geophysical Monograph, **132**: 211–232.

Behar, F., Beaumont, V., and de B. Penteado, H.L. 2001. Rock-Eval 6 technology: performances and developments. Oil & Gas Science and Technology, **56**(2): 111-134.

Beranek, L.P., and Mortensen, J.K. 2011. The timing and provenance record of the Late Permian Klondike orogeny in northwestern Canada and arc-continent collision along western North America. Tectonics, **30**(5), TC5017, doi:10.1029/2010TC002849.

Beranek, L.P., Mortensen, J.K., Lane, L.S., Allen, T.L., Fraser, T.A., Hadlari, T., and Zantvoort, W.G. 2010a. Detrital zircon geochronology of the western Ellesmerian clastic wedge, northwestern Canada: Insights on Arctic tectonics and the evolution of the northern Cordilleran miogeocline. Geological Society of America Bulletin, **122**(11-12): 1899-1911.

Beranek, L.P., Mortensen, J.K., Orchard, M.J., and Ullrich, T. 2010b. Provenance of North American Triassic strata from west-central and southeastern Yukon: correlations with coeval strata in the Western Canada Sedimentary Basin and Canadian Arctic Islands. Canadian Journal of Earth Sciences, **47**(1): 53-73.

Beranek, L.P., Pease, V., Hadlari, T., and Dewing, K. 2015. Silurian flysch successions of Ellesmere Island, Arctic Canada, and their significance to northern Caledonian palaeogeography and tectonics. Journal of the Geological Society, **172**(2): 201-212.

Bird, K.J., and Houseknecht, D.W. 2011. Geology and petroleum potential of the Arctic Alaska petroleum province. Geological Society of London, Memoirs, **35**: 485-499.

Blichert-Toft, J.. 2008. The Hf isotopic composition of zircon reference material 91500. Chemical Geology, **253**(3-4): 252-257.

Bouvier, A., Vervoort, J.D., and Patchett, P.J. 2008. The Lu–Hf and Sm–Nd isotopic composition of CHUR: constraints from unequilibrated chondrites and implications for the bulk composition of terrestrial planets. Earth and Planetary Science Letters, **273**(1): 48-57.

Buchan, K.L., and Ernst, R.E. 2006. Giant dyke swarms and the reconstruction of the Canadian Arctic islands, Greenland, Svalbard and Franz Josef Land: *in* Hanski, E., Mertanen, S., Rämö, T., and Vuollo, J., eds., Dyke Swarms: Time Markers of Crustal Evolution. Netherlands, Balkema Publishers/Taylor and Francis: 27–48.

Bue, E.P., and Andresen, A. 2014. Constraining depositional models in the Barents Sea region using detrital zircon U–Pb data from Mesozoic sediments in Svalbard. Geological Society, London, Special Publications, **386**(1): 261-279.

Burgess, S.D., and Bowring, S.A. 2015. High-precision geochronology confirms voluminous magmatism before, during, and after Earth's most severe extinction. Science Advances, **1**(7), e1500470.

Bustin, R.M. 1986. Organic maturity of late Cretaceous and Tertiary coal measures, Canadian Arctic Archipelago. International Journal of Coal Geology, **6**(1): 71-106.

Cameron, B.I., and Muecke, G.K. 1996. Permian alkaline basalts associated with formation of the Sverdrup Basin, Canadian Arctic. Canadian Journal of Earth Sciences, **33**(10): 1462-1473.

Candan, O., Koralay, O.E., Topuz, G., Oberhänsli, R., Fritz, H., Collins, A.S., and Chen, F. 2015. Late Neoproterozoic gabbro emplacement followed by early Cambrian eclogite-facies metamorphism in the Menderes Massif (W. Turkey): Implications on the final assembly of Gondwana. Gondwana Research, doi:10.1016/j.gr.2015.02.015.

Cawood, P.A., Hawkesworth, C.J., and Dhuime, B. 2012. Detrital zircon record and tectonic setting. Geology, **40**(10): 875-878.

Cecile, M.P., Harrison, J.C., Kos'ko, M.K., and Parrish, R.R. 1991. Precambrian U-Pb ages of igneous rocks, Wrangel Complex, Wrangel Island, USSR. Canadian Journal of Earth Sciences, **28**: 1340-1348.

Chen, Z., Grasby, S.E., and Dewing, K. 2010. Temperature-depth plots for selected petroleum exploration wells, Canadian Arctic Islands. Geological Survey of Canada, open file report 6567, 16 p.

Colpron, M., and Nelson, J.L. 2011. A Palaeozoic NW Passage and the Timanian, Caledonian, and Uralian connections of some exotic terranes in the North American Cordillera: *in* Spencer, A.M., Embry, A.F., Gautier, D.L., Stoupakova, A.V., and Sørensen, K., eds., Arctic Petroleum Geology. Geological Society of London Memoir, **35**: 463-484.

Colpron, M., Nelson, J.L., and Murphy, D.C. 2006. A tectonostratigraphic framework for the pericratonic terranes of the northern Canadian Cordillera: *in* Colpron, M., and Nelson, J. L., eds., Paleozoic evolution and metallogeny of pericratonic terranes at the ancient Pacific margin of North America, Canadian and Alaskan cordillera. Geological Association of Canada Special Paper, **45**: 1–23.

Corcoran, D.V., and Dore, A.G. 2005. A review of techniques for the estimation of magnitude and timing of exhumation in offshore basins. Earth Science Reviews, **72**: 129-168.

Crovisier, J.L., Eberhart, J.P., Thomassin, J.H., Juteau, T., Touray, J.C., and Ehret, G. 1982. Interaction eau de mer-verre basaltique à 50 C^{o}, Formation d'un hydroxycarbonate et de produits silicatés amorphes (Al, Mg) et mal cristallisés (Al, Fe, Mg). Étude en microscopie électronique et par spectrométrie des photoélectrons (E.S.C.A), Academie des Sciences Paris, Comptes Rendus, series II, **294**: 989-994.

de Freitas, T.A., Trettin, H.P., Dixon, O.A., and Mallamo, M. 1999. Silurian System of the Canadian Arctic Archipelago. Bulletin of Canadian Petroleum Geology, **47**: 136-193.

Dewing, K., and Embry, A.F. 2007. Geological and Geochemical Data from the Canadian Arctic Islands: Part I: Stratigraphic Tops from Arctic Islands' Oil and Gas Exploration Boreholes. Geological Survey of Canada, open file report 5442, 7 p.

Dewing, K., and Obermajer, M. 2009. Lower Paleozoic thermal maturity and hydrocarbon potential of the Canadian Arctic Archipelago. Bulletin of Canadian Petroleum Geology, **57**(2): 141-166.

Dewing, K., Obermajer, M., and Goodarzi, F. 2007. Geological and geochemical data from the Canadian Arctic Islands part III: Organic matter reflectance data. Geological Survey of Canada, open file report 5476, 8 p.

Dewing, K., Pratt, B.R., Hadlari, T., Brent, T., Bédard, J., and Rainbird, R.H. 2013. Newly identified impact structure, Prince Albert Peninsula, northwestern Victoria Island, Arctic Canada. Meteoritics and Planetary Science, **48**: 211-223.

Dewing, K., Hadlari, T., Rainbird, R.H., and Bédard, J.H. 2015. Phanerozoic geology, northwestern Victoria Island, Northwest Territories. Geological Survey of Canada, Canadian Geoscience Map 171 (preliminary), scale 1:500 000.

Dhuime, B., Hawkesworth, C., and Cawood, P. 2011. When continents formed. Science, **331**(6014): 154-155.

Doust, H., and Sumner, H.S. 2007. Petroleum systems in rift basins a collective approach in Southeast Asian basins. Petroleum Geoscience, **13**: 127-144.

Dow, W.G. 1977. Kerogen studies and geological interpretations. Journal of Geochemical Exploration, **7**: 79-99.

Drachev, S.S. 2011. Tectonic setting, structure and petroleum geology of the Siberian Arctic offshore sedimentary basins: *in* Spencer, A.M., Embry, A.F., Gautier, D.L., Stoupakova, A.V., and Sørensen, K., eds., Arctic Petroleum Geology. Geological Society of London Memoir, **35**: 369-394.

Durbano, A.M., Pratt, B.R., Hadlari, T., and Dewing, K. 2015. Sedimentology of an early Cambrian tide-dominated embayment: Quyuk formation, Victoria Island, Arctic Canada. Sedimentary Geology, **320**: 1-18.

Embry, A.F. 1983a. Stratigraphic subdivision of the Heiberg Formation, eastern and central Sverdrup Basin, Arctic Islands. Geological Survey of Canada Current Research, v. 83-1B: 205-213.

Embry, A.F. 1983b. The Heiberg Group, western Sverdrup Basin, Arctic Islands. Geological Survey of Canada Current Research, v. 83-1B: 381-389.

Embry, A.F. 1986. Stratigraphic subdivision of the Blind Fiord and Bjorne Formations (Lower Triassic), Sverdrup Basin, Arctic Island. Geological Survey of Canada Current Research, v. 86-1B: 329-340.

Embry, A.F. 1988a. Middle-Upper Devonian sedimentation in the Canadian Arctic Islands and the Ellesmerian orogeny: *in* MacMillan, N.J., Embry, A.F., and Glass, D.J., eds., Devonian of the World. Canadian Society of Petroleum Geologists Memoir, **14**(2): 15-28.

Embry, A.F. 1988b. Triassic sea level changes: evidence from the Canadian Arctic Archipelago: *in* Wilgus, C., ed., Sea Level Changes — an Integrated Approach. Society of Economic Paleontologists and Mineralogists Special Publication, **42**: 249–259.

Embry, A.F. 1990. Geological and geophysical evidence in support of the hypothesis of anticlockwise rotation of northern Alaska. Marine Geology, **93**: 317-329.

Embry, A.F. 1991. Mesozoic history of the Arctic Islands: *in* Trettin, H., ed., Geology of the Innuitian Orogen and Arctic Platform of Canada and Greenland. Geological Survey of Canada, Geology of Canada, **3**: 369-434.

Embry, A.F. 1993. Crockerland—The northwest source area for the Sverdrup Basin, Canadian Arctic Islands. Arctic Geology and Petroleum Potential, Norwegian Petroleum Society Special Publication, **2**: 205-216.

Embry, A.F. 2000. Counterclockwise rotation of the Arctic Alaska plate: best available model or untenable hypothesis for the opening of the Amerasia Basin. Polarforschung, **68**: 247-255.

Embry, A.F. 2009. Crockerland–The Source Area for the Triassic to Middle Jurassic Strata of Northern Axel Heiberg Island, Canadian Arctic Islands. Bulletin of Canadian Petroleum Geology, **57**(2): 129-140.

Embry, A.F. 2011. Petroleum prospectivity of the Triassic–Jurassic succession of Sverdrup Basin, Canadian Arctic Archipelago: *in* Spencer, A.M., Embry, A.F., Gautier, D.L., Stoupakova, A.V., and Sørensen, K., eds., Arctic Petroleum Geology. Geological Society of London Memoir, **35**: 545-558.

Embry, A.F. and Beauchamp, B. 2008. Sverdrup Basin: *in* Miall, A.D., ed., The Sedimentary Basins of the United States and Canada. Amsterdam, Elsevier, 451-471.

Embry, A.F. and Klovan, J.E. 1976. The Middle-Upper Devonian clastic wedge of the Franklinian Geosyncline. Bulletin of Canadian Petroleum Geology, **24**: 485-639.

Embry, A.F., and Suneby, L.B. 1994. The Triassic–Jurassic boundary in the Sverdrup Basin, Arctic Canada. Canadian Society of Petroleum Geologists Memoir, **17**: 857– 868.

Ernst, R.E, and Bleeker, W. 2010. Large igneous provinces (LIPs), giant dyke swarms, and mantle plumes: significance for breakup events within Canada and adjacent regions from 2.5 Ga to the Present. Canadian Journal of Earth Sciences, **47**(5): 695-739.

Ernst, R.E., Hamilton, M.A., Söderlund, U., Hanes, J.A., Gladkochub, D.P., Okrugin, A.V., Kolotilina, T., Mekhonoshin, A.S., Bleeker, W., LeCheminant, A.N. and Buchan, K.L. 2016. Long-lived connection between southern Siberia and northern Laurentia in the Proterozoic. Nature Geoscience, **9**(6): 464-469.

Ershova, V.B., Prokopiev, A.V., Khudoley, A.K., Sobolev, N.N., and Petrov, E.O. 2015. Detrital zircon ages and provenance of the Upper Paleozoic successions of Kotel'ny Island (New Siberian Islands archipelago). Lithosphere, **7**: 40-45.

Estrada, S., and Henjes-Kunst, F. 2013. ^{40}Ar-^{39}Ar and U-Pb dating of Cretaceous continental rift-related magmatism on the northeast Canadian Arctic margin. Zeitschrift der Deutschen Gesellschaft für Geowissenschaften, **164**: 107–130.

Evenchick, C.A., Davis, W.J., Bedard, J.H., Hayward, N., and Friedman, R.M. 2015. Evidence for protracted High Arctic large igneous province magmatism in the central Sverdrup Basin from stratigraphy, geochronology, and paleodepths of saucer-shaped sills. GSA Bulletin, doi: 10.1130/B31190.1.

Feinstein, S., Issler, D.R., Snowdon, L.R., Williams, G.K. 1996. Characterization of major unconformities by paleothermometric and paleobarometric methods: Application to the Mackenzie Plain, Northwest Territories, Canada. Bulletin of Canadian Petroleum Geology, **44**: 55-71.

Franke, D. 2013. Rifting, lithosphere breakup and volcanism: comparison of magma-poor and volcanic rifted margins. Marine and Petroleum Geology, **43**: 63-87.

Gehrels, G., and Pecha, M. 2014. Detrital zircon U-Pb geochronology and Hf isotope geochemistry of Paleozoic and Triassic passive margin strata of western North America. Geosphere, **10**(1): 49-65.

Gottlieb, E.S., Meisling, K.E., Miller, E.L., and Charles, G. 2014. Closing the Canada Basin: Detrital zircon geochronology relationships between the North Slope of Arctic Alaska and the Franklinian mobile belt of Arctic Canada. Geosphere, **10**(6): 1366-1384.

Grantz, A., Eittreim, S., and Dinter, D.A. 1979. Geology and tectonic development of the continental margin north of Alaska. Tectonophysics, **59**(1): 263-291.

Grantz, A., Hart, P.E., and Childers, V.A. 2011. Geology and tectonic development of the Amerasia and Canada Basins, Arctic Ocean: *in* Spencer, A.M., Embry, A.F., Gautier, D.L., Stoupakova, A.V., and Sørensen, K., eds., Arctic Petroleum Geology. Geological Society of London Memoir, **35**: 771–799

Guenthner, W.R., Reiners, P.W., Ketcham, R.A., Nasdala, L., and Giester, G. 2013. Helium diffusion in natural zircon: radiation damage, anisotropy, and the interpretation of zircon (U-Th)/He thermochronology. American Journal of Science, **313**: 145-198.

Guenthner, W.R., Reiners, P.W., and Tian, T. 2014. Interpreting date–eU correlations in zircon (U-Th)/He datasets: A case study from the Longmen Shan, China. Earth and Planetary Science Letters, **403**: 328-339.

Guenthner, W.R., Reiners, P.W., DeCelles, P.G., and Kendall, J. 2015. Sevier belt exhumation in central Utah constrained from complex zircon (U-Th)/He data sets: Radiation damage and He inheritance effects on partially reset detrital zircons. Geological Society of America Bulletin, **127**(3-4): 323-348.

Guynn, J., and Gehrels, G. 2010. Comparison of detrital zircon age distributions using the K-S test. Tuscon, University of Arizona, 16 p.

Hadlari, T., and Rainbird, R.H. 2011. Retro-arc extension and continental rifting: a model for the Paleoproterozoic Baker Lake Basin, Nunavut. Canadian Journal of Earth Sciences, **48**(8): 1232-1258.

Hadlari, T., Davis, W.J., Dewing, K., Heaman, L.M., Lemieux, Y., Ootes, L., Pratt, B.R. and Pyle, L.J. 2012. Two detrital zircon signatures for the Cambrian passive margin of northern Laurentia highlighted by new U-Pb results from northern Canada. Geological Society of America Bulletin, **124**(7-8): 1155-1168.

Hadlari, T., Davis, W.J., and Dewing, K. 2014. A pericratonic model for the Pearya terrane as an extension of the Franklinian margin of Laurentia, Canadian Arctic. Geological Society of America Bulletin, **126**(1-2): 182-200.

Hadlari, T., Swindles, G.T., Galloway, J.M., Bell, K.M., Sulphur, K.C., Heaman, L.M., Beranek, L.P., and Fallas, K.M. 2015. 1.8 billion years of detrital zircon recycling calibrates a refractory part of Earth's sedimentary cycle. PLoS ONE, **10**(12), e0144727.doi:10.1371/ journal.pone.0144727.

Hadlari, T., Midwinter, D., Galloway, J.M., Dewing, K., and Durbano, A.M. 2016. Mesozoic rift to post-rift tectonostratigraphy of the Sverdrup Basin, Canadian Arctic. Marine and Petroleum Geology, doi:10.1016/j.marpetgeo.2016.05.008.

Hall, A., and Stamatakis, M.G. 2000. Hydrotalcite and an amorphous clay mineral in high-magnesium mudstones from the Kozani Basin, Greece. Journal of Sedimentary Research, **70**(3): 549-558.

Harrison, J.C. 1995. Melville Island's salt-based fold belt, Arctic Canada. Geological Survey of Canada, Bulletin 472, 331 p.

Harrison, J.C., and Brent, T.A. 2005. Basins and fold belts of Prince Patrick Island and adjacent areas, Canadian Arctic Islands. Geological Survey of Canada Bulletin, **560**, 197 p.

Hartkopf-Fröder, C., Königshof, P., Littke, R., and Schwarzbauer, J. 2015. Optical thermal maturity parameters and organic geochemical alteration at low grade diagenesis to anchimetamorphism: A review. International Journal of Coal Geology, **150**: 74-119.

Heaman, L.M., Le Cheminant, A.N., and Rainbird, R.H. 1992. Nature and timing of Franklin igneous events, Canada: Implications for a Late Proterozoic mantle plume and the break-up of Laurentia. Earth and Planetary Science Letters, **109**: 117-131.

Heron, P.J., Pysklywec, R.N. and Stephenson, R. 2015. Intraplate orogenesis within accreted and scarred lithosphere: Example of the Eurekan Orogeny, Ellesmere Island. Tectonophysics, **664:** 202-213.

Hourigan, J.K., Reiners, P.W., and Brandon, M.T. 2005. U-Th zonation-dependent alpha ejection in (U-Th)/He chronometry. Geochimica et Cosmochimica Acta, **69**: 3349-3365.

Houseknecht, D.W., and Bird, K.J. 2011. Geology and petroleum potential of the rifted margins of the Canada Basin. Geological Society of London, Memoirs, **35**: 509-526.

Houseknecht, D.W., and Connors, C.D. 2016. Pre-Mississippian tectonic affinity across the Canada Basin–Arctic margins of Alaska and Canada. Geology, G37862-1.

Hu, K., Issler, D.R. and Jessop, A.M. 2010. Well temperature data compilation, correction and quality assessment for the Beaufort-Mackenzie Basin. Geological Survey of Canada, open file report 6057, 14 pp.

Hubbard, R.J., Edrich, S.P., and Rattey, R.P. 1987. Geologic evolution and hydrocarbon habitat of the Arctic Alaska microplate. Marine and Petroleum Geology, **4**: 2-34.

Iles, K.A., Hergt, J.M., Sircombe, K.N., Woodhead, J.D., Bodorkos, S., and Williams, I.S. 2015. Portrait of a reference material: Zircon production in the Middledale Gabbroic Diorite, Australia, and its implications for the TEMORA standard. Chemical Geology, **402**: 140-152.

Issler, D.R., Grist, A.M., and Stasiuk, L.D. 2005. Post-Early Devonian thermal constraints on hydrocarbon source rock maturation in the Keele Tectonic Zone, Tulita area, NWT, Canada, from multi-kinetic apatite fission track thermochronology, vitrinite reflectance and shale compaction. Bulletin of Canadian Petroleum Geology, **53**(4): 405-431.

Issler, D.R., Hu, K., Lane, L.S., and Dietrich, J.R. 2011. GIS compilations of Overpressure, Permafrost Distribution, Geothermal Gradient, and Geology, Beaufort Mackenzie Region, Northern Canada. Geological Survey of Canada, open file report 5689, doi:10.4095/289113

Issler, D.R., Reyes, J., Chen, Z., Hu, K., Negulic, E., Grist, A., Stasiuk, L., and Goodarzi, F. 2012. Thermal History Analysis of the Beaufort-Mackenzie Basin, Arctic Canada: *in* New Understandings of the Petroleum Systems of Continental Margins of the World. Society of Economic Paleontologists and Mineralogists Foundation Bob F. Perkins Research Conference, **32**: 609-641.

Jeletzky, J.A. 1966. Report On Cretaceous and Late Upper Jurassic Fossils, Collected by Petropar Geologists in the Canadian Arctic Archipelago and Adjacent Parts of Arctic Coast. Geological Survey of Canada, paleontological report Km-4-1966-JAJ, 11 p.

Jones, T.A., Jefferson, C.W., and Morrell, G.R. 1992. Assessment of mineral and energy resource potential in the Brock Inlier – Bluenose Lake area, N.W.T. Geological Survey of Canada, open file report 2434, 97 p.

Joussein, E., Petit, S., Churchman, J., Theng, B., Righi, D., and Delvaux, B. 2005. Halloysite clay minerals—a review. Clay Minerals, **40**(4): 383-426.

Ketcham, R.A. 2005. Forward and inverse modelling of low-temperature thermochronometry data. Reviews in Mineralogy and Geochemistry, **58**: 559-664.

Kuzmichev, A.B. 2009. Where does the South Anyui suture go in the New Siberian islands and Laptev Sea?: Implications for the Amerasia basin origin. Tectonophysics, **463**(1): 86-108.

Kuzmichev, A.B. and Pease, V.L. 2007. Siberian trap magmatism on the New Siberian Islands: constraints for Arctic Mesozoic plate tectonic reconstructions. Journal of the Geological Society, London, **164**(5): 959-968.

Lane, L.S. 1997. Canada Basin, Arctic Ocean: Evidence against a rotational origin. Tectonics, **16**: 363-387.

Laverov, N.P., Lobkovsky, L.I., Kononov, M.V., Dobretsov, N.L., Vernikovsky, V.A., Sokolov, S.D., and Shipilov, E.V. 2013. A geodynamic model of the evolution of the Arctic basin and adjacent territories in the Mesozoic and Cenozoic and the outer limit of the Russian Continental Shelf. Geotectonics, **47**(1): 1-30.

Lawton, T.F., and McMillan, N.J. 1999. Arc abandonment as a cause for passive continental rifting: Comparison of the Jurassic Mexican Borderland rift and the Cenozoic Rio Grande rift. Geology, **27**(9): 779-782.

Lawver, L.A., and Scotese, C.R. 1990. A review of tectonic models for the evolution of the Canada Basin: *in* Grantz, A., Johnson, L., and Sweeney, J.F., eds., The Arctic Ocean Region. Geological Society of America, Geology of North America, v. L: 593–618.

Lawver, L.A., Grantz, A., and Gahagan, L. 2002. Plate kinematic evolution of the present Arctic region since the Ordovician. Geological Society of America, **50**: 593-618.

Lawver, L.A., Gahagan, L.M., and Norton, I. 2011. Palaeogeographic and tectonic evolution of the Arctic region during the Palaeozoic: *in* Spencer, A.M., Gautier, D., Stoupakova, A., Embry, A.F., and Sørensen, K., eds., Arctic Petroleum Geology. Geological Society of London Memoir, **35**: 61-77.

Lemieux, Y., Hadlari, T., and Simonetti, A. 2011. Detrital zircon geochronology and provenance of Devono-Mississippian strata in the northern Canadian Cordilleran miogeocline. Canadian Journal of Earth Sciences, **48**(2): 515-541.

Lerand, M. 1973. Beaufort Sea. *In*: The future petroleum provinces of Canada. *Edited by*: R.G. McCrossan. Canadian Society of Petroleum Geologists, Memoir 1, p. 315-386.

Li, C.F., Zhou, Z., Hao, H., Chen, H., Wang, J., Chen, B., and Wu, J. 2008. Late Mesozoic tectonic structure and evolution along the present-day northeastern South China Sea continental margin. Journal of Asian Earth Sciences, **31**: 546-561.

Ludwig, K.R. 1998. On the treatment of concordant uranium-lead ages. Geochemica et Cosmochimica Acta, **62**: 665-676.

Ludwig, K.R. 2003. User's Manual for Isoplot 3.00, A Geochronological Toolkit for Microsoft Excel. Berkeley Geochronology Center Special Publication No. 4, 70 p.

Majorowicz, J.A., and Embry, A.F. 1998. Present heat flow and paleo-geothermal regime in the Canadian Arctic margin: analysis of industrial thermal data and coalification gradients. Tectonophysics, **291**(1): 141-159.

Malitch, K.N., Belousova, E.A., Griffin, W.L., Badanina, I.Y., Pearson, N.J., Presnyakov, S.L., and Tuganova, E.V. 2010. Magmatic evolution of the ultramafic–mafic Kharaelakh intrusion (Siberian Craton, Russia): insights from trace-element, U–Pb and Hf-isotope data on zircon. Contributions to Mineralogy and Petrology, **159**(6): 753-768.

Mayr, U., Beauchamp, B., Embry, A.F., and Harrison, J.C. 2002. Geology of Upper Paleozoic and Mesozoic formations of northern Axel Heiberg Island, parts of NTS 560D, Cape Stallworthy and 560A, Bukken Fiord, Nunavut scale 1:125,000. Geological Survey of Canada, open file report 3513.

Meneley, R.A., Henao, D., and Merritt, R.K. 1975. The northwest margin of the Sverdrup Basin: *in* Yorath, C.J., Parker, E.R., and Glass, D.J., eds., Canada's continental margins and offshore petroleum exploration. Canadian Society of Petroleum Geologists Memoir, **4**: 557-587.

Miall, A.D. 1976. Proterozoic and Paleozoic geology of Banks Island, Arctic Canada. Geological Survey of Canada Bulletin, **258**, 77 p.

Miall, A.D. 1979. Mesozoic and Tertiary geology of Banks Island, Arctic Canada: the history of an unstable cratonic margin. Geological Survey of Canada Memoir, **387**, 235 p.

Miall, A.D. 1986. Effects of Caledonian tectonism in Arctic Canada. Geology, **14**: 904-907.

Midwinter, D., Hadlari, T., Davis, W.J., Dewing, K., and Arnott, R.W.C. 2016. Dual provenance signatures of the Triassic northern Laurentian margin from detrital zircon U-Pb and Hf isotope analysis of Triassic-Jurassic strata in the Sverdrup Basin. Lithosphere, doi:10.1130/L517.1

Miller, E.L., Toro, J., Gehrels, G., Amato, J.M., Prokopiev, A., Tuchkova, M.I., Akinin, V.V., Dumitru, T.A., Moore, T.E., and Cecile, M.P. 2006. New insights into Arctic paleogeography and tectonics from U-Pb detrital zircon geochronology. Tectonics, **25**(3): 1-19.

Miller, E.L., Gehrels, G.E., Pease, V., and Sokolov, S. 2010. Stratigraphy and U-Pb detrital zircon geochronology of Wrangel Island, Russia: Implications for Arctic paleogeography. American Association of Petroleum Geologists Bulletin, **94**(5): 665-692.

Miller, E.L., Soloviev, A.V., Prokopiev, A.V., Toro, J., Harris, D., Kuzmichev, A.B., and Gehrels, G.E. 2013. Triassic river systems and the paleo-Pacific margin of northwestern Pangea. Gondwana Research, **23**(4): 1631-1645.

Moore, T.E., O'Sullivan, P.B., Potter, C.J., and Donelick, R.A. 2015. Provenance and detrital zircon geochronologic evolution of lower Brookian foreland basin deposits of the western Brooks Range, Alaska, and implications for early Brookian tectonism. Geosphere, **11**(1): 93-122.

Moore, T.E., Wallace, W.K., Bird, K.J., Karl, S.M., Mull, C.G., and Dillon, J.T. 1994. Geology of northern Alaska. *In*: The Geology of Alaska. *Edited by*: Plafker, G., and Berg, H.C. The Geology of North America, Geological Society of America, G-1, pp. 49-140.

Morris, N. 2013. Stratigraphy and Geochemistry of Lower Permian volcanics in the Sverdrup Basin, Northwest Ellesmere Island, Nunavut [M.S. thesis]. University of Calgary, 222 p.

Nelson, J.L., Colpron, M., Piercey, S.J., Dusel-Bacon, C., Murphy, D.C., and Roots, C.F. 2006. Paleozoic tectonic and metallogenic evolution of pericratonic terranes in Yukon, northern British Columbia and eastern Alaska: *in* Colpron, M., and Nelson, J.L., eds., Paleozoic evolution and metallogeny of pericratonic terranes at the ancient Pacific margin of North America, Canadian and Alaskan cordillera. Geological Association of Canada, Special Paper, **45**: 323–360.

Nemchin, A.A., and Cawood, P.A. 2005. Discordance of the U–Pb system in detrital zircons: implication for provenance studies of sedimentary rocks. Sedimentary Geology, **182**(1): 143-162.

Nielsen, S.B., Clausen, O.R. and McGregor, E. 2015. Basin% Ro: A vitrinite reflectance model derived from basin and laboratory data. Basin Research, doi:10.1111/bre.12160

Nokleberg, W.J., Parfenov, L.M., Monger, J.W., Norton, I.O., Chand'uk, A.I., Stone, D.B., Scotese, C.R., Scholl, D.W., and Fujita, K., 2000, Phanerozoic tectonic evolution of the Circum-North Pacific: United States Geological Survey, Professional Paper, **1626**, 122 p.

Norris, A.W. 1974. Report on Fragmentary Fossils from the Cape Crozier Area of Banks Island, District of Franklin, 74 31N, 121 06W (NTS 98E); Submitted by Dr. A.D. Miall, August 1, 1973. Geological Survey of Canada, paleontological report 3 AWN 1974, 1 p.

Oakey, G. N., and R. W. Saltus. 2016. Geophysical analysis of the Alpha–Mendeleev ridge complex: Characterization of the High Arctic Large Igneous Province. Tectonophysics, *in press*.

Okulitch, A.V., compiler. 1991. Geology of the Canadian Archipelago, Northwest Territories and North Greenland. Geological Survey of Canada Map 1715A, scale 1:2,000,000.

Omma, J.E., Pease, V., and Scott, R.A. 2011. U–Pb SIMS zircon geochronology of Triassic and Jurassic sandstones on northwestern Axel Heiberg Island, northern Sverdrup Basin, Arctic Canada: *in* Spencer, A.M., Embry, A.F., Gautier, D.L., Stoupakova, A.V., and Sørensen, K., eds., Arctic Petroleum Geology. Geological Society of London Memoir, **35**: 559-566.

Patchett, P.J., Embry, A.F., Ross, G.M., Beauchamp, B., Harrison, J.C., Mayr, U., Isachsen, C., Rosenberg, E., and Spence, G. 2004. Sedimentary cover of the Canadian Shield through Mesozoic time reflected by Nd isotopic and geochemical results for the Sverdrup Basin, Arctic Canada. The Journal of Geology, **112**(1): 39-57.

Pease, V. 2011. Eurasian orogens and Arctic tectonics: an overview: *in* Spencer, A.M., Embry, A.F., Gautier, D.L., Stoupakova, A.V., and Sørensen, K., eds., Arctic Petroleum Geology. Geological Society of London Memoir, **35**: 311–324.

Pease, V., Drachev, S., Stephenson, R., and Zhang, X. 2014. Arctic lithosphere—A review. Tectonophysics, **628**: 1-25.

Pease, V., Kuzmichev, A.B., and Danukalova, M.K. 2015. The New Siberian Islands and evidence for the continuation of the Uralides, Arctic Russia. Journal of the Geological Society, **172**(1): 1-4.

Petrov, O., Morozov, A., Shokalsky, S., Kashubin, S., Artemieva, I.M., Sobolev, N., Petrov, E., Ernst, R.E., Sergeev, S. and Smelror, M. 2016. Crustal structure and tectonic model of the Arctic region. Earth-Science Reviews, **154**: 29-71.

Plafker, G., and Berg, H.C. 1994. Overview of the geology and tectonic evolution of Alaska: *in* Plafker, G., and Berg, H.C., eds., The Geology of Alaska. Geological Society of America, Geology of North America, v. G-1: 989-1021.

Powell, J., Schneider, D.A., Stockli, D., and Fallas, K. 2016. Zircon (U-Th)/He thermochronology of Neoproterozoic strata from the Mackenzie Mountains, Canada: Implications for the Phanerozoic exhumation and deformation history of the northern Canadian Cordillera. Tectonics, **35**, doi:10.1002/2015TC003989.

Rainbird, R.H, Craven, J.A., Turner, E.C., Jackson, V.A., Fischer, B.J., Bouchard, M., Greenman, J.W., and Gibson, T. 2016. Reconnaissance geological mapping, stratigraphy and magnetotelluric survey of northern Brock Inlier, Northwest Territories. Geological Survey of Canada, open file report 7955, 16 p.

Rainbird, R.H., Jefferson, C.W., Hildebrand, R.S., and Worth, J.K. 1994. The Shaler Supergroup and revision of Neoproterozoic stratigraphy in the Amundsen Basin, Northwest Territories. Geological Survey of Canada, current research 1994-C: 61-70.

Rainbird, R.H., Jefferson, C.W., and Young, G.M. 1996. The early Neoproterozoic sedimentary Succession B of northwest Laurentia: correlations and paleogeographic significance. Geological Society of America Bulletin, **108**: 454-470.

Rainbird, R.H., Stern, R.A., Khudoley, A.K., Kropachev, A.P., Heaman, L.M., and Sukhorukov, V.I. 1998. U-Pb geochronology of Riphean sandstone and gabbro from southeast Siberia and its bearing on the Laurentia-Siberia connection. Earth and Planetary Science Letters, **164**: 409-420.

Rayner, N., and Rainbird, R.H. 2013. U–Pb geochronology of the Shaler Supergroup, Victoria Island, northwest Canada: 2009–2013. Geological Survey of Canada, open file report 7419, 62 p.

Reiners, P.W. 2005. Zircon (U-Th)/He Thermochronometry: *in* Reiners, P.W., and Ehlers, T.A., eds., Low-temperature thermochronology: techniques, interpretations, and application. Reviews in Mineralogy and Geochemistry, **58**: 151-179.

Reiners, P.W., Farley, K.A., and Hickes, H.J. 2002. He diffusion and (U–Th)/He thermochronometry of zircon: initial results from Fish Canyon Tuff and Gold Butte. Tectonophysics, **349**(1): 297-308.

Reiners, P.W., Spell, T.L., Nicolescu, S., and Zanetti, K.A. 2004. Zircon (U-Th)/He thermochronometry: He diffusion and comparisons with $^{40}Ar/^{39}Ar$ dating. Geochimica et Cosmochimica Acta, **68**(8): 1857-1887.

Rioux, M., Bowring, S., Kelemen, P., Gordon, S., Dudás, F., and Miller, R. 2012. Rapid crustal accretion and magma assimilation in the Oman-UAE ophiolite: High precision U-Pb zircon geochronology of the gabbroic crust. Journal of Geophysical Research Solid Earth, **117**(B7).

Røhr, T.S., Andersen, T., Dypvik, H., and Embry, A.F. 2010. Detrital zircon characteristics of the Lower Cretaceous Isachsen Formation, Sverdrup Basin: source constraints from age and Hf isotope data. Canadian Journal of Earth Sciences, **47**(3): 255-271.

Sherwood, K.W., Johnson, P.P., Craig, J.D., Zerwick, S.A., Lothamer, R.T., Thurston, D.K., and Hurlbert, S.B. 2002. Structure and stratigraphy of the Hanna trough, US Chukchi shelf, Alaska. Geological Society of America special papers, pp. 39-66.

Söderlund, U., Patchett, P.J., Vervoort, J.D., and Isachsen, C.E. 2004. The ^{176}Lu decay constant determined by Lu-Hf and U-Pb isotope systematics of Precambrian mafic intrusions. Earth and Planetary Science Letters, **219**(3-4): 311-24.

Sokolov, S.D., Bondarenko, G.Y., Layer, P.W., and Kravchenko-Berezhnoy, I.R. 2009. South Anyui suture: tectono-stratigraphy, deformations, and principal tectonic events. Stephan Mueller Special Publication Series, **4**: 201-221.

Stasiuk, L.D., Sweet, A.R., and Issler, D.R. 2006. Reconstruction of burial history of eroded Mesozoic strata using kimberlite shale xenoliths, volcaniclastic and crater facies, Northwest Territories, Canada. International Journal of Coal Geology, **65**: 129-145.

Stern, R.A. 1997. The GSC sensitive high resolution ion microprobe (SHRIMP): analytical techniques of zircon U–Th–Pb age determinations and performance evaluation. Geological Survey of Canada Radiogenic Age and Isotope Studies, Report 10, Current Research: 1-31.

Stern, R.A., and Amelin, Y. 2003. Assessment of errors in SIMS zircon U-Pb geochronology using a natural zircon standard and NIST SRM 610 glass. Chemical Geology, **197**: 111-146.

Sweeney, J.J., and Burnham, A.K. 1990. Evaluation of a simple model of vitrinite reflectance based on chemical kinetics (1). AAPG Bulletin, **74**(10): 1559-157

Sweet, A.R. 1973. Report On 10 Field Samples from Banks Island for A. Miall, Samples C-26370 To C-26376 from 74 31.5N, 121 07W (NTS 98E); Samples C-26377 to C-26378 from Able Creek 73 42N, 120 0.5W (NTS 98D); Sample C-26379 From Able Creek 73 42N, 119 58W (NTS 88C). Geological Survey of Canada, paleontological report AS-7-1973, 2 p.

Thorsteinsson, R. 1974. Carboniferous and Permian stratigraphy of Axel Heiberg Island and western Ellesmere Island, Canadian Arctic Archipelago. Geological Survey of Canada Bulletin, **224**, 115 p.

Trettin, H. P. 1987. Pearya: a composite terrane with Caledonian affinities in northern Ellesmere Island. Canadian Journal of Earth Sciences, **24**(2): 224-245.

Trettin, H.P. 1988. Early Namurian (or older) alkali basalt in the Borup Fiord Formation, northern Axel Heiberg Island, Arctic Canada: Geological Survey of Canada Paper, v. 88-1D: 21-26.

Trettin, H.P., Mayr, U., Long, D.G.F., and Packard, J.J. 1991. Cambrian to Early Devonian basin development, sedimentation and volcanism, Arctic Islands: *in* Trettin, H.P., ed., Geology of the Innuitian Orogen and Arctic Platform of Canada and Greenland. Geological Survey of Canada, Geology of Canada, **3**: 165-238.

Tuchkova, M.I., Sokolov, S., and Kravchenko-Berezhnoy, I.R. 2009. Provenance analysis and tectonic setting of the Triassic clastic deposits in western Chukotka, northeast Russia: *in* Stone, D.B., Fujita, K., Layer, P.W., Miller, E.L., Prokopiev, A.V., and Toro, J., eds., Geology, Geophysics and Tectonics of Northeastern Russia: A Tribute to Leonid Parfenov. Stephan Mueller Special Publication, **4**: 177–200.

Tuchkova, M.I., Sokolov, S.D., Khudoley, A.K., Verzhbitsky, V.E., Hayasaka, Y., and Moiseev, A.V. 2011. Permian and Triassic deposits of Siberian and Chukotka passive margins: sedimentation setting and provenances. Proceedings of the International Conference on Arctic Margins VI, Fairbanks, Alaska: 61-96.

van Acken, D., Thomson, D., Rainbird, R.H., and Creaser, R.A. 2013. Constraining the depositional history of the Neoproterozoic Shaler Supergroup, Amundsen Basin, NW

Canada: Rhenium–osmium dating of black shales from the Wynniatt and Boot Inlet Formations. Precambrian Research, **236**: 124-131.

van der Beek, P., Cloetingh, S., and Andriessen, P. 1994. Mechanisms of extensional basin formation and vertical motions at rift flanks: Constraints from tectonic modelling and fission-track thermochronology. Earth and Planetary Science Letters, **121**(3): 417-433.

Vermeesch, P. 2012 On the visualisation of detrital age distributions. Chemical Geology, **312**: 190-194.

Vernikovsky, V.A., Neimark, L.A., Ponomarchuk, V.A., and Vernikovskaya, A.E. 1995. Geochemistry and age of collisional granitoids and metamorphites of the Kara microcontinent (Northern Taimyr). Russian Geology and Geophysics, **36**(12): 50-64.

Vervoort, J.D., and Patchett, P.J. 1996. Behavior of hafnium and neodymium isotopes in the crust: Constraints from crustally derived granites. Geochimica et Cosmochimica Acta, **60**: 3717–3733.

Vervoort, J.D., Patchett, P.J., Blichert-Toft, J., and Albarede, F. 1999. Relationships between Lu-Hf and Sm-Nd isotopic systems in the global sedimentary system. Earth and Planetary Science Letters, **168**: 79–99.

Villeneuve, M.E., Butterfield, N.J., Cook, D.G., MacLean, B.C., and Rainbird, R.H. 1998. Age of the Cap Mountain (Northwest Territories) Proterozoic section, Sequence B, based on detrital zircon ages. Geological Survey of Canada, Current Research 1998-F, Radiogenic Age and Isotopic Studies Report 11: 117-127.

Wheeler, J.O., Hoffman, P.F., Card, K.D., Davidson, A., Sanford, B.V., Okulitch, A.V., and Roest, W.R. 1996. Geological Map of Canada. Geological Survey of Canada, "A" Series Map 1860A.

Wolfe, M.R., and Stockli, D.F. 2010. Zircon (U–Th)/He thermochronometry in the KTB drill hole, Germany, and its implications for bulk He diffusion kinetics in zircon. Earth and Planetary Science Letters, **295**(1-2): 69-82.

Woodhead, J.D., and Hergt, J.M. 2005. A preliminary appraisal of seven natural zircon reference materials for in situ Hf isotope determination. Geostandards and Geoanalytical Research, **29**(2): 183-195.

Wu, F.Y., Yang, Y.H., Xie, L.W., Yang, J.H., and Xu, P. 2006. Hf isotopic compositions of the standard zircons and baddeleyites used in U–Pb geochronology. Chemical Geology, **234**(1): 105-126.

Yorath, A.C., and Cook, D.G. 1981. Cretaceous and Tertiary stratigraphy and paleogeography, Northern Interior plains, District of Mackenzie. Geological Survey of Canada Memoir 398, 76 p.

Young, G.M. 1981. The Amundsen Embayment, Northwest Territories; relevance to the Upper Proterozoic evolution of North America: *in* Campbell, F.H.A., ed., Proterozoic basins of Canada. Geological Survey of Canada, paper 81-10: 203-218.

Young, G.M., Jefferson, C.W., Delaney, G.D., and Yeo, G.M. 1979. Middle and Upper Proterozoic evolution of the northern Canadian Cordillera and Shield. Geology, **7**: 125-128.

Zhang, X., Omma, J., Pease, V. and Scott, R. 2013. Provenance study of late Paleozoic–Mesozoic sandstones from the Taimyr Peninsula, Arctic Russia: *in* Schmidt, J., ed., Sedimentary Basins and Orogenic Belts. Geosciences, **3**: 502–527.

Zhang, X., Pease, V., Skogseid, J. and Wohlgemuth-Ueberwasser, C. 2015. Reconstruction of tectonic events on the northern Eurasia margin of the Arctic, from U-Pb detrital zircon provenance investigations of late Paleozoic to Mesozoic sandstones in southern Taimyr Peninsula. Geological Society of America Bulletin, **128**(1-2): 29-46.

Zhou, X.M., and Li, W.X. 2000. Origin of Late Mesozoic igneous rocks in Southeastern China: implications for lithosphere subduction and underplating of mafic magmas. Tectonophysics, **326**: 269-287.

Appendix A: Detrital-Zircon Sample Information

Region	Formation/Unit	Sample No.	Age	Reference	Latitude	Longitude
Canadian Arctic						
Sverdrup Basin	Isachsen Formation	C-82218	late Barremian	Rohr et al., 2010	79.950	-85.167
Sverdrup Basin	Isachsen Formation	C-86116	Barremian	Rohr et al., 2010	79.950	-85.167
Sverdrup Basin	Isachsen Formation	C-072382	late Barremian - early Aptian	Rohr et al., 2010	80.883	-70.833
Sverdrup Basin	Isachsen Formation	C-100614	Hauterivian	Rohr et al., 2010	78.617	-89.767
Sverdrup Basin	Isachsen Formation	C-100629	Barremian	Rohr et al., 2010	78.617	-89.767
Sverdrup Basin	Sandy Point Formation	C403747	Aalenian	Omma et al., 2011	80.883	-95.017
Sverdrup Basin	Deer Bay Formation	C403685	Tithonian	Omma et al., 2011	80.467	-95.750
Sverdrup Basin	Blind Fiord Formation	C403730	Early Triassic	Omma et al., 2011	80.950	-92.567
Sverdrup Basin	Pat Bay Formation	C403503	Carnian	Omma et al., 2011	80.817	-94.583
Sverdrup Basin	Sandy Point Formation	C403747	Aalenian	Omma et al., 2011	80.883	-95.017
Sverdrup Basin	Deer Bay Formation	C403685	Tithonian	Omma et al., 2011	80.467	-95.750
Sverdrup Basin	Pat Bay Formation	AE2	Carnian	Miller et al., 2006	80.583	-95.950
Sverdrup Basin	Bjorne Formation	AE1	Olenekian	Miller et al., 2006	79.567	-83.333
Sverdrup Basin	King Christian Formation	11270	Pliensbachian	this study	78.996	-104.570
Sverdrup Basin	Romulus Member	11242	Norian	this study	79.449	-85.561
Sverdrup Basin	Bjorne Formation	11243	Olenekian	this study	79.564	-83.317
D.C.W	Kennedy Channel Formation	C-246356	Neoproterozoic	Anfinson et al., 2012	80.14	-74.758
D.C.W	Archer Fiord Formation	C-412024	Neoproterozoic	Anfinson et al., 2012	80.848	-68.775
D.C.W	Danish River Formation	C-033516	Silurian-Devonian	Anfinson et al., 2012	79.934	-81.02
D.C.W	Bird Fiord Formation	C-198555	Middle Devonian	Anfinson et al., 2012	76.734	-93.501
D.C.W	Strathcona Fiord Formation	C-245720	Middle Devonian	Anfinson et al., 2012	78.468	-82.333
D.C.W	Strathcona Fiord Formation	C-174904	Middle Devonian	Anfinson et al., 2012	77.464	-83.666
D.C.W	Hecla Bay Formation	C-245739	Mid-Late Devonian	Anfinson et al., 2012	78.451	-82.449
D.C.W	Hecla Bay Formation	C-246257	Mid-Late Devonian	Anfinson et al., 2012	76.436	-103.088
D.C.W	Hecla Bay Formation	C-133818	Mid-Late Devonian	Anfinson et al., 2012	76.022	-112.56
D.C.W	Hecla Bay Formation	C-128665	Mid-Late Devonian	Anfinson et al., 2012	75.186	-115.11
D.C.W	Fram Formation	C-245747	Late Devonian	Anfinson et al., 2012	78.434	-82.566
D.C.W	Fram Formation	C-245760	Late Devonian	Anfinson et al., 2012	78.434	-82.566
D.C.W	Fram Formation	C-140199	Late Devonian	Anfinson et al., 2012	76.626	-90.834
D.C.W	Beverley Inlet Formation	C-128790	Late Devonian	Anfinson et al., 2012	74.89	-109.146
D.C.W	Beverley Inlet Formation	C-133862	Late Devonian	Anfinson et al., 2012	75.247	-117.636
D.C.W	Beverley Inlet Formation	C-198959	Late Devonian	Anfinson et al., 2012	76.269	-119.438
D.C.W	Parry Islands Formation	C-245984	Late Devonian	Anfinson et al., 2012	76.684	-100.801
D.C.W	Parry Islands Formation	C-246260	Late Devonian	Anfinson et al., 2012	76.436	-103.088
D.C.W	Parry Islands Formation	C-134039	Late Devonian	Anfinson et al., 2012	75.577	-106.081
D.C.W	Parry Islands Formation	C-207286	Late Devonian	Anfinson et al., 2012	76.267	-119.92
Russia						
Chukotka	Carnian T3k	CH3.1B	Carnian	Miller et al., 2006	67.868	166.290
Chukotka	Carnian T3k	CH2.6	Carnian	Miller et al., 2006	68.062	166.412
Chukotka	Norian T3n	CH26.5	Norian	Miller et al., 2006	69.157	165.038

Chukotka	Carnian T3k	09/321	Upper Triassic	Tuchkova et al., 2011	66.698	176.728
Chukotka	Lower Triassic T2?	09/358	Lower-Middle Triassic	Tuchkova et al., 2011	67.158	178.142
Wrangel Island	Triassic Sandstone	ELM06 WR8	Triassic	Miller et al., 2010	71.025	179.208
Wrangel Island	Triassic Sandstone	ELM06 WR46B	Triassic	Miller et al., 2010	70.984	179.545
Wrangel Island	Triassic Sandstone	ELM06 WR51B	Triassic	Miller et al., 2010	71.015	179.513
Alaska						
Lisburne Hills	Otuk Formation	94CL10	Upper Triassic	Miller et al., 2006	68.869	166.060
Lisburne Hills	Otuk Formation	94CL53	Upper Triassic	Miller et al., 2006	68.861	166.015
North Slope	Karen Creek Sandstone	EB-KC	Late-Triassic-Early Jurassic	Gottlieb et al., 2014	69.348	-139.634
North Slope	Karen Creek Sandstone	WE-KC	Late-Triassic-Early Jurassic	Gottlieb et al., 2014	69.488	-143.134
North Slope	Sag River Formation	ES-SR	Late-Triassic-Early Jurassic	Gottlieb et al., 2014	70.918	-154.618
Yukon						
YTT Platform	Jones Lake Formation	JL1 - 17LB05	Early Triassic	Beranek et al., 2010	62.816	-129.697
YTT Platform	Jones Lake Formation	JL2 - 29LB05	Early Triassic	Beranek et al., 2010	62.817	-129.689
YTT Platform	Jones Lake Formation	OG1 - 10LB06	Early - Late Triassic	Beranek et al., 2010	64.424	-138.136
YTT Platform	Jones Lake Formation	OG2 - 15LB06	Early - Late Triassic	Beranek et al., 2010	64.419	-138.146
YTT Platform	Jones Lake Formation	OG3 - 18LB06	Early - Late Triassic	Beranek et al., 2010	64.416	-138.149
YTT Platform	Jones Lake Formation	OG4 - 19LB06	Early - Late Triassic	Beranek et al., 2010	64.411	-138.153
YTT Platform	Jones Lake Formation	SL - 11LB07	Late Triassic	Beranek et al., 2010	62.297	-131.910
YTT Platform	Hoole Formation	HL - 09LB07	Late Triassic	Beranek et al., 2010	61.882	-132.865
YTT Platform	Toad Formation	TF - 2002LHA10-1C	Early Triassic	Beranek et al., 2010	60.727	-124.845
YTT Overlap	marine strata	1-1	Late Ladinian	Beranek & Mortensen, 2011	61.304	-129.600
YTT Overlap	marine strata	2-1	Late Ladinian	Beranek & Mortensen, 2011	61.304	-129.600
YTT Overlap	marine strata	3-1	Late Ladinian	Beranek & Mortensen, 2011	60.457	-128.939
YTT Overlap	Ross River Area	4-1	late Ladinian-early Carnian	Beranek & Mortensen, 2011	61.761	-126.436
YTT Overlap	McNeil Lake Area	5-1	Norian	Beranek & Mortensen, 2011	61.223	-131.616
YTT Overlap	McNeil Lake Area	5-2	Norian	Beranek & Mortensen, 2011	61.231	-131.625
YTT Overlap	Table Mountain Formation	6-1	Carnian to Rhaetian	Beranek & Mortensen, 2011	59.211	-129.645
YTT Overlap	Table Mountain Formation	6-2	Carnian to Rhaetian	Beranek & Mortensen, 2011	59.187	-129.675
YTT Overlap	Table Mountain Formation	6-3	Carnian to Rhaetian	Beranek & Mortensen, 2011	59.200	-129.653
YTT Overlap	Table Mountain Formation	6-4	Carnian to Rhaetian	Beranek & Mortensen, 2011	59.200	-129.653
YTT Overlap	Northern Finlayson Lake belt	7-1	base of pre-Norian	Beranek & Mortensen, 2011	61.893	-130.656
YTT Overlap	Northern Finlayson Lake belt	7-2	base of pre-Norian	Beranek & Mortensen, 2011	61.878	-130.895
YTT Overlap	Northern Finlayson Lake belt	7-3	overlying pre-Norian	Beranek & Mortensen, 2011	61.856	-130.886
YTT Overlap	Northern Finlayson Lake belt	7-4	overlying pre-Norian	Beranek & Mortensen, 2011	61.858	-130.885
YTT Overlap	American Creek	8-1	Carnian to Norian	Beranek & Mortensen, 2011	64.481	-141.212
YTT Overlap	Clinton Creek complex	9-1	Early to Middle Norian	Beranek & Mortensen, 2011	64.451	-140.721
YTT Overlap	Clinton Creek complex	9-2	Early to Middle Norian	Beranek & Mortensen, 2011	64.442	-140.729
YTT Overlap	Clinton Creek complex	9-3	Early to Middle Norian	Beranek & Mortensen, 2011	64.442	-140.729
YTT Overlap	Clinton Creek complex	9-4	Early to Middle Norian	Beranek & Mortensen, 2011	64.442	-140.729
YTT Overlap	Tummel Fault Zone	10-1	Anisian to Carnian	Beranek & Mortensen, 2011	62.300	-134.808

Note: D.C.W = Devonian clastic wedge

Appendix B: U-Pb Geochronology

										Isotope Ratios							Model Age (Ma)						Best age	±		Used in study
Analysis	U (ppm)	Th (ppm)	Th/U	206Pb* (ppm)	204Pb/206Pb	± 204Pb/206Pb	f(206)204	208*Pb/206*Pb	± 208Pb/206Pb	207*Pb/235U	±207Pb/235U	206*Pb/238U	±206Pb/238U	Corr Coeff	207*Pb/206*Pb	±207Pb/206Pb	206Pb/238U	±206Pb/238U	207Pb/206Pb	±207Pb/206Pb	Disc. (%)	Prob	(Ma)	(Ma)		
King Christian Formation, Pliensbachian, 78.996, -104.570																										
11270-001.1	392.50	125.42	0.32	82.88	0.00	0.00	-0.04	0.10	0.00	3.04	0.04	0.25	0.00	0.94	0.09	0.00	1416.88	15.56	1417.12	8.63	0.02	0.98	1417.07	3.8	0	Used
11270-002.1	63.54	15.39	0.24	10.57	0.00	0.00	0.03	0.07	0.01	2.13	0.04	0.19	0.00	0.77	0.08	0.00	1141.51	13.27	1192.72	20.62	4.68	0.00	1156.01	5.6	0	Used
11270-005.1	432.19	221.42	0.51	88.09	0.00	0.00	0.03	0.16	0.00	2.90	0.03	0.24	0.00	0.95	0.09	0.00	1372.54	13.02	1393.21	6.69	1.65	0.00	1388.94	3.0	0	Used
11270-006.1	133.55	47.46	0.36	26.33	0.00	0.00	0.19	0.13	0.00	3.48	0.07	0.23	0.00	0.69	0.11	0.00	1332.17	16.18	1800.56	25.71	28.76	0.00	1407.64	7.6	100	Not-used
11270-007.1	264.39	87.95	0.33	82.49	0.00	0.00	0.16	0.09	0.00	6.07	0.08	0.36	0.00	0.93	0.12	0.00	1997.46	22.34	1973.34	9.13	-1.42	0.05	1976.83	4.3	0	Used
11270-008.1	325.95	304.93	0.94	69.69	0.00	0.00	0.11	0.30	0.00	3.24	0.04	0.25	0.00	0.92	0.09	0.00	1432.91	15.80	1516.90	9.53	6.17	0.00	1495.18	4.0	100	Not-used
11270-009.1	273.75	229.27	0.84	86.64	0.00	0.00	0.01	0.26	0.01	6.37	0.08	0.37	0.00	0.90	0.13	0.00	2022.06	18.58	2034.89	9.26	0.73	0.22	2032.35	4.1	0	Used
11270-010.1	350.70	128.39	0.37	75.35	0.00	0.00	0.21	0.11	0.00	3.49	0.06	0.25	0.00	0.84	0.10	0.00	1439.06	19.51	1644.09	17.97	13.91	0.00	1548.39	6.8	100	Not-used
11270-011.1	184.38	68.07	0.37	44.25	0.00	0.00	0.08	0.12	0.00	3.92	0.05	0.28	0.00	0.92	0.10	0.00	1588.31	17.78	1654.82	9.96	4.53	0.00	1639.34	4.3	0	Used
11270-012.1	170.44	149.73	0.88	43.32	0.00	0.00	0.11	0.28	0.00	4.14	0.05	0.30	0.00	0.91	0.10	0.00	1670.78	16.41	1649.25	9.60	-1.48	0.02	1654.78	4.2	0	Used
11270-013.1	216.92	35.47	0.16	66.36	0.00	0.00	0.04	0.05	0.00	6.09	0.08	0.36	0.00	0.94	0.12	0.00	1963.93	21.62	2013.43	7.97	2.85	0.00	2007.67	3.7	0	Used
11270-014.1	425.73	160.56	0.38	25.15	0.00	0.00	0.21	0.13	0.00	0.52	0.01	0.07	0.00	0.66	0.06	0.00	428.71	5.06	413.12	31.37	-3.90	0.32	428.30	2.5	0	Used
11270-015.1	259.80	79.23	0.30	37.55	0.00	0.00	0.09	0.10	0.00	1.70	0.02	0.17	0.00	0.86	0.07	0.00	1002.52	10.07	1019.13	13.29	1.76	0.05	1008.54	4.0	0	Used
11270-016.1	115.65	84.24	0.73	28.92	0.00	0.00	0.03	0.22	0.00	4.13	0.05	0.29	0.00	0.90	0.10	0.00	1647.28	16.67	1678.17	10.01	2.09	0.00	1670.05	4.3	0	Used
11270-017.1	295.45	164.38	0.56	75.59	0.00	0.00	0.20	0.17	0.00	4.50	0.12	0.30	0.01	0.99	0.11	0.00	1680.51	39.12	1793.88	7.80	7.18	0.00	1789.99	3.6	100	Not-used
11270-018.1	249.92	211.71	0.85	54.76	0.00	0.00	0.17	0.25	0.01	3.42	0.05	0.26	0.00	0.92	0.10	0.00	1464.60	16.10	1572.43	9.73	7.66	0.00	1544.70	4.1	100	Not-used
11270-019.1	393.52	219.22	0.56	71.22	0.00	0.00	-0.01	0.17	0.00	2.38	0.03	0.21	0.00	0.93	0.08	0.00	1232.51	11.89	1246.15	7.94	1.20	0.06	1241.96	3.3	0	Used
11270-020.1	304.30	209.87	0.69	84.87	0.00	0.00	0.05	0.20	0.01	5.60	0.07	0.32	0.00	0.96	0.13	0.00	1812.59	19.26	2030.47	5.90	12.30	0.00	2014.49	2.6	100	Not-used
11270-021.1	286.32	115.24	0.40	16.03	0.00	0.00	0.21	0.13	0.01	0.52	0.01	0.07	0.00	0.61	0.06	0.00	407.09	6.60	509.45	47.92	20.73	0.00	408.38	3.3	100	Not-used
11270-022.1	513.11	245.80	0.48	145.78	0.00	0.00	0.06	0.15	0.00	5.41	0.07	0.33	0.00	0.98	0.12	0.00	1841.96	19.21	1934.13	4.70	5.48	0.00	1929.29	2.2	100	Not-used
11270-024.1	197.86	50.13	0.25	43.13	0.00	0.00	0.14	0.07	0.00	3.25	0.05	0.25	0.00	0.87	0.09	0.00	1457.97	17.08	1486.47	13.93	2.14	0.01	1475.11	5.4	0	Used
11270-025.1	400.74	220.24	0.55	69.07	0.00	0.00	0.02	0.18	0.00	2.26	0.04	0.20	0.00	0.97	0.08	0.00	1178.82	17.67	1234.19	7.63	4.91	0.00	1225.91	3.4	0	Used
11270-027.1	209.34	314.90	1.50	52.81	0.00	0.00	0.07	0.48	0.01	4.07	0.05	0.29	0.00	0.93	0.10	0.00	1659.85	15.96	1634.23	8.05	-1.78	0.00	1639.48	3.6	0	Used
11270-028.1	586.33	300.74	0.51	168.69	0.00	0.00	0.15	0.16	0.00	5.58	0.09	0.33	0.01	0.97	0.12	0.00	1862.26	26.44	1967.62	6.89	6.16	0.00	1961.45	3.2	100	Not-used
11270-029.1	298.36	101.44	0.34	71.83	0.00	0.00	0.04	0.11	0.00	3.75	0.04	0.28	0.00	0.95	0.10	0.00	1592.71	15.34	1566.09	6.97	-1.92	0.00	1570.71	3.2	0	Used
11270-030.1	311.13	162.45	0.52	98.91	0.00	0.00	0.08	0.16	0.00	6.39	0.07	0.37	0.00	0.96	0.13	0.00	2029.84	18.70	2031.16	5.46	0.08	0.89	2031.06	2.6	0	Used
11270-031.1	205.95	115.64	0.56	47.67	0.00	0.00	0.11	0.18	0.00	3.82	0.06	0.27	0.00	0.90	0.10	0.00	1538.09	17.87	1677.55	12.02	9.34	0.00	1635.39	4.9	100	Not-used
11270-033.1	226.42	68.81	0.30	29.67	0.00	0.00	0.52	0.08	0.01	1.82	0.03	0.15	0.00	0.71	0.09	0.00	915.10	11.29	1351.08	24.98	34.59	0.00	942.89	5.5	100	Not-used
11270-034.1	273.10	215.12	0.79	35.99	0.00	0.00	0.11	0.26	0.00	1.47	0.02	0.15	0.00	0.84	0.07	0.00	920.16	9.21	917.01	14.04	-0.37	0.71	919.21	3.8	0	Used
11270-035.1	215.65	61.02	0.28	55.20	0.00	0.00	0.05	0.10	0.00	4.80	0.06	0.30	0.00	0.94	0.12	0.00	1681.28	16.28	1908.43	7.47	13.51	0.00	1873.46	3.2	100	Not-used
11270-038.1	159.67	130.96	0.82	34.36	0.00	0.00	0.40	0.26	0.01	3.18	0.05	0.25	0.00	0.79	0.09	0.00	1441.28	17.41	1466.74	19.71	1.94	0.05	1452.37	6.6	0	Used
11270-040.1	223.26	237.77	1.06	9.52	0.00	0.00	0.37	0.34	0.02	0.37	0.02	0.05	0.00	0.49	0.05	0.00	312.22	6.32	348.67	83.97	10.71	0.39	312.39	3.2	0	Used
11270-041.1	239.60	75.80	0.32	66.34	0.00	0.00	0.13	0.10	0.00	5.36	0.10	0.32	0.01	0.94	0.12	0.00	1800.97	26.45	1964.80	11.08	9.55	0.00	1942.43	4.8	100	Not-used
11270-042.1	383.71	127.50	0.33	88.16	0.00	0.00	0.40	0.08	0.00	4.20	0.06	0.27	0.00	0.96	0.11	0.00	1528.00	18.86	1860.59	7.45	20.06	0.00	1825.35	3.0	100	Not-used
11270-044.1	191.59	21.89	0.11	32.72	0.00	0.00	0.09	0.03	0.00	2.19	0.05	0.20	0.00	0.87	0.08	0.00	1169.10	22.10	1193.38	22.70	2.22	0.12	1180.89	7.9	0	Used
11270-045.1	237.22	91.78	0.39	104.98	0.00	0.00	0.04	0.11	0.00	13.95	0.24	0.52	0.01	0.97	0.20	0.00	2678.72	37.17	2796.33	6.77	5.14	0.00	2792.81	3.2	100	Not-used
11270-046.1	314.48	225.46	0.72	77.60	0.00	0.00	0.07	0.22	0.00	3.96	0.07	0.29	0.00	0.94	0.10	0.00	1627.77	23.97	1623.36	11.42	-0.31	0.74	1624.18	5.2	0	Used
11270-047.1	86.72	32.98	0.38	12.84	0.00	0.00	0.44	0.13	0.01	1.72	0.06	0.17	0.00	0.57	0.07	0.00	1025.07	17.47	1001.25	53.41	-2.57	0.39	1022.68	8.3	0	Used
11270-050.1	1113.21	706.37	0.63	42.32	0.00	0.00	2.55	0.17	0.02	0.36	0.05	0.04	0.00	0.14	0.06	0.01	279.15	5.08	563.77	288.66	51.58	0.07	279.14	2.5	0	Used
11270-051.1	50.24	28.63	0.57	8.73	0.00	0.00	0.24	0.18	0.01	2.20	0.04	0.20	0.00	0.66	0.08	0.00	1187.36	14.55	1166.72	30.20	-1.94	0.22	1183.39	6.5	0	Used
11270-052.1	297.80	161.60	0.54	18.00	0.00	0.00	0.24	0.18	0.00	0.53	0.01	0.07	0.00	0.51	0.05	0.00	438.31	4.53	382.39	40.48	-15.13	0.01	437.49	2.2	0	Used
11270-053.1	221.58	124.38	0.56	38.09	0.00	0.00	0.10	0.18	0.00	2.15	0.03	0.20	0.00	0.86	0.08	0.00	1176.03	11.91	1149.09	13.12	-2.56	0.00	1163.81	4.4	0	Used
11270-055.1	247.66	78.16	0.32	93.84	0.00	0.00	0.04	0.09	0.00	10.21	0.11	0.44	0.00	0.97	0.17	0.00	2355.44	21.40	2536.97	4.53	8.53	0.00	2530.04	2.1	100	Not-used
11270-056.1	74.86	22.99	0.31	18.03	0.00	0.00	0.15	0.09	0.00	3.90	0.06	0.28	0.00	0.83	0.10	0.00	1593.01	17.63	1638.71	15.42	3.15	0.00	1618.87	5.8	0	Used
11270-059.1	315.74	168.08	0.53	97.57	0.00	0.00	0.03	0.16	0.00	5.99	0.08	0.36	0.00	0.83	0.12	0.00	1980.87	18.19	1968.21	12.85	-0.75	0.26	1972.43	5.2	0	Used
11270-061.1	480.91	253.33	0.53	128.65	0.00	0.00	0.05	0.16	0.00	4.72	0.06	0.31	0.00	0.96	0.11	0.00	1747.68	18.53	1798.22	5.99	3.21	0.00	1793.61	2.8	0	Used
11270-063.1	157.61	90.50	0.57	44.82	0.00	0.00	0.16	0.16	0.00	5.55	0.07	0.33	0.00	0.93	0.12	0.00	1843.48	17.79	1980.68	7.91	7.96	0.00	1959.49	3.5	100	Not-used
11270-064.1	94.51	65.05	0.69	23.52	0.00	0.00	0.09	0.22	0.00	4.01	0.05	0.29	0.00	0.88	0.10	0.00	1640.32	16.96	1632.57	11.95	-0.54	0.46	1635.14	4.9	0	Used
11270-068.1	255.07	269.72	1.06	64.84	0.00	0.00	0.01	0.33	0.00	4.13	0.05	0.30	0.00	0.95	0.10	0.00	1671.02	15.70	1645.73	6.25	-1.74	0.00	1649.25	2.9	0	Used
11270-069.1	198.48	92.86	0.47	34.07	0.00	0.00	0.15	0.14	0.00	2.15	0.03	0.20	0.00	0.84	0.08	0.00	1174.53	11.88	1148.16	14.02	-2.51	0.00	1163.44	4.5	0	Used
11270-071.1	877.71	248.04	0.28	140.99	0.00	0.00	0.43	0.09	0.01	2.38	0.12	0.19	0.00	0.46	0.09	0.00	1105.09	23.69	1476.20	86.31	27.33	0.00	1116.85	11.7	100	Not-used
11270-072.1	417.51	267.09	0.64	138.43	0.00	0.00	0.02	0.19	0.01	6.83	0.08	0.39	0.00	0.96	0.13	0.00	2104.11	19.23	2076.06	5.14	-1.58	0.00	2077.97	2.5	0	Used
11270-074.1	284.75	159.02	0.56	17.30	0.00	0.00	0.26	0.18	0.01	0.54	0.01	0.07	0.00	0.54	0.06	0.00	440.65	4.78	433.81	39.35	-1.63	0.73	440.55	2.4	0	Used
11270-091.1	141.09	95.32	0.68	36.22	0.00	0.00	0.07	0.21	0.01	4.34	0.08	0.30	0.01	0.92	0.11	0.00	1685.58	25.31	1718.24	13.69	2.16	0.02	1710.94	6.0	0	Used
11270-092.2	328.08	131.10	0.40	11.67	0.00	0.00	0.50	0.12	0.01	0.29	0.01	0.04	0.00	0.52	0.05	0.00	261.62	5.32	249.43	78.28	-4.99	0.76	261.57	2.7	0	Used
11270-093.1	159.53	280.71	1.76	45.56	0.00	0.00	0.03	0.54	0.01	5.29	0.10	0.33	0.01	0.94	0.12	0.00	1850.40	27.34	1884.81	11.55	2.10	0.02	1879.69	5.3	0	Used
11270-095.1	661.82	186.58	0.28	37.00	0.00	0.00	0.77	0.07	0.01	0.50	0.03	0.07	0.00	0.23	0.06	0.00	406.50	4.82	453.29	114.55	10.65	0.42	406.57	2.4	0	Used
11270-097.1	106.46	38.16	0.36	20.41	0.00	0.00	0.07	0.12	0.01	2.70	0.06	0.22	0.00	0.84	0.09	0.00	1298.93	20.57	1374.11	21.53	6.04	0.00	1334.39	7.5	100	Not-used
11270-098.1	149.18	56.20	0.38	33.58	0.00	0.00	0.51	0.10	0.01	3.36	0.10	0.26	0.00	0.62	0.09	0.00	1500.10	23.82	1486.22	42.93	-1.05	0.57	1496.80	10.4	0	Used
11270-099.1	353.47	91.72	0.26	81.39	0.00	0.00	0.36	0.08	0.00	4.10	0.08	0.27	0.00	0.93	0.11	0.00	1530.86	24.89	1816.88	12.78	17.67	0.00	1765.32	5.2	100	Not-used
11270-104.1	235.28	62.48	0.27	63.08	0.00	0.00	-0.02	0.08	0.00	4.70	0.08	0.31	0.01	0.95	0.11	0.00	1751.04	25.71	1787.32	10.31	2.32	0.01	1782.41	4.7	0	Used
11270-105.1	203.49	153.69	0.76	48.34	0.00	0.00	0.09	0.24	0.01	3.87	0.07	0.28	0.00	0.92	0.10	0.00	1573.92	23.56	1651.64	13.06	5.30	0.00	1633.93	5.6	100	Not-used
11270-106.1	245.41	30.69	0.13	31.77	0.00	0.00	0.31	0.03	0.00	1.45	0.03	0.15	0.00	0.76	0.07	0.00	904.83	14.21	924.90	29.34	2.33	0.22	908.56	6.4	0	Used
11270-107.1	189.76	80.37	0.42	45.11	0.00	0.00	0.03	0.13	0.00	3.86	0.07	0.28	0.00	0.92	0.10	0.00	1575.01	23.60	1644.32	13.07	4.75	0.00	1628.51	5.6	0	Used
11270-108.1	98.09	48.02	0.49	5.68	0.00	0.00	0.14	0.18	0.01	0.54	0.02	0.07	0.00	0.49	0.06	0.00	420.64	7.26	517.90	68.77	19.40	0.01	421.39	3.6	0	Used
11270-109.1	150.50	144.99	0.96	45.13	0.00	0.00	0.19	0.29	0.01	5.78	0.12	0.35	0.01	0.94	0.12	0.00	1930.35	31.61	1957.29	12.69	1.59	0.11	1953.60	5.8	0	Used

Analysis	U (ppm)	Th (ppm)	Th/U	206Pb* (ppm)	204Pb/206Pb	± 204Pb/206Pb	f(206)204	208*Pb/206*Pb	± 208Pb/206Pb	Isotope Ratios 207*Pb/235U	±207Pb/235U	206*Pb/238U	±206Pb/238U	Corr Coeff	207*Pb/206*Pb	±207Pb/206Pb	Model Age (Ma) 206Pb/238U	±206Pb/238U	207Pb/206Pb	±207Pb/206Pb	Disc. (%)	Prob	Best age (Ma)	± (Ma)	Used in study
Romulus Member, Heiberg Formation, Norian, 79.449, -85.561																									
11242-001.1	399.01	82.47	0.21	52.63	0.00	0.00	0.13	0.07	0.00	1.48	0.02	0.15	0.00	0.82	0.07	0.00	920.84	10.77	924.13	17.93	0.38	0.75	922	4.6	0 Used
11242-002.1	246.02	49.62	0.20	11.99	0.00	0.00	1.18	0.08	0.01	0.42	0.02	0.06	0.00	0.34	0.05	0.00	355.70	5.82	368.76	105.07	3.64	0.80	356	2.9	0 Used
11242-003.1	553.94	128.57	0.23	59.32	0.00	0.00	0.01	0.07	0.00	1.11	0.02	0.12	0.00	0.86	0.06	0.00	757.41	8.80	762.51	15.39	0.71	0.56	759	3.8	0 Used
11242-004.1	146.06	114.95	0.79	11.43	0.00	0.00	0.20	0.24	0.01	0.72	0.02	0.09	0.00	0.51	0.06	0.00	561.97	7.61	502.43	53.06	-12.38	0.02	561	3.8	0 Used
11242-005.1	149.37	140.36	0.94	60.20	0.00	0.00	0.08	0.29	0.01	10.72	0.16	0.47	0.01	0.94	0.17	0.00	2480.10	28.79	2513.92	8.34	1.62	0.02	2511	4.0	0 Used
11242-007.1	381.08	248.97	0.65	11.95	0.00	0.00	1.35	0.21	0.01	0.23	0.01	0.04	0.00	0.30	0.05	0.00	231.15	4.05	1.04	135.87	-22483.13	0.00	231	2.0	100 Not-used
11242-008.1	336.24	258.41	0.77	39.65	0.00	0.00	0.25	0.25	0.01	1.18	0.02	0.14	0.00	0.66	0.06	0.00	829.15	10.10	692.16	31.25	-21.10	0.00	813	4.7	100 Not-used
11242-009.1	130.46	100.11	0.77	48.89	0.00	0.00	0.05	0.26	0.01	10.78	0.16	0.44	0.01	0.94	0.18	0.00	2333.78	28.03	2645.31	8.75	14.02	0.00	2622	3.8	100 Not-used
11242-010.1	214.87	124.83	0.58	13.76	0.00	0.00	0.40	0.18	0.01	0.57	0.02	0.07	0.00	0.40	0.05	0.00	463.52	7.51	411.22	84.80	-13.18	0.21	463	3.7	0 Used
11242-011.2	119.75	105.19	0.88	5.13	0.00	0.00	1.00	0.30	0.02	0.36	0.02	0.05	0.00	0.24	0.05	0.00	313.91	4.27	283.50	130.35	-10.99	0.64	314	2.1	0 Used
11242-012.2	38.06	98.38	2.59	10.14	0.00	0.00	0.29	0.81	0.02	4.83	0.11	0.31	0.01	0.77	0.11	0.00	1742.25	26.05	1845.25	25.18	6.37	0.00	1795	9.2	100 Not-used
11242-013.2	920.77	812.86	0.88	35.53	0.00	0.00	0.13	0.30	0.01	0.33	0.01	0.04	0.00	0.74	0.05	0.00	283.26	3.29	317.57	24.40	11.04	0.01	284	1.6	0 Used
11242-014.1	131.63	187.40	1.42	4.11	0.00	0.00	1.92	0.49	0.04	0.23	0.02	0.04	0.00	0.14	0.05	0.00	230.19	3.21	-53.80	236.51	537.43	0.01	230	1.6	0 Used
11242-015.2	103.09	88.14	0.86	3.89	0.00	0.00	0.70	0.30	0.02	0.30	0.02	0.04	0.00	0.43	0.05	0.00	277.21	7.67	194.39	139.76	-43.53	0.23	277	3.8	0 Used
11242-016.1	72.19	35.16	0.49	31.25	0.00	0.00	0.45	0.14	0.00	11.88	0.19	0.50	0.01	0.91	0.17	0.00	2630.48	31.94	2566.84	11.37	-3.02	0.00	2574	5.4	0 Used
11242-017.1	108.02	81.07	0.75	30.05	0.00	0.00	0.13	0.22	0.01	4.73	0.09	0.32	0.00	0.82	0.11	0.00	1808.42	23.41	1729.80	19.36	-5.21	0.00	1762	7.4	100 Not-used
11242-019.1	1008.56	44.88	0.04	532.64	0.00	0.00	0.04	0.01	0.00	25.35	0.39	0.61	0.01	0.93	0.30	0.00	3089.19	34.87	3465.01	8.43	13.62	0.00	3447	3.6	100 Not-used
11242-023.2	240.13	149.78	0.62	29.22	0.00	0.00	0.20	0.19	0.00	1.34	0.02	0.14	0.00	0.76	0.07	0.00	853.97	10.09	888.32	22.45	4.13	0.01	859	4.6	0 Used
11242-026.2	135.97	180.53	1.33	56.34	0.00	0.00	0.03	0.39	0.01	12.18	0.18	0.48	0.01	0.89	0.18	0.00	2537.71	28.20	2681.41	11.53	6.48	0.00	2662	5.2	100 Not-used
11242-027.2	212.03	275.25	1.30	89.86	0.00	0.00	0.05	0.38	0.00	13.00	0.17	0.49	0.01	0.97	0.19	0.00	2585.37	27.20	2751.76	5.35	7.33	0.00	2746	2.5	100 Not-used
11242-029.2	467.84	158.46	0.34	39.30	0.00	0.00	0.13	0.16	0.00	0.89	0.02	0.10	0.00	0.93	0.07	0.00	601.50	13.06	808.78	18.37	26.84	0.00	660	5.7	100 Not-used
11242-030.1	591.79	318.53	0.54	20.52	0.00	0.00	0.22	0.18	0.01	0.28	0.01	0.04	0.00	0.52	0.05	0.00	255.09	3.07	176.95	47.04	-45.04	0.00	255	1.5	100 Not-used
11242-031.2	63.79	49.45	0.78	2.52	0.00	0.00	0.41	0.29	0.02	0.39	0.02	0.05	0.00	0.30	0.06	0.00	290.32	4.35	629.99	106.66	55.13	0.00	290	2.2	100 Not-used
11242-034.1	89.49	48.42	0.54	6.11	0.00	0.00	0.13	0.19	0.01	0.62	0.02	0.08	0.00	0.46	0.06	0.00	493.07	7.32	473.52	65.47	-4.29	0.55	493	3.6	0 Used
11242-035.1	450.25	160.12	0.36	138.38	0.00	0.00	0.04	0.12	0.00	6.45	0.09	0.36	0.00	0.96	0.13	0.00	1971.65	21.80	2108.41	6.13	7.52	0.00	2099	2.8	100 Not-used
11242-037.2	184.22	74.66	0.41	6.19	0.00	0.00	0.53	0.13	0.01	0.26	0.01	0.04	0.00	0.41	0.05	0.00	247.16	4.45	109.51	96.04	-128.13	0.00	247	2.2	0 Used
11242-038.1	438.07	272.99	0.62	19.75	0.00	0.00	0.52	0.22	0.01	0.37	0.01	0.05	0.00	0.54	0.05	0.00	329.72	5.27	225.44	58.67	-47.46	0.00	329	2.6	100 Not-used
11242-040.1	916.18	439.60	0.48	34.49	0.00	0.00	0.11	0.16	0.00	0.31	0.01	0.04	0.00	0.69	0.05	0.00	276.50	3.25	250.45	29.21	-10.62	0.07	276	1.6	0 Used
11242-041.2	330.32	65.43	0.20	11.63	0.00	0.00	0.12	0.06	0.00	0.28	0.01	0.04	0.00	0.56	0.05	0.00	259.04	3.13	196.49	42.69	-32.48	0.00	259	1.6	0 Used
11242-046.1	130.42	63.48	0.49	4.73	0.00	0.00	2.79	0.16	0.02	0.32	0.08	0.04	0.00	0.09	0.05	0.01	266.71	6.22	398.16	584.58	33.70	0.67	267	3.1	0 Used
11242-047.1	208.65	69.10	0.33	27.12	0.00	0.00	0.08	0.10	0.00	1.47	0.02	0.15	0.00	0.81	0.07	0.00	908.27	10.83	937.79	19.23	3.37	0.01	915	4.8	0 Used
11242-048.1	213.84	235.11	1.10	11.98	0.00	0.00	0.39	0.35	0.01	0.50	0.01	0.07	0.00	0.58	0.06	0.00	407.16	6.83	444.90	54.16	8.75	0.17	408	3.4	0 Used
11242-049.1	376.03	121.19	0.32	10.91	0.00	0.00	0.19	0.11	0.01	0.25	0.01	0.03	0.00	0.54	0.05	0.00	214.15	2.92	327.39	49.00	35.17	0.00	214	1.5	100 Not-used
11242-050.1	179.44	111.59	0.62	45.75	0.00	0.00	0.11	0.19	0.00	4.31	0.06	0.30	0.00	0.91	0.11	0.00	1675.53	19.11	1720.54	11.15	2.97	0.00	1709	4.8	0 Used
11242-051.1	198.88	99.19	0.50	12.10	0.00	0.00	0.34	0.16	0.01	0.54	0.01	0.07	0.00	0.49	0.06	0.00	441.24	5.51	415.94	51.79	-6.29	0.33	441	2.7	0 Used
11242-052.1	189.71	229.96	1.21	6.75	0.00	0.00	0.12	0.39	0.02	0.32	0.01	0.04	0.00	0.56	0.06	0.00	261.59	5.02	455.23	63.76	43.40	0.00	262	2.5	100 Not-used
11242-053.1	173.92	78.95	0.45	35.13	0.00	0.00	0.11	0.15	0.00	3.02	0.06	0.24	0.00	0.88	0.09	0.00	1361.42	21.21	1492.32	17.24	9.73	0.00	1441	6.7	100 Not-used
11242-054.1	124.11	72.19	0.58	5.20	0.00	0.00	0.98	0.19	0.02	0.36	0.03	0.05	0.00	0.25	0.05	0.00	307.08	5.40	369.86	157.43	17.38	0.43	307	2.7	0 Used
11242-055.1	214.12	201.72	0.94	79.23	0.00	0.00	0.08	0.28	0.00	9.12	0.13	0.43	0.01	0.89	0.15	0.00	2309.20	24.67	2385.14	11.36	3.79	0.00	2372	5.1	0 Used
11242-056.1	30.77	24.69	0.80	8.54	0.00	0.00	-0.06	0.27	0.01	4.92	0.11	0.32	0.01	0.81	0.11	0.00	1804.69	29.00	1807.63	24.38	0.19	0.88	1806	9.3	0 Used
11242-059.1	170.02	142.29	0.84	52.26	0.00	0.00	0.06	0.26	0.01	6.09	0.09	0.36	0.00	0.93	0.12	0.00	1971.98	22.15	2005.82	8.89	1.96	0.00	2001	4.1	0 Used
11242-060.1	55.72	35.92	0.64	18.14	0.00	0.00	0.12	0.21	0.01	6.86	0.12	0.38	0.01	0.88	0.13	0.00	2071.16	27.96	2116.67	15.20	2.51	0.00	2106	6.6	0 Used
11242-061.1	69.19	42.52	0.61	27.86	0.00	0.00	0.14	0.19	0.00	10.69	0.17	0.47	0.01	0.92	0.17	0.00	2478.12	30.55	2512.11	10.43	1.63	0.03	2509	4.9	0 Used
11242-062.1	126.99	47.59	0.37	32.57	0.00	0.00	0.05	0.11	0.00	4.27	0.06	0.30	0.00	0.89	0.10	0.00	1684.43	19.96	1693.28	12.54	0.59	0.45	1691	5.3	0 Used
11242-066.1	402.12	187.64	0.47	23.74	0.00	0.00	0.04	0.16	0.00	0.52	0.01	0.07	0.00	0.75	0.06	0.00	428.57	5.07	417.87	24.33	-2.65	0.39	428	2.5	0 Used
11242-067.1	70.62	186.01	2.63	19.81	0.00	0.00	0.05	0.80	0.01	5.04	0.09	0.33	0.00	0.87	0.11	0.00	1821.98	23.71	1831.25	15.61	0.58	0.51	1828	6.5	0 Used
11242-068.1	178.41	80.21	0.45	11.59	0.00	0.00	0.09	0.15	0.01	0.60	0.01	0.08	0.00	0.61	0.06	0.00	470.00	5.89	503.64	36.70	6.93	0.07	471	2.9	0 Used
11242-070.1	515.20	191.09	0.37	175.61	0.00	0.00	0.02	0.11	0.00	7.56	0.10	0.40	0.01	0.98	0.14	0.00	2154.29	24.43	2204.69	4.45	2.69	0.00	2203	2.1	0 Used
11242-071.1	554.77	166.79	0.30	16.17	0.00	0.00	0.31	0.09	0.00	0.23	0.01	0.03	0.00	0.49	0.05	0.00	215.12	2.55	134.56	50.34	-60.87	0.00	215	1.3	0 Used
11242-072.1	487.73	265.48	0.54	135.93	0.00	0.00	0.11	0.17	0.00	5.42	0.10	0.32	0.01	0.98	0.12	0.00	1811.37	28.26	1972.86	6.81	9.38	0.00	1965	3.1	100 Not-used
11242-074.1	250.57	209.81	0.84	12.79	0.00	0.00	0.62	0.28	0.01	0.42	0.01	0.06	0.00	0.49	0.05	0.00	372.23	6.30	225.59	70.72	-66.91	0.00	370	3.1	100 Not-used
11242-076.1	284.65	125.73	0.44	10.56	0.00	0.00	0.15	0.15	0.01	0.32	0.01	0.04	0.00	0.53	0.05	0.00	272.51	3.33	363.70	45.03	25.61	0.00	273	1.7	100 Not-used
11242-077.1	482.82	692.95	1.44	15.39	0.00	0.00	0.41	0.48	0.01	0.25	0.01	0.04	0.00	0.48	0.05	0.00	234.92	3.13	93.88	58.87	-152.99	0.00	234	1.6	100 Not-used
11242-078.1	246.11	79.30	0.32	9.74	0.00	0.00	0.90	0.08	0.01	0.30	0.01	0.05	0.00	0.32	0.05	0.00	290.24	4.11	46.60	103.83	-534.73	0.00	289	2.0	100 Not-used
11242-079.1	372.25	311.39	0.84	21.73	0.00	0.00	0.55	0.26	0.01	0.49	0.01	0.07	0.00	0.58	0.05	0.00	423.75	7.22	293.11	56.18	-46.06	0.00	421	3.6	100 Not-used
11242-081.1	781.95	411.07	0.53	23.32	0.00	0.00	0.09	0.18	0.01	0.25	0.00	0.03	0.00	0.71	0.05	0.00	219.98	2.70	260.67	28.36	15.88	0.00	220	1.3	0 Used
11242-082.1	120.16	89.61	0.75	13.96	0.00	0.00	0.04	0.22	0.01	1.26	0.02	0.14	0.00	0.74	0.07	0.00	817.61	10.41	859.07	25.89	5.14	0.00	823	4.9	0 Used
11242-083.1	256.19	148.78	0.58	18.17	0.00	0.00	0.59	0.17	0.01	0.65	0.02	0.08	0.00	0.54	0.06	0.00	511.47	8.21	484.77	58.08	-5.73	0.36	511	4.1	0 Used
11242-084.1	239.61	247.59	1.03	14.15	0.00	0.00	-0.19	0.35	0.01	0.57	0.01	0.07	0.00	0.73	0.06	0.00	428.68	7.49	607.88	36.72	30.47	0.00	432	3.7	100 Not-used
11242-085.1	600.65	162.49	0.27	24.76	0.00	0.00	0.03	0.10	0.00	0.36	0.01	0.05	0.00	0.80	0.05	0.00	302.12	4.83	390.39	27.10	23.14	0.00	304	2.4	100 Not-used
11242-086.1	250.75	224.43	0.90	13.20	0.00	0.00	-0.08	0.30	0.01	0.46	0.01	0.06	0.00	0.63	0.05	0.00	383.33	4.67	396.52	34.90	3.43	0.46	384	2.3	0 Used
11242-090.1	344.97	292.62	0.85	12.44	0.00	0.00	0.21	0.29	0.01	0.31	0.01	0.04	0.00	0.56	0.05	0.00	265.19	3.59	325.04	46.44	18.80	0.01	265	1.8	0 Used
11242-091.1	262.67	156.04	0.59	112.18	0.00	0.00	0.17	0.17	0.00	11.08	0.21	0.50	0.01	0.98	0.16	0.00	2601.74	39.57	2472.56	6.42	-6.35	0.00	2476	3.3	100 Not-used
11242-092.1	338.68	292.25	0.86	30.65	0.00	0.00	0.35	0.29	0.01	0.91	0.02	0.11	0.00	0.75	0.06	0.00	645.77	11.03	706.48	34.16	9.03	0.00	651	5.3	100 Not-used
11242-093.1	335.05	264.53	0.79	12.96	0.00	0.00	0.44	0.25	0.01	0.32	0.01	0.05	0.00	0.41	0.05	0.00	284.01	3.47	246.73	63.40	-15.44	0.24	284	1.7	0 Used
11242-094.1	428.15	344.39	0.80	16.86	0.00	0.00	0.31	0.27	0.01	0.33	0.01	0.05	0.00	0.63	0.05	0.00	288.92	4.56	298.61	45.44	3.32	0.67	289	2.3	0 Used
11242-095.1	158.13	63.72	0.40	8.98	0.00	0.00	0.87	0.12	0.01	0.47	0.02	0.07	0.00	0.31	0.05	0.00	412.57	5.34	266.33	93.87	-56.69	0.00	412	2.7	0 Used
11242-096.1	248.54	57.01	0.23	10.55	0.00	0.00	0.84	0.09	0.01	0.33	0.02	0.05	0.00	0.30	0.05	0.00	311.07	5.75	135.03	141.28	-133.55	0.01	311	2.9	0 Used
11242-097.1	101.05	69.98	0.69	7.69	0.00	0.00	0.13	0.23	0.01	0.73	0.02	0.09	0.00	0.63	0.06	0.00	547.51	8.99	602.50	45.90	9.52	0.02	549	4.4	0 Used
11242-098.1	215.06	82.73	0.38	11.74	0.00	0.00	0.18	0.13	0.01	0.50	0.01	0.06	0.00	0.55	0.06	0.00	397.22	4.92	482.54	42.44	18.23	0.00	398	2.5	100 Not-used
11242-099.1	315.63	124.69	0.40	106.81	0.00	0.00	0.03	0.13	0.00	7.49	0.26	0.39	0.00	0.36	0.14	0.00	2141.09	22.97	2200.34	56.70	3.16	0.06	2149	10.7	0 Used
11242-101.1	116.18	98.79	0.85	8.35	0.00	0.00	0.13	0.29	0.01	0.68	0.02	0.08	0.00	0.64	0.06	0.00	517.70	8.62	558.00	45.92	7.52	0.09	519	4.2	0 Used
11242-102.1	139.58	49.97	0.36	6.38	0.00	0.00	0.52	0.10	0.01	0.37	0.02	0.05	0.00	0.31	0.05	0.00	334.11	4.42	220.38	95.55	-52.96	0.01	334	2.2	0 Used
11242-104.1	21.52	15.43	0.72	5.78	0.00	0.00	0.88	0.22	0.01	4.63	0.15	0.31	0.01	0.62	0.11	0.00	1753.65	31.68	1755.74	47.30	0.14	0.94	1754	13.2	0 Used
11242-105.1	215.41	176.01	0.82	8.76	0.00	0.00	0.36	0.29	0.01	0.34	0.01	0.05	0.00	0.46	0.05	0.00	298.02	4.41	323.65	65.53	8.10	0.44	298	2.2	0 Used

Analysis	U (ppm)	Th (ppm)	Th/U	206Pb* (ppm)	204Pb/206Pb	± 204Pb/206Pb	f(206)204	208*Pb/206*Pb	± 208Pb/206Pb	207*Pb/235U	±207Pb/235U	206*Pb/238U	±206Pb/238U	Corr Coeff	207*Pb/206*Pb	±207Pb/206Pb	206Pb/238U	±206Pb/238U	207Pb/206Pb	±207Pb/206Pb	Disc. (%)	Prob	Best age (Ma)	± (Ma)	Used in study
										Isotope Ratios							Model Age (Ma)								
Cape O'Brien Member, Bjorne Formation, Olenekian, 79.564, -83.317																									
11243-001.1	78.53	56.90	0.72	12.10	0.00	0.00	0.54	0.23	0.01	1.80	0.05	0.18	0.00	0.57	0.07	0.00	1063.23	14.31	1008.56	42.93	-5.88	0.01	1057.33	6.7	0 Used
11243-002.1	18.37	12.57	0.68	2.83	0.00	0.00	1.75	0.17	0.02	1.83	0.13	0.18	0.00	0.31	0.07	0.01	1063.20	21.72	1041.09	139.00	-2.30	0.75	1062.65	10.7	0 Used
11243-003.1	32.27	18.43	0.57	5.19	0.00	0.00	0.91	0.19	0.01	2.03	0.10	0.19	0.01	0.62	0.08	0.00	1105.37	29.47	1168.09	73.56	5.84	0.12	1113.36	13.8	0 Used
11243-004.1	78.27	61.20	0.78	20.15	0.00	0.00	0.23	0.23	0.01	4.32	0.08	0.30	0.00	0.82	0.10	0.00	1689.62	21.63	1706.17	18.51	1.10	0.24	1699.17	7.0	0 Used
11243-005.1	384.13	26.70	0.07	22.55	0.00	0.00	0.25	0.02	0.00	0.51	0.01	0.07	0.00	0.68	0.05	0.00	426.19	5.89	389.00	34.36	-9.88	0.03	425.01	2.9	0 Used
11243-006.1	80.23	57.98	0.72	4.74	0.00	0.00	1.10	0.22	0.03	0.50	0.03	0.07	0.00	0.24	0.05	0.00	428.78	6.20	320.00	139.91	-35.14	0.11	428.48	3.1	0 Used
11243-007.1	329.11	155.07	0.47	19.56	0.00	0.00	0.37	0.16	0.01	0.52	0.01	0.07	0.00	0.55	0.05	0.00	431.24	5.17	406.73	42.36	-6.23	0.25	430.86	2.6	0 Used
11243-008.1	147.32	52.66	0.36	31.88	0.00	0.00	0.18	0.10	0.00	3.23	0.06	0.25	0.00	0.74	0.09	0.00	1448.35	17.25	1488.10	23.13	2.98	0.01	1462.31	7.0	0 Used
11243-009.1	521.68	45.41	0.09	46.33	0.00	0.00	0.08	0.04	0.00	0.92	0.02	0.10	0.00	0.95	0.06	0.00	634.17	14.48	755.88	15.80	16.90	0.00	689.46	5.5	100 Not-used
11243-010.1	407.17	154.03	0.38	70.42	0.00	0.00	0.11	0.13	0.00	2.13	0.03	0.20	0.00	0.90	0.08	0.00	1182.53	14.96	1116.90	13.21	-6.43	0.00	1145.73	4.9	100 Not-used
11243-011.1	19.09	23.65	1.24	4.61	0.00	0.00	0.67	0.40	0.05	3.49	0.23	0.28	0.01	0.34	0.09	0.01	1596.56	32.60	1427.79	120.67	-13.35	0.00	1582.28	15.5	0 Used
11243-012.1	227.51	73.05	0.32	33.67	0.00	0.00	0.00	0.11	0.00	1.75	0.03	0.17	0.00	0.87	0.07	0.00	1024.71	12.00	1029.67	14.57	0.52	0.60	1026.71	4.6	0 Used
11243-013.1	292.35	90.25	0.31	44.21	0.00	0.00	0.27	0.11	0.00	1.77	0.03	0.18	0.00	0.81	0.07	0.00	1045.29	12.01	1015.31	18.27	-3.20	0.01	1036.08	5.0	0 Used
11243-014.1	184.80	50.71	0.27	29.48	0.00	0.00	0.09	0.09	0.00	1.99	0.03	0.19	0.00	0.83	0.08	0.00	1098.03	13.02	1136.86	17.02	3.71	0.00	1112.14	5.2	0 Used
11243-015.1	42.63	45.48	1.07	19.01	0.00	0.00	0.24	0.30	0.01	13.13	0.24	0.52	0.01	0.91	0.18	0.00	2695.16	36.43	2684.86	12.30	-0.47	0.59	2685.92	5.8	0 Used
11243-016.1	123.07	45.12	0.37	20.71	0.00	0.00	0.00	0.12	0.00	2.15	0.03	0.20	0.00	0.84	0.08	0.00	1153.04	14.21	1188.15	17.25	3.23	0.00	1167.08	5.5	0 Used
11243-017.1	51.37	34.90	0.68	8.00	0.00	0.00	0.60	0.20	0.01	1.84	0.06	0.18	0.00	0.52	0.07	0.00	1073.40	15.59	1027.76	52.88	-4.82	0.09	1069.49	7.4	0 Used
11243-018.1	487.90	1326.24	2.72	212.15	0.00	0.00	0.02	0.80	0.01	12.72	0.16	0.51	0.01	0.99	0.18	0.00	2640.38	26.16	2673.03	3.37	1.49	0.01	2672.51	1.6	0 Used
11243-020.1	415.69	104.51	0.25	56.75	0.00	0.00	0.09	0.08	0.00	1.55	0.02	0.16	0.00	0.88	0.07	0.00	950.82	10.77	950.08	13.51	-0.08	0.93	950.53	4.2	0 Used
11243-021.1	137.89	56.57	0.41	8.24	0.00	0.00	0.19	0.12	0.01	0.55	0.01	0.07	0.00	0.51	0.06	0.00	433.51	5.61	511.10	50.08	15.70	0.00	434.24	2.8	0 Used
11243-023.1	19.94	42.33	2.12	5.08	0.00	0.00	0.87	0.66	0.02	4.11	0.15	0.30	0.01	0.57	0.10	0.00	1672.83	31.68	1636.89	56.86	-2.49	0.27	1664.08	13.8	0 Used
11243-024.1	16.91	8.91	0.53	5.34	0.00	0.00	0.79	0.15	0.01	6.42	0.21	0.37	0.01	0.70	0.13	0.00	2016.69	38.99	2053.51	40.71	2.09	0.19	2034.17	14.2	0 Used
11243-025.1	98.28	51.22	0.52	21.63	0.00	0.00	0.20	0.16	0.01	3.27	0.06	0.26	0.00	0.81	0.09	0.00	1470.33	18.38	1481.59	19.51	0.85	0.40	1475.61	6.7	0 Used
11243-026.1	186.02	80.46	0.43	29.87	0.00	0.00	0.09	0.13	0.00	1.98	0.03	0.19	0.00	0.83	0.08	0.00	1104.84	13.07	1112.18	17.02	0.72	0.49	1107.56	5.2	0 Used
11243-027.1	121.22	123.11	1.02	50.19	0.00	0.00	0.08	0.30	0.00	11.25	0.16	0.48	0.01	0.95	0.17	0.00	2535.90	28.60	2550.91	7.79	0.71	0.31	2549.88	3.7	0 Used
11243-028.1	140.52	58.99	0.42	20.95	0.00	0.00	0.20	0.13	0.01	1.76	0.03	0.17	0.00	0.74	0.07	0.00	1031.62	12.66	1023.56	24.56	-0.85	0.56	1029.92	5.6	0 Used
11243-029.1	943.81	288.01	0.31	162.31	0.00	0.00	0.00	0.10	0.00	2.18	0.03	0.20	0.00	0.96	0.08	0.00	1176.38	12.73	1169.57	6.37	-0.64	0.34	1170.95	2.9	0 Used
11243-030.1	50.97	27.83	0.55	7.87	0.00	0.00	-0.20	0.21	0.01	2.01	0.05	0.18	0.00	0.65	0.08	0.00	1065.68	15.60	1219.02	36.56	13.64	0.00	1084.74	7.4	100 Not-used
11243-031.1	218.78	60.05	0.27	38.19	0.00	0.00	0.15	0.09	0.00	2.23	0.03	0.20	0.00	0.84	0.08	0.00	1192.61	13.85	1186.84	16.22	-0.53	0.59	1190.18	5.3	0 Used
11243-032.1	540.86	316.84	0.59	149.00	0.00	0.00	0.06	0.18	0.00	4.82	0.06	0.32	0.00	0.97	0.11	0.00	1793.24	20.24	1781.03	5.60	-0.79	0.25	1781.91	2.7	0 Used
11243-033.1	70.81	30.50	0.43	14.56	0.00	0.00	0.10	0.14	0.01	2.98	0.06	0.24	0.00	0.80	0.09	0.00	1383.86	18.75	1428.08	21.66	3.44	0.00	1402.58	7.1	0 Used
11243-034.1	120.46	104.54	0.87	60.25	0.00	0.00	0.15	0.25	0.00	17.23	0.24	0.58	0.01	0.96	0.21	0.00	2957.91	32.01	2941.05	6.08	-0.71	0.30	2941.64	3.0	0 Used
11243-035.1	94.49	71.20	0.75	25.38	0.00	0.00	0.25	0.24	0.01	4.56	0.08	0.31	0.00	0.84	0.11	0.00	1753.74	21.60	1727.34	16.72	-1.75	0.05	1737.24	6.6	0 Used
11243-036.1	387.99	139.08	0.36	83.01	0.00	0.00	0.11	0.11	0.00	3.10	0.04	0.25	0.00	0.93	0.09	0.00	1433.61	15.70	1429.79	9.38	-0.30	0.68	1430.80	4.0	0 Used
11243-037.1	88.83	111.66	1.26	18.11	0.00	0.00	0.47	0.37	0.01	2.81	0.06	0.24	0.00	0.70	0.09	0.00	1372.93	17.52	1333.02	27.95	-3.32	0.02	1361.39	7.4	0 Used
11243-038.1	328.09	97.40	0.30	19.79	0.00	0.00	0.19	0.09	0.00	0.53	0.01	0.07	0.00	0.62	0.05	0.00	437.51	5.23	397.08	34.89	-10.53	0.02	436.51	2.6	0 Used
11243-039.1	428.75	146.74	0.34	79.48	0.00	0.00	-0.01	0.11	0.00	2.46	0.03	0.22	0.00	0.94	0.08	0.00	1259.60	13.90	1261.90	8.90	0.20	0.78	1261.23	3.7	0 Used
11243-040.1	158.75	109.03	0.69	9.55	0.00	0.00	0.43	0.24	0.01	0.54	0.02	0.07	0.00	0.32	0.06	0.00	436.39	5.57	449.11	86.39	2.93	0.77	436.44	2.8	0 Used
11243-041.1	249.70	70.72	0.28	37.93	0.00	0.00	0.00	0.09	0.00	1.79	0.03	0.18	0.00	0.88	0.07	0.00	1049.75	12.13	1029.69	13.69	-2.11	0.03	1040.89	4.5	0 Used
11243-042.1	204.33	94.05	0.46	42.19	0.00	0.00	0.05	0.14	0.00	2.94	0.04	0.24	0.00	0.89	0.09	0.00	1388.64	15.91	1396.92	12.18	0.66	0.41	1393.86	4.8	0 Used
11243-043.1	422.87	215.58	0.51	74.31	0.00	0.00	0.05	0.16	0.00	2.29	0.03	0.20	0.00	0.92	0.08	0.00	1199.79	13.36	1226.03	10.22	2.35	0.00	1216.40	4.1	0 Used
11243-044.1	58.85	42.04	0.71	27.68	0.00	0.00	0.22	0.20	0.01	14.85	0.25	0.55	0.01	0.93	0.20	0.00	2814.59	35.20	2798.95	10.18	-0.69	0.39	2800.16	4.9	0 Used
11243-045.1	178.22	135.19	0.76	53.27	0.00	0.00	0.09	0.24	0.01	5.62	0.09	0.35	0.01	0.95	0.12	0.00	1924.99	25.40	1912.04	9.15	-0.78	0.34	1913.54	4.3	0 Used
11243-046.1	299.94	91.07	0.30	68.00	0.00	0.00	0.05	0.09	0.00	3.37	0.04	0.26	0.00	0.93	0.09	0.00	1509.96	16.64	1481.62	9.31	-2.15	0.00	1488.46	4.1	0 Used
11243-047.1	124.50	47.05	0.38	34.39	0.00	0.00	0.00	0.11	0.00	4.87	0.09	0.32	0.01	0.94	0.11	0.00	1797.43	25.81	1796.93	11.35	-0.03	0.97	1797.01	5.2	0 Used
11243-048.1	251.49	301.18	1.20	63.59	0.00	0.00	0.05	0.37	0.00	4.13	0.06	0.29	0.00	0.93	0.10	0.00	1663.31	18.40	1656.54	9.00	-0.46	0.51	1657.86	4.1	0 Used
11243-049.1	104.45	59.82	0.57	6.47	0.00	0.00	0.00	0.19	0.01	0.62	0.02	0.07	0.00	0.74	0.06	0.00	448.95	8.50	679.82	38.49	35.15	0.00	452.98	4.2	100 Not-used
11243-050.1	492.51	310.43	0.63	124.27	0.00	0.00	0.04	0.20	0.00	4.05	0.05	0.29	0.00	0.96	0.10	0.00	1660.23	17.64	1626.00	6.38	-2.39	0.00	1630.05	3.0	0 Used
11243-051.1	144.84	140.72	0.97	33.51	0.00	0.00	0.08	0.30	0.01	3.48	0.05	0.27	0.00	0.88	0.09	0.00	1537.42	17.99	1504.33	13.52	-2.47	0.00	1516.31	5.4	0 Used
11243-052.1	177.12	59.75	0.34	30.39	0.00	0.00	0.14	0.11	0.00	2.18	0.03	0.20	0.00	0.82	0.08	0.00	1173.86	13.86	1175.18	17.65	0.12	0.91	1174.37	5.5	0 Used
11243-053.1	326.37	59.55	0.18	69.89	0.00	0.00	0.15	0.06	0.00	3.29	0.19	0.25	0.00	0.35	0.10	0.01	1434.87	25.24	1543.14	100.09	7.82	0.04	1440.32	12.3	0 Used
11243-054.1	155.24	46.08	0.30	25.09	0.00	0.00	0.40	0.09	0.00	1.93	0.04	0.19	0.00	0.70	0.07	0.00	1111.16	13.40	1056.57	26.66	-5.63	0.00	1099.59	5.9	100 Not-used
11243-055.1	100.69	43.16	0.43	22.99	0.00	0.00	0.09	0.13	0.01	3.43	0.06	0.27	0.00	0.84	0.09	0.00	1519.66	18.73	1500.92	16.56	-1.40	0.14	1509.14	6.2	0 Used
11243-056.1	328.86	128.48	0.39	70.94	0.00	0.00	0.05	0.13	0.00	3.12	0.04	0.25	0.00	0.93	0.09	0.00	1444.17	15.99	1428.73	9.55	-1.21	0.10	1432.81	4.1	0 Used
11243-057.1	139.52	84.02	0.60	35.77	0.00	0.00	0.09	0.18	0.00	4.21	0.06	0.30	0.00	0.89	0.10	0.00	1683.52	19.72	1668.05	12.45	-1.05	0.19	1672.48	5.3	0 Used
11243-058.1	175.86	58.79	0.33	37.54	0.00	0.00	0.16	0.11	0.00	3.10	0.06	0.25	0.00	0.92	0.09	0.00	1430.69	23.28	1435.31	14.32	0.36	0.74	1434.05	6.1	0 Used
11243-059.1	280.83	95.53	0.34	45.04	0.00	0.00	0.16	0.11	0.00	1.96	0.03	0.19	0.00	0.85	0.08	0.00	1103.58	12.61	1093.65	15.42	-0.99	0.32	1099.59	4.9	0 Used
11243-060.1	221.11	150.84	0.68	12.92	0.00	0.00	0.41	0.22	0.01	0.51	0.01	0.07	0.00	0.46	0.05	0.00	424.19	5.24	382.77	55.06	-11.18	0.13	423.76	2.6	0 Used
11243-061.1	90.31	40.14	0.44	14.42	0.00	0.00	0.48	0.14	0.01	1.87	0.04	0.19	0.00	0.60	0.07	0.00	1099.11	14.43	1013.76	38.66	-9.16	0.00	1087.51	6.7	100 Not-used
11243-062.1	99.88	37.97	0.38	19.91	0.00	0.00	0.23	0.12	0.00	2.80	0.05	0.23	0.00	0.75	0.09	0.00	1345.08	16.92	1370.67	23.54	2.07	0.08	1353.69	6.9	0 Used
11243-063.1	319.74	43.89	0.14	48.62	0.00	0.00	0.12	0.04	0.00	1.78	0.03	0.18	0.00	0.87	0.07	0.00	1050.59	12.16	1009.59	14.72	-4.40	0.00	1033.79	4.7	0 Used
11243-064.1	150.26	148.84	0.99	36.37	0.00	0.00	0.15	0.31	0.01	3.95	0.06	0.28	0.00	0.88	0.10	0.00	1600.28	18.62	1655.27	13.15	3.75	0.00	1637.12	5.4	0 Used
11243-065.1	51.30	10.30	0.20	14.05	0.00	0.00	0.40	0.05	0.00	4.77	0.10	0.32	0.01	0.77	0.11	0.00	1784.12	24.62	1775.08	23.96	-0.58	0.60	1779.47	8.6	0 Used
11243-067.1	353.27	106.35	0.30	46.97	0.00	0.00	0.15	0.09	0.00	1.49	0.02	0.15	0.00	0.84	0.07	0.00	927.62	10.76	923.53	16.27	-0.48	0.68	926.37	4.5	0 Used
11243-068.1	120.67	83.61	0.69	30.10	0.00	0.00	0.18	0.22	0.01	4.02	0.06	0.29	0.00	0.86	0.10	0.00	1643.27	19.52	1632.76	14.94	-0.73	0.39	1636.64	5.9	0 Used
11243-069.1	261.65	130.94	0.50	40.78	0.00	0.00	0.04	0.17	0.00	1.90	0.03	0.18	0.00	0.88	0.08	0.00	1074.94	12.39	1090.29	13.78	1.53	0.10	1081.78	4.6	0 Used
11243-070.1	101.14	42.56	0.42	15.95	0.00	0.00	0.52	0.12	0.01	1.90	0.04	0.18	0.00	0.62	0.08	0.00	1086.64	13.82	1071.64	34.96	-1.52	0.42	1084.58	6.4	0 Used
11243-071.1	387.02	76.75	0.20	104.41	0.00	0.00	0.00	0.07	0.00	5.16	0.07	0.31	0.00	0.97	0.12	0.00	1760.73	18.86	1943.40	5.91	10.73	0.00	1929.12	2.6	100 Not-used
11243-072.1	75.94	52.69	0.69	22.02	0.00	0.00	0.36	0.21	0.01	5.36	0.09	0.34	0.00	0.83	0.12	0.00	1875.16	23.53	1883.81	17.43	0.53	0.55	1880.74	7.0	0 Used
11243-073.1	68.79	72.21	1.05	16.75	0.00	0.00	0.21	0.32	0.01	3.98	0.07	0.28	0.00	0.81	0.10	0.00	1608.66	20.93	1657.29	19.86	3.32	0.00	1634.13	7.2	0 Used
11243-074.1	77.76	38.18	0.49	11.36	0.00	0.00	0.23	0.16	0.01	1.76	0.04	0.17	0.00	0.66	0.07	0.00	1012.94	13.57	1068.46	33.54	5.61	0.00	1020.19	6.3	0 Used
11243-075.1	84.71	43.03	0.51	18.42	0.00	0.00	0.13	0.16	0.01	3.26	0.06	0.25	0.00	0.81	0.09	0.00	1455.02	18.44	1495.49	19.08	3.02	0.00	1474.44	6.7	0 Used
11243-076.1	234.90	89.89	0.38	13.79	0.00	0.00	0.46	0.13	0.01	0.49	0.01	0.07	0.00	0.46	0.05	0.00	426.27	5.20	306.20	55.67	-40.53	0.00	424.80	2.6	100 Not-used
11243-077.1	90.04	50.01	0.56	15.08	0.00	0.00	0.29	0.19	0.01	2.12	0.04	0.19	0.00	0.70	0.08	0.00	1148.15	14.81	1172.13	28.80	2.23	0.14	1153.05	6.6	0 Used
11243-078.1	14.81	12.99	0.88	2.25	0.00	0.00	3.30	0.27	0.03	1.47	0.19	0.18	0.00	0.19	0.06	0.01	1048.95	23.83	609.71	276.96	-78.13	0.00	1042.27	11.8	100 Not-used
11243-079.1	291.21	99.77	0.34	52.69	0.00	0.00	0.05	0.11	0.00	2.40	0.03	0.21	0.00	0.91	0.08	0.00	1232.18	13.88	1262.24	11.34	2.62	0.00	1250.24	4.4	0 Used
11243-080.1	34.94	13.50	0.39	8.67	0.00	0.00	0.81	0.10	0.01	3.91	0.11	0.29	0.01	0.62	0.10	0.00	1636.64	25.11	1589.98	41.18	-3.32	0.05	1623.60	10.6	0 Used
11243-081.1	137.22	51.08	0.37	19.75	0.00	0.00	0.25	0.11	0.00	1.70	0.03	0.17	0.00	0.72	0.07	0.00	998.59	12.25	1024.92	26.06	2.77	0.07	1003.21	5.6	0 Used
11243-082.1	45.57	2.64	0.06	10.86	0.00	0.00	0.58	0.01	0.00	3.72	0.10	0.28	0.00	0.58	0.10	0.00	1578.03	22.48	1574.02	42.47	-0.29	0.87	1577.15	9.9	0 Used
11243-083.1	59.80	25.01	0.42	28.09	0.00	0.00	0.12	0.12	0.00	15.75	0.25	0.55	0.01	0.94	0.21	0.00	2812.33	34.22	2896.42	8.71	3.58	0.00	2891.50	4.1	0 Used
11243-084.1	278.54	135.96	0.49	72.88	0.00	0.00	0.09	0.15	0.00	4.56	0.06	0.30	0.00	0.94	0.11	0.00	1714.07	18.73	1776.14	8.33	3.98	0.00	1766.22	3.7	0 Used
11243-085.1	82.92	63.67	0.77	12.94	0.00	0.00	0.29	0.26	0.01	1.85	0.03	0.18	0.00	0.66	0.07	0.00	1076.34	12.11	1035.18	27.97	-4.32	0.01	1069.54	5.5	0 Used
11243-086.1	133.99	84.60	0.63	7.98	0.00	0.00	0.21	0.22	0.01	0.55	0.01	0.07	0.00	0.51	0.06	0.00	432.03	4.80	499.64	42.87	13.99	0.00	432.69	2.4	0 Used
11243-087.1	70.04	55.15	0.79	28.19	0.00	0.00	0.11	0.24	0.00	10.55	0.14	0.47	0.01	0.93	0.16	0.00	2477.20	25.47	2489.36	8.24	0.59	0.36	2488.21	3.9	0 Used
11243-088.1	89.08	100.02	1.12	26.14	0.00	0.00	0.25	0.33	0.01	5.24	0.07	0.34	0.00	0.86	0.11	0.00	1894.61	19.70	1819.83	12.65	-4.74	0.00	1841.91	5.3	0 Used
11243-089.1	160.67	55.17	0.34	72.76	0.00	0.00	0.08	0.10	0.00	13.90	0.26	0.53	0.01	0.91	0.19	0.00	2729.57	37.74	2752.23	13.01	1.01	0.26	2749.85	6.1	0 Used
11243-090.1	489.46	280.75	0.57	28.69	0.00	0.00	0.03	0.20	0.01	0.53	0.01	0.07	0.00	0.81	0.06	0.00	425.58	6.75	478.41	25.95	11.41	0.00	428.44	3.3	100 Not-used
11243-091.1	217.99	137.98	0.63	29.09	0.00	0.00	0.18	0.19	0.01	1.51	0.03	0.16	0.00	0.78	0.07	0.00	931.01	14.66	937.96	27.47	0.80	0.66	932.54	6.5	0 Used
11243-092.1	123.61	58.57	0.47	57.50	0.00	0.00	0.10	0.14	0.00	14.40	0.26	0.54	0.01	0.97	0.19	0.00	2789.60	38.98	2767.30	7.65	-0.99	0.26	2768.14	3.8	0 Used
11243-093.1	164.15	114.77	0.70	41.05	0.00	0.00	0.20	0.21	0.01	4.01	0.08	0.29	0.00	0.88	0.10	0.00	1647.05	24.88	1622.29	16.85	-1.73	0.10	1630.10	7.0	0 Used
11243-094.1	90.40	91.71	1.01	25.23	0.00	0.00	0.07	0.30	0.01	5.24	0.11	0.32	0.01	0.88	0.12	0.00	1813.81	28.48	1910.76	17.06	5.82	0.00	1885.76	7.2	100 Not-used
11243-095.1	237.75	124.05	0.52	51.67	0.00	0.00	0.13	0.16	0.00	3.31	0.06	0.25	0.00	0.91	0.09	0.00	1454.02	21.87	1523.87	14.72	5.12	0.00	1502.45	6.1	100 Not-used
11243-096.1	70.67	34.47	0.49	15.62	0.00	0.00	0.27	0.14	0.01	3.30	0.08	0.26	0.00	0.76	0.09	0.00	1475.77	24.45	1491.15	30.39	1.15	0.43	1481.78	9.6	0 Used
11243-097.1	492.21	186.57	0.38	96.20	0.00	0.00	0.05	0.12	0.00	2.68	0.05	0.23	0.00	0.96	0.09	0.00	1321.48	19.43	1325.00	8.88	0.29	0.74	1324.39	4.0	0 Used
11243-098.1	47.62	24.47	0.51	8.68	0.00	0.00	0.48	0.15	0.01	2.39	0.08	0.21	0.00	0.58	0.08	0.00	1240.43	22.42	1240.46	54.95	0.00	1.00	1240.44	10.4	0 Used
11243-099.1	28.60	25.33	0.89	8.62	0.00	0.00	0.71	0.27	0.01	5.60	0.18	0.35	0.01	0.67	0.12	0.00	1938.15	36.93	1892.30	44.01	-2.81	0.11	1918.93	14.0	0 Used
11243-100.1	95.79	119.58	1.25	25.80	0.00	0.00	0.32	0.37	0.01	4.73	0.10	0.31	0.01	0.84	0.11	0.00	1758.06	27.66	1791.40	21.21	2.13	0.05	1779.07	8.4	0 Used
11243-101.1	65.41	176.03	2.69	29.08	0.00	0.00	0.15	0.79	0.01	13.46	0.27	0.52	0.01	0.93	0.19	0.00	2689.04	41.24	2730.11	12.36	1.84	0.06	2726.79	5.8	0 Used
11243-103.1	700.38	65.96	0.09	327.55	0.00	0.00	0.02	0.03	0.00	14.88	0.24	0.54	0.01	0.99	0.20	0.00	2802.02	36.91	2811.57	3.16	0.42	0.61	2811.50	1.6	0 Used
11243-103.2	227.69	82.11	0.36	142.47	0.00	0.00	0.05	0.10	0.00	33.89	0.58	0.73	0.01	0.98	0.34	0.00	3527.60	45.73	3651.18	4.59	4.39	0.00	3650.02	2.2	0 Used
11243-104.1	125.08	98.63	0.79	50.82	0.00	0.00	0.02	0.25	0.01	10.72	0.20	0.47	0.01	0.95	0.16	0.00	2496.80	36.32	2501.73	9.67	0.24	0.79	2501.40	4.7	0 Used
11243-105.1	115.29	46.34	0.40	7.30	0.00	0.00	1.06	0.10	0.01	0.59	0.04	0.07	0.00	0.26	0.06	0.00	458.56	7.96	520.71	145.16	12.36	0.40	458.71	4.0	0 Used
11243-106.1	281.70	46.98	0.17	38.01	0.00	0.00	0.19	0.05	0.00	1.53	0.03	0.16	0.00	0.81	0.07	0.00	940.63	14.66	947.81	24.95	0.81	0.62	942.46	6.3	0 Used
11243-107.1	55.17	13.09	0.24	7.82	0.00	0.00	1.14	0.06	0.01	1.50	0.08	0.16	0.00	0.36	0.07	0.00	984.36	18.03	802.52	107.22	-24.44	0.00	977.52	8.8	100 Not-used
11243-108.1	107.58	65.22	0.61	29.87	0.00	0.00	0.03	0.19	0.01	5.48	0.11	0.32	0.01	0.91	0.12	0.00	1805.76	27.52	2000.38	14.06	11.15	0.00	1963.07	6.0	100 Not-used
11243-109.1	223.54	110.61	0.49	13.35	0.00	0.00	0.47	0.17	0.01	0.53	0.03	0.07	0.00	0.31	0.06	0.00	433.41	7.13	433.85	114.64	0.11	0.99	433.41	3.6	0 Used
11243-110.1	26.91	0.84	0.03	7.63	0.00	0.00	0.33	0.02	0.01	5.41	0.16	0.33	0.01	0.73	0.12	0.00	1838.42	35.66	1941.29	37.06	6.09	0.00	1886.82	13.0	100 Not-used
11243-111.1	451.53	243.21	0.54	117.23	0.00	0.00	0.06	0.16	0.00	4.53	0.08	0.30	0.00	0.97	0.11	0.00	1702.46	24.39	1776.39	7.06	4.73	0.00	1771.01	3.3	0 Used
11243-112.1	30.22	46.43	1.54	10.62	0.00	0.00	0.65	0.43	0.04	8.53	0.24	0.41	0.01	0.78	0.15	0.00	2211.61	40.58	2359.04	29.35	7.38	0.00	2308.40	11.9	100 Not-used
11243-113.1	178.22	101.11	0.57	80.48	0.00	0.00	0.13	0.17	0.00	14.46	0.26	0.53	0.01	0.97	0.20	0.00	2723.39	37.99	2822.13	7.27	4.29	0.00	2818.83	3.4	0 Used
11243-114.1	73.05	25.71	0.35	14.40	0.00	0.00	0.46	0.11	0.01	2.67	0.08	0.23	0.00	0.65	0.08	0.00	1332.08	22.59	1299.06	42.95	-2.81	0.17	1324.72	9.9	0 Used
11243-116.1	40.36	34.92	0.87	7.89	0.00	0.00	0.12	0.28	0.01	2.79	0.08	0.23	0.00	0.69	0.09	0.00	1321.95	24.86	1400.68	42.27	6.22	0.00	1340.95	10.9	0 Used
11243-117.1	246.85	94.98	0.38	42.62	0.00	0.00	0.02	0.11	0.00	2.20	0.04	0.20	0.00	0.89	0.08	0.00	1180.71	18.21	1182.81	17.39	0.19	0.87	1181.81	6.3	0 Used
11243-118.1	162.26	42.98	0.26	22.48	0.00	0.00	0.20	0.09	0.01	1.58	0.04	0.16	0.00	0.74	0.07	0.00	964.05	15.45	959.08	32.28	-0.56	0.78	963.12	7.0	0 Used

Appendix C: Zircon Hf Isotopic Data

Table DR3: Zircon Hf isotopic data

Sample	176Hf/ 177Hf	± 2SE	176Hf/177Hf bias corrected	± 2SE	176Lu/ 177Hf	Detrital-zircon Age	1σ	176Yb/ 177Hf	176Hf/ 177Hf (t)	εHf	εHf(t)	±	Model Age (Ma)
Sverdrup Basin: this study													
11242-071_all	0.28231	3.80E-05	0.282352	3.80E-05	8.90E-04	215	3	0.00089	0.2823488	-15.30	-10.65	1.35	1490
11242-081_all	0.28260	3.60E-05	0.282640	3.60E-05	2.37E-03	220	3	0.00237	0.2826306	-5.11	-0.56	1.27	990
11242-014_all	0.28279	6.40E-05	0.282824	6.40E-05	2.20E-03	230	3	0.00220	0.2828149	1.39	6.18	2.26	661
11242-077_all	0.28274	5.80E-05	0.282781	5.80E-05	1.88E-03	234	3	0.00188	0.2827732	-0.13	4.79	2.05	734
11242-037.2	0.28262	5.36E-05	0.282659	5.36E-05	1.21E-03	247	4	0.00121	0.2826533	-4.46	0.83	1.90	942
11242-030.1	0.28262	3.53E-05	0.282658	3.53E-05	2.02E-03	255	3	0.00202	0.282648	-4.50	0.82	1.25	949
11270-092.2	0.28268	4.62E-05	0.282721	4.62E-05	1.34E-03	262	5	0.00134	0.2827143	-2.27	3.32	1.63	830
11242-052_all	0.28270	2.90E-05	0.282740	2.90E-05	1.25E-03	262	5	0.00125	0.2827343	-1.58	4.03	1.20	795
11242-090_all	0.32435	7.87E-04	0.282793	3.40E-05	1.35E-03	265	4	0.00135	0.2827863	0.28	5.95	1.20	702
11242-046.1	0.28241	4.69E-05	0.282450	4.69E-05	1.45E-03	267	6	0.00145	0.2824432	-11.83	-6.16	1.66	1308
11242-076.1	0.28227	3.18E-05	0.282314	3.18E-05	6.83E-04	273	3	0.00068	0.2823109	-16.64	-10.70	1.20	1541
11242-040.1	0.28242	2.72E-05	0.282463	2.72E-05	1.37E-03	276	3	0.00137	0.2824562	-11.38	-5.49	1.20	1283
11242-015.2	0.28227	5.37E-05	0.282307	5.37E-05	1.13E-03	277	8	0.00113	0.2823009	-16.91	-10.97	1.90	1557
11270-050.1	0.28212	8.10E-05	0.282162	8.10E-05	6.44E-03	279	5	0.00644	0.2821284	-22.03	-17.02	2.87	1862
11242-013.2	0.28263	3.25E-05	0.282673	3.25E-05	3.13E-03	284	3	0.00313	0.2826565	-3.96	1.77	1.15	926
11242-093.1	0.28256	4.40E-05	0.282601	4.40E-05	1.25E-03	284	3	0.00125	0.2825943	-6.51	-0.43	1.56	1036
11242-094.1	0.28248	6.22E-05	0.282524	6.22E-05	2.41E-03	289	5	0.00241	0.2825105	-9.25	-3.28	2.20	1183
11242-078.1	0.28242	3.84E-05	0.282457	3.84E-05	1.44E-03	289	4	0.00144	0.2824492	-11.60	-5.44	1.36	1291
11242-031_all	0.28208	3.60E-05	0.282123	3.60E-05	6.30E-04	290	4	0.00063	0.28212	-23.40	-17.07	1.28	1873
11242-105.1	0.28285	5.32E-05	0.282892	5.32E-05	1.05E-03	298	4	0.00105	0.2828858	3.77	10.20	1.88	516
11242-085.1	0.28257	5.87E-05	0.282605	5.87E-05	1.47E-03	304	5	0.00147	0.2825965	-6.37	0.10	2.08	1026
11242-096.1	0.28268	5.83E-05	0.282720	5.83E-05	2.05E-03	311	6	0.00205	0.2827078	-2.31	4.18	2.06	828
11242-38_all	0.28275	5.52E-05	0.282788	5.52E-05	3.10E-03	329	5	0.00310	0.282769	0.12	6.76	1.95	714
11242-102_all	0.28290	3.80E-05	0.282943	3.80E-05	2.79E-03	334	4	0.00279	0.282926	5.60	12.42	1.34	435
Siberian craton: Malitch et al., 2010													
844-1_7.1	0.282907	8.20E-05			2.99E-03	229		0.1347	0.282894		9	1.4	520
844-6_28.2	0.282777	4.40E-04			2.51E-03	233		0.0973	0.282766		4.5	7.8	700
844-1_22.1	0.283007	9.20E-05			2.23E-03	235		0.1111	0.282997		12.7	1.6	360
844-1_26.1	0.282983	6.40E-05			2.82E-03	237		0.1154	0.282971		11.8	1.1	400
844-1_24.1	0.282917	6.20E-05			1.70E-03	240		0.0787	0.282909		9.7	1.1	480
844-1_6.1	0.282956	6.80E-05			3.64E-03	242		0.1709	0.28294		10.8	1.2	450
844-6_33.1	0.283066	8.20E-05			2.25E-03	243		0.0877	0.283056		15	1.4	270
844-1_3.1	0.282832	6.40E-05			2.21E-03	245		0.0956	0.282822		6.7	1.1	620
844-1_12.1	0.282869	8.60E-05			3.61E-03	246		0.1676	0.282852		7.8	1.5	580
844-6_35.1	0.282856	9.80E-05			1.54E-03	248		0.0658	0.282849		7.8	1.7	570
844-1_14.1	0.282913	8.60E-05			1.90E-03	249		0.0868	0.282904		9.7	1.5	490
844-1_20.1	0.282962	1.62E-04			2.05E-03	249		0.0742	0.282952		11.5	2.9	420
844-10,11_40.1	0.282825	4.00E-05			2.71E-03	249		0.1209	0.282812		6.5	0.7	630
844-10,11_41.1	0.283078	1.06E-04			2.46E-03	249		0.1103	0.283067		15.5	1.9	260
844-1_2.1	0.283073	1.12E-04			3.23E-03	250		0.1898	0.283058		15.2	2	270
844-1_15.1	0.282992	7.60E-05			3.22E-03	253		0.1311	0.282977		12.4	1.3	390
844-6_36.1	0.283101	1.30E-04			3.37E-03	255		0.1308	0.283085		16.3	2.3	230
844-1_13.1	0.282887	9.80E-05			3.04E-03	255		0.1162	0.282873		8.8	1.7	550
844-1_16.1	0.282825	8.80E-05			3.10E-03	256		0.1132	0.28281		6.6	1.6	640
844-6_28.1	0.282767	2.20E-04			1.91E-03	257		0.0687	0.282758		4.8	3.9	710
844-1_10.2	0.282765	8.80E-05			2.33E-03	265		0.0697	0.282753		4.8	1.6	720
844-7_37.2	0.282692	2.40E-04			2.38E-03	270		0.0739	0.28268		2.3	4.2	820
844-1_10.1	0.28282	5.20E-05			2.14E-03	338		0.0766	0.282806		8.3	0.9	630
844-7_37.1	0.282796	1.92E-04			2.34E-03	355		0.0666	0.28278		7.7	3.4	670
Devonian Clastic Wedge: Anfinson et al. 2012b													
PArry_71b	0.282706	5.70E-05			1.08E-03	383		0.04551		-2.78	5.48	2.02	823
Parry1_82	0.282777	4.20E-05			5.08E-04	383		0.0189		-0.29	8.11	1.49	692
Parry1_58	0.28277	5.20E-05			1.05E-03	404		0.042		-0.52	8.2	1.84	705
Parry2_30	0.282683	6.90E-05			2.22E-04	422		0.00777		-3.6	5.75	2.44	842
Parry1_67	0.282625	6.70E-05			7.76E-04	427		0.03334		-5.64	3.65	2.36	951
Parry2_27	0.282536	8.30E-05			3.37E-04	428		0.0108		-8.8	0.64	2.95	1103
Parry1_38	0.282608	5.70E-05			1.06E-03	438		0.04342		-6.28	3.18	2.02	984
Parry1_47	0.282459	5.30E-05			9.52E-04	439		0.03785		-11.52	-2.02	1.88	1245
Parry2_109	0.282704	6.30E-05			4.21E-03	441		0.18129		-2.88	5.72	2.22	859
Parry2_10	0.282602	4.90E-05			6.80E-04	450		0.0283		-6.48	3.35	1.74	985
Parry1_29	0.282417	6.60E-05			7.04E-04	519		0.03261		-13.02	-1.7	2.34	1295
Parry2_63	0.282634	5.50E-05			2.75E-04	523		0.00984		-5.32	6.25	1.93	901
Parry1_96	0.282577	4.30E-05			1.64E-03	526		0.07175		-7.34	3.82	1.52	1025
Parry1_27	0.282589	5.20E-05			9.60E-04	527		0.04128		-6.94	4.48	1.86	993
Parry1_75	0.282572	5.20E-05			1.20E-03	530		0.05057		-7.52	3.88	1.84	1026

Parry2_71	0.282566	5.20E-05			6.03E-04	533	0.02607		-7.73	3.94	1.83	1025
Parry1_73	0.282624	6.10E-05			9.55E-04	535	0.03373		-5.69	5.9	2.16	929
Parry1_62	0.282469	4.00E-05			6.53E-04	536	0.02702		-11.18	0.53	1.41	1198
Parry1_48	0.282526	4.90E-05			4.72E-04	541	0.02019		-9.16	2.74	1.72	1092
Parry1_106	0.28256	4.90E-05			6.47E-04	541	0.02781		-7.95	3.88	1.72	1035
Parry1_64	0.282572	4.90E-05			1.31E-03	549	0.05332		-7.52	4.25	1.73	1023
Parry1_103	0.282604	3.80E-05			8.60E-04	651	0.03254		-6.41	7.76	1.34	932
Parry2_88	0.28271	5.00E-05			3.59E-04	651	0.01463		-2.66	11.73	1.75	734
Parry1_102	0.282756	4.20E-05			4.13E-04	653	0.01671		-1.01	13.4	1.49	652
Parry1_49	0.282532	6.20E-05			4.96E-04	656	0.02071		-8.94	5.5	2.2	1050
Parry1_51	0.282725	5.00E-05			4.92E-04	656	0.01963		-2.13	12.32	1.78	709
Parry2_104	0.28267	3.90E-05			3.22E-04	656	0.01236		-4.07	10.45	1.4	802
Parry3_10	0.282853	5.70E-05			1.99E-03	664	0.08354		2.42	16.39	2.01	512
Parry3_41(05)	0.282651	6.40E-05			7.34E-04	674	0.03263		-4.74	9.99	2.27	840
Parry3_13	0.282602	4.50E-05			1.80E-03	678	0.07718		-6.49	7.85	1.61	950
Parry2_24	0.282348	6.00E-05			7.00E-05	683	0.00371		-15.47	-0.25	2.12	1360
Parry1_69	0.282329	7.80E-05			4.87E-04	706	0.01909		-16.14	-0.61	2.75	1397
New Siberian Islands: Akinin et al, 2015												
ZH13_1	0.282658		0.2827	3.0E–05		613		0.282687	-4.5	10.2	1.1	723
ZH38_3	0.282712		0.282754	3.0E–05		622		0.28273	-2.6	12	1.1	723
ZH38_8	0.282667		0.282709	5.1E–05		629		0.282668	-4.2	9.9	1.8	688
ZH38_4	0.282735		0.282777	2.8E–05		631		0.282741	-1.8	12.5	1	728
ZH38_1	0.282716		0.282758	2.5E–05		633		0.282739	-2.4	12.5	0.9	733
ZH13_7	0.282634		0.282676	4.1E–05		634		0.282653	-5.3	9.5	1.5	703
ZH38_9	0.282721		0.282763	2.6E–05		637		0.282738	-2.3	12.6	0.9	733
ZH25_5	0.282494		0.282536	4.0E–05		638		0.28253	-10.3	5.2	1.4	708
ZH38_5	0.282697		0.282739	2.3E–05		662		0.282724	-3.1	12.6	0.8	738
ZH13_6	0.282618		0.28266	2.7E–05		724		0.282637	-5.9	11	1	728
ZH1_1	0.282225		0.282267	5.7E–05		931		0.282257	-19.8	2.2	2	678
ZH29_9	0.282086		0.282128	3.7E–05		1010		0.28212	-24.7	-0.9	1.3	713
ZH29_7	0.282047		0.282089	4.8E–05		1163		0.282079	-26.1	1.1	1.7	693
ZH29_8	0.282192		0.282234	2.9E–05		1169		0.282218	-21	6.2	1	728
ZH29_4	0.2821		0.282142	2.6E–05		1205		0.282126	-24.2	3.7	0.9	733
ZH25_9	0.281787		0.281829	4.4E–05		1431		0.281803	-35.3	-2.6	1.6	698
ZH1_7	0.281887		0.281929	4.1E–05		1511		0.281916	-31.8	3.3	1.5	703
ZH13_2	0.281575		0.281617	4.1E–05		1880		0.281585	-42.8	0	1.5	703

Converted from εNd	**Detrital-zircon Age**	**εNd(t)**	**εHf (Nd conversion)**	**Model Age (Ma)**
Arctic Alaska: Amato et al., 2009				
BM4	390	–0.38	2.4332	840
91G-43	565	–2.73	-0.7628	1360
92.2A-44	565	–2.16	0.0124	1870
92.2A-51	565	–0.98	1.6172	1100
KM4	565	–0.86	1.7804	1230
87SB69-1	565	–0.76	1.9164	1240
92.4A-132A	565	–0.35	2.474	1120
92.2A-38	565	–0.30	2.542	1160
90P12-5	565	–0.23	2.6372	1100
91G-42	565	0.3	3.358	990
92.2A-39c	565	1.43	4.8948	950
KM2b	680	–2.66	-0.6676	1370
CN1	680	–2.57	-0.5452	1470
KM1b	687	–3.95	-2.422	1390
BM1	870	0.14	3.1404	1380
Sverdrup Basin: Morris, 2013				
NM 2-5	276	-4.046	-2.5526	1716
NM 4-9	276	-5.87	-5.0332	2240
NM 5-13	276	-4.421	-3.0626	2052
NM 5-15	276	-3.991	-2.4778	1473
NM 10-4	276	-5.05	-3.918	1428
NM 11-7	276	-5.369	-4.3518	1692

Note: From this study, a Lu-Hf correction of 0.6222425 was used; each study area sorted by detrital-zircon age

Appendix D: Detrital-Zircon Spot Images

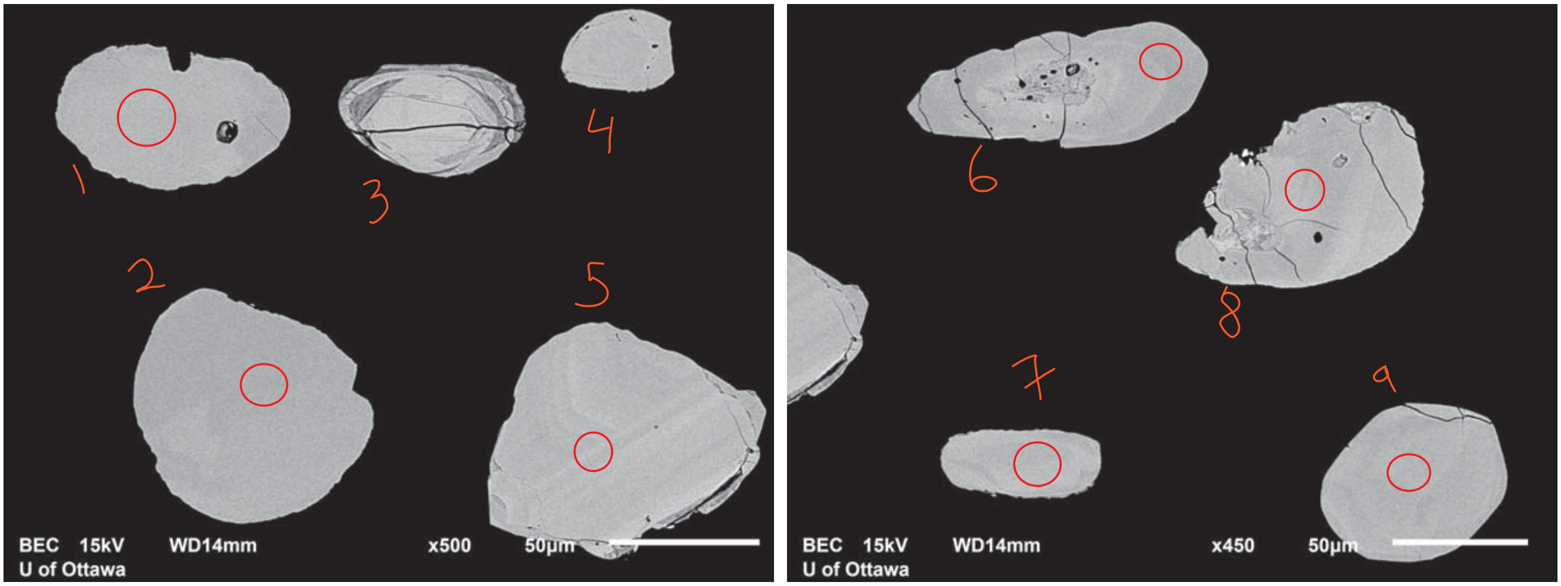

King Christian Formation (#11270)

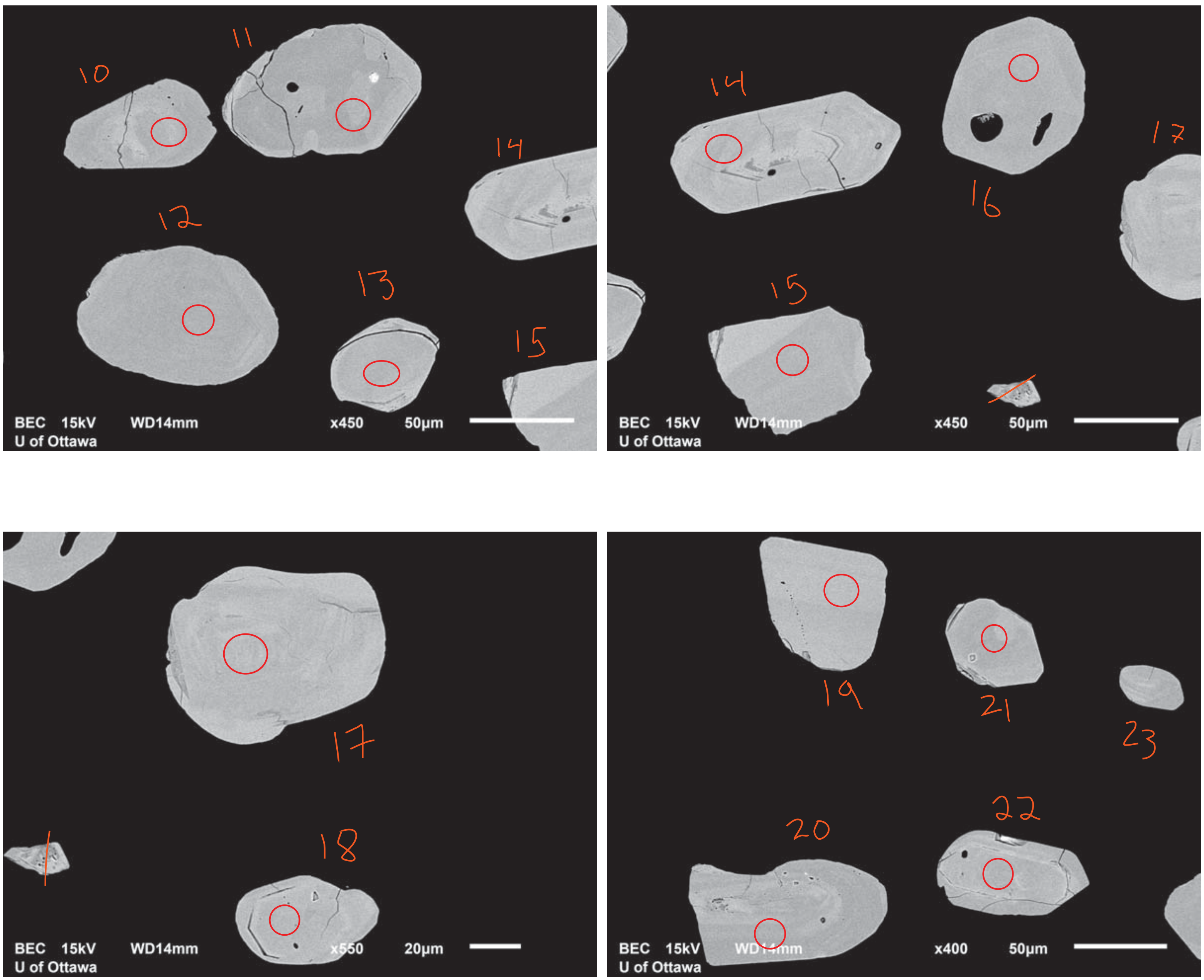

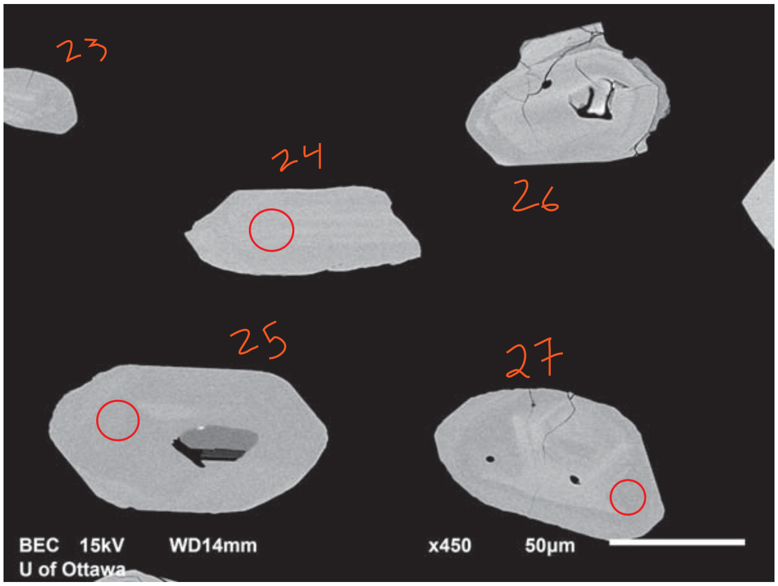
23
24
26
25
27
BEC 15kV WD14mm x450 50µm
U of Ottawa

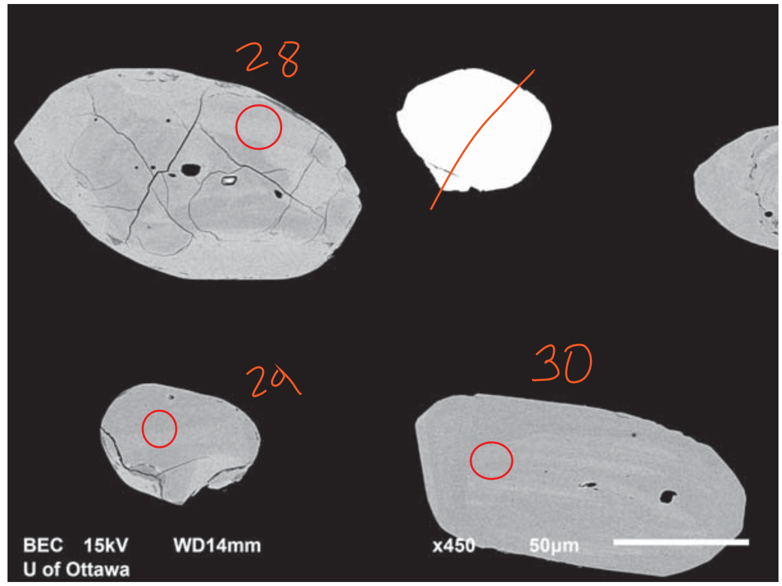
28
29
30
BEC 15kV WD14mm x450 50µm
U of Ottawa

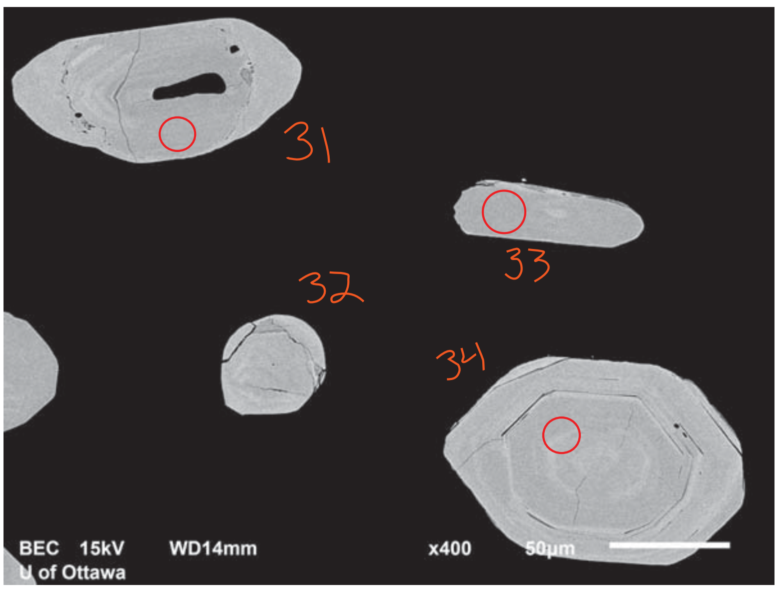
31
33
32
34
BEC 15kV WD14mm x400 50µm
U of Ottawa

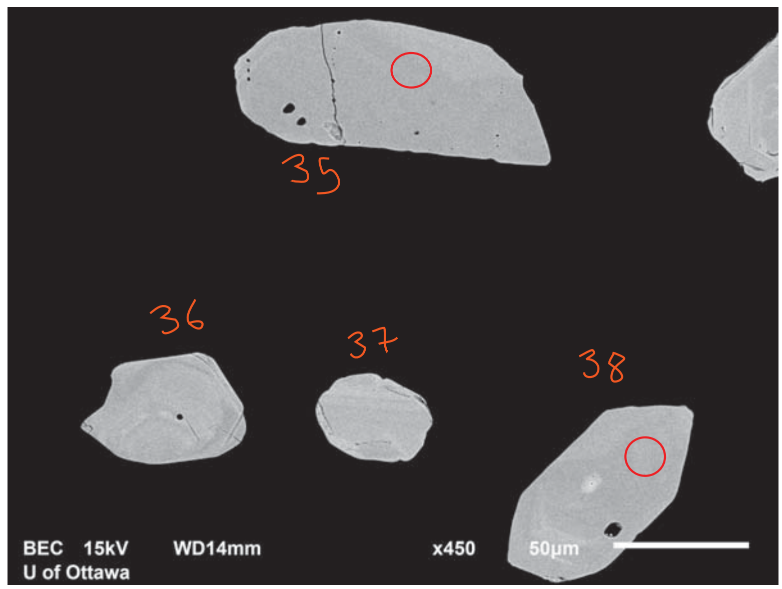
35
36
37
38
BEC 15kV WD14mm x450 50µm
U of Ottawa

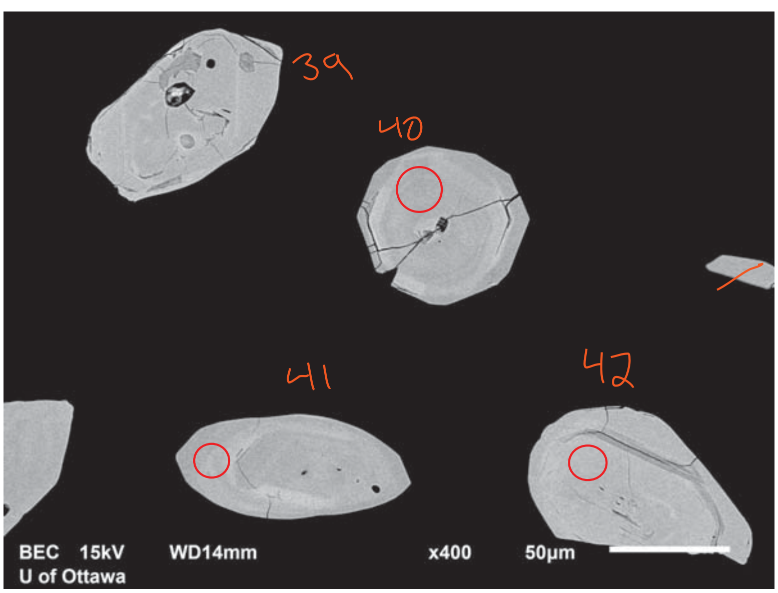
39
40
41
42
BEC 15kV WD14mm x400 50µm
U of Ottawa

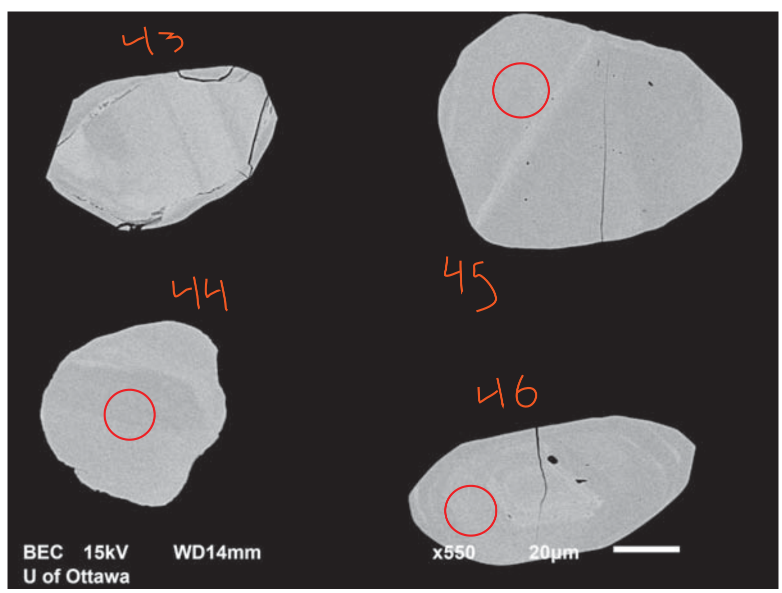
43
44
45
46
BEC 15kV WD14mm x550 20µm
U of Ottawa

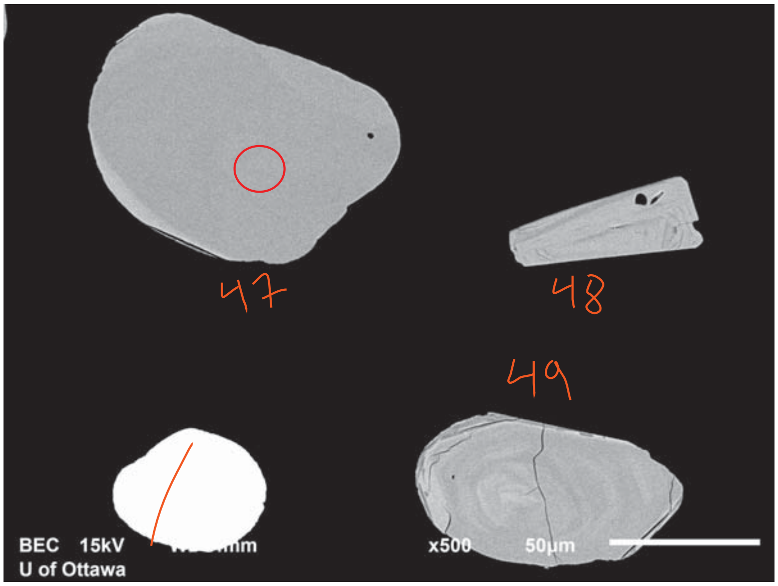
47
48
49
BEC 15kV
x500 50µm
U of Ottawa

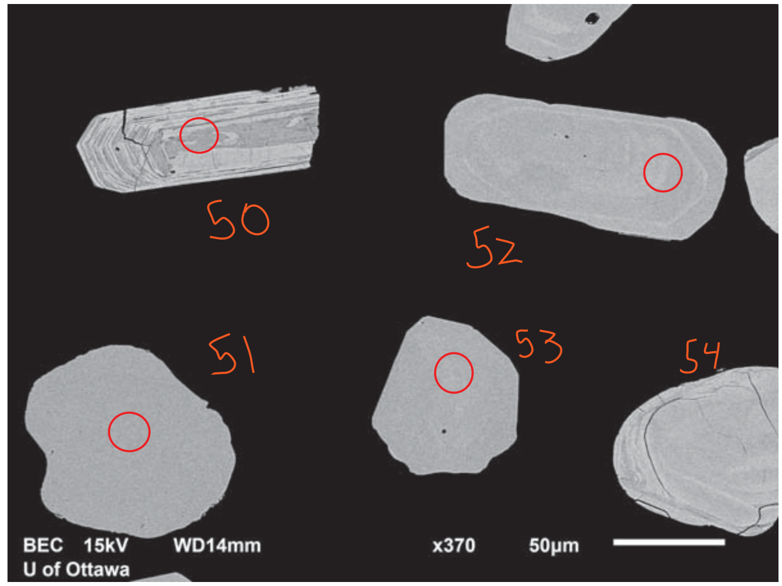
50
52
51
53
54
BEC 15kV WD14mm
x370 50µm
U of Ottawa

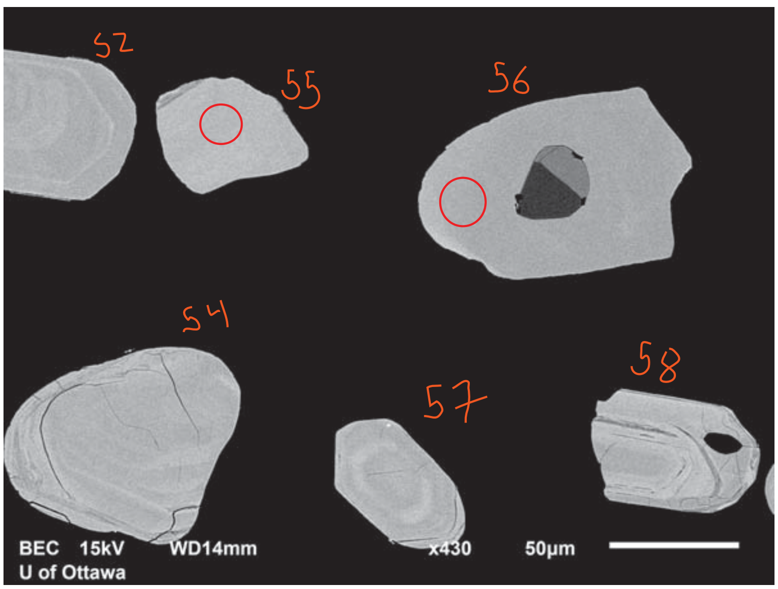
52
55
56
54
57
58
BEC 15kV WD14mm
x430 50µm
U of Ottawa

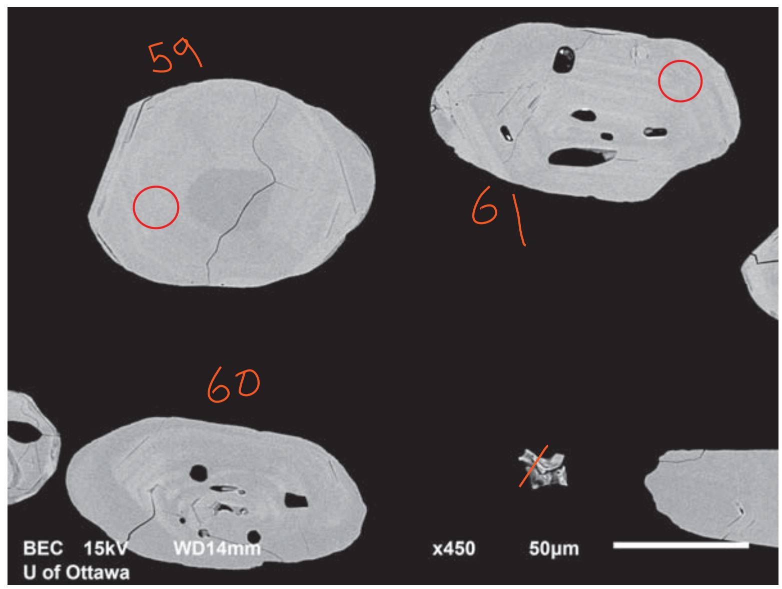
59
61
60
BEC 15kV WD14mm
x450 50µm
U of Ottawa

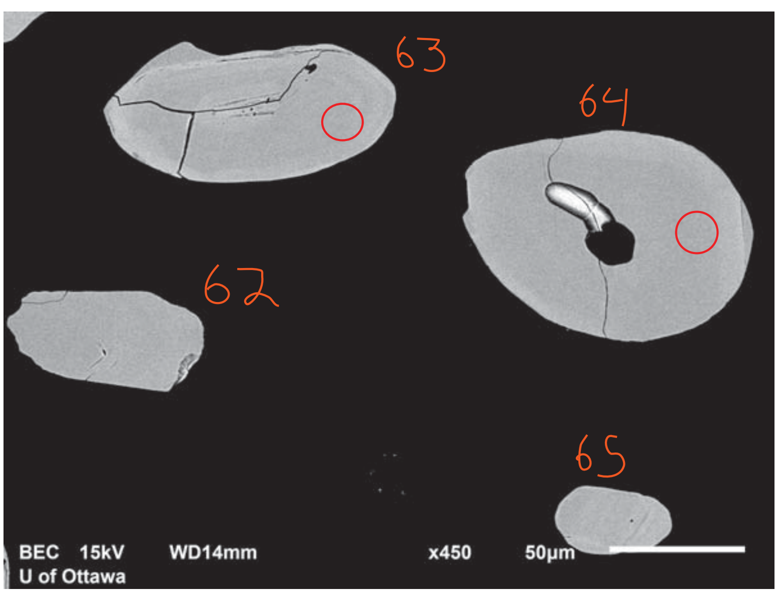
63
64
62
65
BEC 15kV WD14mm
x450 50µm
U of Ottawa

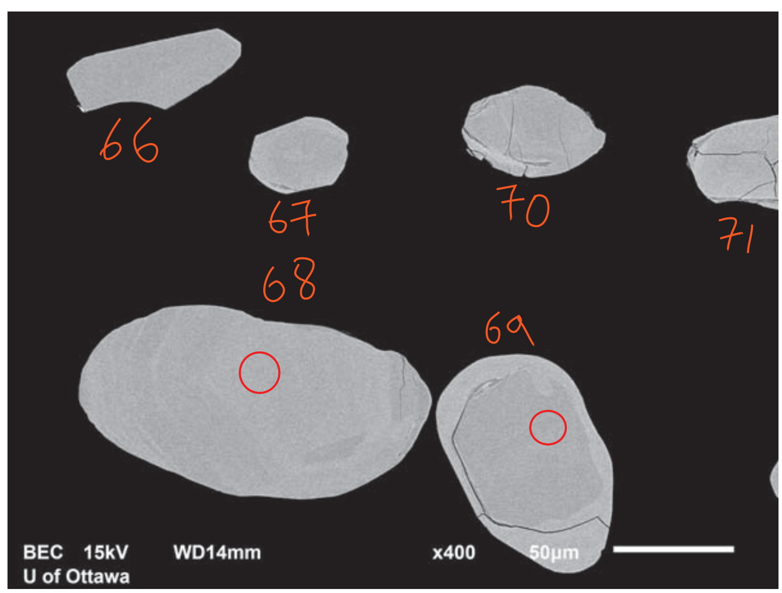
66
67
70
71
68
69
BEC 15kV WD14mm
x400 50µm
U of Ottawa

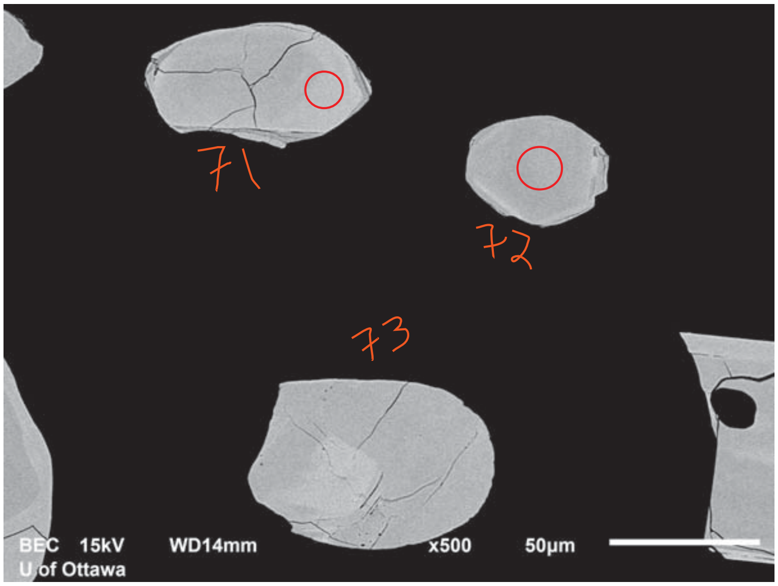
71
72
73
BEC 15kV WD14mm x500 50µm
U of Ottawa

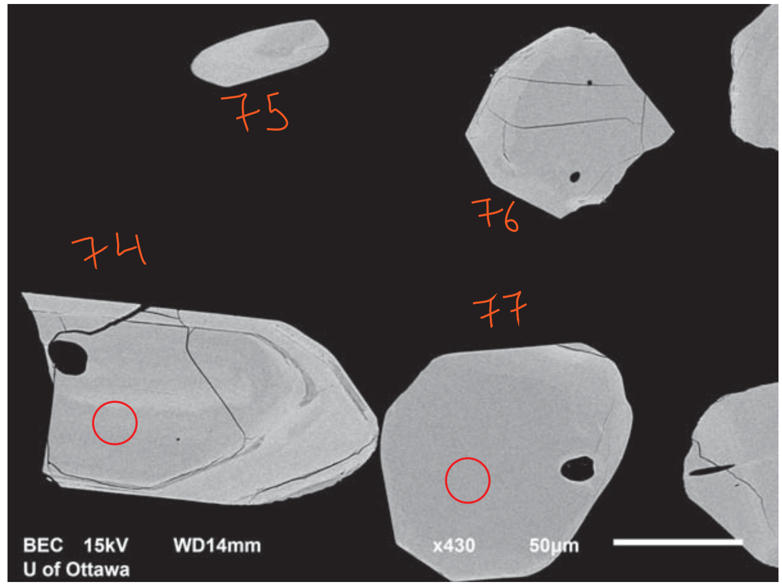
75
76
74
77
BEC 15kV WD14mm x430 50µm
U of Ottawa

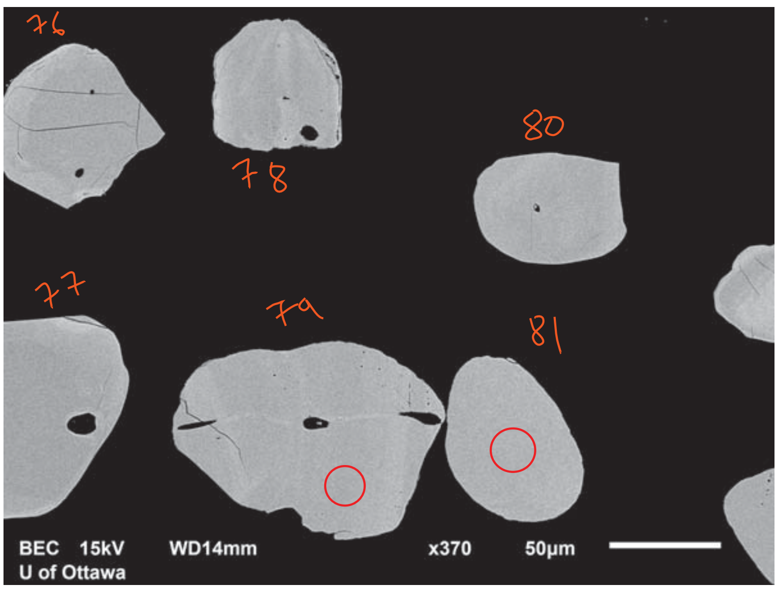
76
78
80
77
79
81
BEC 15kV WD14mm x370 50µm
U of Ottawa

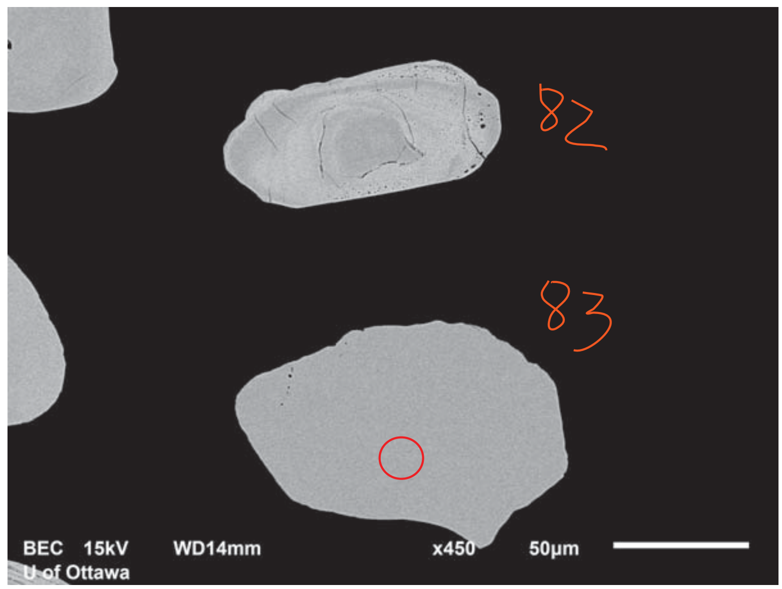
82
83
BEC 15kV WD14mm x450 50µm
U of Ottawa

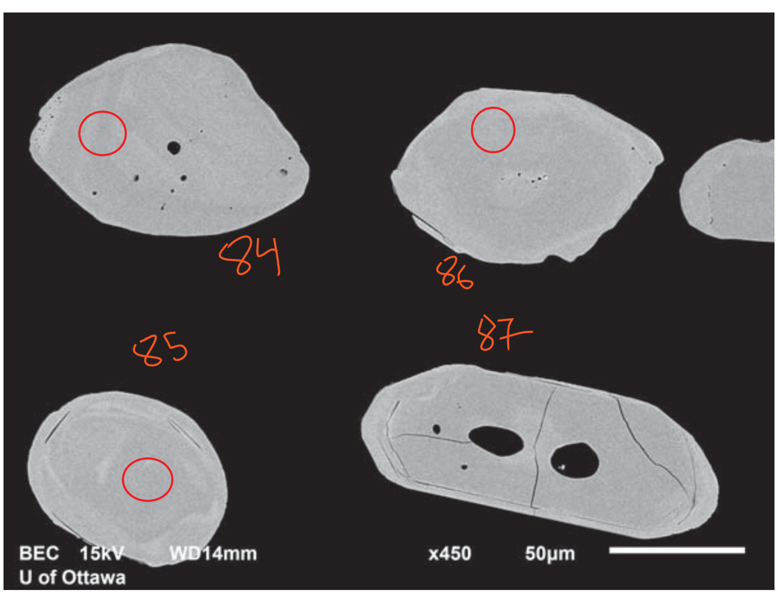
84
86
85
87
BEC 15kV WD14mm x450 50µm
U of Ottawa

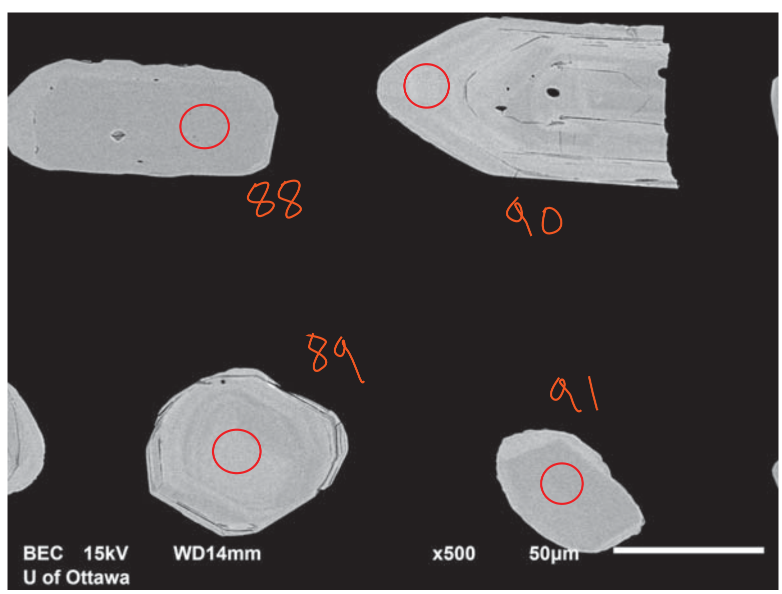
88
90
89
91
BEC 15kV WD14mm x500 50µm
U of Ottawa

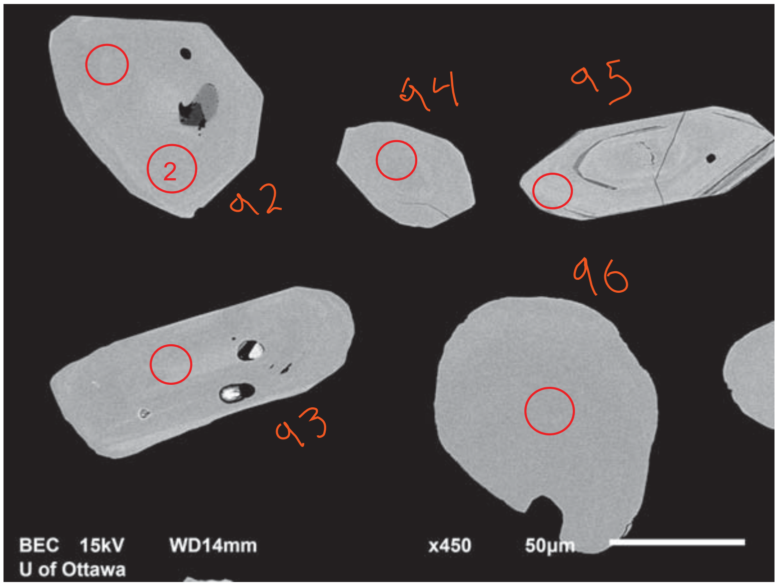

92
2
93
94
95
96
BEC 15kV WD14mm x450 50µm
U of Ottawa

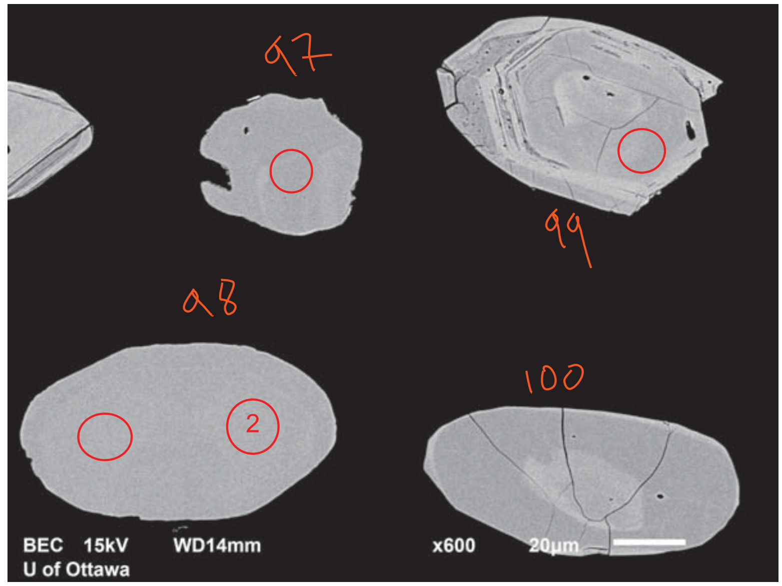

97
98
2
99
100
BEC 15kV WD14mm x600 20µm
U of Ottawa

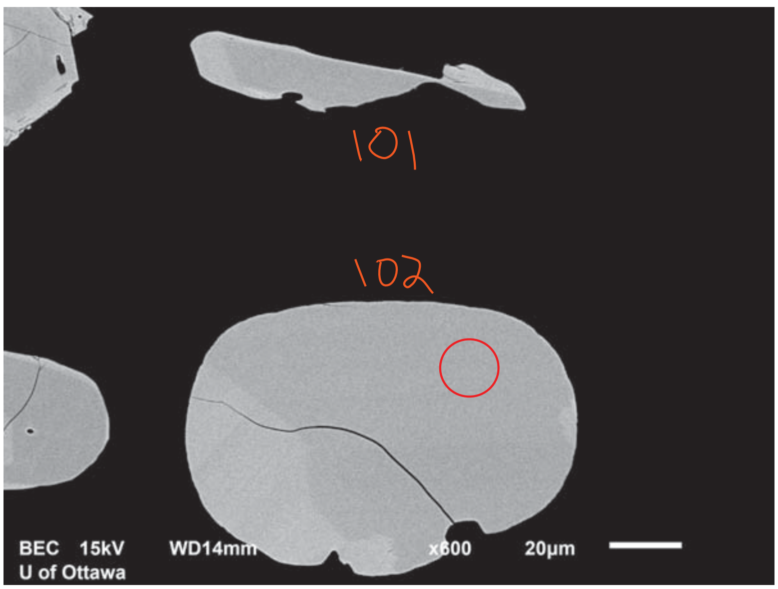

101
102
BEC 15kV WD14mm x600 20µm
U of Ottawa

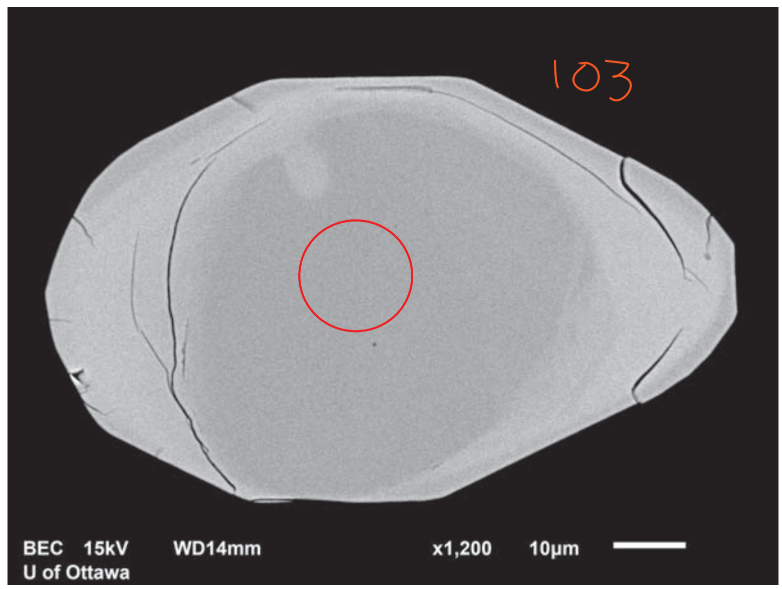

103
BEC 15kV WD14mm x1,200 10µm
U of Ottawa

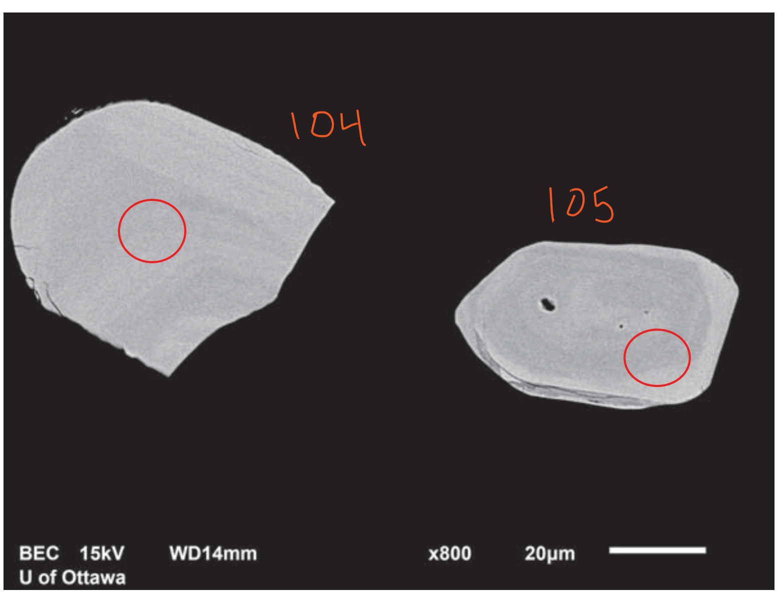

104
105
BEC 15kV WD14mm x800 20µm
U of Ottawa

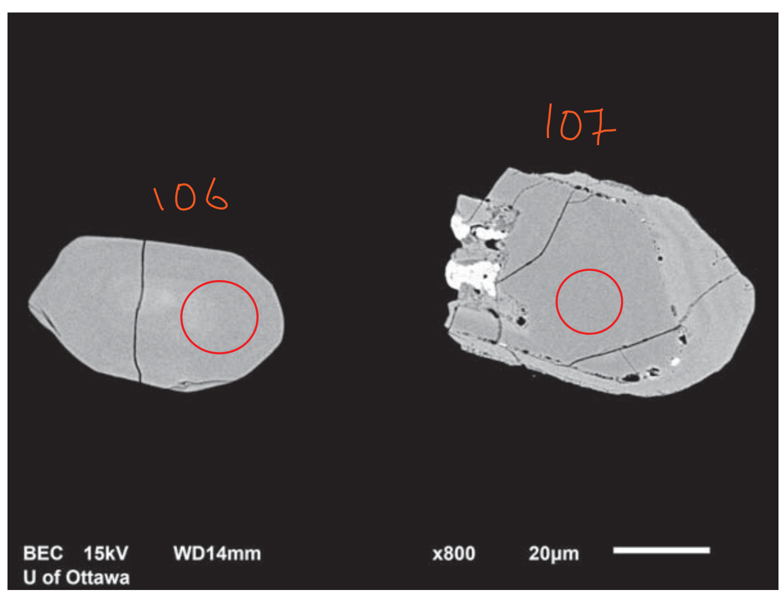

106
107
BEC 15kV WD14mm x800 20µm
U of Ottawa

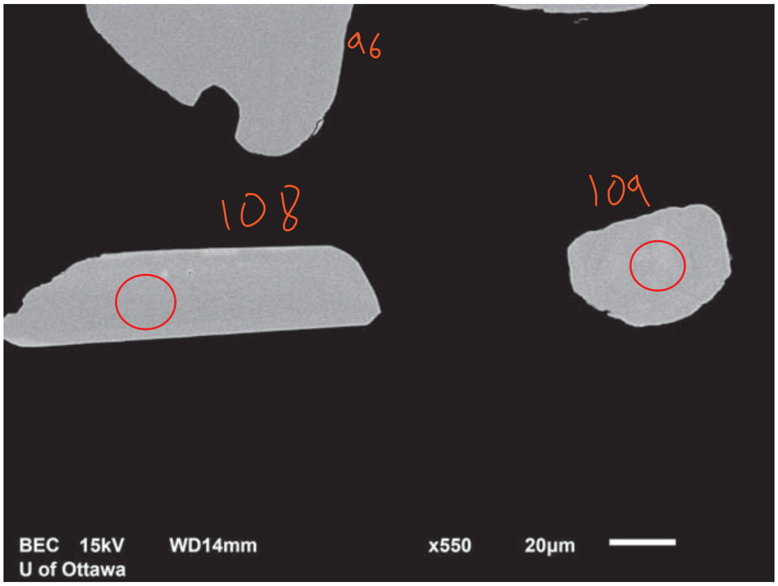
96
108
109
BEC 15kV WD14mm x550 20µm
U of Ottawa

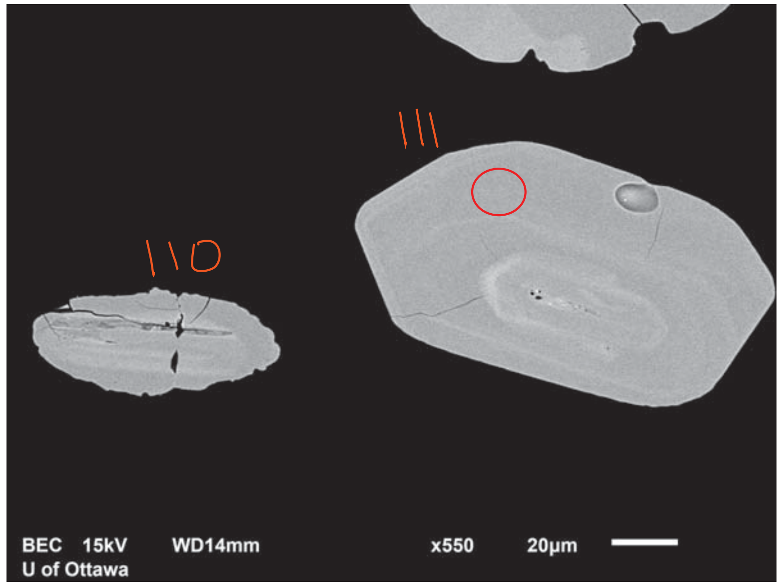
111
110
BEC 15kV WD14mm x550 20µm
U of Ottawa

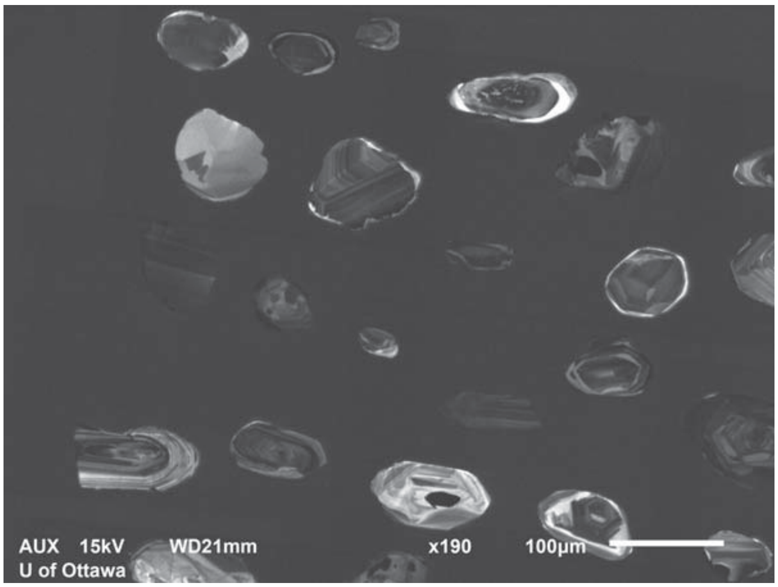
AUX 15kV WD21mm x190 100µm
U of Ottawa

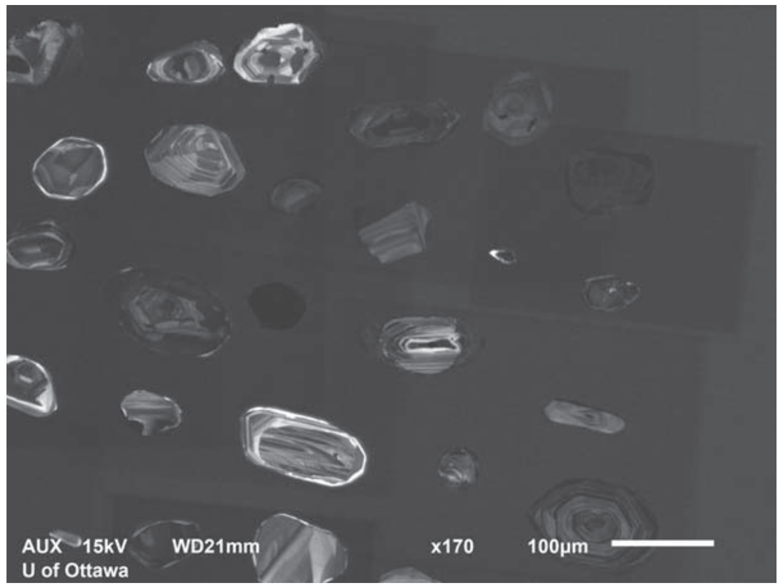
AUX 15kV WD21mm x170 100µm
U of Ottawa

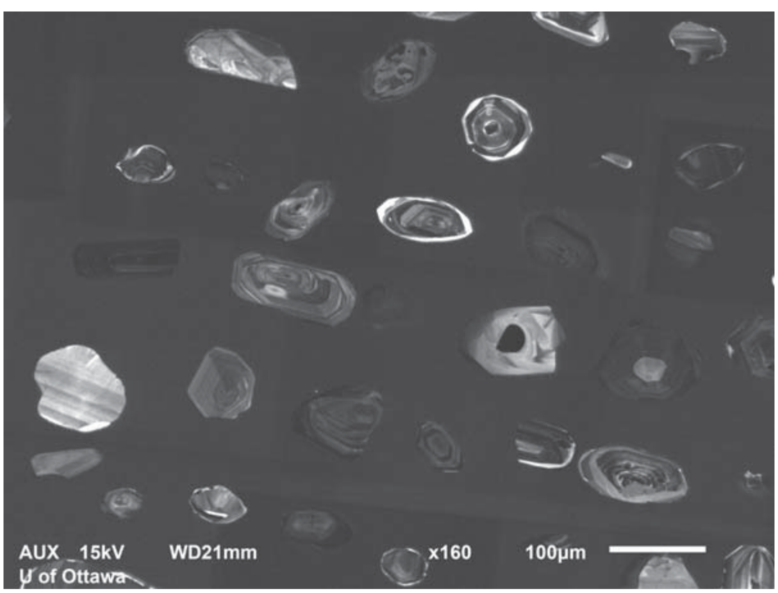
AUX 15kV WD21mm x160 100µm
U of Ottawa

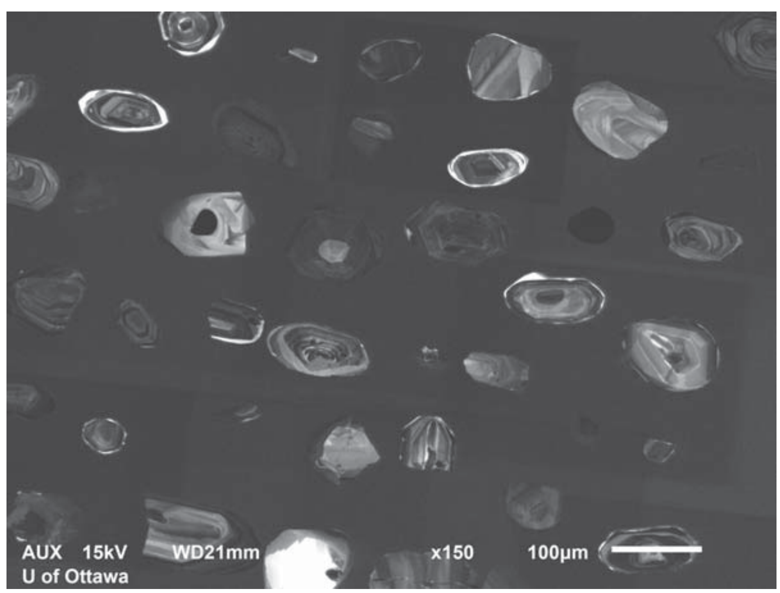
AUX 15kV WD21mm x150 100µm
U of Ottawa

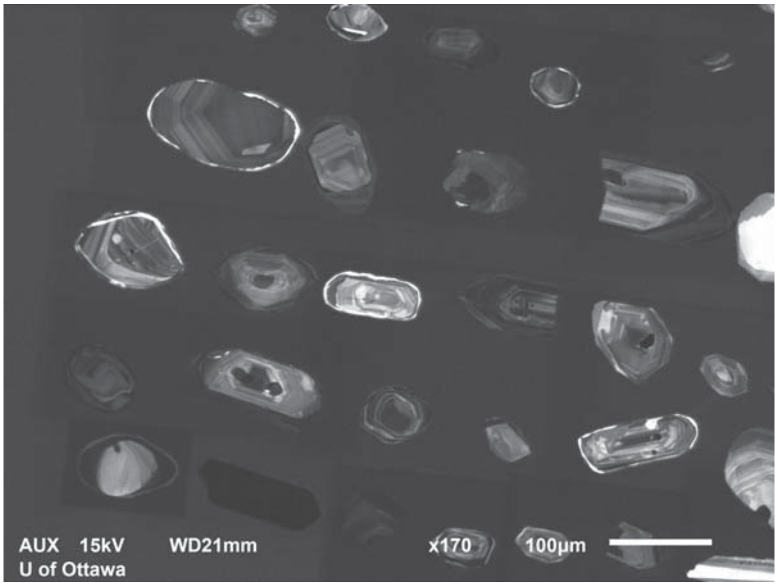
AUX 15kV WD21mm x170 100µm
U of Ottawa

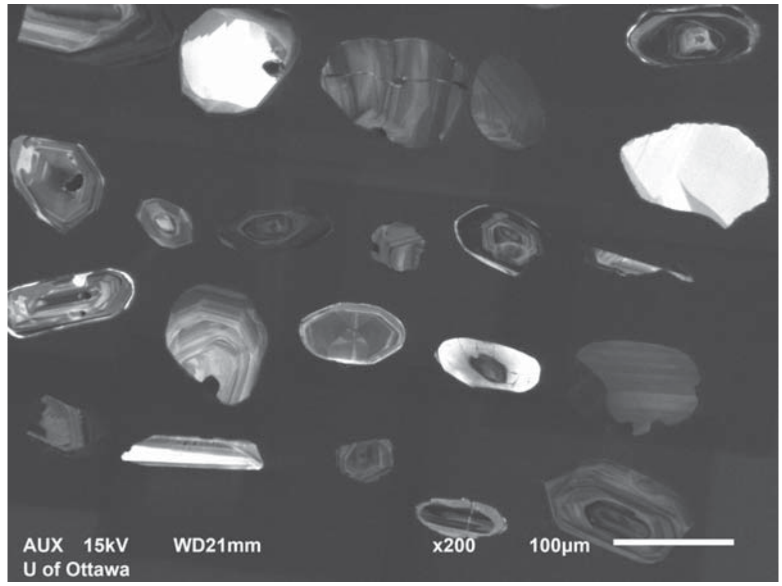
AUX 15kV WD21mm x200 100µm
U of Ottawa

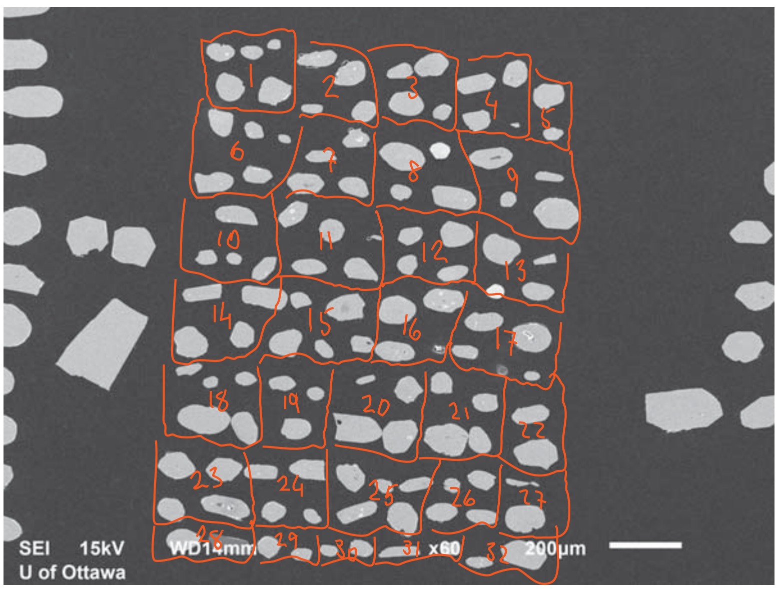
SEI 15kV WD14mm x60 200µm
U of Ottawa
1
2
3
4
5
6
7
8
9
10
11
12
13
14
15
16
17
18
19
20
21
22
23
24
25
26
27
28
29
30
31
32

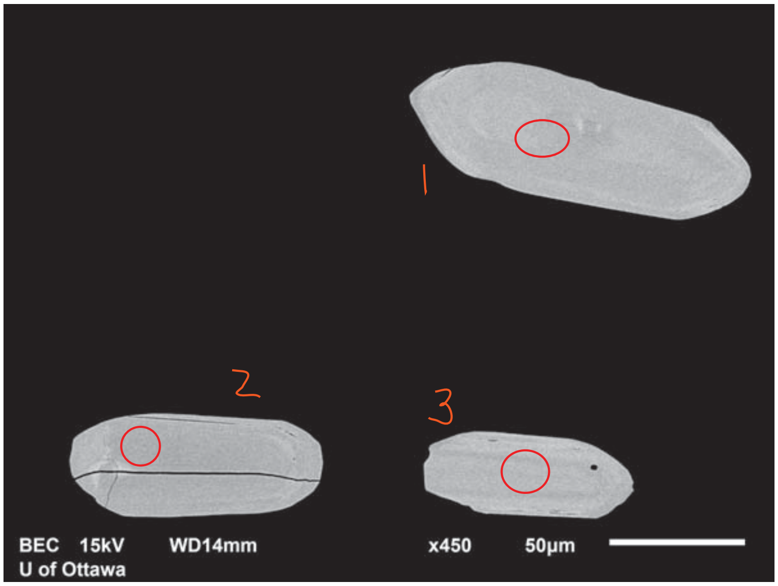

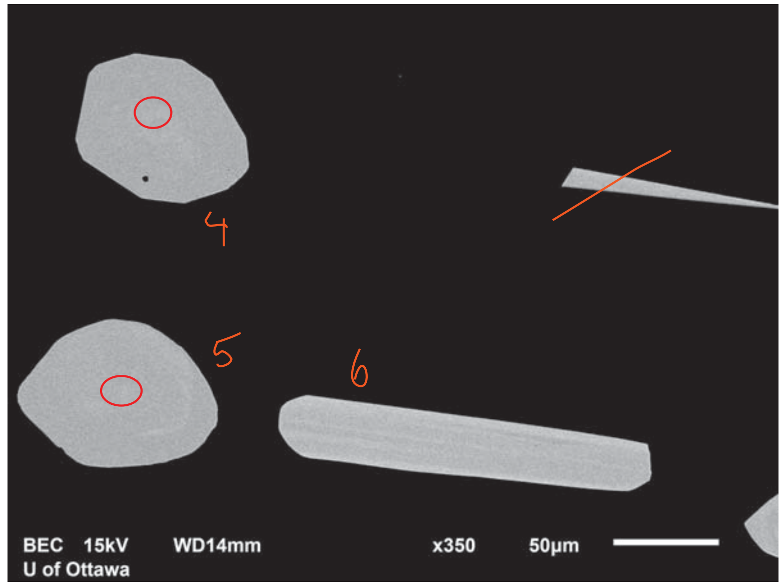

Lower Heiberg Formation, Romulus Member (#11242)

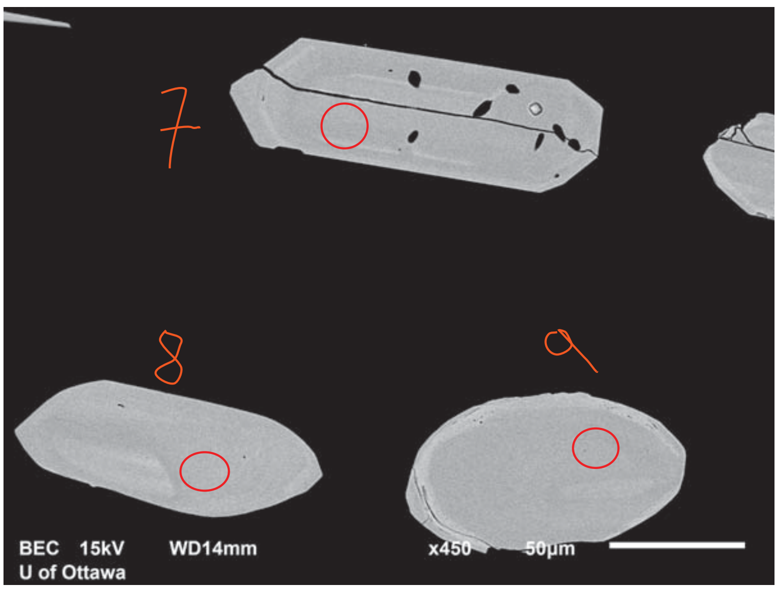

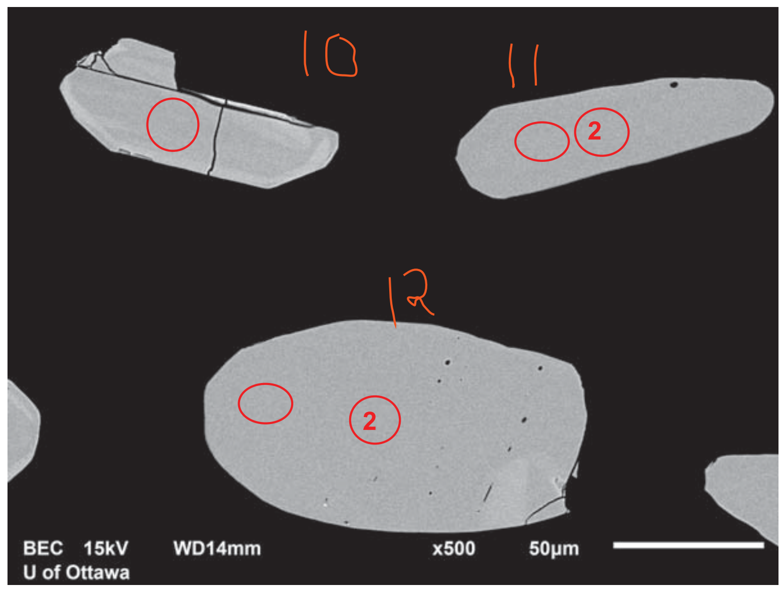

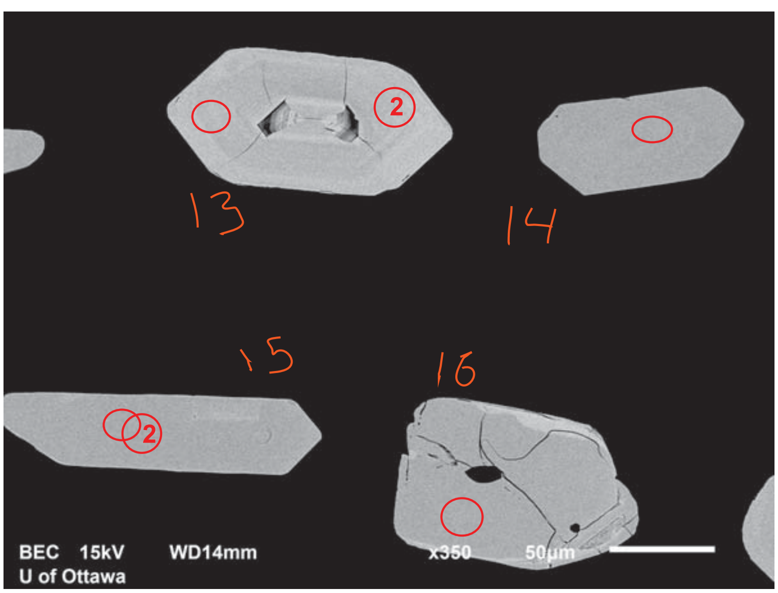

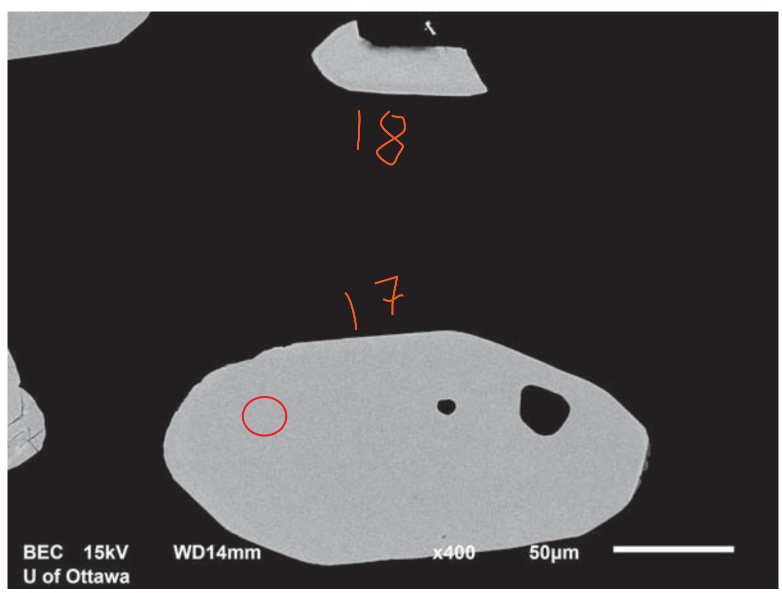

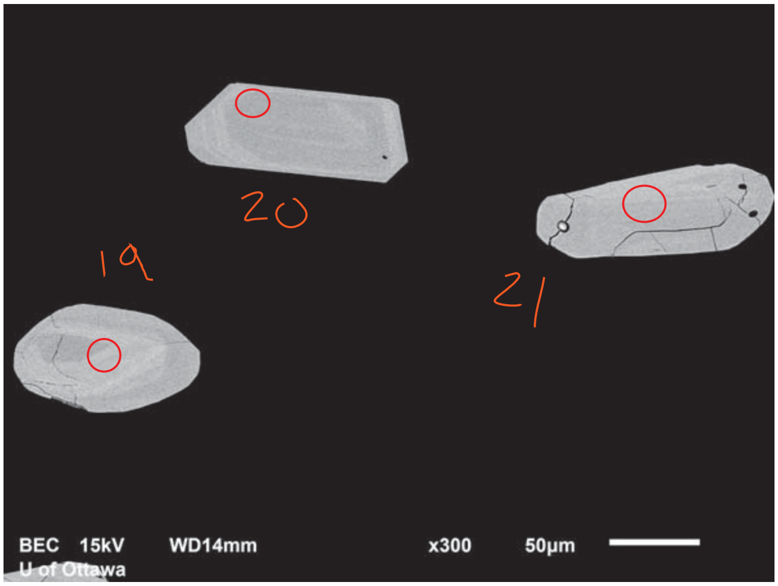
20
19
21
BEC 15kV WD14mm x300 50µm
U of Ottawa

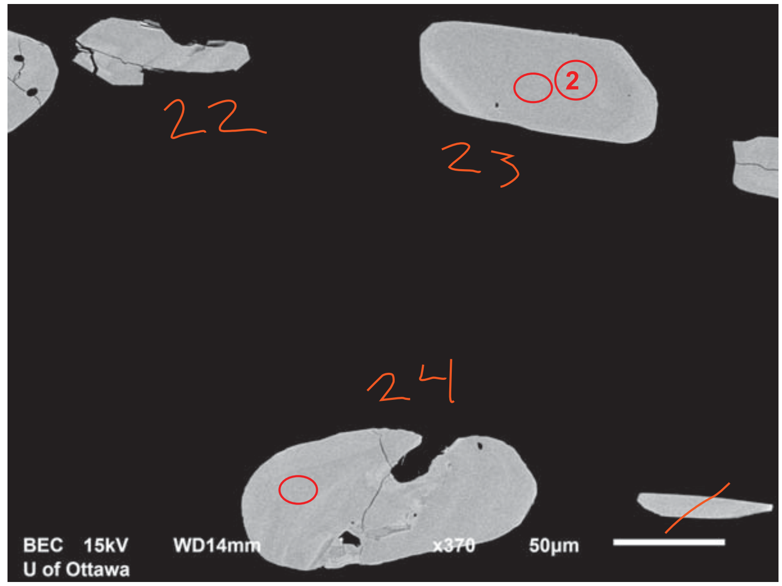
2
22
23
24
BEC 15kV WD14mm x370 50µm
U of Ottawa

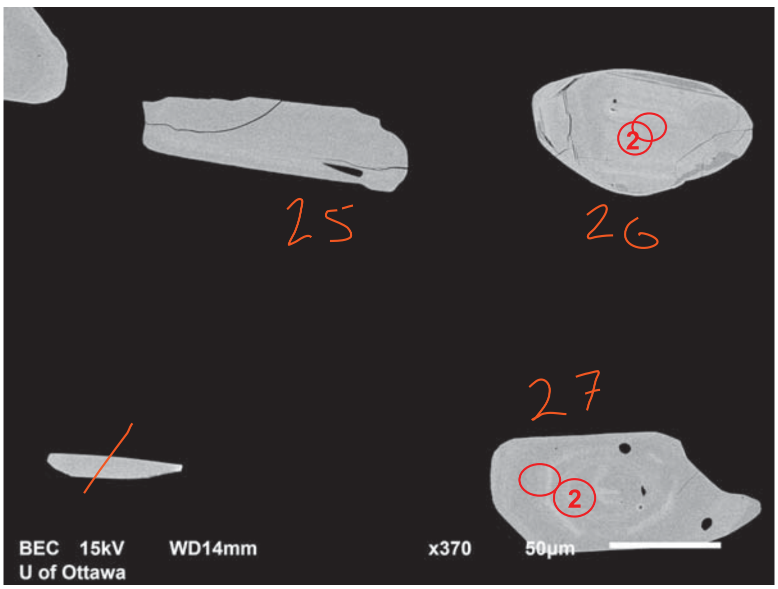
2
25
26
27
2
BEC 15kV WD14mm x370 50µm
U of Ottawa

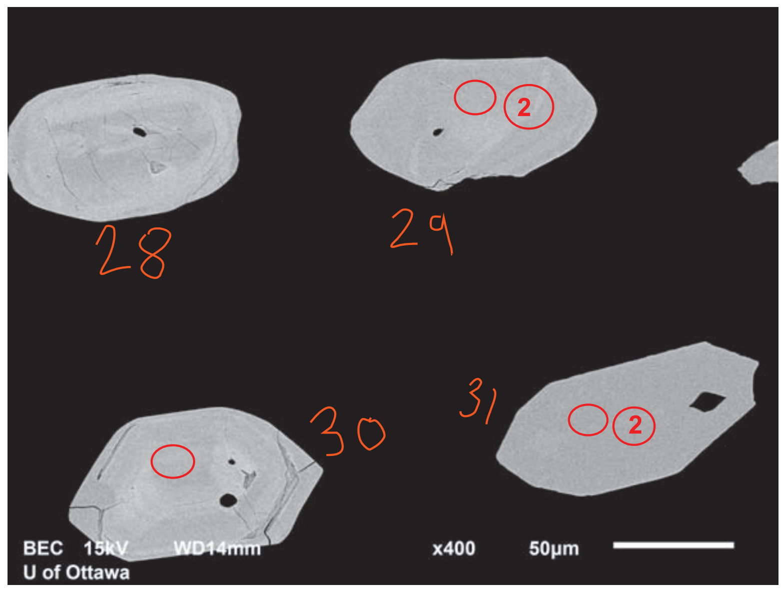
2
28
29
30
31
2
BEC 15kV WD14mm x400 50µm
U of Ottawa

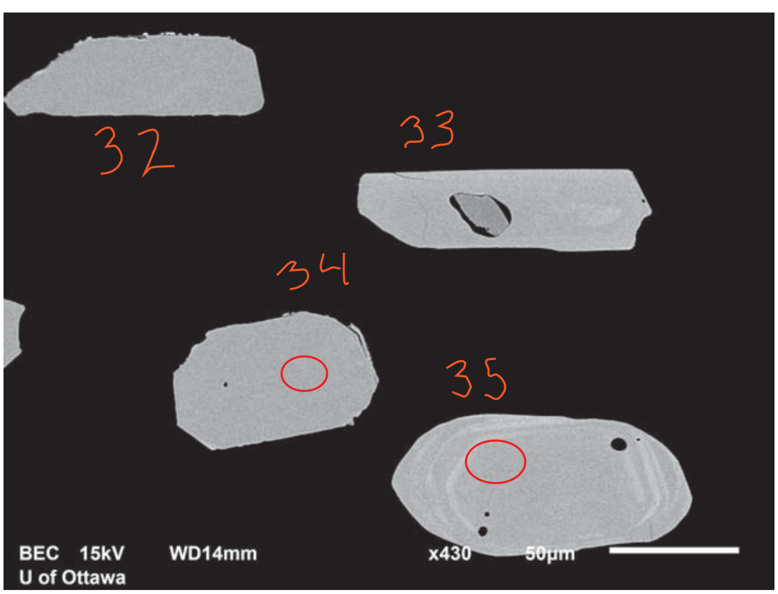
32
33
34
35
BEC 15kV WD14mm x430 50µm
U of Ottawa

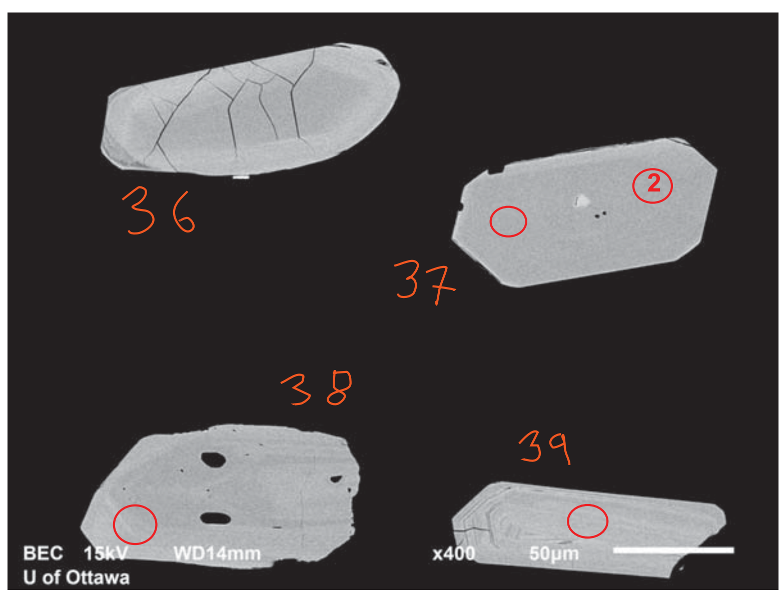
36
2
37
38
39
BEC 15kV WD14mm x400 50µm
U of Ottawa

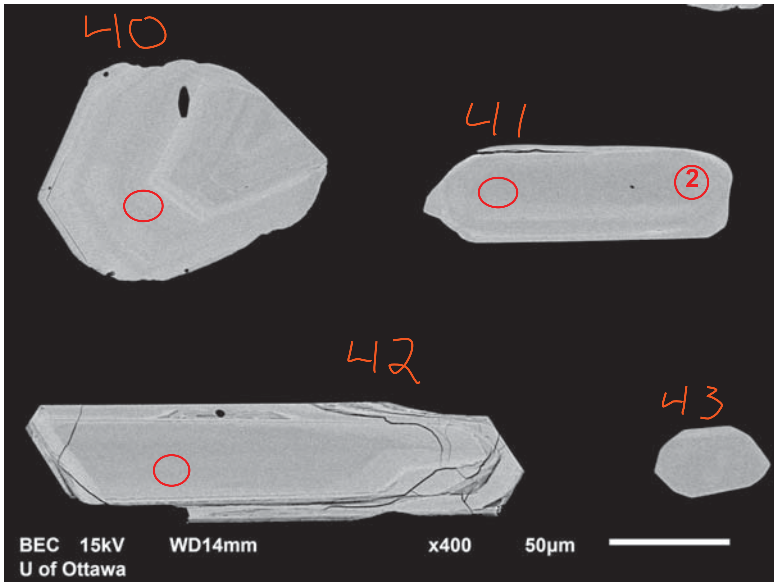
40
41
2
42
43
BEC 15kV WD14mm x400 50µm
U of Ottawa

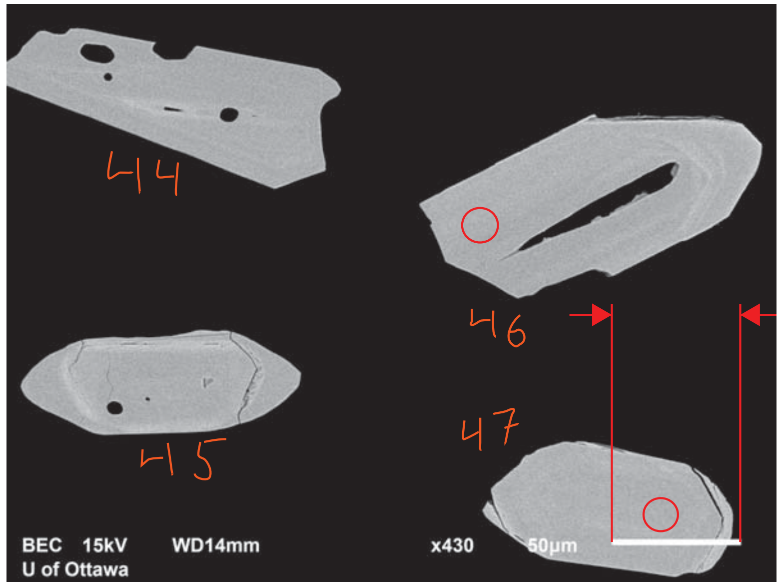
44
46
45
47
BEC 15kV WD14mm x430 50µm
U of Ottawa

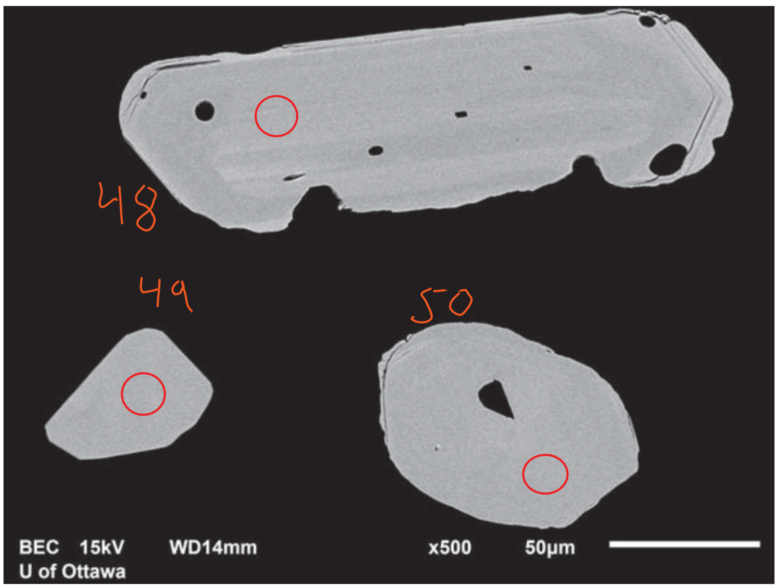
48
49
50
BEC 15kV WD14mm x500 50µm
U of Ottawa

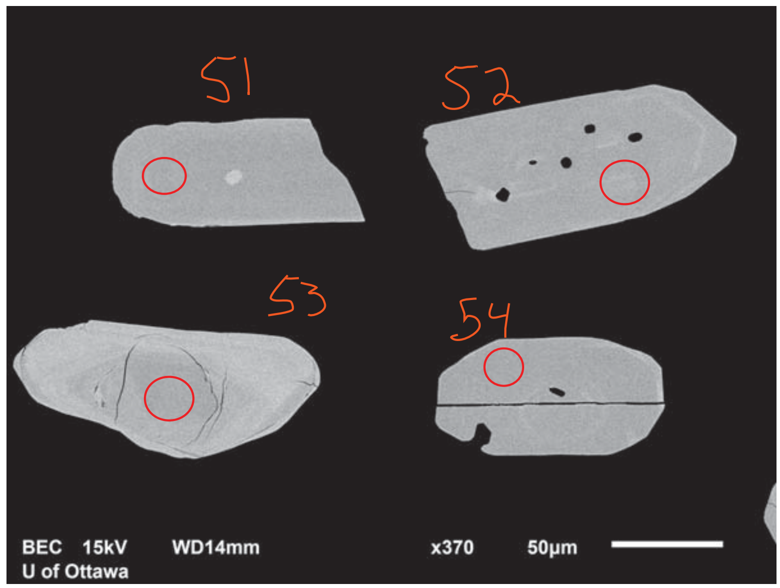
51
52
53
54
BEC 15kV WD14mm x370 50µm
U of Ottawa

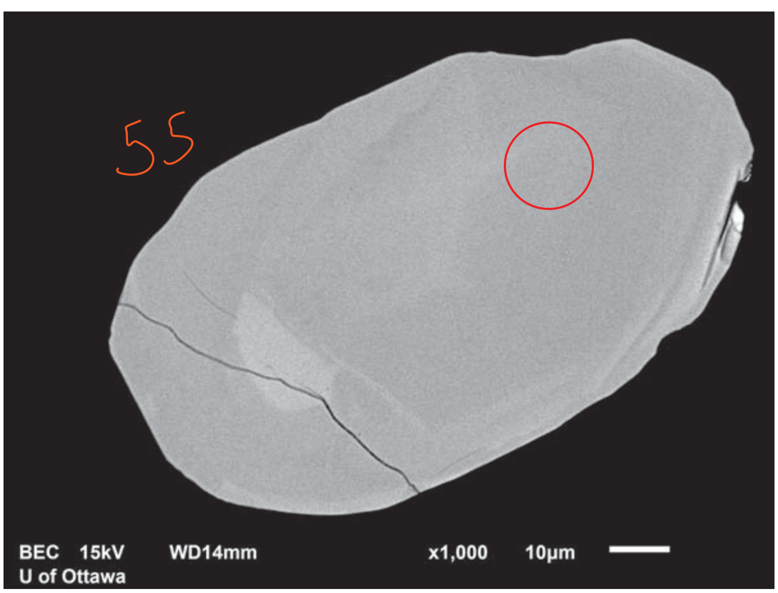
55
BEC 15kV WD14mm x1,000 10µm
U of Ottawa

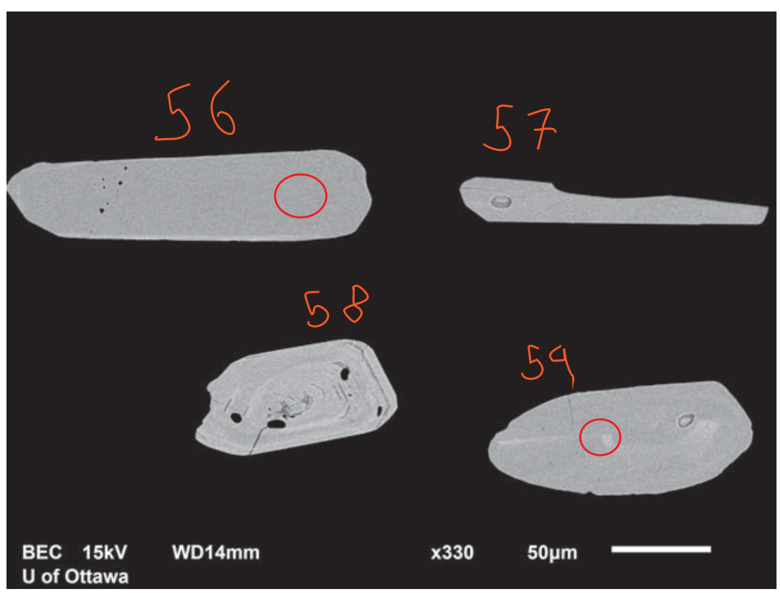
56
57
58
59
BEC 15kV WD14mm x330 50µm
U of Ottawa

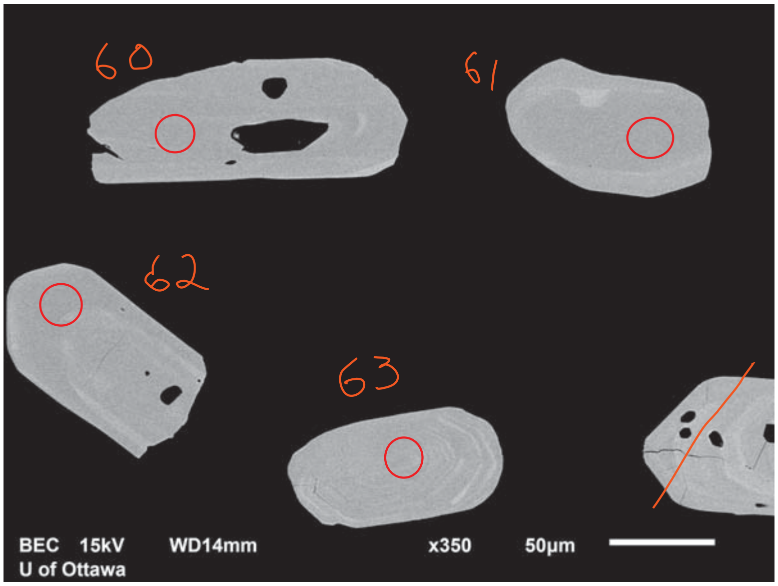
60
61
62
63
BEC 15kV WD14mm x350 50µm
U of Ottawa

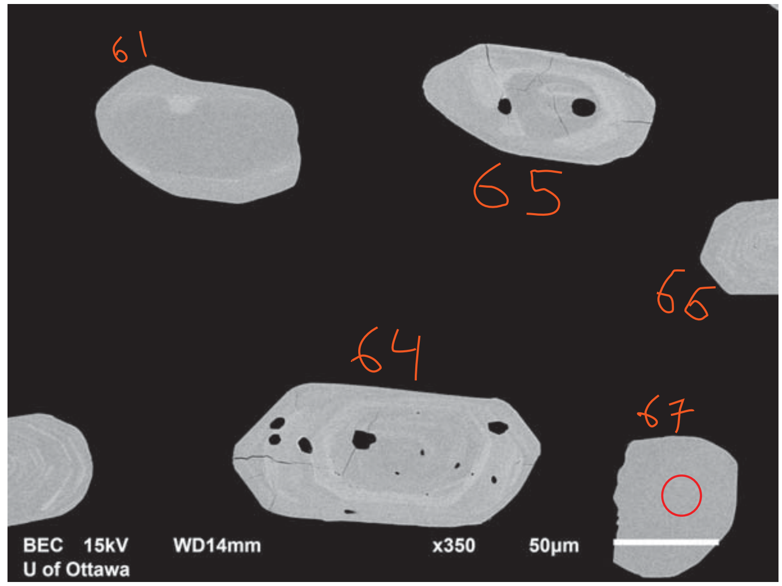
61
65
66
64
67
BEC 15kV WD14mm x350 50µm
U of Ottawa

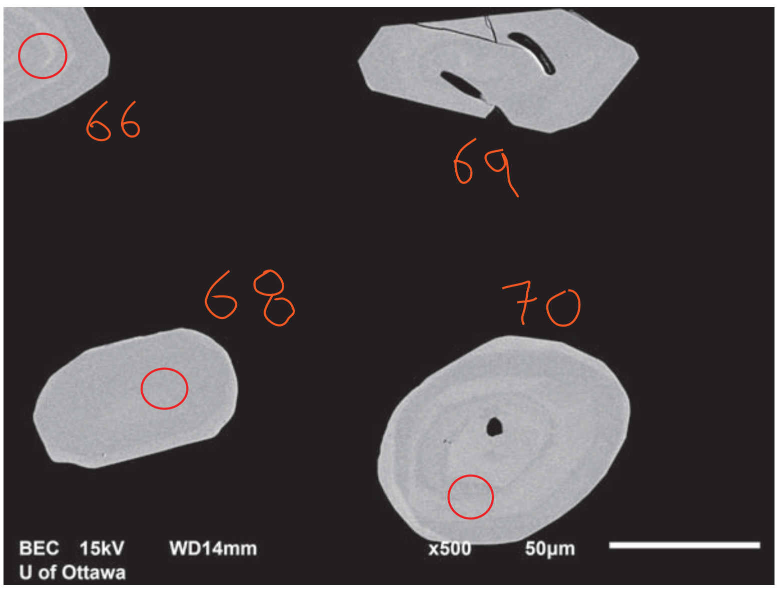
66
69
68
70
BEC 15kV WD14mm x500 50µm
U of Ottawa

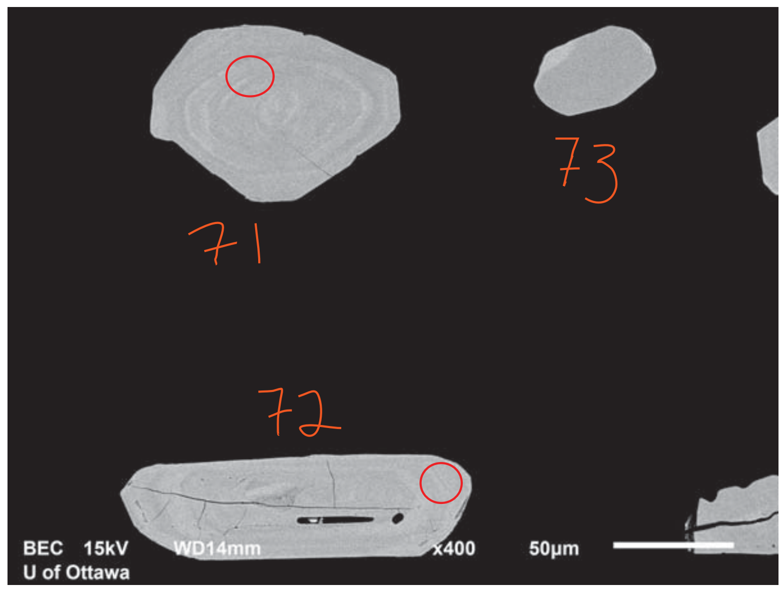
71
73
72
BEC 15kV WD14mm x400 50µm
U of Ottawa

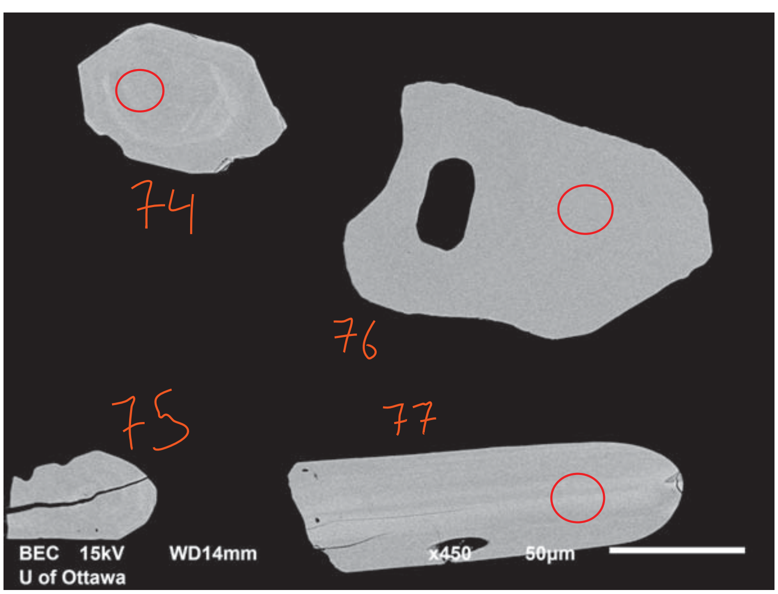
74
76
75
77
BEC 15kV WD14mm x450 50µm
U of Ottawa

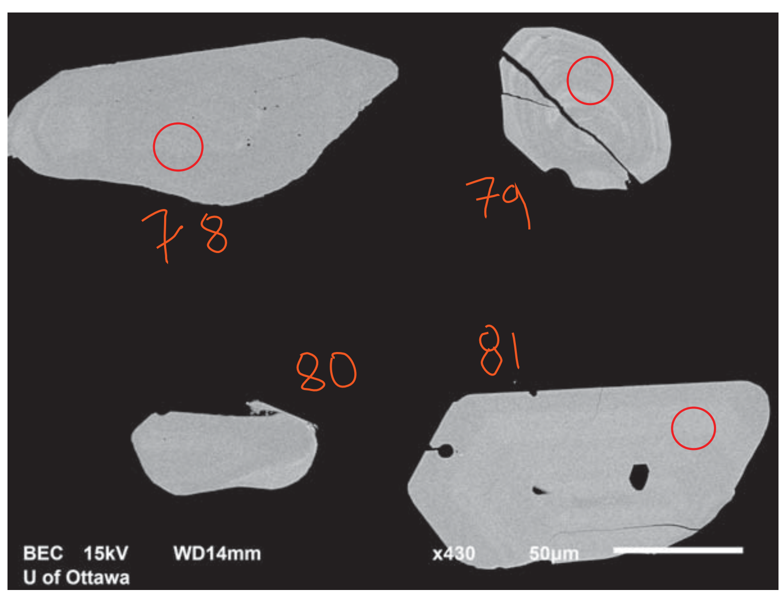
78
79
80
81
BEC 15kV WD14mm x430 50µm
U of Ottawa

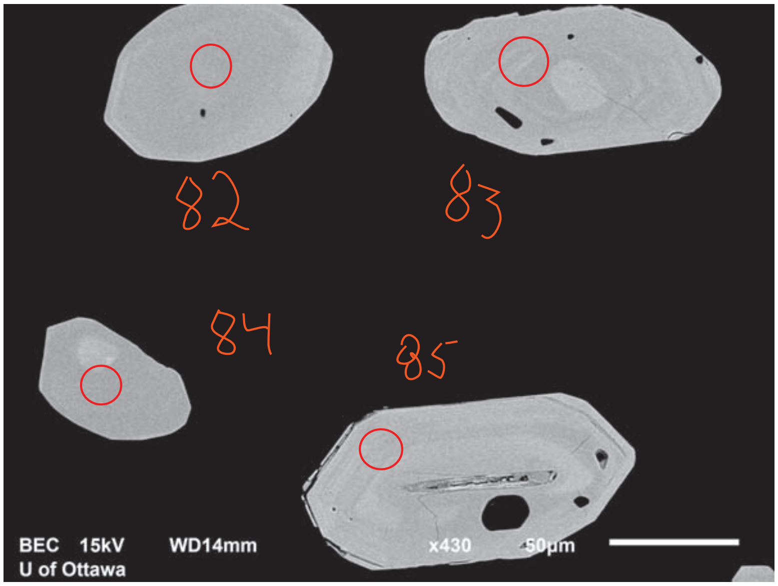
82
83
84
85
BEC 15kV WD14mm x430 50µm
U of Ottawa

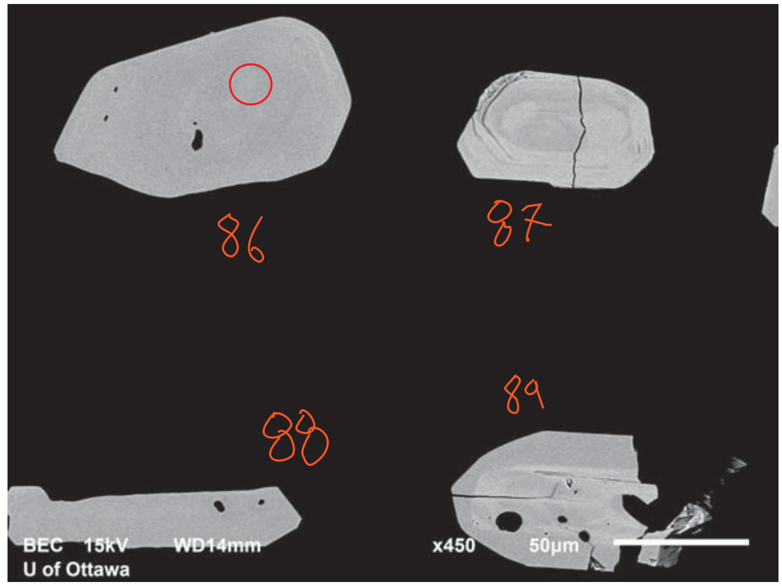
86
87
88
89
BEC 15kV WD14mm x450 50µm
U of Ottawa

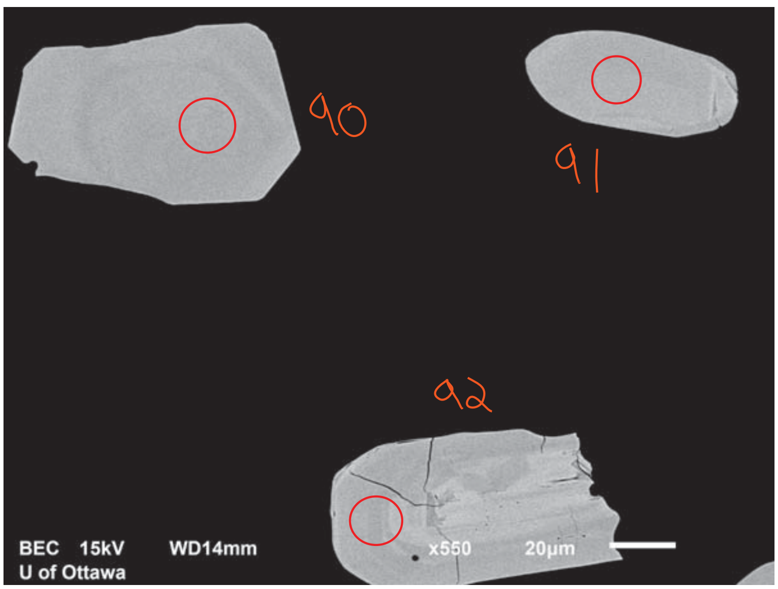
90
91
92
BEC 15kV WD14mm x550 20µm
U of Ottawa

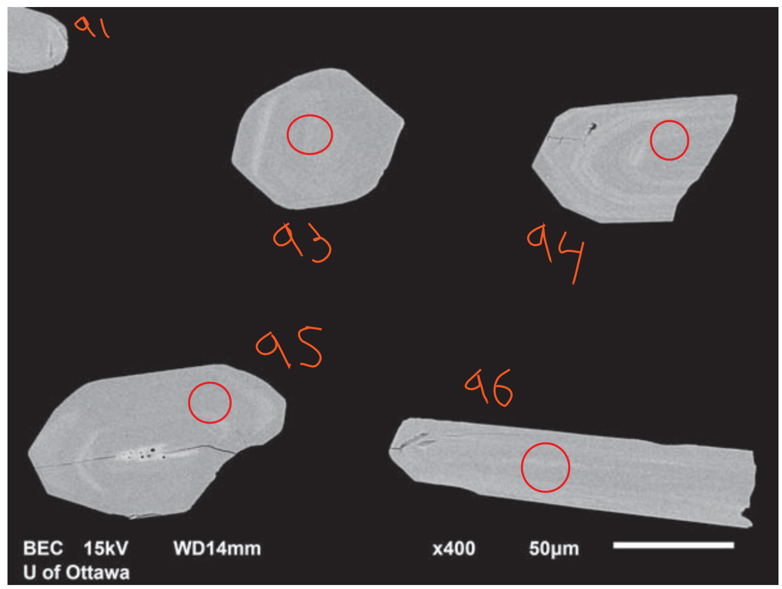
91
93
94
95
96
BEC 15kV WD14mm x400 50µm
U of Ottawa

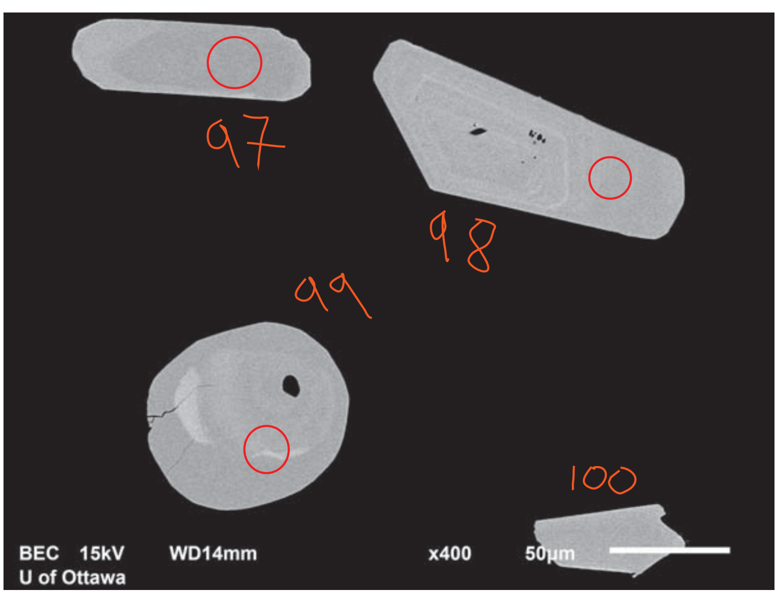
97
98
99
100
BEC 15kV WD14mm x400 50µm
U of Ottawa

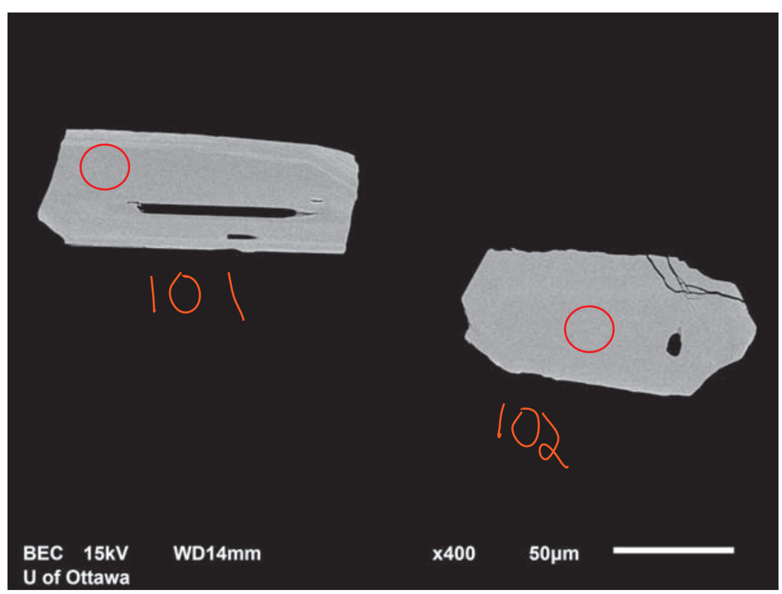
101
102
BEC 15kV WD14mm x400 50µm
U of Ottawa

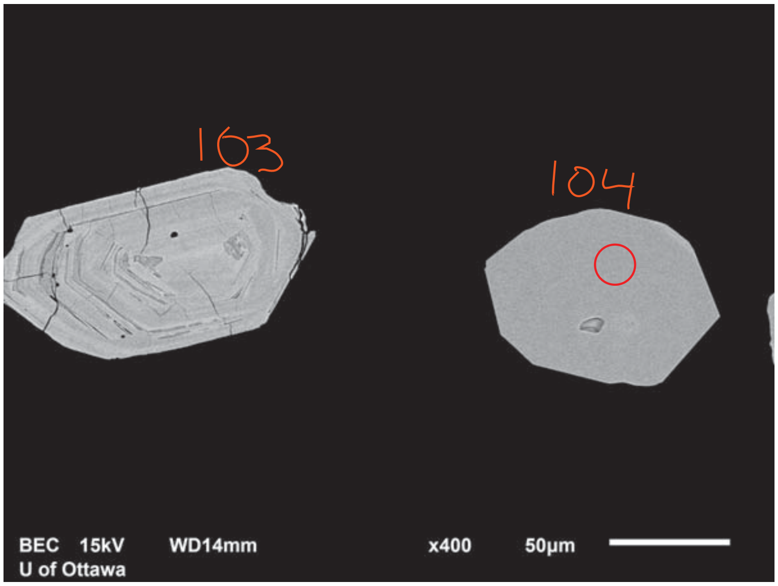
103
104
BEC 15kV WD14mm x400 50µm
U of Ottawa

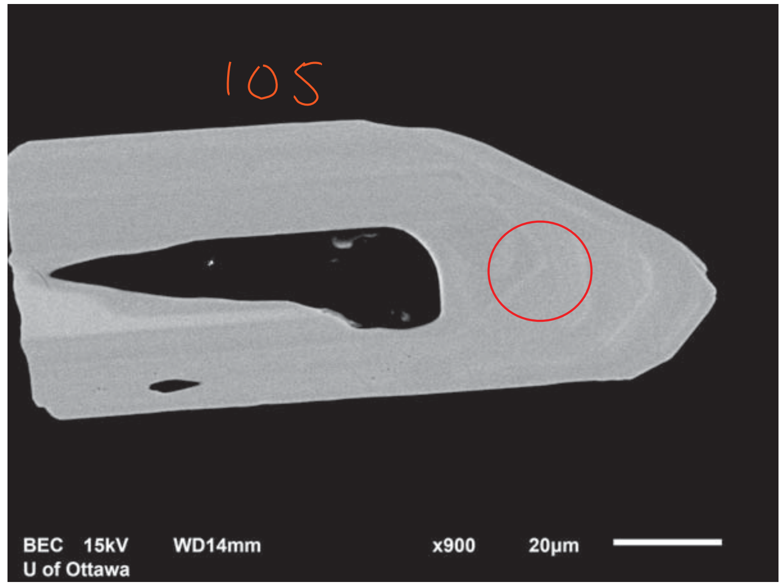
105
BEC 15kV WD14mm x900 20µm
U of Ottawa

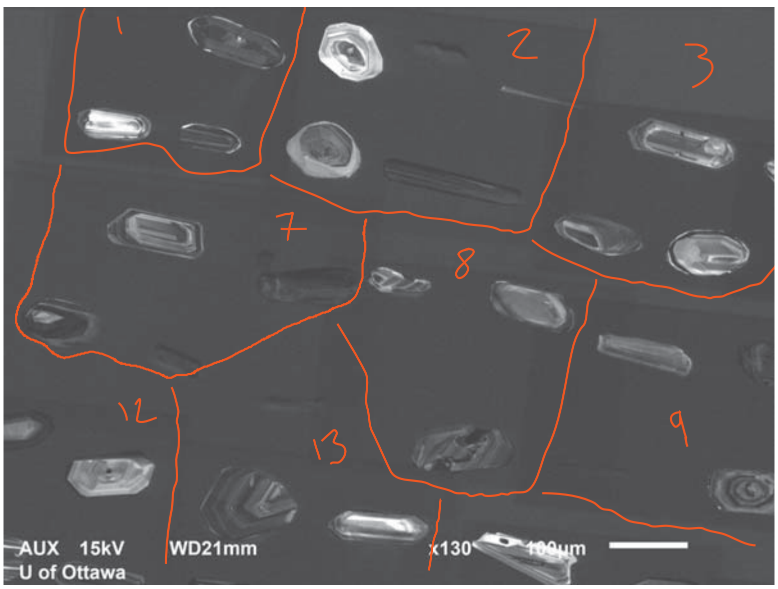
1
2
3
7
8
12
13
9
AUX 15kV WD21mm x130 100µm
U of Ottawa

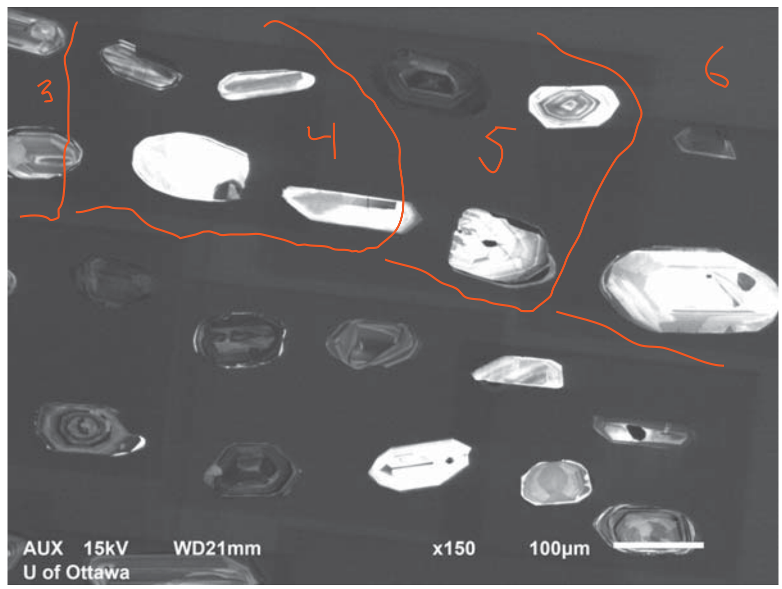
3
4
5
6
AUX 15kV WD21mm x150 100µm
U of Ottawa

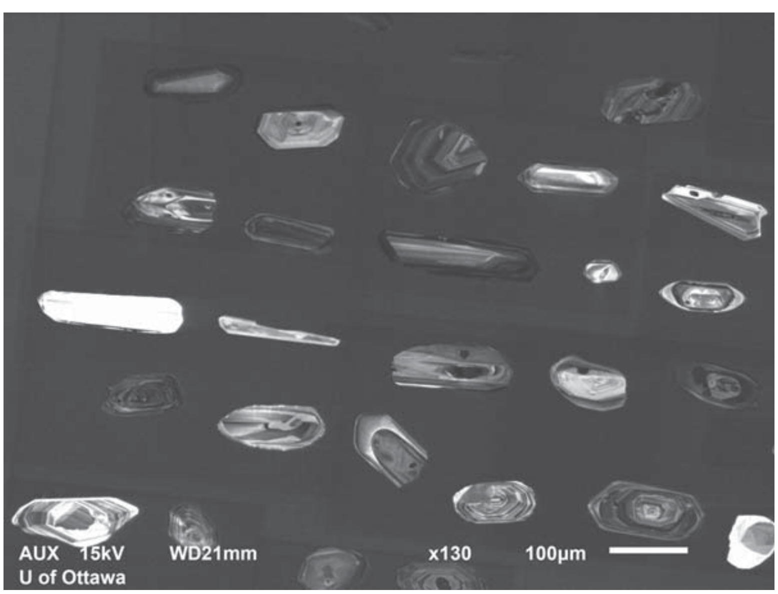
AUX 15kV WD21mm x130 100µm
U of Ottawa

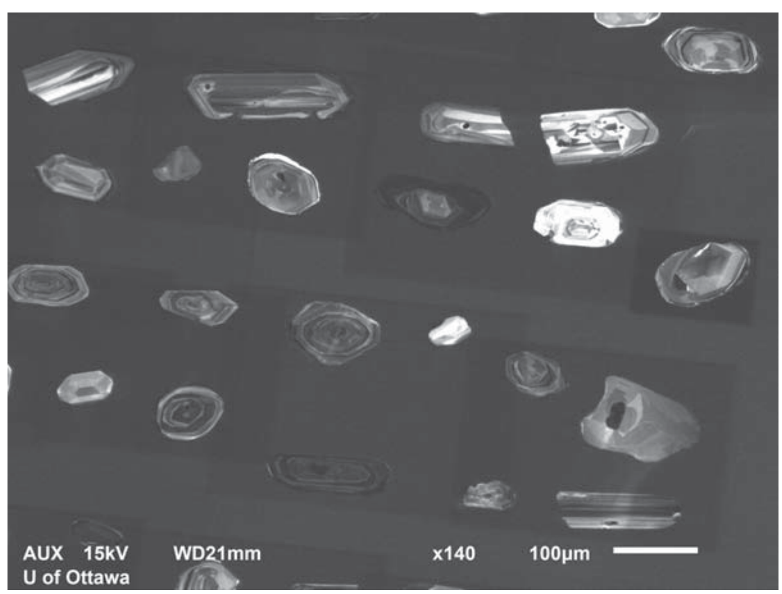
AUX 15kV WD21mm x140 100µm
U of Ottawa

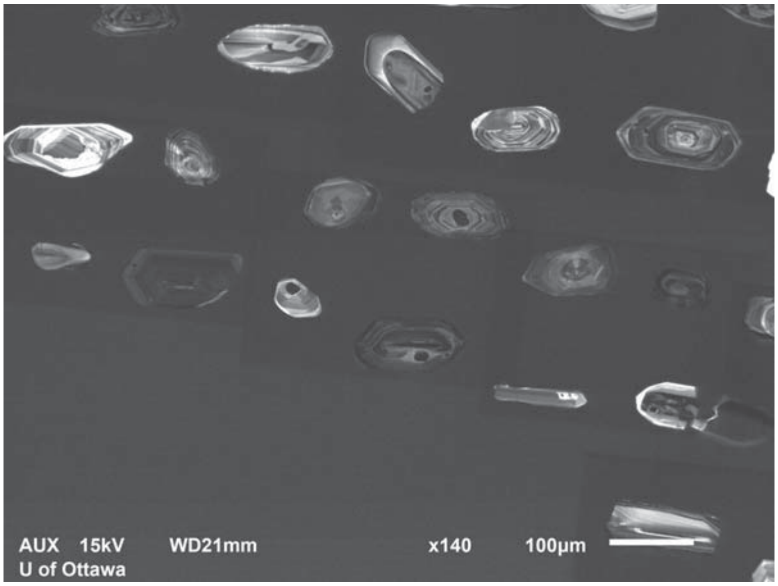
AUX 15kV WD21mm x140 100µm
U of Ottawa

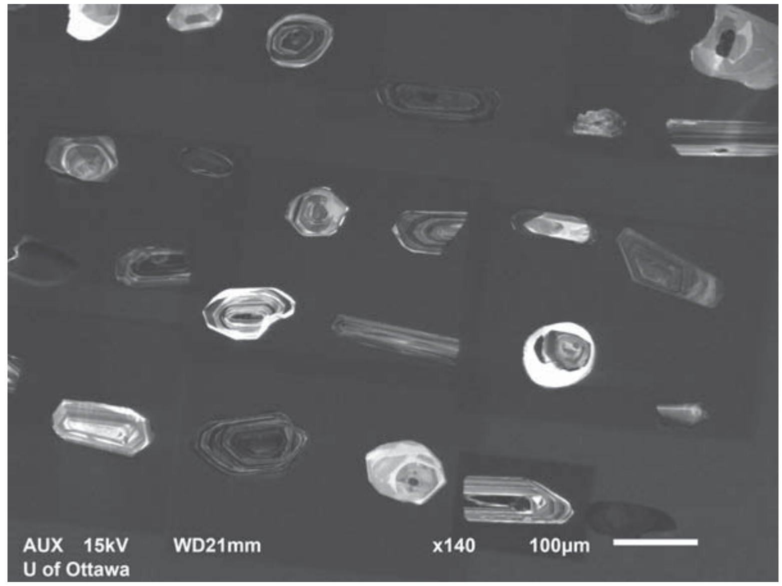
AUX 15kV WD21mm x140 100µm
U of Ottawa

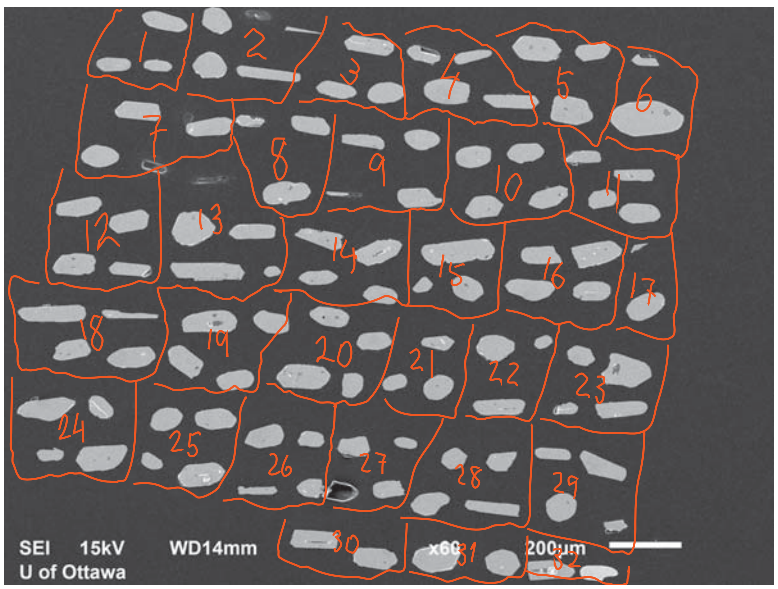
SEI 15kV WD14mm x60 200µm
U of Ottawa
1
2
3
4
5
6
7
8
9
10
11
12
13
14
15
16
17
18
19
20
21
22
23
24
25
26
27
28
29
30
31
32

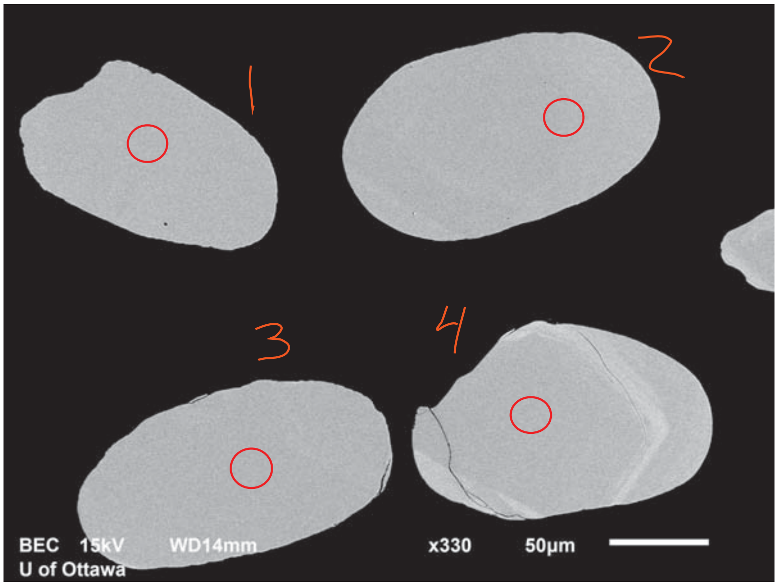

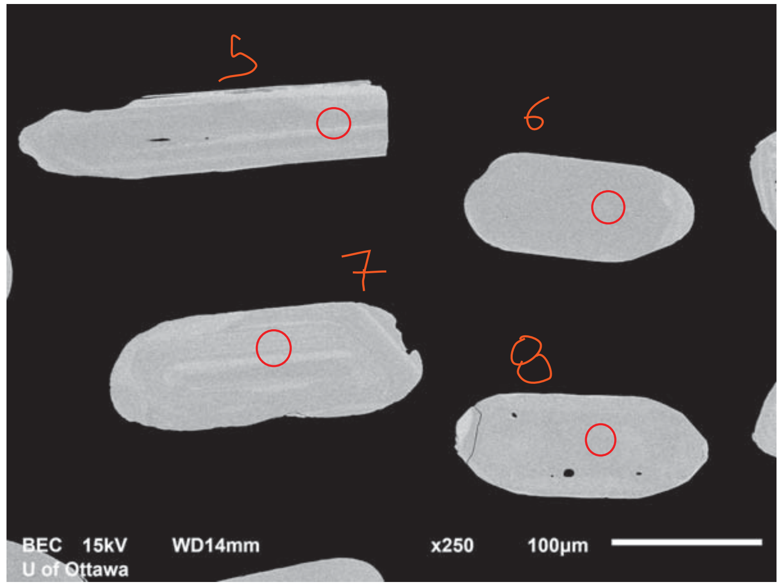

Bjorne Formation (#11243)

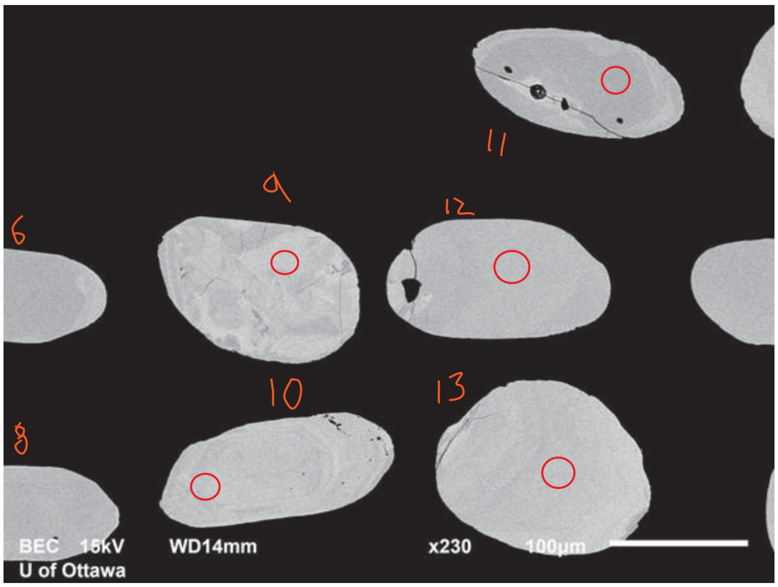

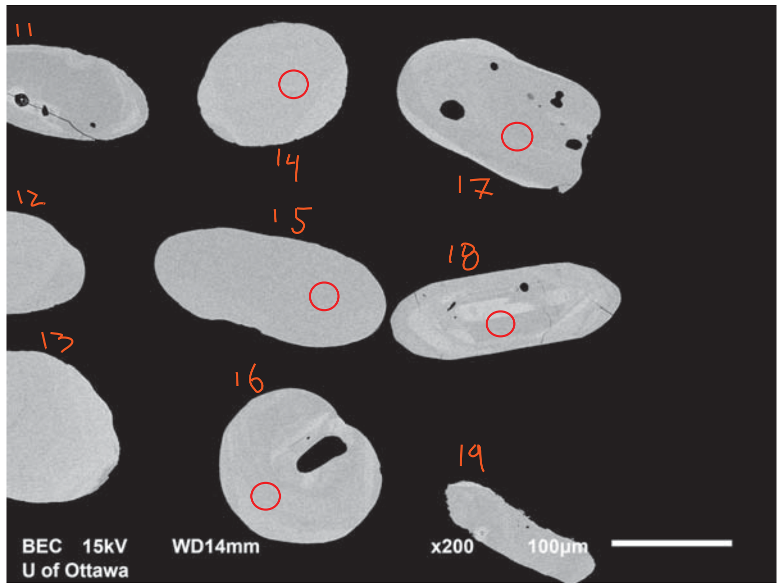

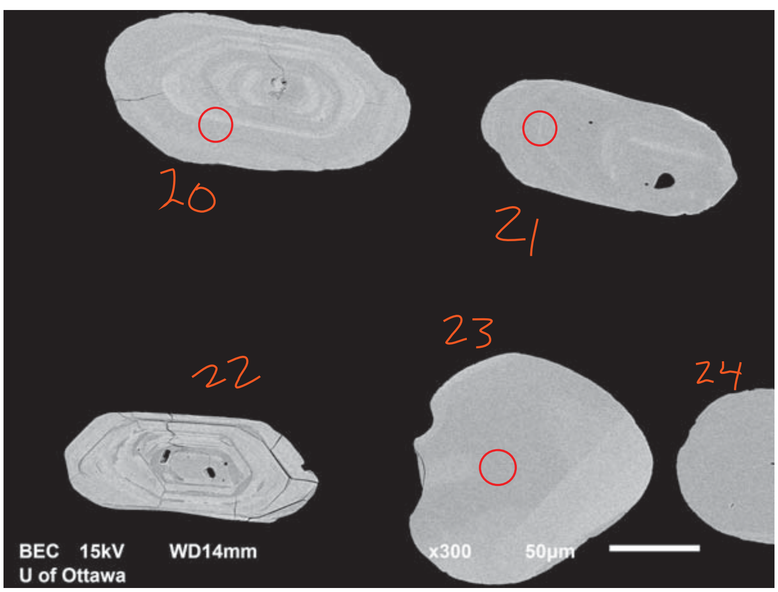

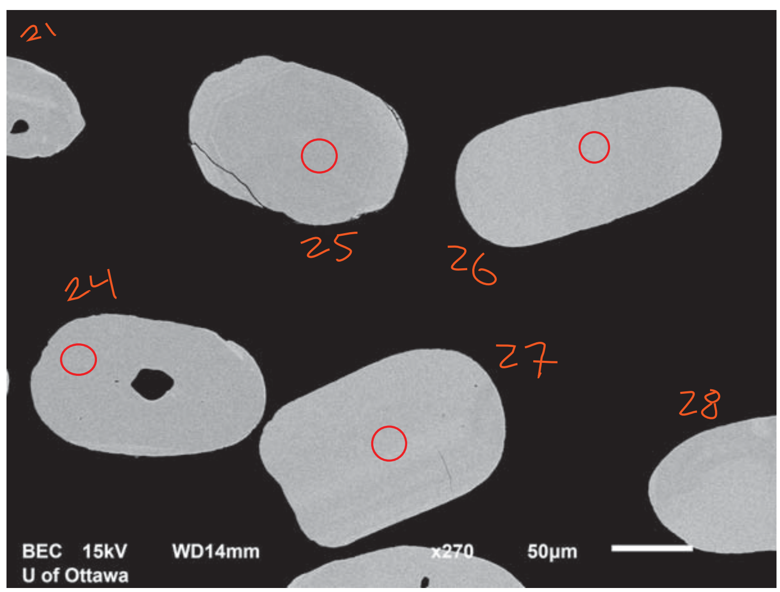

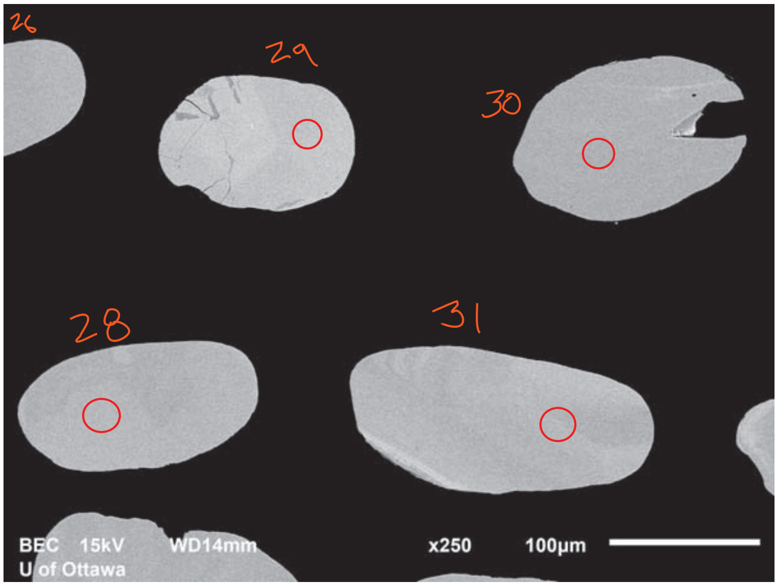
29
30
28
31
BEC 15kV WD14mm x250 100µm
U of Ottawa

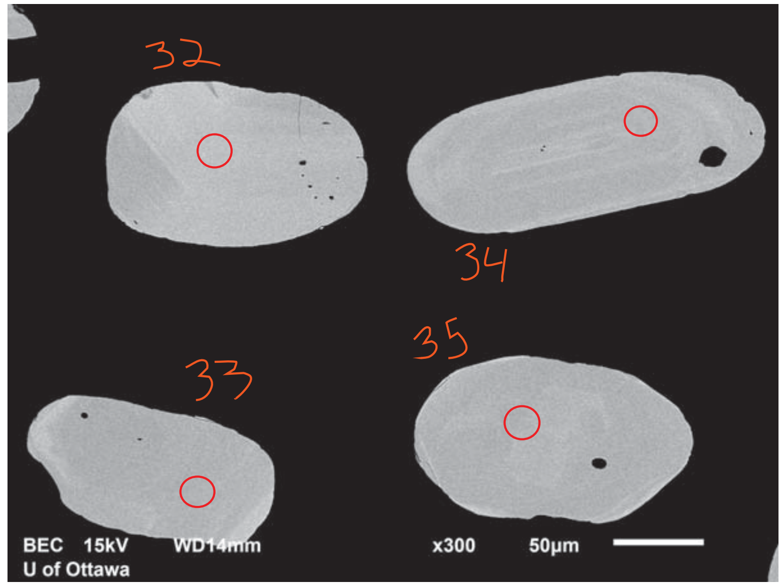
32
34
33
35
BEC 15kV WD14mm x300 50µm
U of Ottawa

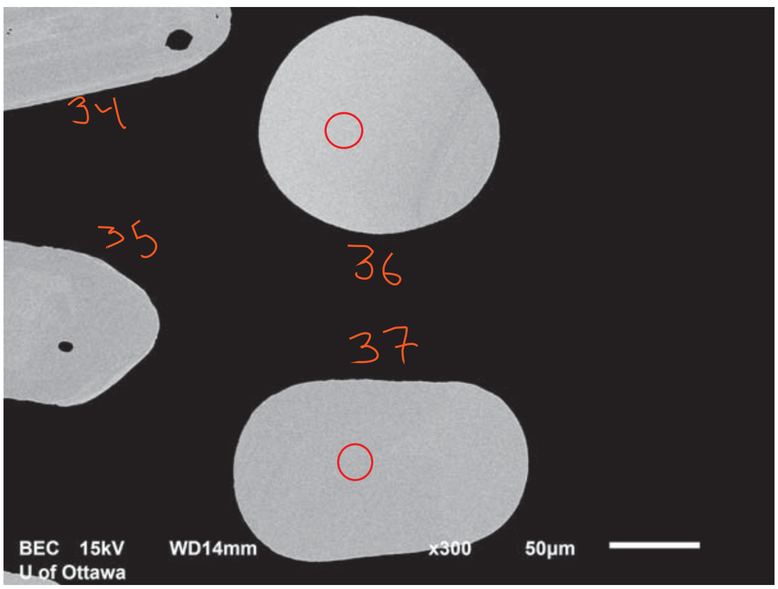
34
35
36
37
BEC 15kV WD14mm x300 50µm
U of Ottawa

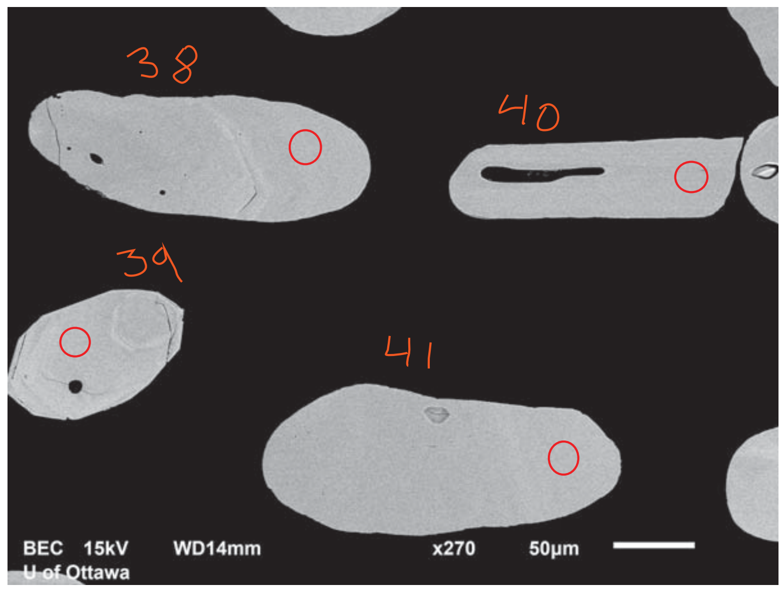
38
40
39
41
BEC 15kV WD14mm x270 50µm
U of Ottawa

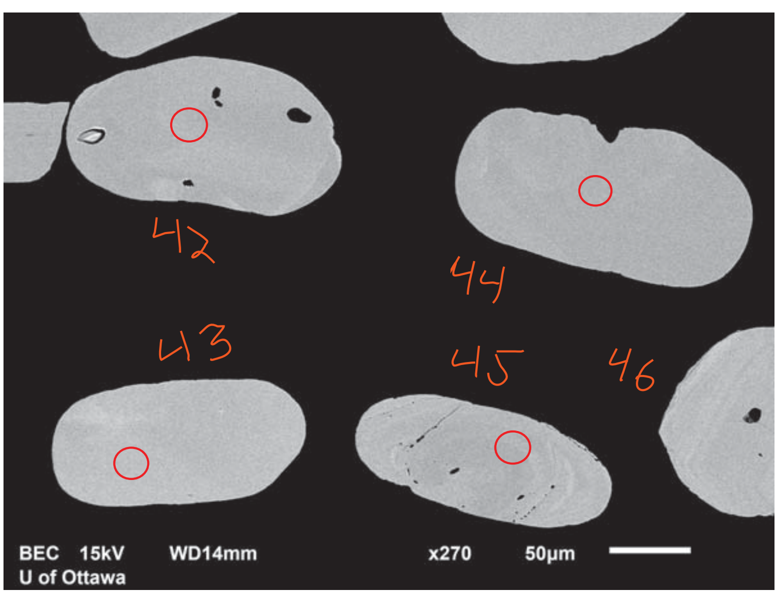
42
44
43
45
46
BEC 15kV WD14mm x270 50µm
U of Ottawa

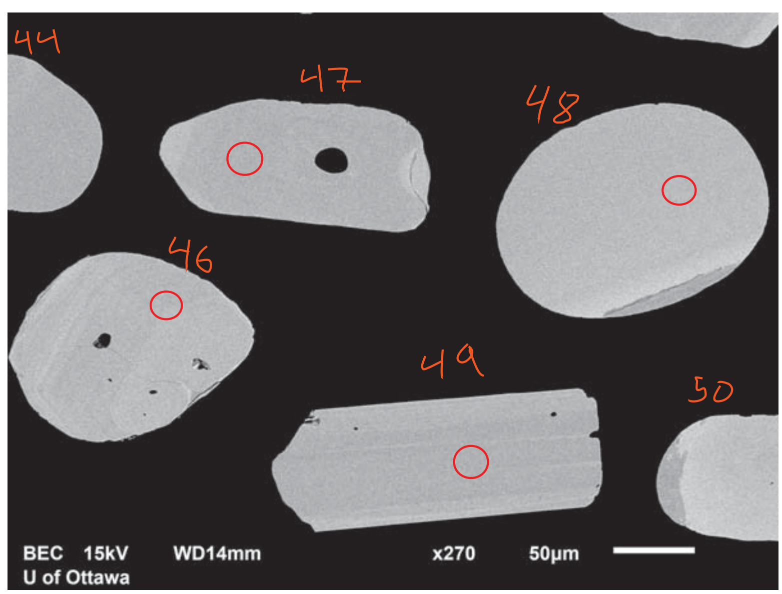
44
47
48
46
49
50
BEC 15kV WD14mm x270 50µm
U of Ottawa

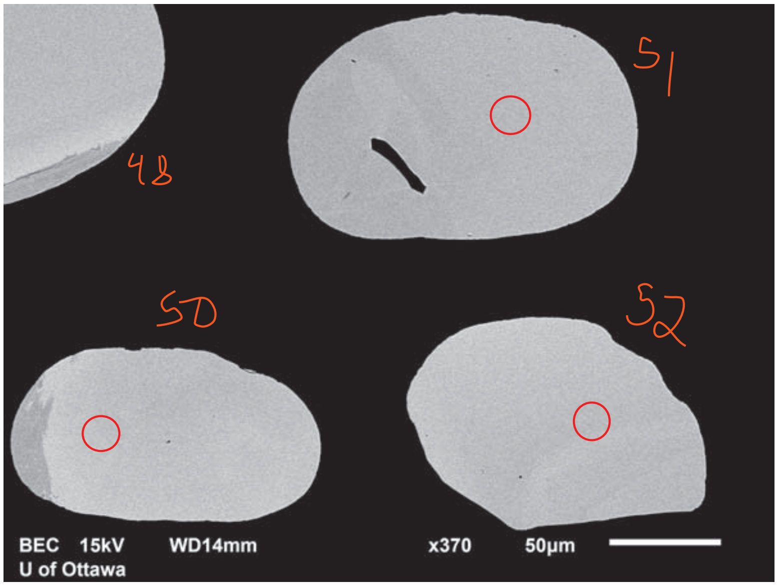
48
51
50
52
BEC 15kV WD14mm x370 50µm
U of Ottawa

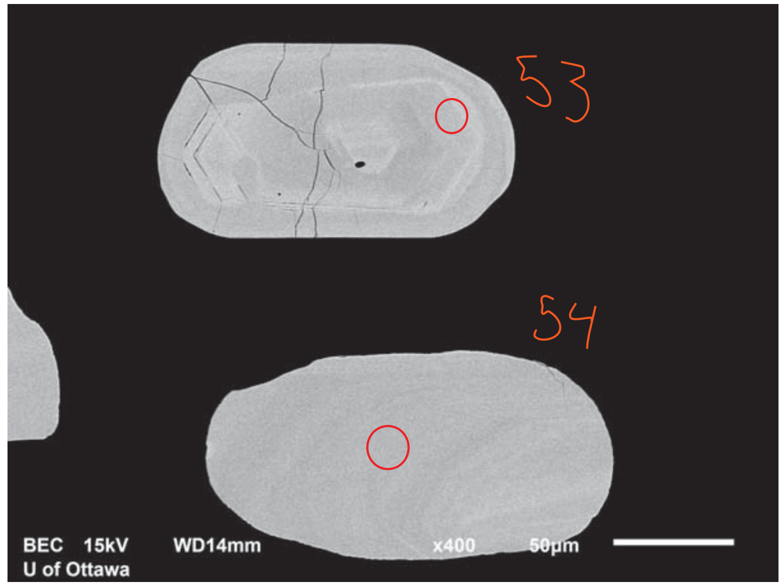
53
54
BEC 15kV WD14mm x400 50µm
U of Ottawa

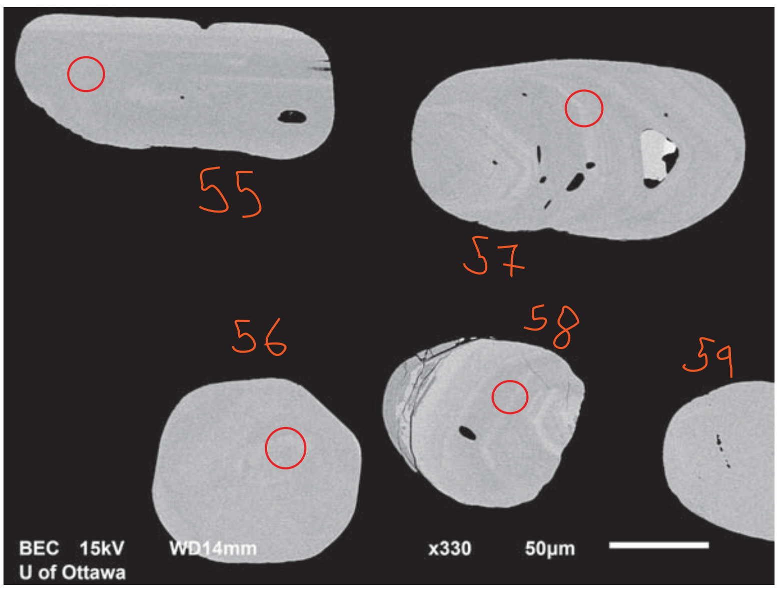
55
57
56
58
59
BEC 15kV WD14mm x330 50µm
U of Ottawa

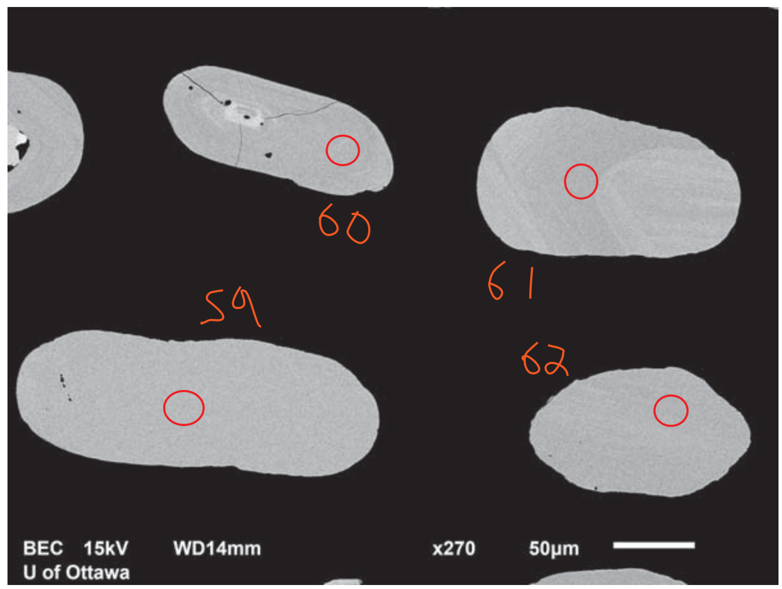
60
61
59
62
BEC 15kV WD14mm x270 50µm
U of Ottawa

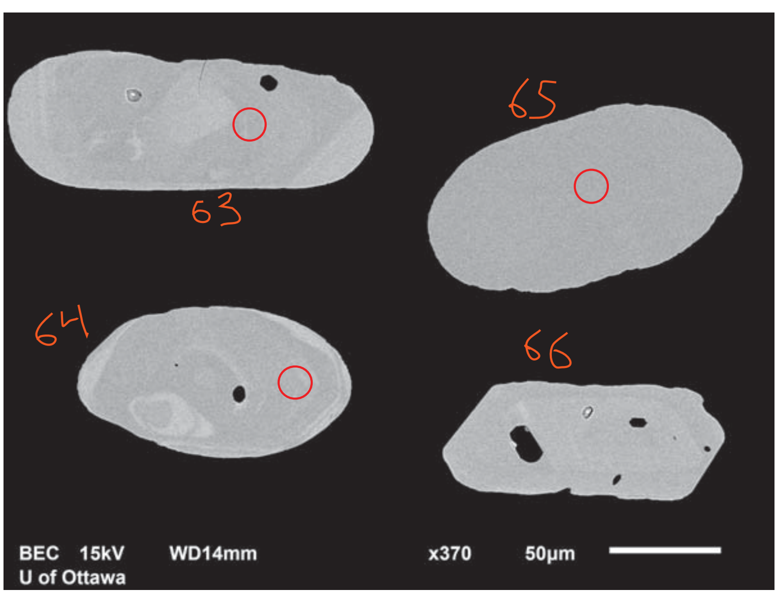
65
63
64
66
BEC 15kV WD14mm x370 50µm
U of Ottawa

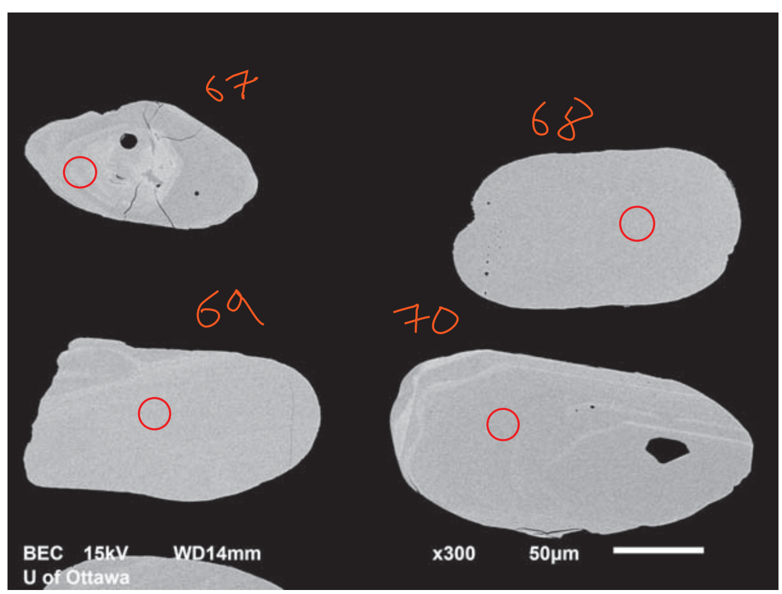
67
68
69
70
BEC 15kV WD14mm x300 50µm
U of Ottawa

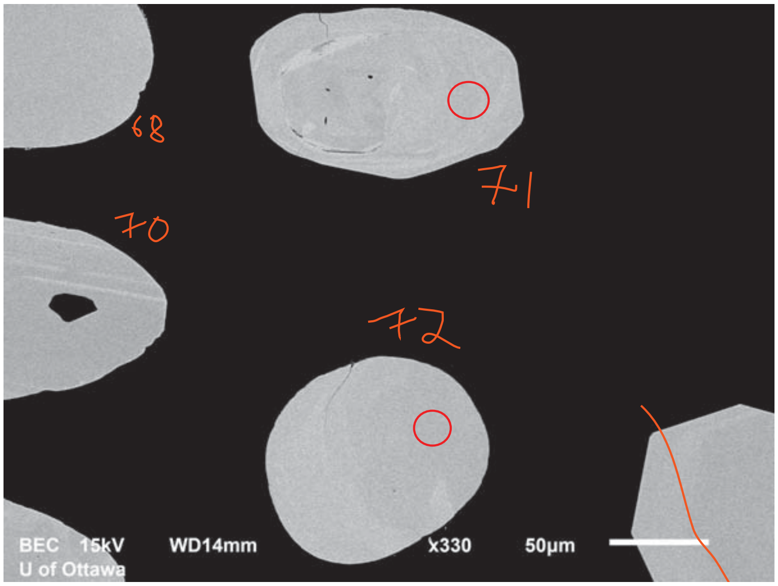
68
71
70
72
BEC 15kV WD14mm x330 50µm
U of Ottawa

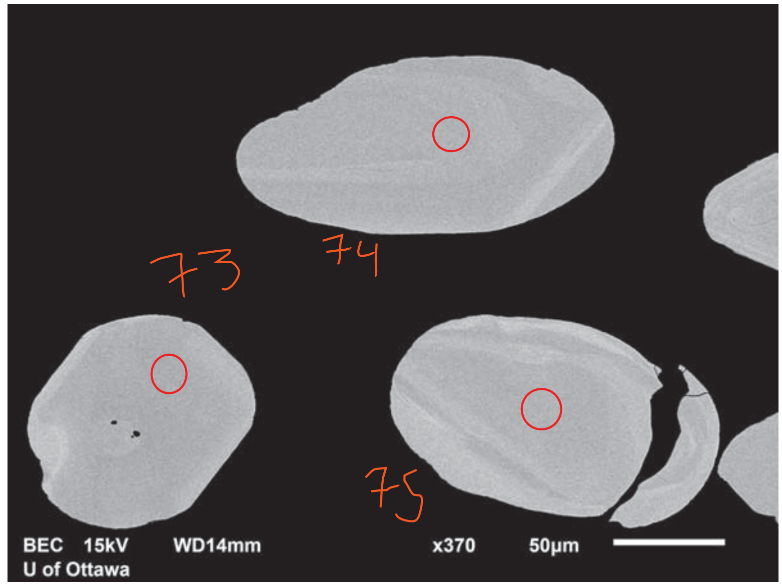
73
74
75
BEC 15kV WD14mm x370 50µm
U of Ottawa

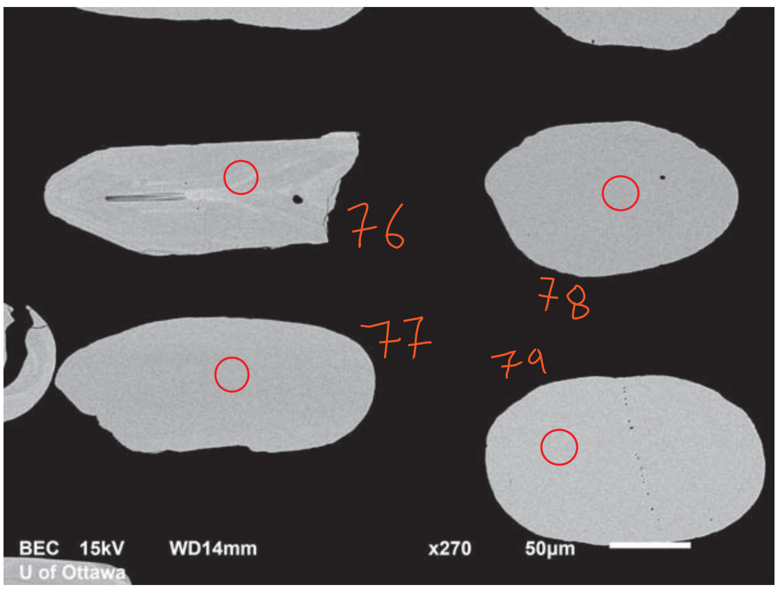
76
78
77
79
BEC 15kV WD14mm x270 50µm
U of Ottawa

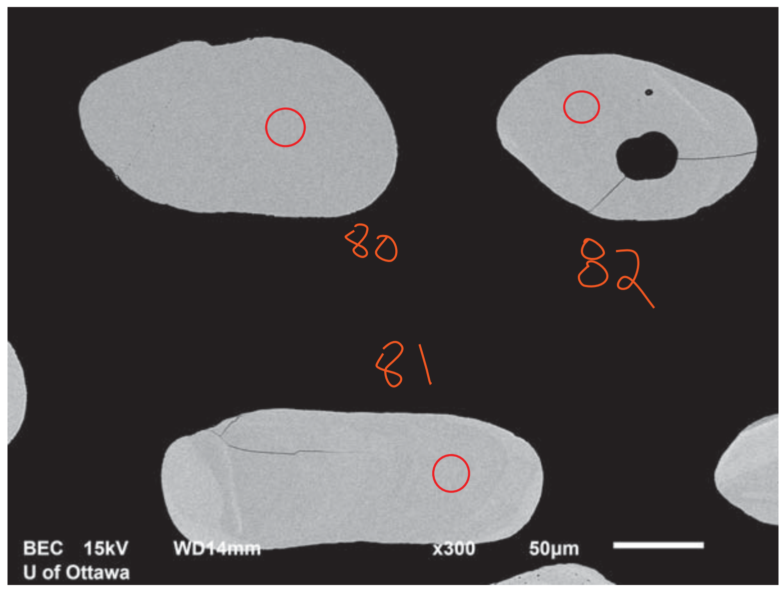
80
82
81
BEC 15kV WD14mm x300 50µm
U of Ottawa

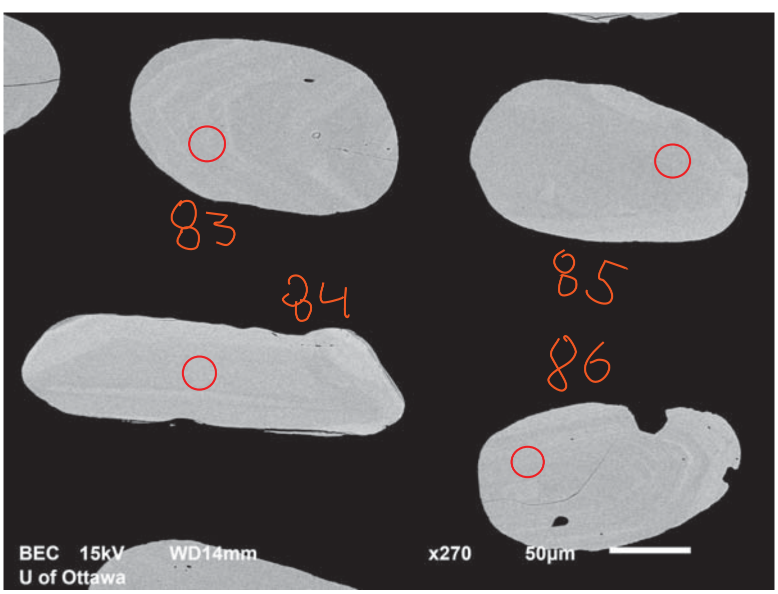
83
84
85
86
BEC 15kV WD14mm x270 50µm
U of Ottawa

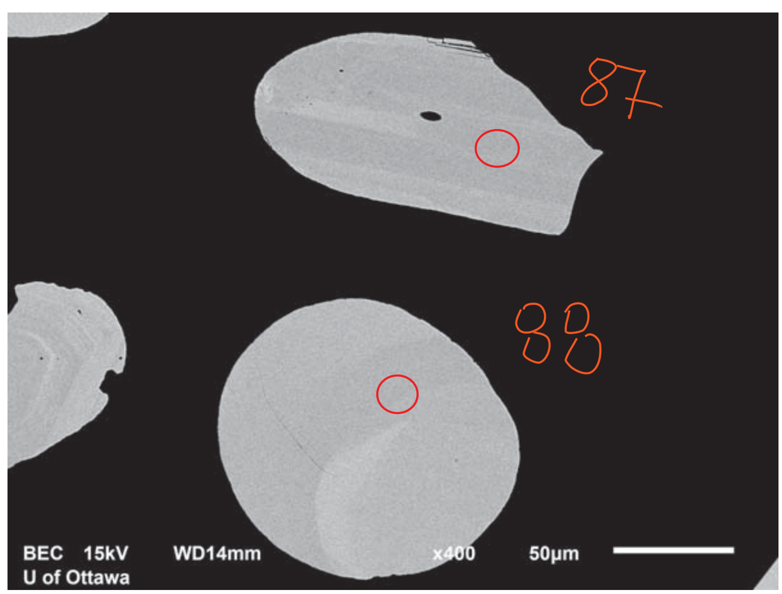
87
88
BEC 15kV WD14mm x400 50µm
U of Ottawa

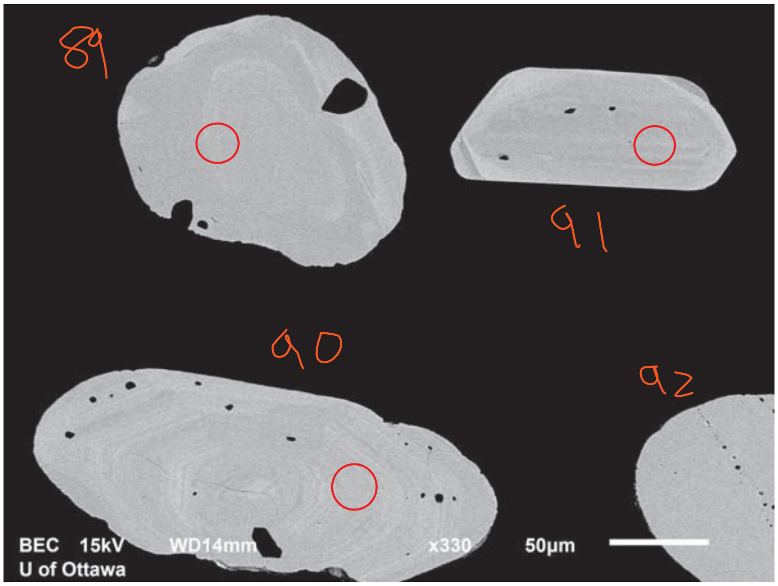
89
91
90
92
BEC 15kV WD14mm x330 50µm
U of Ottawa

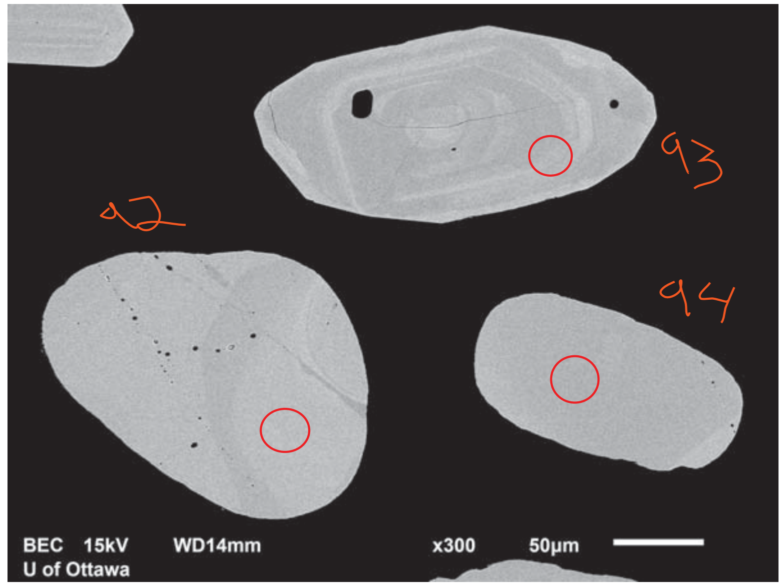
93
92
94
BEC 15kV WD14mm x300 50µm
U of Ottawa

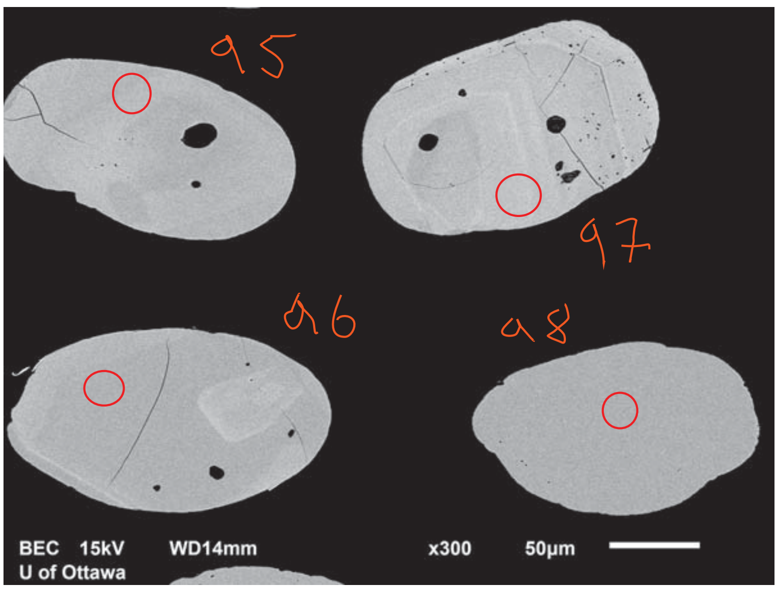
95
97
96
98
BEC 15kV WD14mm x300 50µm
U of Ottawa

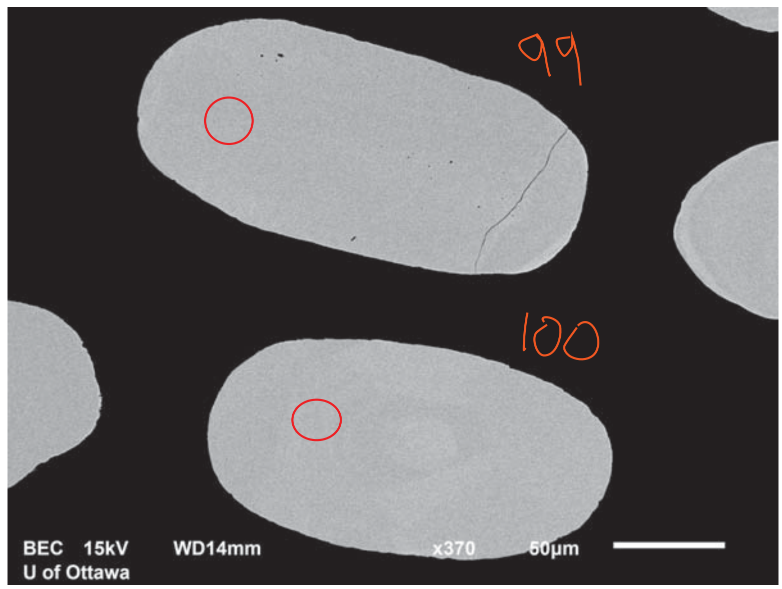
99
100
BEC 15kV WD14mm x370 50µm
U of Ottawa

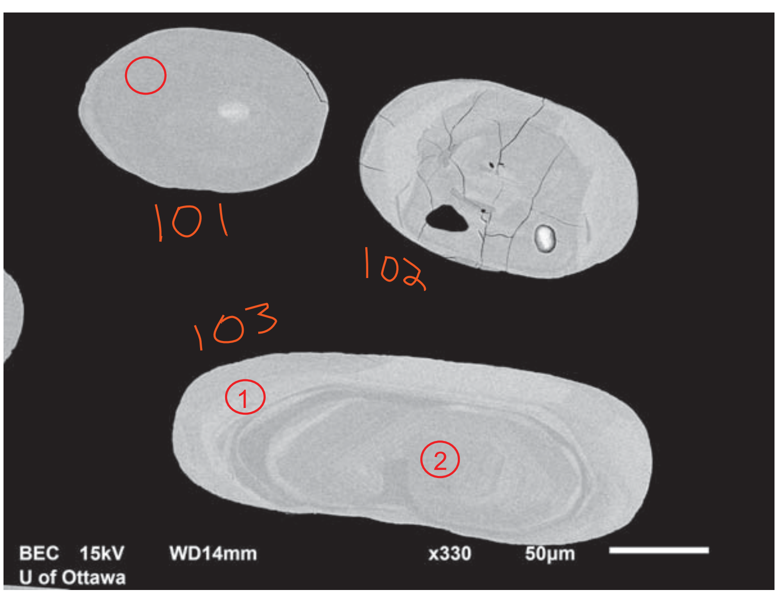
101
102
103
1
2
BEC 15kV WD14mm x330 50µm
U of Ottawa

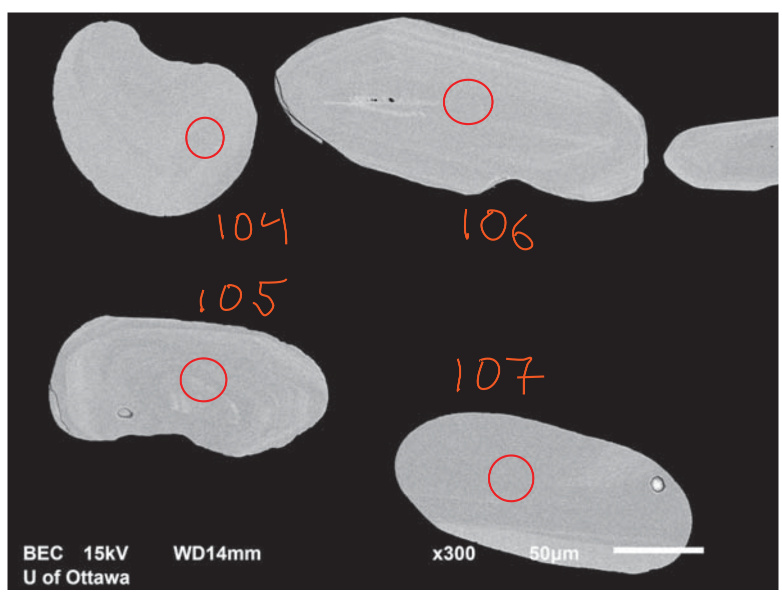
104
106
105
107
BEC 15kV WD14mm x300 50µm
U of Ottawa

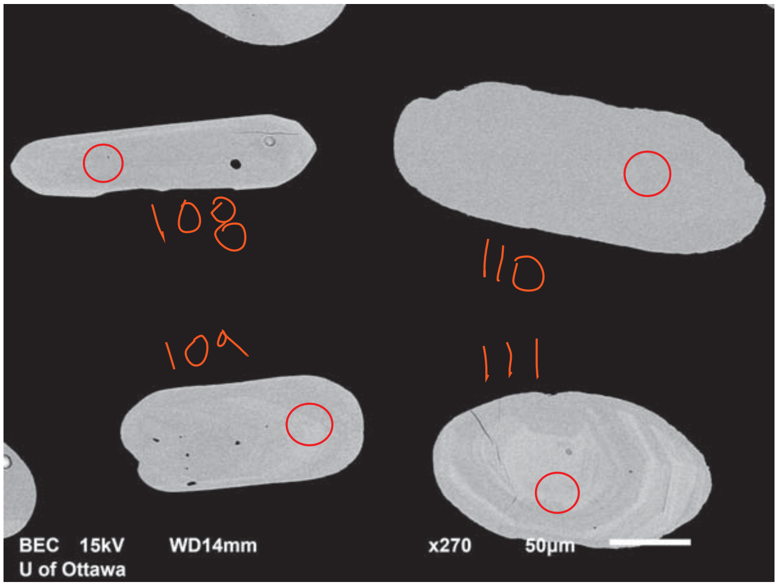
108
110
109
111
BEC 15kV WD14mm x270 50µm
U of Ottawa

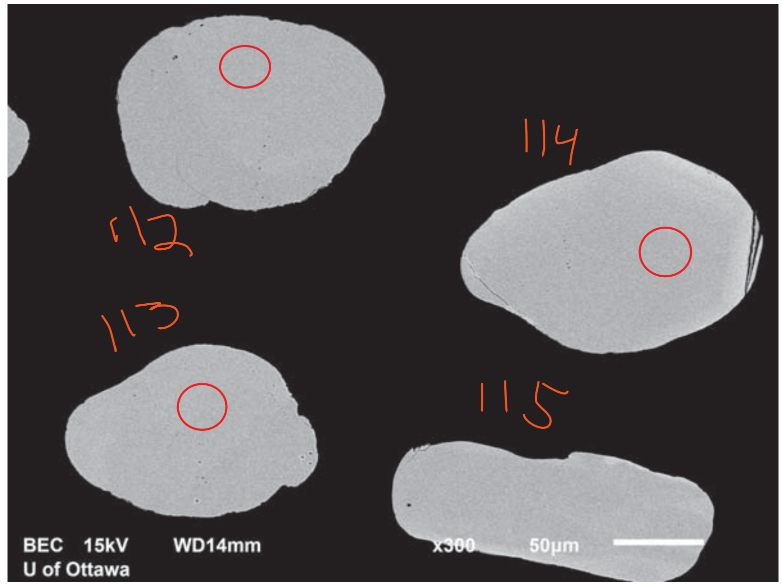
114
112
113
115
BEC 15kV WD14mm x300 50µm
U of Ottawa

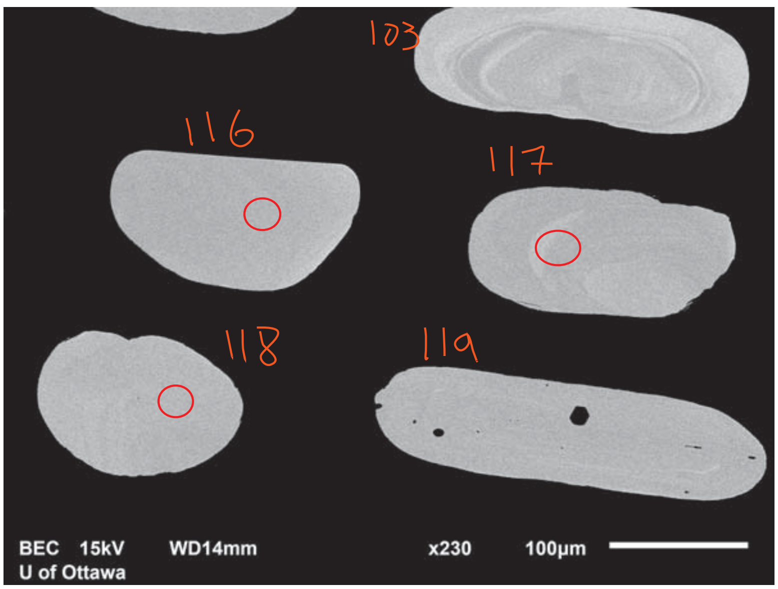
103
116
117
118
119
BEC 15kV WD14mm x230 100µm
U of Ottawa

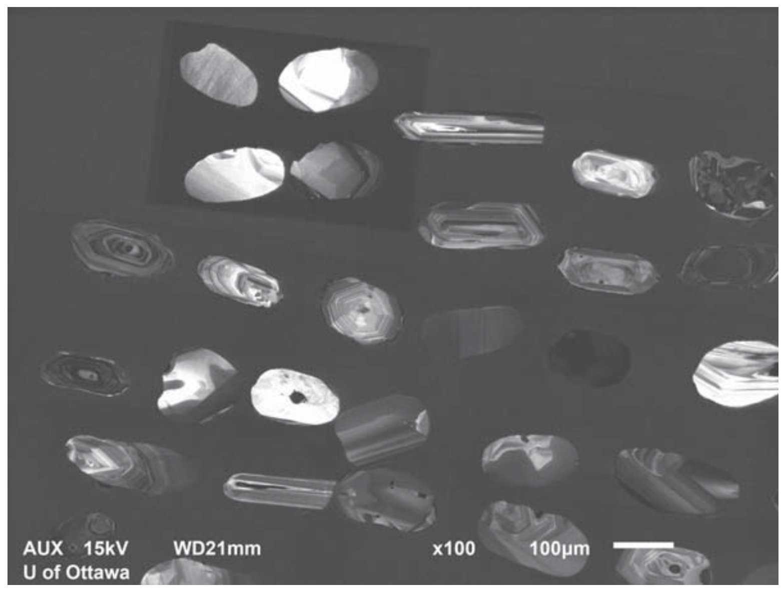
AUX 15kV WD21mm x100 100µm
U of Ottawa

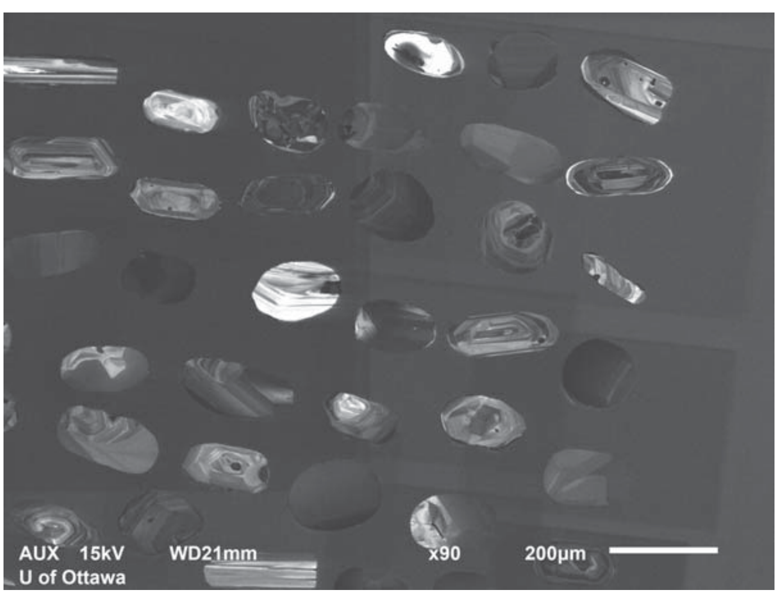
AUX 15kV WD21mm x90 200µm
U of Ottawa

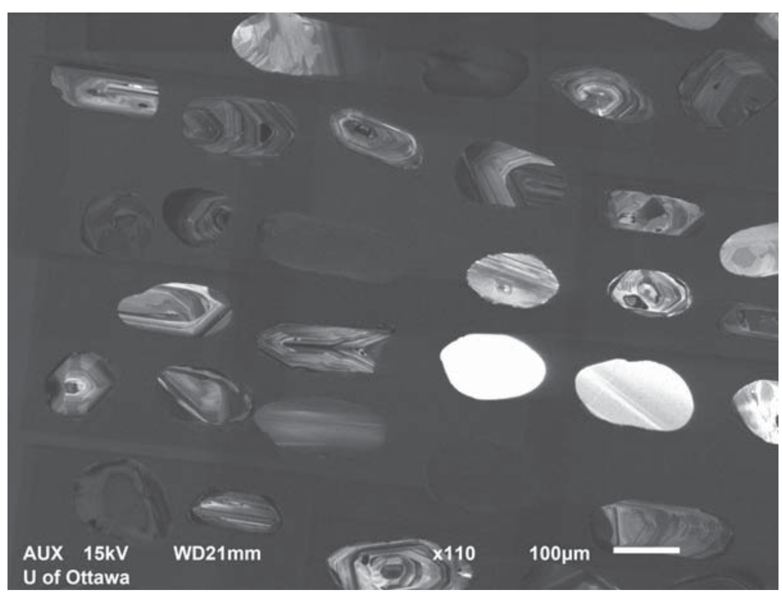
AUX 15kV WD21mm x110 100µm
U of Ottawa

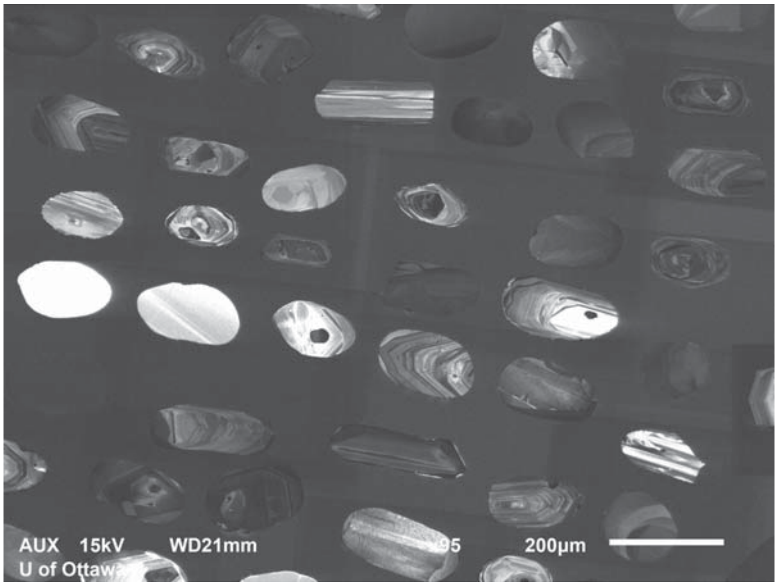
AUX 15kV WD21mm
x95 200µm
U of Ottawa

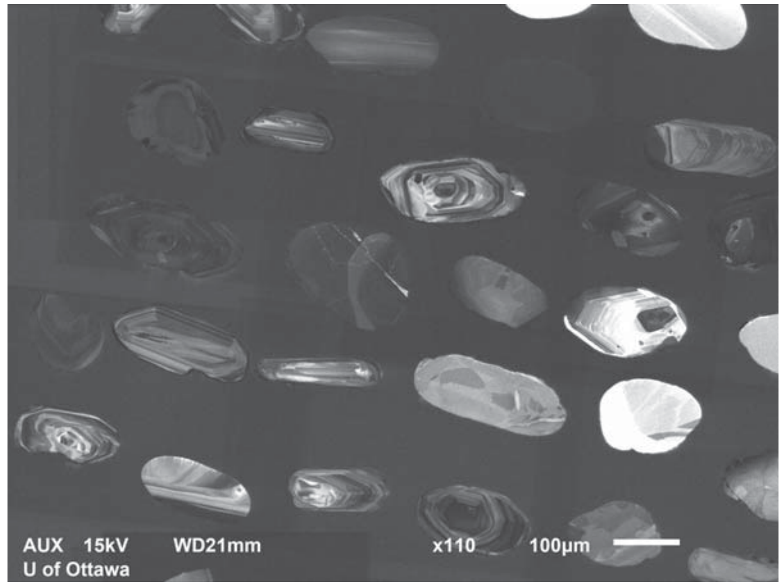
AUX 15kV WD21mm
x110 100µm
U of Ottawa

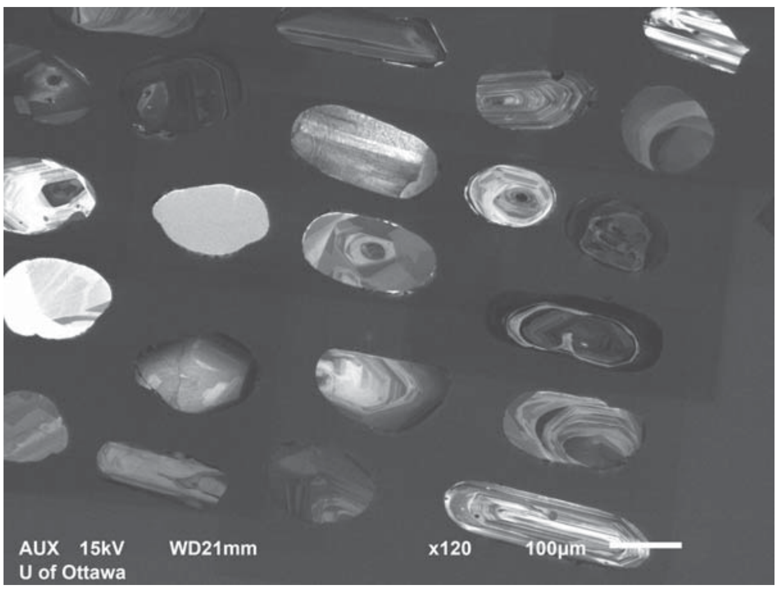
AUX 15kV WD21mm
x120 100µm
U of Ottawa

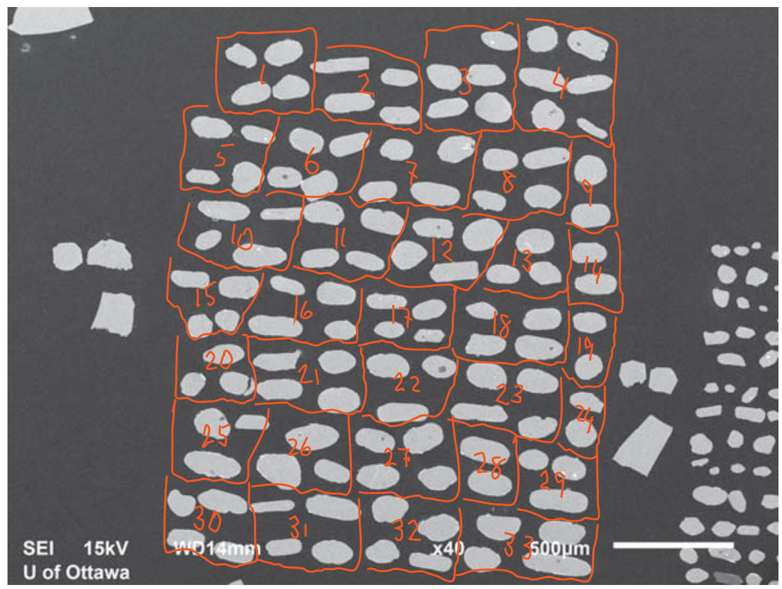
SEI 15kV WD14mm
x40 500µm
U of Ottawa